



Kent Academic Repository

Perry, Christopher, H. (1990) *In-situ dust mass distribution measurements from Giotto encounter with comet P/Halley*. Doctor of Philosophy (PhD) thesis, University of Kent.

Downloaded from

<https://kar.kent.ac.uk/94581/> The University of Kent's Academic Repository KAR

The version of record is available from

<https://doi.org/10.22024/UniKent/01.02.94581>

This document version

UNSPECIFIED

DOI for this version

Licence for this version

CC BY-NC-ND (Attribution-NonCommercial-NoDerivatives)

Additional information

This thesis has been digitised by EThOS, the British Library digitisation service, for purposes of preservation and dissemination. It was uploaded to KAR on 25 April 2022 in order to hold its content and record within University of Kent systems. It is available Open Access using a Creative Commons Attribution, Non-commercial, No Derivatives (<https://creativecommons.org/licenses/by-nc-nd/4.0/>) licence so that the thesis and its author, can benefit from opportunities for increased readership and citation. This was done in line with University of Kent policies (<https://www.kent.ac.uk/is/strategy/docs/Kent%20Open%20Access%20policy.pdf>). If you ...

Versions of research works

Versions of Record

If this version is the version of record, it is the same as the published version available on the publisher's web site. Cite as the published version.

Author Accepted Manuscripts

If this document is identified as the Author Accepted Manuscript it is the version after peer review but before type setting, copy editing or publisher branding. Cite as Surname, Initial. (Year) 'Title of article'. To be published in **Title of Journal**, Volume and issue numbers [peer-reviewed accepted version]. Available at: DOI or URL (Accessed: date).

Enquiries

If you have questions about this document contact ResearchSupport@kent.ac.uk. Please include the URL of the record in KAR. If you believe that your, or a third party's rights have been compromised through this document please see our [Take Down policy](https://www.kent.ac.uk/guides/kar-the-kent-academic-repository#policies) (available from <https://www.kent.ac.uk/guides/kar-the-kent-academic-repository#policies>).

In-Situ Dust Mass Distribution
Measurements from the Giotto Encounter
with Comet P/Halley

A thesis submitted for the degree of

Doctor of Philosophy

by

Christopher H. Perry

University of Kent at Canterbury

1990

ABSTRACT

On the night of the 13/14th of March 1986 the European Space Agency's Giotto spacecraft passed within 600km of the nucleus of comet P/Halley. On board the spacecraft was an impressive array of experiments designed to study all aspects of the cometary coma and provide high resolution images of the nucleus.

The principle experiment designed to measure the coma dust mass distribution was called the Dust Impact Detection System (DIDSY). The design operation and performance of this experiment are considered and details are provided of post-mission recalibration, including the development of a software simulation to aid in the interpretation of the returned data.

The faulty operation of one of the DIDSY sensors resulted in the use of the front end channels of the Particulate Impact Analyser Experiment (PIA) to provide information on particles of mass $10^{-19}\text{kg} \leq m \leq 10^{-15}\text{kg}$. The techniques used to extract the required information and calibrate the sensor using encounter data and the inter-relationship between different operating modes is described.

The analysis of impacts which caused multiple detection by two or more of the DIDSY sensors is described and the results from these multi-sensor events used to extend the measured mass range up to 10^{-5}kg .

A mass distribution representative of the coma passed through by Giotto was constructed and this is combined with a simple model to obtain the dust production rate and dust to gas ratio.

ACKNOWLEDGEMENTS

I wish to thank my supervisor, Professor Tony McDonnell, for his invaluable guidance and support. Acknowledgment must go to all those too numerous to mention who played their part in making the Giotto mission and DIDSY experiment the success that it undoubtedly was. Special thanks to the DIDSY data analysis team at UKC; Dr Simon Green, Stefano Nappo, Dr George Pankiewicz, and Dr John Zarnecki, who spent many hours sifting through calibration data, considering calibration and data analysis techniques and offering useful suggestions. Thanks also to Tim Stevenson for his assistance in the understanding of the operation of the DIDSY hardware and software, without which the software model of the experiment might not have been possible.

I would also like to express my appreciation to the DIDSY and PIA teams at the Max Planck Institut für Kernphysik, Heidelberg. Dr E. Grün, Dr D. Maas, Dr L. Massonne, Dr J. Kissel and Dr P. Hisung for his help on the PIA analysis.

I gratefully acknowledge the S.E.R.C. for the provision of a postgraduate research grant (B/86321682).

Finally I wish to thank all my family and friends for their support.

CONTENTS

ABSTRACT	ii
ACKNOWLEDGEMENTS	iii
CONTENTS	iv
Chapter 1: INTRODUCTION	1
Chapter 2: THE GIOTTO MISSION	7
2.1 Target selection	10
2.2 The Giotto spacecraft	13
2.3 The DIDSY experiment	20
2.3.1 Piezoelectric momentum sensors	20
2.3.2 Penetration type sensors	23
2.3.3 Impact plasma detection	25
2.3.4 Data processing unit	27
2.4 The Particulate Impact Analyser	32
2.5 Other Giotto dust experiments	35
Chapter 3: DIDSY CALIBRATION	36
3.1 Absolute sensitivity	38
3.1.1 Accelerator measurements	39
3.1.2 Low velocity micro bead measurements	40
3.1.3 Piezoelectric stimulation measurements	41
3.1.4 Laser stimulation measurements	42
3.1.5 MSM sensitivities	43
3.2 Experiment signal transfer function	44
3.3 Relative shield sensitivity	48
3.4 Effective area calculation	52
3.4.1 Effective area calculation for MSM	54
3.5 Mass thresholds	60
3.6 Integration times and corrections for experimental dead times	63
Chapter 4: A SOFTWARE MODEL OF THE GIOTTO DIDSY EXPERIMENT	68
4.1 DIDSY: System testing prior to encounter	70
4.2 Software simulation of DIDSY	72

4.2.1 Simulation of the DIDSY hardware	72
4.2.2 Simulation of the digital sub-systems	74
4.2.2.1 Simulation of IPM-P	74
4.2.2.2 Simulation of CIS	76
4.2.2.3 Simulation of MSM, RSM	77
4.2.2.4 Simulation of the IPM-M	81
4.2.3 Simulation of the CDF	81
4.2.3.1 Simulation of the CDF interface	83
4.2.3.2 The CDP1802 emulator	86
4.3 Testing of the simulation	89
4.4 Simulation of real input data	92
4.5 Dead Times	95
 Chapter 5: PERFORMANCE OF THE DIDSY EXPERIMENT	 97
5.1 Cruise phase operation	98
5.2 Raw data reduction	100
5.2.1 Real time analysis	100
5.2.2 Reduction of the flight experiment tape	101
5.3 DIDSY encounter performance	104
5.3.1 Operation of the IPM sub-system	108
5.3.2 Operation of the CIS sub-system	113
5.3.3 Operation of the MSM/RSM sub-system	115
5.4 Operation of the central data formatter	117
5.4.1 Over counting in DID 2 AND DID 3 mode	119
5.4.2 Over counting of IPM-M events	120
5.4.3 Spurious resets of the DIDSY experiment	122
5.5 DIDSY flux rates	127
 Chapter 6: PARTICULATE IMPACT ANALYSER	 128
6.1 PIA Operation	130
6.1.1 The front end channels	130
6.1.2 On board processing	131
6.2 Decoding the flight experiment tape	133
6.3 Calibration	140
6.3.1 Shutter operation (Effective area)	140
6.3.2 Sensitivity and noise considerations for the front end channels	141
6.3.3 Dead time effects	147
6.3.4 Mass calibration	148

6.4 PIA flux rates	155
6.5 Limitations of the analysis	163
Chapter 7: ANALYSIS OF THE DIDSY 'DISCRETE' DATA	164
7.1 IPM-M 'discrete' data analysis	165
7.2 DID 4 'discrete' data analysis	167
7.3 Multi-Sensor 'discrete' data analysis	169
7.4 Total encounter fluence	180
7.4.1 Calculation of the momentum derating factor	183
7.5 Additional in-situ evidence for large grains	185
Chapter 8: THE DUST ENVIRONMENT OF COMET P/HALLEY	188
8.1 The coma mass distribution at small and intermediate masses	189
8.2 Possible explanations for an excess of large grains	192
8.2.1 Model 1 - Outbursts	192
8.2.2 Model 2 - Large mass excess throughout the coma	194
8.2.2 Model 3 - Asymmetric trajectories of large grains	194
8.3 The nucleus dust mass distribution	196
8.3.1 The dust mass distribution at the nucleus	196
8.3.2 The nucleus dust production rate and dust to gas ratio	199
8.3.3 Comparison of coma and nucleus mass and area distributions	201
Chapter 9: CONCLUSIONS	205
REFERENCES	210
APPENDIX 1: DIDSY flight software	218
APPENDIX 2: Byte corrections for resets	224
APPENDIX 3: 'Category 4' discrete events	226
APPENDIX 4: Publications	231

CHAPTER 1

INTRODUCTION

Prior to the spacecraft encounters with comet P/Halley the main source of information on the nature and distribution of cometary dust grains was gathered from remote observations of comets and from laboratory measurements of micrometeoroids collected from the upper atmosphere. Two types of remote observation were used to determine the dust mass distribution, modelling of the thermal emission spectra and modelling of the dynamics in dust features such as jets and halos (Divine *et al.*, 1986). In both cases the observations were subject to bias by those grains which dominated the scattering cross section.

The modelling of the infrared thermal emission spectra is based on the assumption of an equilibrium state between absorbed and emitted radiation, where the efficiency of emission and therefore temperature of the grain is dependent on the grain size (Hanner, 1983). Grains greater in size than about $10\mu\text{m}$ will exhibit temperatures close to a black body, while the temperature of smaller particles must rise significantly before equilibrium is reached. The situation becomes more complicated if non-equilibrium conditions occur (e.g. large slowly rotating grains), or if the composition or surface texture differs from what is assumed.

The modelling of dust features involves the calculation of particle trajectories under the interaction of solar gravitational attraction and solar radiation pressure (Probstein, 1969). The trajectory of a particle, or jet of particles, emitted from the surface of a comet will depend on the particles size, composition and mass. It also depends on its emission velocity from the surface and hence on the gas production rate. Within about 4AU the gas production is dominated by sublimation of water ice (Delsemme, 1987), however at greater distances where volatile components may be locked in a water ice matrix, the mechanism for emission and outburst is less clear. These factors will be particularly important during consideration of future cometary

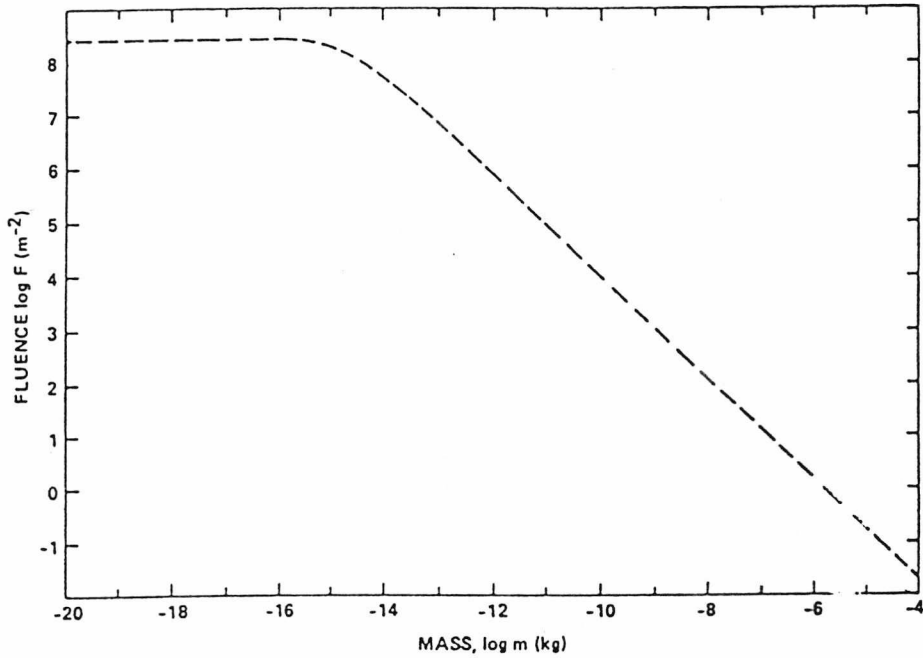


Figure 1.1: A total encounter fluence prediction for the Giotto spacecraft from (Divine & Newburn, 1987).

rendezvous missions (e.g. Rosetta) which will almost certainly take place at large heliocentric distances.

Based on the techniques described above, predictions were produced to describe the dust distribution along the Giotto trajectory. Figure 1.1 shows the predicted Giotto encounter fluence based on the pre-encounter modelling of Divine *et al.*, (1986). Of particular note is the lack of any particles below masses of $\sim 10^{-15}$ kg and a constant mass distribution slope continuing for masses above $\sim 10^{-9}$ kg, these represent the two regions of the mass distribution which, due to either low thermal emission, or small scattering cross section, are not normally viewed in ground based observations.

The Giotto probe (see Chapter 2) was ESA's first interplanetary mission and joined two spacecraft from Japan and two from Russia to make up a small armada of space probes with the aim of making the most wide ranging and detailed study of the cometary environment ever. In terms of dust

instrumentation, Giotto had two experiments dedicated to the observation and analysis of the dust coma, the Dust Impact Detection System (DIDSY) was designed to measure the distribution of different sized particles within the coma, and the Particulate Impact Analyser, was designed to measure the composition of impacting dust grains.

Throughout this work reference will be made to three specific mass ranges which correspond to the three particular regions of interest, defined below:-

- i) Small mass particles $10^{-19}\text{kg} \leq m \leq 10^{-15}\text{kg}$
- ii) Intermediate mass particles $10^{-13}\text{kg} \leq m \leq 10^{-9}\text{kg}$
- iii) Large mass particles $10^{-9}\text{kg} \leq m \leq 10^{-5}\text{kg}$

Data for each of these mass ranges comes from a different dataset, small particles from the Particulate Impact Analyser (PIA) (Chapter 6), intermediate from the Dust Impact Detection System (DIDSY) 'binned' data (Chapter 5) and large masses from the DIDSY 'discrete' data (Section 7.3).

The failure to release the cover which was used to protect the most sensitive of the DIDSY sensors from damage during the firing of the kick motor, was a major set back. Especially since none of the other DIDSY sensors provided anything approaching the same sensitivity. To overcome this loss, a method was devised to use front end detectors from the PIA experiment as absolute flux detectors. This analysis, the results from it and its limitations are described in Chapter 6.

In an attempt to improve the reliability of the DIDSY data a complete re-appraisal of the available calibration data sets was carried out (Chapter 3). In addition, a software model of the experiment was developed so that the effect of the high flux rates observed at encounter, on the operation of the experiment, could be calculated. The design, implementation and testing of the

simulation are presented in Chapter 4. It was used extensively in the analysis of the returned telemetry stream, for the identification and rejection of erroneous data. In some cases it was possible to correct previously unreliable data based on the results from the simulation.

The analysis of a special sub-set of the data, where multiple sensors detected a single impact, provided information on the mass distribution at large masses ($m > 10^{-9}$ kg). The analysis (Section 7.3) used the ratio between the signal levels on two sensors to determine the position of the impact site and hence the sensitivity appropriate for the calculation of the mass of the particle.

Combining data from PIA, DIDSY 'binned' and DIDSY 'discrete' data has allowed for the calculation of a total encounter fluence (Section 7.4) which is representative of the region of the coma passed through by the space probe and which covers a mass range of over 12 orders of magnitude. Of particular interest, are the observations at small, and large masses, which were inaccessible to the remote observations on which many of the pre-encounter dust coma models were based. The small mass data showed higher fluxes at greater distances from the comet (Section 8.1) than expected. The large mass too showed an excess over pre-encounter models both from DIDSY measurements (Section 7.3) and also from measurements by other instruments on Giotto (Section 7.5). If this excess is representative of the coma as a whole, it has important implications for the optical and infrared remote observations. Three possible models which could account for the excess based on different nucleus and coma distributions are considered (Section 8.2).

In Section 8.3 two fluence distributions, one based on the observed mass distribution, and the other similar but without the large mass excess are used to determine the nucleus emission function, dust production rate and by comparison to the gas measurements made by the NMS experiment (Krankowsky *et al.*, 1986), the dust-to-gas ratio. It is no surprise that the results obtained differ markedly.

Finally, the conclusion considers the state of the dust experiments after the encounter with Halley in connection with a proposal to extend the mission and send Giotto on to a second cometary encounter.

Initial plans for a joint European and U.S. cometary flyby and rendezvous mission failed due to technical problems and lack of funding from the U.S. Undeterred the European Space Agency (ESA) decided to 'go it alone' with their own flyby mission; ESA's first interplanetary spaceprobe. The spacecraft was named "Giotto" after the Italian painter Giotto di Bondone, who, in his painting "The adoration of the Magi", depicted the Star of Bethlehem as a comet, based on the spectacular 1301 apparition of comet Halley. Giotto was not the first mission to a comet, nor the only mission to visit comet P/Halley during its 1986 apparition. These missions, and in particular their ability to measure the coma dust distribution, are considered briefly below.

The first in-situ measurements of a comet were made by the International Cometary Explorer (ICE) spacecraft when it passed less than 8000km tailward of comet Giacobini-Zinner on 11 September 1985 (Brandt *et al.*, 1988). The spacecraft was not a dedicated cometary mission but a solar-terrestrial physics satellite which had been re-targeted via an intricate set of orbital manoeuvres. Originally named ISEE-3, the spacecraft had been designed to measure the interaction between the solar wind and the Earth's magnetic field. The spacecraft's scientific payload consisted mainly of plasma and magnetometer experiments and did not include any dedicated dust experiments. However, some dust measurements were made by the detection of impact plasma by the plasma wave experiment. These indicated an approximate r^{-2} radial dependence and dominant particle size in the range $10^{-13}\text{kg} < m < 10^{-15}\text{kg}$ (Brandt *et al.*, 1988). ICE carried on to encounter comet Halley on March 25, 1986 but with a miss distance of more than 10^7km on the sunward side of the comet, it provided no additional information on cometary dust.

In addition to Giotto, another four dedicated missions from two space agencies encountered Halley during its 1986 apparition. Two of the spacecraft, Sakigake and Suisei, were produced by Japan's Institute of Space and Astronomical Science (ISAS). The remaining two missions, Vega 1 and Vega 2,

were produced by Russia's Space Research Institute. Unlike the ICE spacecraft, all of these missions passed on the sunward side of the comet.

Sakigake and Suisei (Hirao, 1986) were almost identical spacecraft with the exception of the experiments that they carried. They were small, each having a scientific payload of less than 15kg . Nevertheless the missions were an amazing achievement for the ISAS and their new M-3S II launchers. Sakigake was launched in January 1985 and represented a test spacecraft for the Suisei mission to comet Halley which was launched 7 months later. The scientific payload of Sakigake consisted of plasma-wave, solar wind and magnetic field experiments, while the principle experiment on Suisei was an ultra-violet imager. Neither of the spacecraft included detectors for cometary dust. Suisei and Sakigake reached closest approach on 8th March 1986 (1.51×10^5 km) and 11th March 1986 (6.99×10^6 km) respectively. At these large distances the dust flux was expected to be very low (Divine *et al.*, 1986) and have no noticeable effect on the spacecraft. However, two large impacts of several milligrams in size, caused abrupt changes to the attitude of Suisei, just before and after closest approach (Hirao & Itoh, 1987); a clear indication of a higher than expected density of large particles.

Vega 1 and Vega 2 were essentially identical spacecraft. The encounter with comet Halley represented only part of a joint mission. The other half involving a flyby of Venus during which balloons were dropped into the Venusian atmosphere (Sagdeev *et al.*, 1986). The Vega spacecraft included an extensive scientific payload of more than 125kg. Experimentation for imaging, spectroscopy, magnetic field measurements and the study of dust, gas and plasma were all included (Grard *et al.*, 1986). The dust experiments provided measurements of the dust distribution over the mass range 10^{-19} kg $< m < 10^{-9}$ kg (Mazets *et al.*, 1987; Vaisberg *et al.*, 1987) during the Vega 1 and Vega 2 encounters on 6 March 1986 (8890km closest approach) and 9 March 1986 (8030km closest approach). Comparison of Vega and Giotto results have been

presented in Pankiewicz, 1989. The Vega dust experiments could not readily detect particles with masses greater than 10^{-9} kg due to the low flux rates and small sensor areas involved. However, more recently, some attempts have been made, using the encounter data from the plasma-wave and Langmuir probe experiments, to identify the impact plasma from large events hitting the spacecraft structure (Trotignon *et al.*, 1987; Laakso *et al.*, 1989).

2.1 TARGET SELECTION

In deciding a target for a cometary flyby mission a number of factors both technical and scientific have to be considered. On the scientific side a target is required with a high dust and gas production and that is likely to exhibit features of interest such as outbursts, tail discontinuities and jet structure. These requirements best fit fresh, new comets and generally excluded shorter period comets which are seen to be less active, due to a build up of an insulating dust mantle over a number of perihelion passages (Whipple, 1950).

As important as the scientific criteria are the technical aspects of a mission, measurements can only be successfully completed if the ballistic trajectory of the spacecraft passes within a suitably close distance of the comet. This requirement is split into two separate issues.

- i) Having a good ephemeris so that the position of the comet is known well in advance to allow for mission planning. This excludes comets which have been observed for the first time and long period comets where insufficient data is available from previous apparitions to build an accurate ephemeris. Namely, those comets most likely to satisfy the scientific criteria!

ii) Constraints on the spacecraft delivery and telemetry systems. The lower the energy requirement for the transfer from the geocentric transfer orbit to the heliocentric intercept orbit, the greater the payload opportunities (in terms of available mass) for a particular launch vehicle (in the case of Giotto the ESA Ariane-1). Such energy constraints realistically limit non-gravity assisted missions to within the plane of the ecliptic and so a target with either favourable ascending or descending nodes is required. In this case favourable means small heliocentric distance for higher cometary activity and greater solar cell output and small geocentric distance for improved telemetry link (and better opportunities for coincident remote observations).

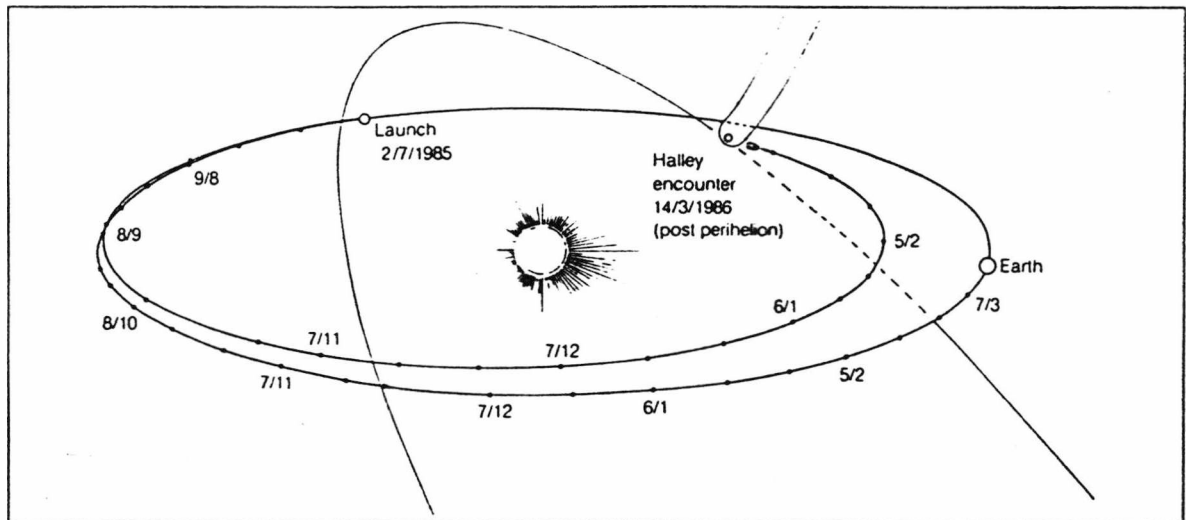


Figure 2.1: The Giotto orbit from launch on 2 July 1985 until encounter with Comet P/Halley on 13/14 March 1986 (from Reinhard, 1988). The encounter occurred at the descending node of Halley's orbit and due to the retrograde nature of the comet's motion resulted in a relative encounter velocity of 68.4kms^{-1}

Comet	Period (years)	Perihelion distance (AU)	Inclination (degrees)	Favourable perihelion	Departure velocity (km/s)*
Encke	3.31	0.341	11.9	1990 Nov 3.6	10
				2000 Sep 28.7	10
Temple-2	5.27	1.369	12.5	1988 Sep 16.7	4
				1999 Sep 6.6	3
Honda-Mrkos-Pajdusakova	5.28	0.579	13.1	1990 Sep 20.0	4
				1996 Jan 17.3	10
Tutle-Giacobini-Kresak	5.58	1.124	9.9	1990 Feb 6.6	8
D'Arrest	6.23	1.164	16.7	1995 Jul 7.0	6.5
Giacobini-Zinner	6.52	0.996	31.7	1985 Sep 4.0	3
				1998 Nov 9.7	4
Borelly	6.76	1.316	30.2	1987 Dec 18.2	5
				1994 Oct 28.1	9
Arend-Rigaux	6.83	1.442	17.9	1984 Dec 1.4	6
Crommelin	27.89	0.743	28.9	1984 Sep 1.0	5
Halley	76.09	0.587	162.2	1986 Feb 9.3	3

Table 2.1: Orbital characteristics of ten comets selected by ESA as possible targets for a cometary encounter mission between 1984 and 2000.

* The departure hyperbolic velocity required to intercept the comet, lower velocities require less energy and are therefore preferable.

For ESA's first interplanetary mission, a short list of ten possible candidates (Table 2.1) with perihelion passages from 1984 to the year 2000, were chosen from the more than 1000 recorded comets (Reinhard, 1986). Comet P/Halley best fitted both the scientific and technical requirements. Halley had been observed in all of its last 30 apparitions and displayed an activity comparable to that of new comets. Being so well observed, meant that an

accurate ephemeris had been calculated. In addition the low energy requirement for an intercept orbit made Halley an excellent choice. The most significant disadvantage was that due to the retrograde nature of P/Halley's orbit, the relative encounter velocity between spacecraft and comet would be high ($\sim 70\text{kms}^{-1}$) resulting in an increased hazard from hypervelocity dust impacts. Figure 2.1 shows the orbit of P/Halley around perihelion relative to the ecliptic plane. A post-perihelion encounter was favourable for an Ariane launch from Kourou and had the added advantage of a lower heliocentric distance (Reinhard, 1986).

2.2 THE GIOTTO SPACECRAFT

The Giotto spacecraft (Figure 2.2) was based on the design of the ESA Geostationary Satellite (GEOS) series of satellites, which were used for Earth remote sensing. The main differences were:-

- i) An increase in size to accommodate the larger scientific payload of 58.9kg.
- ii) An increased solar array required to power the spacecraft.
- iii) The addition of a kick motor to transfer from the geocentric to heliocentric intercept orbit.
- iv) The addition of de-spun high gain antenna.
- v) The addition of a meteoroid protection system.

The requirement for a meteoroid protection system arose due to the high relative encounter velocity; damage to the spacecraft by hypervelocity dust impacts represented a serious hazard to the mission (Reinhard, 1979; Hughes, 1979). To lessen the risk to vital spacecraft components a dual-sheet bumper shield was designed, consisting of a 1mm aluminium front 'sacrificial' shield separated by 230mm from a 15mm composite Kevlar and polyurethane rear

shield. Particles with masses greater than the penetration limit of the front shield would be 'shocked' during their passage through the shield resulting in complete or partial vaporization of the particle. The jet of material would spread in the intervening space between the shields resulting in a distribution of the impulse over a larger area of the rear shield. By spreading the energy of the impacting particle over a larger region, the degree of protection afforded by

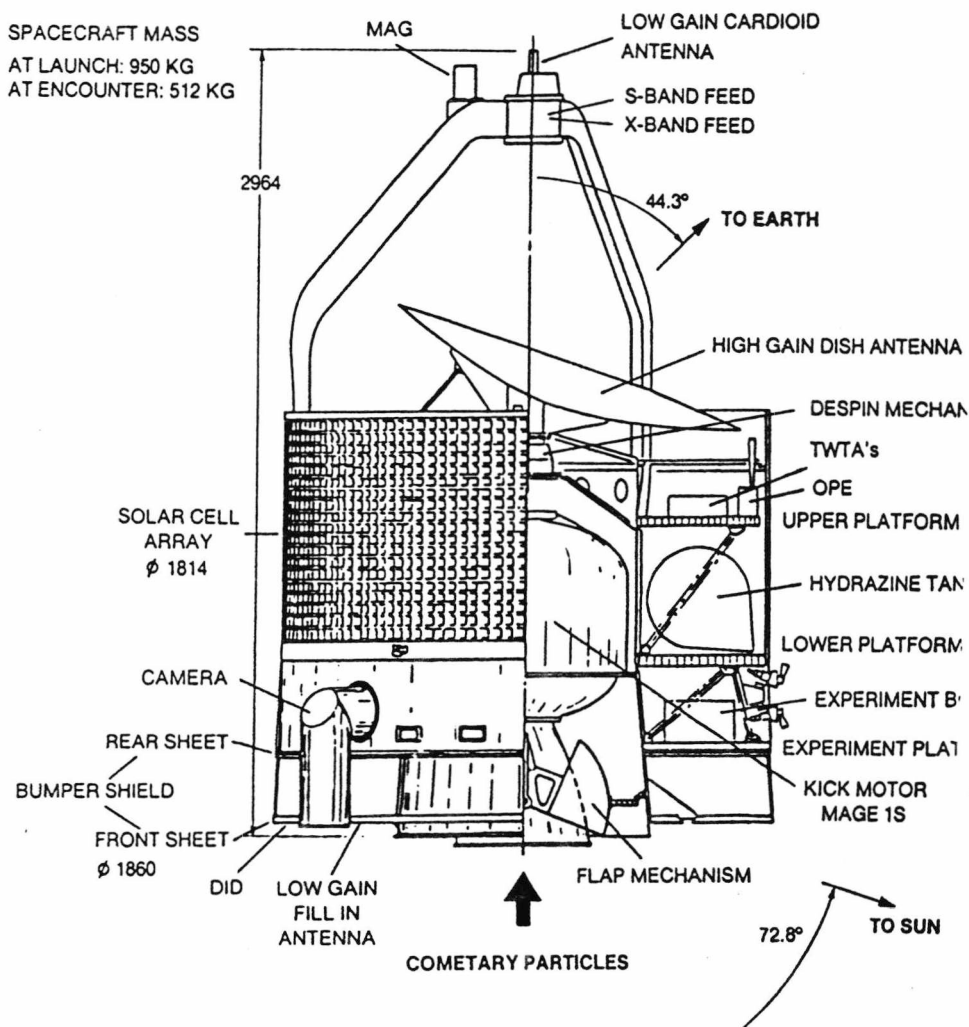


Figure 2.2: Cross section of the Giotto spacecraft (from Reinhard, 1988) showing the front and rear bumper shields at the bottom and the high gain antenna at the top. The spacecraft velocity vector is downwards.

a shield of given mass was considerably enhanced (Reinhard, 1986). The dual bumper shield weighed only 50kg yet was able to stop a 0.1g particle travelling at the encounter velocity. To obtain similar results from a single aluminium shield would have required a shield more than 8cm thick (Reinhard,1988) and weighing more than 600kg.

The spacecraft telemetry system made use of a 1.4m high gain antenna which could operate in two modes; S-band (2.1GHz uplink and 2.3GHz downlink) and a higher power consumption X-band (8.4 GHz downlink). The S-band mode was used mainly for housekeeping operations, while the higher bandwidth X-band mode was used during encounter to provide a 46kbits⁻¹ data rate (40kbits⁻¹ of science). The spacecraft was spin stabilized with a period of ~4s. Since the spin axis was aligned with the relative velocity vector of the spacecraft, continuous communications during encounter could only be maintained by inclining the high gain antenna at 44.3° to the spin axis and using a despun mechanism. The pointing requirements of the X-band signal were very stringent, a misalignment of $\geq 1^\circ$ resulting in the possible loss of signal. Therefore, to ensure correct alignment, a closed-loop system between the despun mechanism and the sun-sensor was used; thus changes in the spacecraft spin period were automatically accounted for.

The Giotto telemetry stream was split into manageable units called 'Frames', each telemetry frame lasted ~0.35s at 46kbits⁻¹. The telemetry frames produced during encounter consisted of 2040 bytes, comprising synch, frame number and timing information, a block of 32 bytes of housekeeping data, a block of 1744 bytes of science data and a block of 256 bytes Reed Solomon encoding information. The science data block was built up from 8 recycles of 218 science bytes, the location of data from a particular experiment was fixed within the 218 byte block. Each group of 64 frames were collectively know as a 'Format', the frame counter giving the position of a particular frame (0 to 63),

Format	Description
'HK Format'	Housekeeping data only - No science data
Science 'Format 1'	Higher allocation for plasma experiments, Lower allocation for dust experiments.
Science 'Format 2'	Higher allocation for dust experiments, Lower allocation for plasma experiments.
Science 'Format 3'	Cruise Science mode. No dust experiments or NMS

Table 2.2: The different telemetry formats available to the Giotto spacecraft. Only 'Format 1' and 'Format 2' were used during the encounter.

within a format. The spacecraft could operate in one of four formats (Table 2.2). The formats differed in their allocation of the available 2040 bytes within a frame, between scientific experiments and spacecraft systems. During the night of encounter only the science formats, 'Format 1' and 'Format 2' were used (see Section 5.3). In the case of DIDSY, 'Format 1' provided 2 locations within the 218 byte cycle (words 107 and 213) while in 'Format 2' a higher allocation of 5 locations (words 34, 71, 107, 140, and 177) were available.

Giotto was launched from Kourou, French Guiana on 2 July 1985 by an Ariane-1 rocket which placed the spacecraft in a geostationary transfer orbit with a semi-major axis, $a=24000\text{km}$, eccentricity, $e=0.73$ and inclination $i=7^\circ$. After three orbits, the on-board solid rocket kick motor was fired resulting in a velocity increment of 1400ms^{-1} and placing Giotto into the required heliocentric, comet Halley intercept orbit (see Figure 2.1). During the following eight month cruise phase of the mission, regular tracking, communication and testing of the spacecraft systems and scientific payload were carried out using ESA's 15m ground station at Carnarvon and the 64m dish at Parkes. Three orbit correction manoeuvres were performed during this time, on 26 August 1985, 12

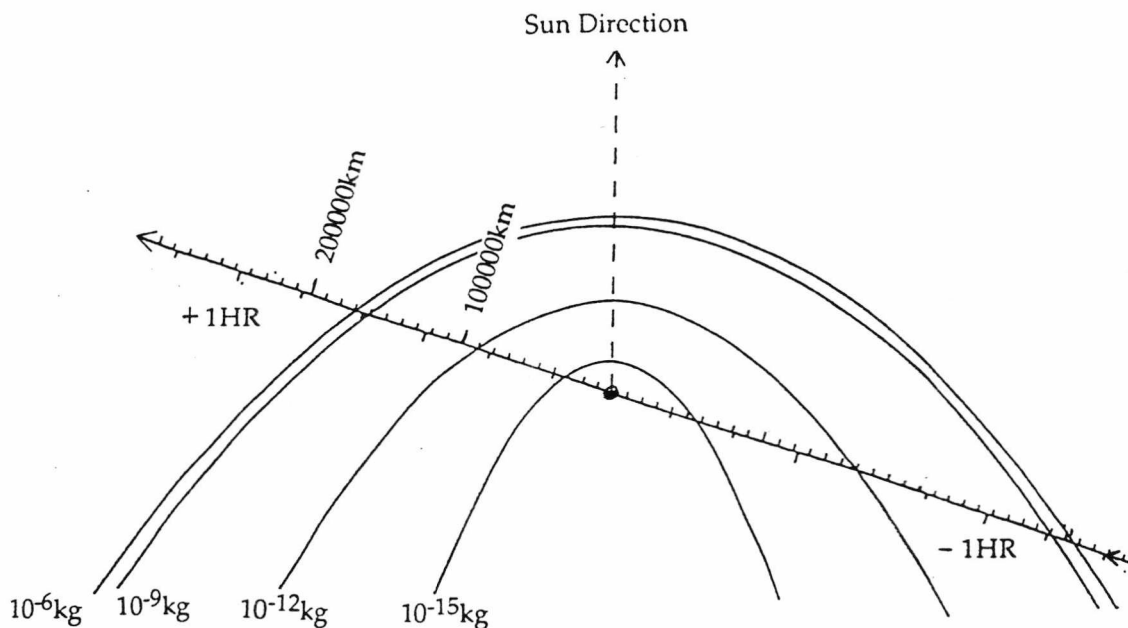


Figure 2.3: The path of the Giotto spacecraft in a fixed cometocentric coordinate system. Dust envelopes are shown derived from pre-encounter models.

February 1986 and 12 March 1986. The last of these manoeuvres, used information from the Vega 1 and Vega 2 encounters to reduce the uncertainty ellipsoid on the position of Halley and allow for more accurate 'aiming' of the Giotto trajectory; the so called 'Pathfinder' concept. The orientation of the Sun, Earth and comet relative to the spacecraft, on the night of encounter, is indicated in Figure 2.2. The spacecraft trajectory through the coma of Halley is shown in a cometocentric coordinate system in Figure 2.3.

The scientific payload of Giotto consisted of 10 experiments most of which were mounted on the experiment platform located just above the rear shield (see Figure 2.4). The experiments can be divided into three groups corresponding to the different disciplines specified in the scientific objectives of

the Giotto Science Working Group (Reinhard, 1981), namely optical, plasma and gas, and dust although there was some degree of overlap. A list of all the experiments together with acronym, power and telemetry budgets is given in Table 2.3. Of particular relevance to this work are those experiments which either directly measured cometary dust impacts or were able to infer impacts from some other measurements. These will be considered in more detail in the following sections.

Experiment	Mass (kg)	Power (W)	F1 (bs ⁻¹)*	F2 (bs ⁻¹)*
Halley Multicolour Camera (HMC)	13.51	11.5	20058	20058
Optical Probe Experiment (OPE)	1.32	1.2	723	723
Energetic Particle Analyser (EPA)	0.95	0.7	181	181
Johnstone Plasma Analyser (JPA)	4.70	4.4	3975	1265
Magnetometer (MAG)	1.36	0.8	1265	1265
Neutral Mass Spectrometer (NMS)	12.70	11.3	4156	4156
Reme Plasma Analyser (RPA)	3.21	3.4	2530	1807
Dust Impact Detection System (DID)	2.26	1.9	361	903
Radio-science Experiment (GRE)**	-	-	-	-
Particulate Impact Analyser (PIA)	9.89	9.1	2891	5782
Total	58.90	50.6	39393	39393

Table 2.3: The scientific payload of the Giotto spacecraft split into three groups corresponding to the types of measurement made, optical, gas/plasma, and dust.

* F1 and F2 represent the experiment telemetry allocation for each of the two telemetry modes used during the encounter.

** The Giotto Radio Science Experiment involved ground based analysis of the spacecraft radio signal to obtain dust and gas column densities and did not include any dedicated hardware on the spacecraft itself.

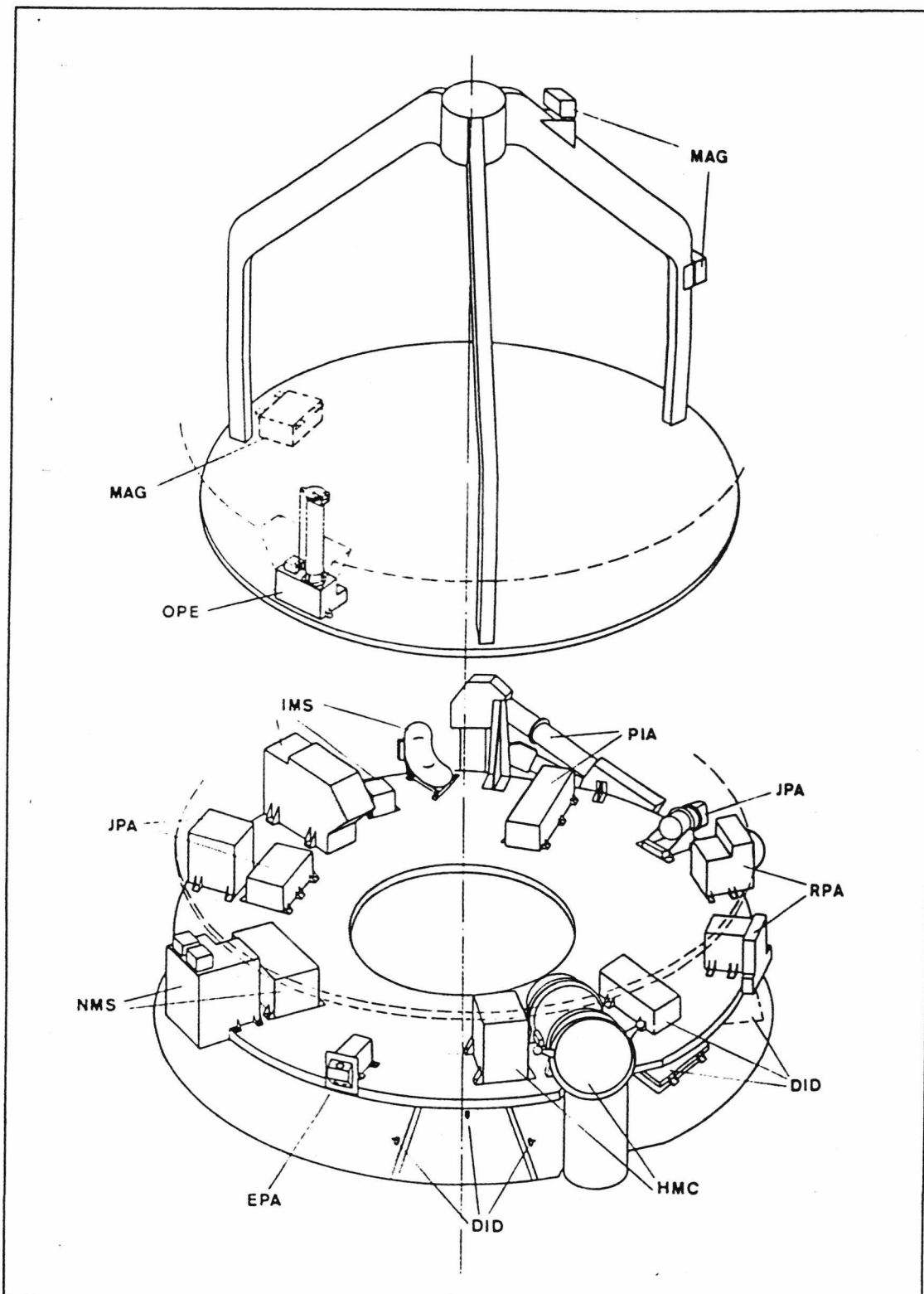


Figure 2.4: Location on the spacecraft of Giotto's ten hardware experiments (from Reinhard, 1986) most are mounted on the experiment platform positioned behind the rear bumper shield. The experiments and their acronyms are also listed in Table 2.3.

2.3 DIDSY EXPERIMENT

The dust impact detection system or DIDSY, was the principal experiment on Giotto designed to make measurements of the mass distribution of grains along the spacecraft trajectory. The development and production of the experiment involved 15 institutions in Europe and the U.S.A. and was coordinated by the Unit for Space Sciences, at the University of Kent under the leadership of the experiments principal investigator (Prof. J.A.M. McDonnell) and project manager (Dr J.C. Zarnecki).

To cover a particle mass range from 10^{-19} kg to $\sim 10^{-5}$ kg three different detection techniques were used:-

- i) Large to intermediate masses - $m \gtrsim 10^{-12}$ kg - Piezoelectric detection and shield penetration. Large particles from coincidence measurements.
- ii) Intermediate masses - $m \gtrsim 10^{-13}$ kg - Detection of foil penetration.
- iii) Intermediate to small masses - $m \gtrsim 10^{-19}$ kg - Impact plasma detection.

Each of these methods is considered in more detail below together with a description of the functions carried out by the experiment's data processing unit. Additional information can be found in McDonnell *et al.*, 1986 and McDonnell, 1987

2.3.1 PIEZOELECTRIC MOMENTUM SENSORS

These types of sensors were first used to detect dust particles as far back as the late 1940's (Bohn & Nadig, 1950) when they were flown by US scientists on captured V2 rockets. The operation is based on the detection of the vibrational bending wave generated by the impact of a dust grain on the target. An ultrasonically resonant piezoelectric crystal is mechanically attached to the

target plate and converts the bending wave produced by an impact into an electrical signal. The output signal is found to be proportional to the net impulse imparted by an impact at a particular point on the target (McDonnell, 1969) but varies with position. The positional dependence is caused by a combination of signal attenuation related to the distance of the impact site from the sensor, and interference caused by different signal propagation paths; both are dependent on the target geometry and material. For impacts in the hypervelocity regime (velocities $\geq 5\text{kms}^{-1}$, McDonnell *et al.*, 1984) and which do not penetrate the target, the momentum transferred is greater than that carried by the particle itself, since target material is also vaporised and ejected. The total momentum transferred to the target for non-penetrating particles is given by Equation 2.1 where m and v are the mass and relative velocity respectively and ϵ is the momentum enhancement factor. For the Giotto encounter velocity of $\sim 68\text{kms}^{-1}$ a value for ϵ of 11 is used (McDonnell *et al.*, 1984; Wallis, 1986).

$$\mathbf{p} = \epsilon \cdot m\mathbf{v} \quad (2.1)$$

For particles which penetrate the target, the enhancement factor must be derated to account for the momentum which is transferred through the target and not captured (Equation 2.2).

$$\mathbf{p} = \epsilon \cdot m\mathbf{v} \left(\frac{m_{\text{pen}}}{m} \right)^\gamma \quad (2.2)$$

Where m_{pen} is the penetrating mass threshold which for particles at velocities of 68kms^{-1} impacting on a 1mm thick aluminium target is found to be in the range $1 \times 10^{-9}\text{kg}$ to $5 \times 10^{-9}\text{kg}$ (McDonnell, 1979). γ is the momentum derating factor which defines how quickly the momentum enhancement falls off with increasing mass, and which is assigned a nominal value of 0.66 (Wallis, 1986) based on energy partition theory.

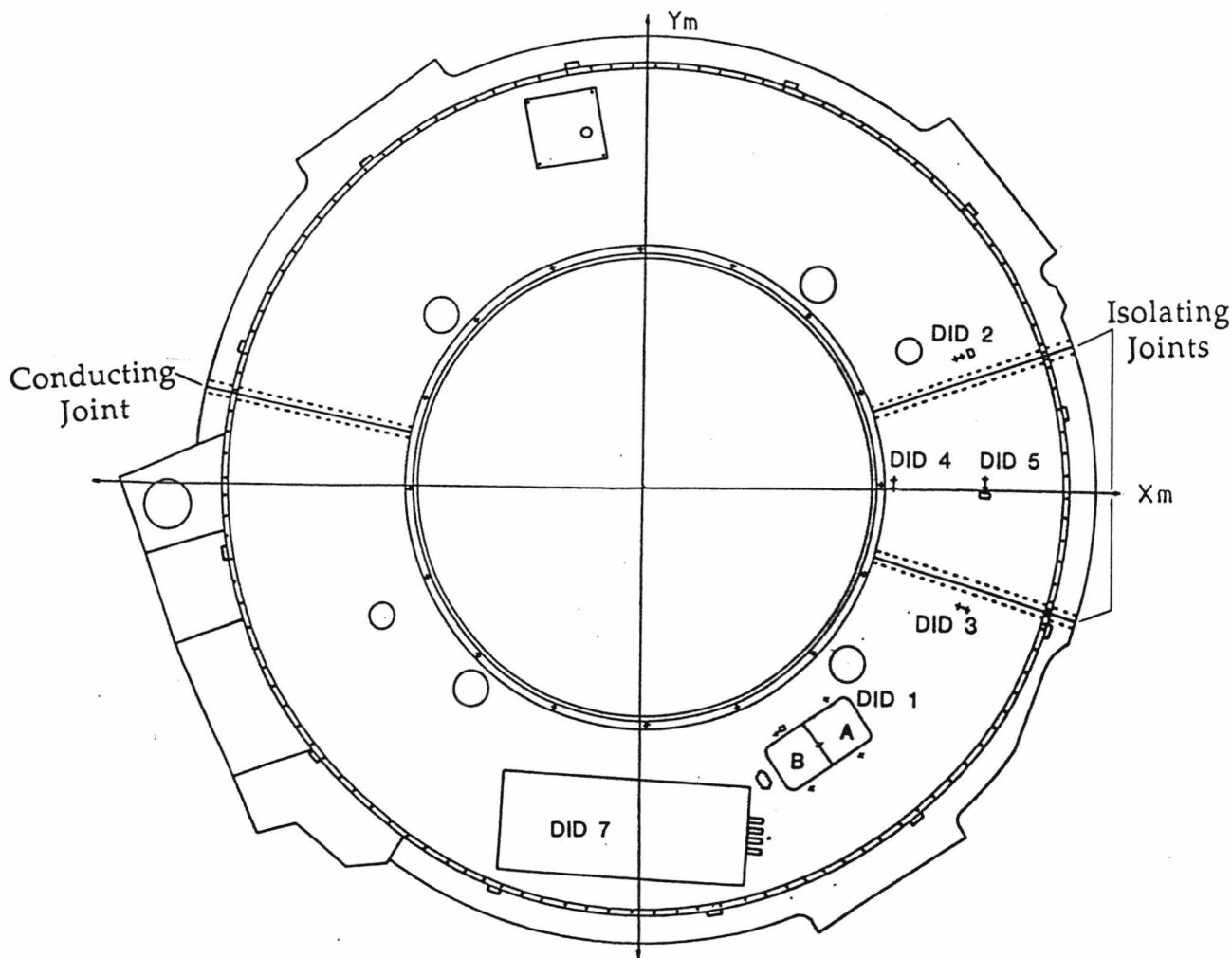


Figure 2.5: The Giotto front bumper shield showing the location of the DIDSY detectors. DID 5 is mounted on the rear Kevlar shield at the same angular position as DID 4, but approximately half way between the inner and outer edges of the shield. The view is from the direction of incoming dust particles (i.e. upwards in Figure 2.2).

The DIDSY experiment uses five of these piezoelectric type sensors, three are mounted on the rear side of the front bumper shield, DID 2 and DID 3 on the large sector and DID 4 on the small sector, the two sectors are joined by acoustically isolating joints (Figure 2.5). These sensors are collectively known as the MSM or 'Meteoroid Shield Momentum' sensors. Another piezoelectric

sensor, IPM-M, is attached to the target plate of the impact plasma sensor whilst the final one, DID 5, is mounted on the top side of the rear bumper shield and hence is only able to detect those particles which can penetrate the front shield. DID 5 is alternatively named the RSM or 'Rear Shield Momentum' sensor. The signal produced by each sensor is passed through a 200kHz filter (approximately equal to the resonant frequency of the crystal) which results in a slight loss of sensitivity but improves immunity from lower frequency noise produced by mechanically and thermally induced 'creaking' of the spacecraft.

As was stated above, the signal produced by this type of sensor is dependent on the position of the impact relative to the sensors. This is a particular consideration for those sensors mounted on the front shield where it's large size and intricate design (including rivets and cut-out sections) results in a complex sensitivity function. Which must be corrected for during data analysis, this is done using pre-launch calibration measurements (see Section 3.4.1). An additional consideration in the design of the sensor electronics is to prevent the multiple counting of a single event due to reflections of the bending wave from the edges of the shield and at the isolating joints (Reading & Ridgeley, 1983). This is achieved by using a ramped threshold which is set when an initial impact is detected and where only new events which exceed the threshold will trigger the sensor. This method imposes a limit on the rate at which events can be detected and at high impact rates the recorded counts must be corrected for the sensor 'dead time' introduced by this method (Section 3.6)

2.3.2 PENETRATION TYPE SENSORS

The DIDSY experiment employs two types of penetration sensor. As mentioned above one of the piezoelectric microphone sensors is mounted on the rear shield 230mm behind the front 1mm aluminium shield. Only particles

penetrating the front shield can be detected by the DID 5 sensors and even then, due to the high acoustic attenuation of the Kevlar from which the rear shield is constructed, only particle fragments and ejecta hitting close to, or directly on the, sensor will produce a measurable signal.

The other penetration sensor used by DIDSY is the Capacitor Impact Sensor (CIS or DID 7) . The CIS sensor consists of a 20 μm aluminium foil forming the top electrode which is bonded to a thin sheet of dielectric (25 μm Kapton) which has a 1000 \AA film of aluminium deposited on the bottom surface (Mandeville *et al.*, 1983), this sandwich was bonded onto the front shield (see Figure 2.6). A 50V bias voltage was placed across the electrodes to form a simple parallel plate capacitor with an area of 0.1m². When a particle with mass greater than a certain limiting mass hits the sensor a conduction path is set up between the two electrodes causing the capacitor to discharge, the change in voltage across the plates being detected by the sub-system's electronics. The conduction path can be manifest by either an electro-mechanical break-down of the dielectric, a plasma path caused by the ionisation of particle and target

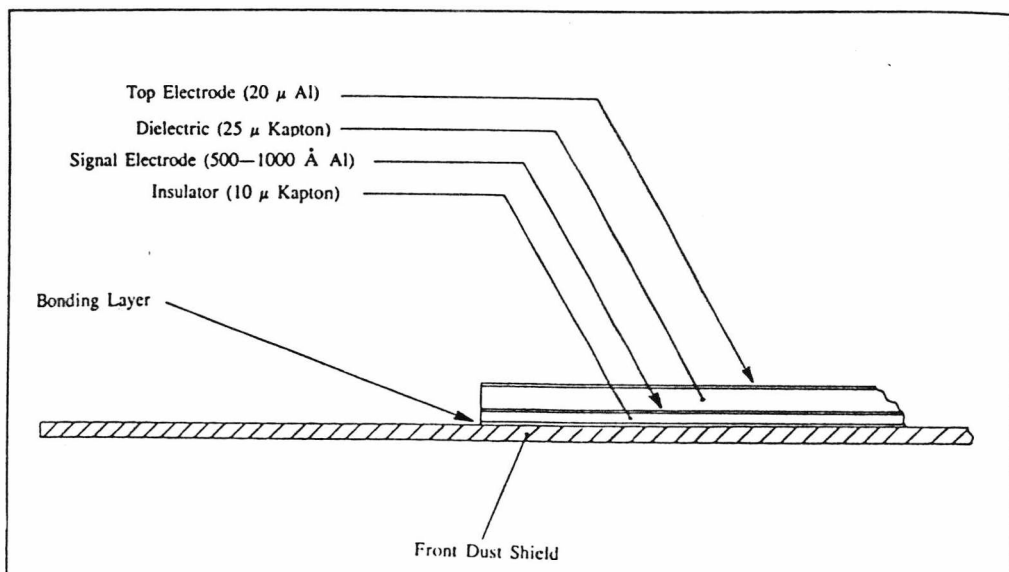


Figure 2.6: A cross section of the CIS sensor, taken from McDonnell *et al.*, 1986.

material, or a mechanical short between the upper and lower electrodes. Since the ionised region is in general only temporary, after a short delay the sensor can be re-charged ready for the detection of further impacts. In the case of a mechanical short, successive charge and discharge sequences will vaporize the conducting material. Prior to Giotto this type of sensor had been used on the Pegasus series of satellites to detect micrometeoroids (Naumann, 1966).

2.3.3 IMPACT PLASMA DETECTION

This method relies on the detection of the free ions produced by hypervelocity impacts of dust grains on a solid target. The rapid dissipation of energy at the surface results in a non-equilibrium cloud of ions and electrons which can be separated by an electric field and the total charge measured by charge sensitive amplifiers connected to the electrodes. The technique was originally suggested by Friichtenicht (Friichtenicht, 1964) and subsequently used on Earth orbiting and interplanetary probes (Berg & Richardson, 1969; Dietzel *et al*, 1973). The use of electron, ion coincidence logic provides reliability, even at high sensitivity and in high ambient plasma conditions.

The DIDSY impact plasma sub-system (DID 1) consists of two very similar sensor, IPM-PA and IPM-PB, each with a sensitive area of 59.6cm². The IPM-PB sensors differs from IPM-PA in that it has thin penetration film attached to it's front face (see Figure 2.7). In principle the film (2.5µm aluminised Mylar) acts as a mass filter where the penetration limit is a function of velocity and density. Since the encounter velocity for Giotto is constant, comparison of the count rates on the two IPM-P sensors yields information on particle densities. Calibration of the sensor was carried out by J.R. Göller, E. Grün and D. Mass of the Max Planck Institut Fur Kernphysik, Heidelberg using

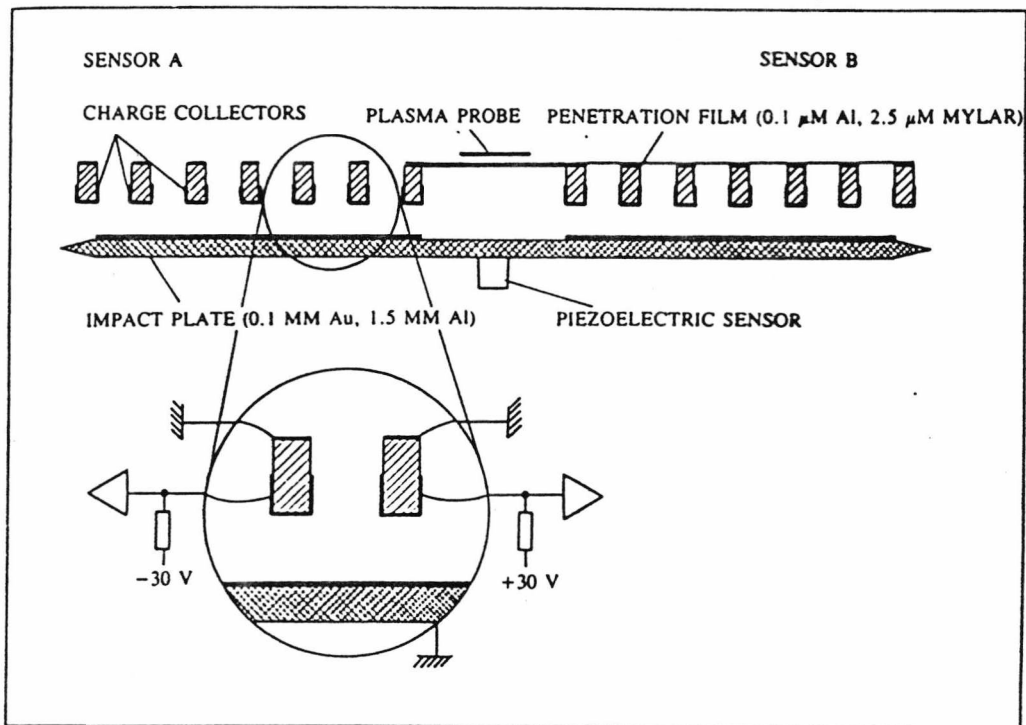


Figure 2.7: Cross section of the IPM-P sensor taken from McDonnell et al., 1986.

dust accelerators at Heidelberg and Munich. Experimentally it is found that at constant velocity the charge is related to the mass of the impacting grain by Equation 2.3.

$$Q = k m^a \quad (2.3)$$

Where Q is the released charge, m the particle mass and a is a constant found to have a value very close to unity (Göller *et al.*, 1987), resulting in a linear relationship between mass and charge. The constant of proportionality k is found to be a function of impact speed, particle composition, sensor geometry and electronics design. Measurements made at lower velocities and extrapolated to 69kms^{-1} using the IPM-PA sensor and electronics, give charge yields for Carbon, Silicate and Iron of $3 \times 10^6 \text{Ckg}^{-1}$, $3 \times 10^6 \text{Ckg}^{-1}$ and $7 \times 10^5 \text{Ckg}^{-1}$ respectively (Göller *et al.*, 1987).

The IPM unit consisting of the impact plasma detectors, a piezoelectric sensor (IPM-M) used to provide coincidence detection for larger events and an ambient plasma monitor (IPM-A) provided by ESA, was mounted on the rear side of the front bumper shield behind a cut-out section which allowed incoming dust grains to hit the sensor directly. To prevent contamination of the sensor during launch and firing of the MAGE 1S kick motor, the cut-out section of the shield was protected by a cover (DID 8) which when released was designed to roll back revealing the IPM unit below. The cover was constructed from three layers of 7.5 μ m Kapton film each layer separated by ~2mm. The inner two layers were perforated to allow for outgassing. The failure of the cover to deploy when commanded a month before encounter and the effect that this had on the operation of the IPM sensors is considered in Section 5.3.1.

2.3.4 DATA PROCESSING UNIT

The data processing unit of the DIDSY experiment is known as the central data formatter or CDF. The CDF controls the interface between the spacecraft's on board data handler (OBDH) and the DID sub-systems, receiving commands from the spacecraft, sending data for transmission to Earth and handling the accumulation of incoming data and the calculation of pulse height analysis (PHA) data. In addition, the CDF contains the electronics for the voltage multiplexer used to select which housekeeping line should be passed to the spacecraft and the control logic for the cover release mechanism.

The CDF works on a standard double buffer principle where data is accumulated in one buffer while data from the previous data gathering interval (DGI) is passed to the spacecraft's OBDH system for transmission to Earth. To ensure that the experiment remains in step with the operation of the OBDH, access to the buffer is by direct memory access (DMA) and the point at

Telemetry Mode	Telemetry Allocation (bs ⁻¹)	Length Of DGI (s)
Format 1 / 46kbs-1	361	2.83
Format 1 / 23kbs-1	180	5.66
Format 2 / 46kbs-1	903	1.13 *
Format 2 / 23kbs-1	451	2.26

Table 2.4. This table shows the relationship between telemetry mode and the length of a DIDSY data gathering interval.

* Note that all DIDSY events on the night of encounter occurred while in this mode.

which the buffers are switched from accumulation to transmission and vice versa is governed by the position of the DMA pointer. Hence, the length of a data gathering interval is directly related to the telemetry mode of the spacecraft (Table 2.4).

In terms of data processing the sensors described above are divided into three sub-systems, IPM (IPM-P and IPM-M), CIS, and DID 2 to DID 5 (MSM and RSM). The sub-systems operate and are processed separately with the exception of a co-incidence line from CIS which is used to help determine a category for the 'discrete' data from the MSM and RSM sensors. In the case of the multi-sensor subsystems, a signal on one sensor will generally result in the CDF reading information from the other sensors within the sub-system. The telemetry available to the DIDSY experiment was such that at the high flux rates expected at encounter information on every particle detected by each of the sensors could not be transmitted back to Earth. Instead the CDF produced two types of data called 'discrete' and 'binned' data.

The 'discrete' data contains the raw amplitude information taken directly from the outputs of the analogue-to-digital converters. In the case of

Category Number	Category Definition
1	CIS coincidence with any combination of MSM
2	DID 2 and DID 3 and DID 4
3*	DID 5 without any MSM
4	DID 4 only
5	Any other combination

Table 2.5: The definitions used by the DIDSY CDF to categorise an MSM/RSM event. 'Category 1' has the highest priority and 'Category 5' the lowest.

*This definition is used by the category counter but amplitude information from an RSM event will be placed in 'Category 3' even if one or more of the MSM sensors was active.

the MSM/RSM sub-system each discrete event is placed in one of five available categories, according to the rules laid down in Table 2.5. Information from only one event in each category is stored; a new event will overwrite existing data in the same category. In this way the last event detected in a DGI will be transmitted resulting in an unbiased sample. A counter is also provided for each category which contains the number of events assigned to the category within the DGI. In addition the maximum signal detected in each DGI on any of the MSM sensors is returned, the least significant two bits being replaced by the DID sensor number minus 1.

The 'discrete' data for the IPM-P sensor is handled in a very similar way except that there are seven categories (Table 2.6) instead of the five for MSM/RSM. The IPM-M sensor also provides discrete data although in this case no categorisation of the data occurs, the information returned corresponding to the last IPM-M event detected. In addition to the event amplitude, the IPM-M electronics 'latch' the output of the analogue-to digital converter as soon as an

Category Number	Category Definition
1 **	Calibration Data
2	Sensor A electron/ion coincidence
3	Sensor B electron/ion coincidence
4	Sensor A/IPM-M coincidence
5	Sensor B/IPM-M coincidence
6 *	Sensor A no coincidence data
7 *	Sensor B no coincidence data

Table 2.6: The definitions used by the DIDSY CDF to categorise an IPM-P event.
+ No category counter exists for the calibration data ('Category Data')
*Amplitude information from categories 1,6 and 7 are combined. 'Category 1' data cannot be overwritten by subsequent 'Category 6' or 'Category 7' events.

impact is detected. Due to propagation delays the 'latched' value corresponds to the sensor level before the impact, thus providing important diagnostic information.

The third sub-system described above, CIS, is purely an impact counter and provides no amplitude information and therefore no 'discrete' data.

The 'binned' data is derived from a pulse height analysis (PHA) of the event amplitude, where the magnitude of the event is used to define which, out of a limited number of counters, should be incremented (Table 2.7). In the case of the MSM/RSM sub-system three sets of counters are used for DID 5, DID 4 and for a combination of DID 2 and DID 3, consisting of 4, 6 and 6 'bins' respectively. The sets of counters are incremented completely independently, even in the case of a multi-sensor event. The PHA calculation for the DID2/3 counters depends on the operational mode of the CDF. Table 2.8 lists the description of each of the four modes and the calculation which combines the DID 2 and DID 3 amplitudes into a single value, which is then passed to the 'binning' procedure. The experiment can be telecommanded into any one of these individual modes, however, during normal operation the mode is cycled.

In auto cycle mode a counter is set at the start of each format, this steps through each of the four modes, changing at the start of each new DGI. After a complete cycle the experiment remains in the preferred mode until the start of the next format. For the Halley encounter the preferred mode was set to DID 2 OR DID 3 (the most sensitive mode). The mode cycling operated normally until just prior to closest approach (see Section 5.4.3) at which point it underwent a change before settling in the DID 2 AND DID 3 mode (least sensitive mode), with no-cycling selected.

Sensor	Bin 1	Bin 2	Bin 3	Bin 4	Bin 5	Bin 6
IPM-M	1	181	209	250	-	-
DID 2 / DID 3	1	160	190	215	230	245
DID 4	1	165	189	213	233	243
DID 5	1	149	194	250	-	-

Table 2.7: The digital amplitudes used by the CDF PHA algorithm. For example, 'Bin 1' for IPM-M contains the number of events with digital amplitudes in the range 1 to 180 inclusive.

MSM Mode	Description	Value used for PHA
0	DID 2 AND DID 3	$(DID 2 + DID 3)/2$
1	DID 2 NOT DID 3	DID 2
2	DID 3 NOT DID 2	DID 3
3	DID 2 OR DID 3	$MAX(DID 2, DID 3)$

Table 2.8: The four MSM modes used by the DIDSY experiment. The preferred mode for encounter operation was DID 2 OR DID 3, the other modes only being used once per format.

2.4 THE PARTICULATE IMPACT ANALYSER

The design of the Particulate Impact Analyser experiment (PIA) was coordinated by the principal investigator, Dr J Kissel, Max Plank Institut fur Kernphysik, Heidelberg, FRG (Kissel, 1986). As with the DIDSY experiment the PIA team was made up of a number of institutions from Europe and the US each with their own responsibility for production of hardware, software and data processing. The group at Canterbury was responsible for the dust flux analysis and comparison with the results from DIDSY. This work, which involved the analysis of the PIA front end channels is described in Chapter 6. A brief description of the full operation of the PIA experiment is given below.

Figure 2.8 shows the layout of the experiment which is technically very similar to that of the PUMA1 and PUMA 2 dust analysers flown on board the Vega 1 and Vega 2 spacecraft. Dust enters the baffle at a relative velocity of $\sim 68\text{kms}^{-1}$ and impacts with the target material which in the case of PIA was a foil of silver doped with platinum. To ensure that the system does not become saturated at high flux rates a shutter is used in front of the target, the shutter opening is elliptical which transforms to a disc on the target, which is tilted at an angle of 45 degrees relative to the direction of the dust. On impact with the target, the particle, together with some of the target material, is ionized to produce a plasma (Kissel & Krueger, 1986). The impact is detected by the photomultiplier which measures the light flash from the plasma and a charge sensitive amplifier connected to the target which detects the formation of the plasma. An acceleration grid at a potential of -2kV attracts the positive ions and another charge sensitive amplifier detects the ions as they pass through the grid. The photomultiplier, target and accelerator make up the three front end detectors which are used to trigger a sampling cycle. In addition to these three channels there are two diagnostic channels, the catcher which measures the

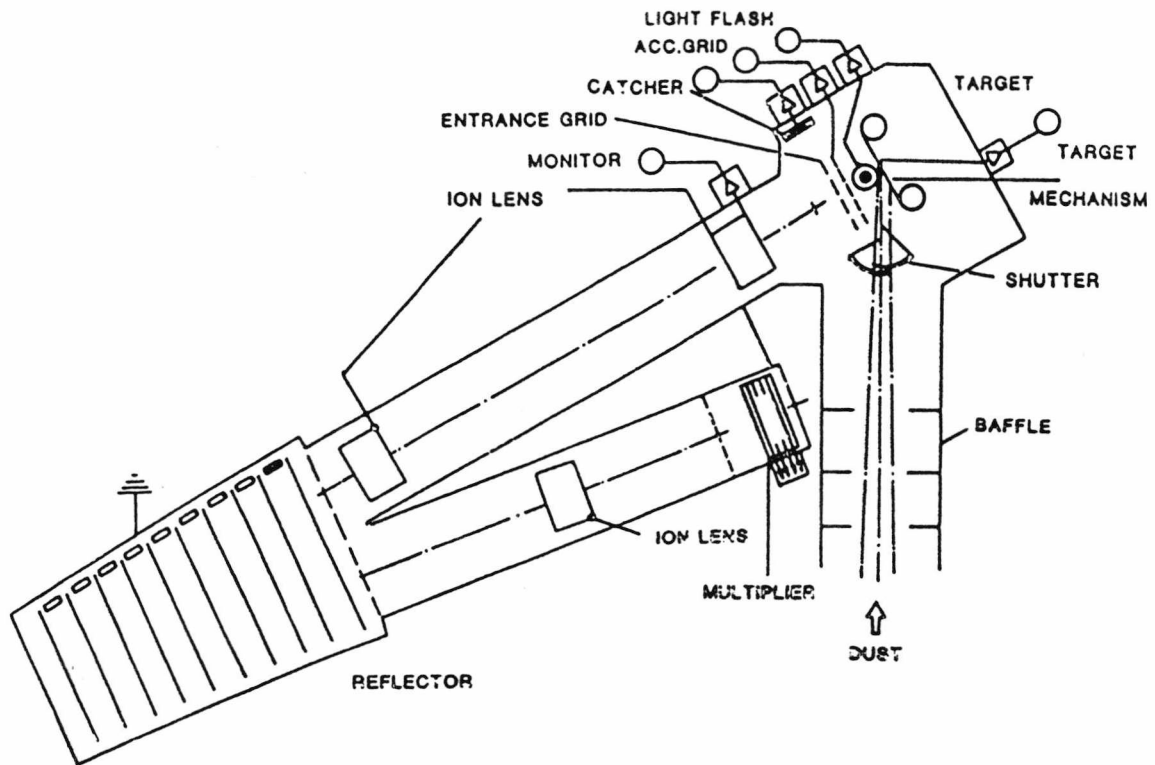


Figure 2.8: Schematic of the Particulate Impact Analyser. Information from the target, acceleration grid and light flash (photometer) is used to calculate the absolute dust flux for $m \geq 10^{-19}\text{kg}$ (see Chapter 6).

degree of ionisation from secondary ejecta and the monitor which detects the cloud of positive ions as they enter the drift tube. A series of ion lenses accelerates the ions which causes a spread of ion velocity proportional to the ratio m/q . The ions pass through the ion reflector which is used to bend the drift tube thus allowing a longer tube overall and a greater separation of the different ions and resulting in a better mass resolution than would otherwise be obtained. Finally the m/q differentiated ion cloud is detected by a multiplier which has a dynamic range of five orders of magnitude. The time of arrival and amplitude of each signal is recorded by the on board electronics for transmission back to Earth. Figure 2.9 shows three spectra recorded by PIA on

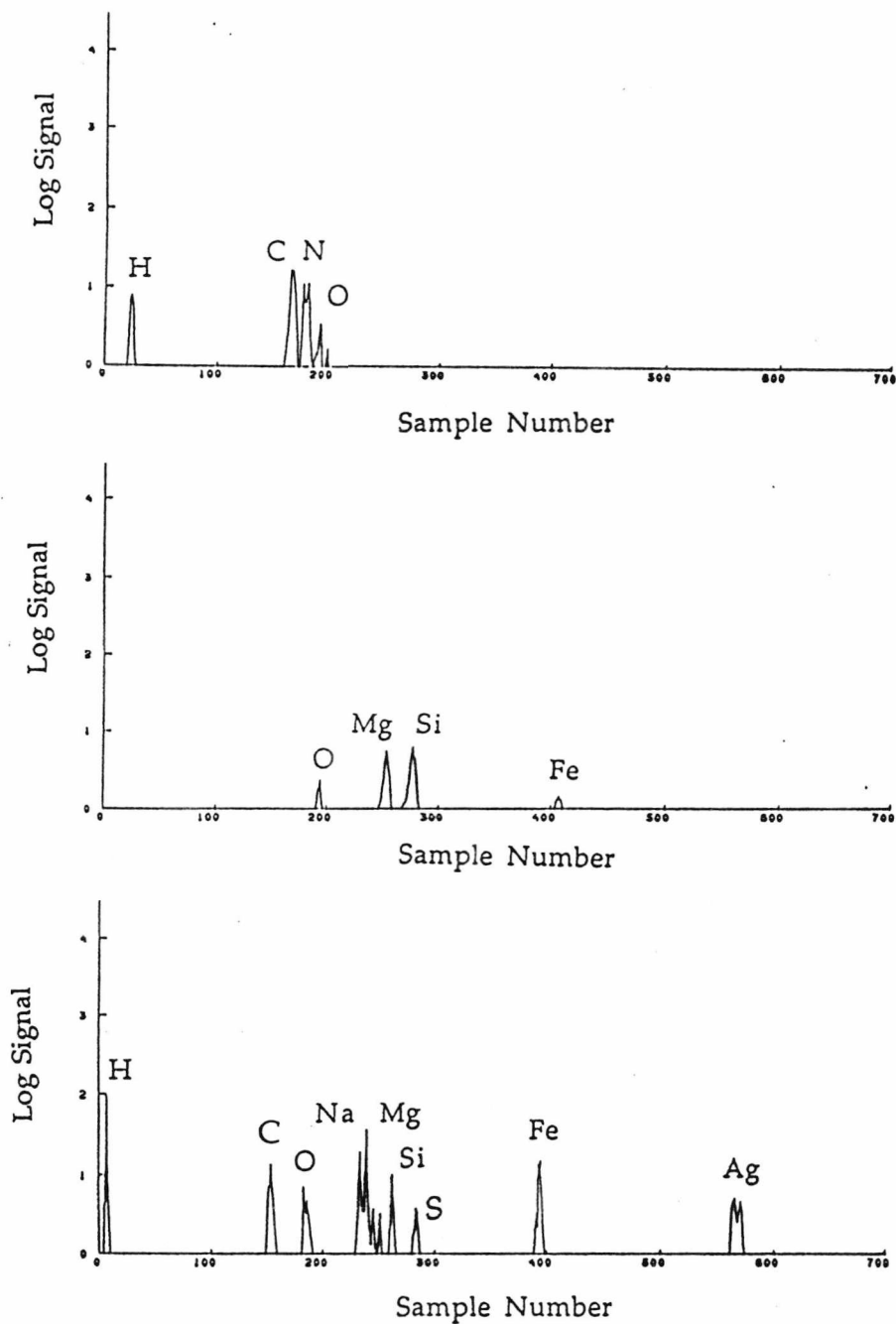


Figure 2.9: Three spectra recorded by PIA during the encounter with P/Halley. The spectra are typical of the three main classes found in the coma, CHON, Silicates and Mixed.

the night of encounter. The spectra are representative of the three main groups of particles observed in the coma of P/Halley, namely CHON, silicate and 'mixed' (Kissel et al., 1986). In theory it is possible to determine the mass and density of each impacting particle from its mass spectrum, however, attempts by the group at Heidelberg to do this type of analysis have not, to date, been entirely successful.

2.5 OTHER GIOTTO DUST EXPERIMENTS

In addition to the two principal dust experiments described above, a number of the other experiments on board Giotto made measurements of the coma dust flux, or were able to detect individual impacts due to anomalous behaviour. A list of these experiments and the methods used is given in Table 2.9.

Experiment/System	Measurement type and technique
HMC	Optical imaging of scattered light. Detection of shifts in spacecraft orientation due to large dust impacts
OPE	Column density from optical scattering of grains back along the Giotto trajectory.
GRE	Deceleration of spacecraft from Doppler shift of radio signal, total deceleration caused by combination of dust and gas. Instantaneous change due to large dust grains also detectable.
IMS-HERS, HIS and JPA-FIS	Detection of impact plasma from large events.
Spacecraft System e.g. Star mapper, solar cells.	Change in performance due to dust impact.
Spacecraft attitude	Change in spacecraft attitude/spin due to large impact resulting in loss of high gain antenna signal.

Table 2.9: Summary of the other experiments on Giotto able to make dust measurements.

CHAPTER 3

DIDSY CALIBRATION

The raw 'binned' counts measured by the DIDSY sub-systems represent the number of impacts on a sensor during an integration period. Three calibration parameters are required to convert these measured counts to more useful absolute flux rates incident on the sensor. They are the effective area, the mass sensitivity and the integration time.

The effective area is the area of the sensor over which an impacted can be detected. This is only constant if the mass sensitivity of the sensor is constant across its entire area. This is true for the CIS and IPM-P sensors and has also been assumed for the IPM-M sensor, where the variation in sensitivity is small. The same cannot be said of the MSM sensors, where the sensitivity varies by more than four orders of magnitude across the shield (Section 3.3). In such cases the sensing area is mass dependent and the number of counts observed within a bin will vary as a function of the cumulative mass distribution index α (Section 3.4).

The derivation of the mass sensitivity can be divided into two parts, the absolute sensitivity of the sensor (for example the voltage output per unit momentum input, for one of the microphone sensors), (Section 3.1) and the transfer function from sensor output to the digital value measured by the DIDSY central data formatter (Section 3.2).

The final parameter, the integration time, does not necessarily correspond to the length of a DIDSY data gathering interval (Section 2.3.4). It is dependent on the count rate on the particular sensor (due to hardware response times) and also, to a lesser extent, on the activity of other sensors (due to processing delays in the CDF).

The information presented in this chapter is split into two parts, Sections 3.1 to 3.3 deal with the available calibration data sets, while Sections 3.4 to 3.6 describe the methods used to derive the parameters described above, from the calibration data. The majority of the calibration measurements were carried out prior to launch; however, after completion of the initial DIDSY data analysis in

1987, a complete reassessment of the available data sets and processing methods was carried out. This was done to ensure that the most accurate and reliable data was in use and details of changes resulting from this reassessment have been given in the text.

In addition to the 'binned' count rates, some DIDSY data was returned in the form of digital amplitudes, the 'discrete' data. The analysis of this data uses the same calibration information as the 'binned' data but in a less processed form and some additional factors must be taken into consideration. These will be considered separately in Chapter 7.

3.1 ABSOLUTE SENSITIVITY

The absolute sensitivity of the a sensor is the relationship between a property of a dust impact and the voltage output of the sensor. In the case of the piezoelectric sensors (MSM, RSM and IPM-M), the measured parameter is the momentum exchanged between the particle and the shield, while for the IPM-P sensor, the induced charge from an impact is measured. It was shown in Section 2.3 that for particles travelling at an almost constant relative velocity, both the momentum exchange and the induced charge produced during an impact, scale linearly with increasing mass (providing the mass is below the penetration mass of the shield). In these cases the absolute sensitivity is the constant of proportionality in the linear relationship.

The calibration of the IPM-P sensor was undertaken by the co-investigator group at Heidelberg using the hypervelocity dust accelerator at the Max Planck Institute, Heidelberg. Their work showed an absolute charge sensitivity of $3.33 \times 10^{-7} \text{kgC}^{-1}$ (Göller, 1986) and a charge detection threshold of $\sim 3 \times 10^{-14} \text{C}$ ($\cong 10^{-20} \text{kg}$) for the IPM-PA sensor. The actual interpretation of the IPM-P encounter data was complicated by problems with the DID 8 cover

(Section 5.3.1) and resulted in a re-analysis of the mass sensitivity both on theoretical and experimental grounds (Maas *et al.*, 1989).

The absolute calibration of the momentum sensors required a method of simulating the momentum imparted by particles of mass $\geq 10^{-13}$ kg travelling at 68kms^{-1} . This combination of mass and velocity was beyond those attainable using the available laboratory facilities. It was therefore necessary to extrapolate lower velocity measurements made using an electrostatic dust accelerator or bead drop measurements, or to use a high energy pulsed laser to simulate the momentum imparted to the shield by impacts at 68kms^{-1} .

3.1.1 ACCELERATOR MEASUREMENTS

Due to the physical size of the Giotto front bumper shield, tests with the University of Kent's 2MV electrostatic dust accelerator could not be carried out with the sensors attached in their flight configuration. Instead, the flight MSM and RSM sensors were attached to 2cm diameter aluminium discs which were then mounted in the accelerator and shot with particles of mass 10^{-16} kg to 10^{-13} kg, at velocities from 8kms^{-1} to 1kms^{-1} (McDonnell *et al.*, 1984; Green *et al.*, 1988). The output of the sensor was fed through a 200kHz filter (matching the frequency response of the filter in the DIDSY electronics) to an amplifier, the output from which was measured using a storage oscilloscope. The sensor sensitivities (after correction for amplifier gain) varied from $190 \pm 80 \text{kVN}^{-1}\text{s}^{-1}$ for the DID 2 sensor to $1250 \pm 730 \text{kVN}^{-1}\text{s}^{-1}$ for the DID 3 sensor (Evans, 1988). The variation was much larger than the quoted manufacturers specification for sensor-to-sensor variability which may have been due to selection effects caused by poor geometric alignment of the accelerator and the sensor, the sensitivity being very position dependent close to the sensor. Due to the high velocities involved in these tests a correction has to be made for the momentum enhancement caused by ejecta being thrown off during crater

formation. Assuming an average velocity of $\sim 5\text{kms}^{-1}$, the momentum enhancement factor is 2.5 ± 1.0 (McDonnell *et al.*, 1984). Using this value to correct the absolute sensitivities gives a range from $76 \pm 32\text{kVN}^{-1}\text{s}^{-1}$ to $500 \pm 292\text{kVN}^{-1}\text{s}^{-1}$. However, the sensitivity variation over the small discs is found to be more uniform and more prone to reflections than the Giotto shield (Evans, 1988), therefore, these sensitivities are considered to be upper limits.

The electrostatic accelerator was also used for the calibration of the IPM-M unit. The sensitivity variation across the sensors geometric area was found to be small, less than an order of magnitude from maximum to minimum (Evans, 1984). To account for this sensitivity variation the IPM unit was mounted so that particles from the accelerator would impact in an area along the short axis, half way between the sensor and the edge of the plate. These measurements gave a sensitivity of $5.0\text{kVN}^{-1}\text{s}^{-1}$ for the configuration most similar to the flight electronics (Evans, 1988). This value represents the average sensitivity for the IPM-M sensor across the whole IPM-M unit compared to the peak values given for the MSM sensors above. It is therefore used in conjunction with the full geometric area of the target plate rather than a mass dependent effective area.

3.1.2 LOW VELOCITY MICRO BEAD MEASUREMENTS

The small discs used in the accelerator tests were also used in micro-bead calibration experiments (Evans 1984; Evans, 1988). These involved dropping four types of bead (three made of glass, ranging in size from $210\mu\text{m}$ to $1000\mu\text{m}$ and one steel, $1000\mu\text{m}$ in diameter) from a height of 0.2m . Due to the low velocities involved a correction was required for the 'contact' time of the impact. The 'contact' time is the time over which the bead exchanges its momentum and defines the frequency spectrum of the bending wave. For hypervelocity impacts, the momentum exchange is essentially instantaneous

and all frequencies are equally excited. This is not the case for the low velocity bead measurements and a correction factor based on the Fourier transform of the pressure function was developed to try and take account of this (Evans, 1988). The bead drop measurements indicated absolute sensitivities for the MSM and RSM sensors in the range $9\text{kVN}^{-1}\text{s}^{-1}$ to $41\text{kVN}^{-1}\text{s}^{-1}$. As with the accelerator measurements the variation between sensors was found to be large. This was probably due to the very steep sensor response as a function of distance close to the sensor, and variation in impact position of the beads when they were dropped from 0.2m. Additional bead drop and piezoelectric ('pinger', see Section 3.1.3) tests were carried out in 1988 by S.F. Green of the University of Kent, during the reappraisal of DIDSY calibration data. These confirmed that the signal output for bead drops above the sensor were not reproducible and, at best, could be used to produce the average sensitivity over a region of a few square millimetres above the sensor. The peak sensitivity was found to be a factor of 2.6 ± 1.0 greater than this average (S.F.Green, personal communication, 1988).

Bead drop tests were also carried out on the IPM-M sensor, however, in this case the alignment problem was not significant since the calibration point was some distance away from the sensor, and the variation in sensitivity with distance at this point was relatively small. The sensitivity determined using this method was $5.4\text{kVN}^{-1}\text{s}^{-1}$ for the flight assembly (Evans, 1988) which compares well with the value determined from accelerator tests.

3.1.3 PIEZOELECTRIC STIMULATION MEASUREMENTS

Piezoelectric ('pinger') stimulation uses the rapid expansion of a small piezoelectric crystal when a high voltage pulse is passed through it, to impart momentum to a target. The impulse produced could be calibrated by comparison with bead drop measurements at the same position. The great

advantage over other methods was that it was quick and easy to use. However, there was some question about the transfer mechanism, particularly if the pinger was not well shielded. In some cases a signal on the sensor was obtained even when the pinger was held close to, but not in mechanical contact with, the sensor. During the reappraisal of calibration data previous pinger measurements were considered unreliable and rejected as a primary data source.

3.1.4 LASER STIMULATION MEASUREMENTS

It has been shown (Burton, 1983; Ridgeley, 1985; Hill, 1988) that a well focused pulsed laser beam can produce a good simulation of a hypervelocity impact. This is due to its ability to dump a large amount of energy (0.1 to 100J) into a target in a short space of time (~10 to 100ns), parameters which are similar to those observed in hypervelocity impacts. For the calibration of Giotto two sets of measurements using lasers of different powers were made.

One set of measurements were made using a 1J Q-switched pulsed laser at the Rutherford Appleton Laboratory (RAL). A total of 2173 shots were fired over the RAL mock-up shield, the signal being monitored by a set of MSM sensors mounted in their flight configuration (Reading & Ridgeley, 1983). Eight of the shots (3 on DID 2, 2 on DID 3 and 3 on DID 4) were accurately aligned with the sensors to provide peak sensitivity measurements. These shots were analysed by S.F. Green and G.S. Pankiewicz of the University of Kent, using an empirical formula to relate the laser energy to the impact momentum, Equation 3.1 (Burton, 1983).

$$p = 10^{-5} E^{0.75} \quad (3.1)$$

From the analysis a sensitivity of $100 \pm 41 \text{ kVN}^{-1} \text{ s}^{-1}$ (Panciewicz, 1989), applicable to all the MSM sensors, was derived. This represented the peak sensitivity

directly on the sensor and was not directly comparable with either the accelerator, or the bead drop measurements, which were averaged over a small area around the sensor. Assuming that the peak value is some 2.6 times more sensitive than the averaged data (Section 3.1.2), the laser shots yield an average sensitivity of $38 \pm 16 \text{ kVN}^{-1} \text{ s}^{-1}$.

The second set of laser calibration measurements were carried out using the 100J Krypton Fluoride excimer 'SPRITE' laser, also at the RAL. The principal aim of the tests was to study the effect of marginal penetration on 0.5mm and 1mm aluminium target plates, and to determine the signal obtained from a sensor mounted behind the target plate, in a similar configuration to RSM (Evans, 1988). A similar analysis to that used on the shield laser measurements, was also applied to this data. Out of the 38 shots for which information was available all but three were excluded either because they showed signs of marginal penetration, or because they were made on 0.5mm aluminium (the Giotto shield was constructed from 1mm aluminium). The sensitivity obtained was $4.5 \pm 1.5 \text{ kVN}^{-1} \text{ s}^{-1}$ (Pankiewicz, 1989), comparable to the bead drop and accelerator measurements. This value was considered a lower limit because of the flatter sensitivity response of the target plates used, compared to the Giotto shield.

3.1.4 MSM SENSITIVITIES

Analysis of all the available data sets suggests an absolute sensitivity for the MSM sensors in the range 3 to 300 $\text{kVN}^{-1} \text{ s}^{-1}$. Based on the assumption that the values determined from the accelerator measurements were upper limits and that the values from the 'SPRITE' lasers tests were a lower limit, an absolute sensitivity for the MSM sensors of $20^{+20}_{-10} \text{ kVN}^{-1} \text{ s}^{-1}$ for bead drop type measurements, equivalent to $50^{+50}_{-25} \text{ kVN}^{-1} \text{ s}^{-1}$ for peak laser type calibration is considered appropriate. The sensitivity is assumed to be the same for all

sensors and replaces the values of 12, 13 and 14kVN-1s-1 (for DID 2, DID 3 and DID 4 respectively) suggested in Evans, 1988.

Since DID 5 (RSM) can only be stimulated by particles which have penetrated the front shield, the output produced cannot be directly related to the momentum of the impacting particle. Instead a single mass threshold corresponding to the marginal penetration limit of the front shield is used, Section 3.5

3.2 EXPERIMENT SIGNAL TRANSFER FUNCTION

The experiment transfer function relates the output from the physical sensor to the digital output of the Analogue-to-Digital (A-to-D) converter which is recorded by the experiment. Therefore it can only be determined for those sensors which produce amplitude information, namely the momentum and plasma sensors but not for the CIS sensor (Section 2.3.2) which only measures the number of events above its mass threshold. The calibration of the IPM-P sensor was carried out by the co-investigator group at Heidelberg, West Germany, led by Dr E. Grün and will not be considered here.

The transfer function for the momentum sensors, DID 2, DID 3, DID 4, DID 5 and IPM-M and was determined using similar techniques to those used for the absolute sensitivity calibration (see Section 3.1) and additionally by direct electrical stimulation of the front end channels, the input voltage was monitored using a storage scope and the digital output was recorded by the Electrical Ground Support Equipment (EGSE). The design of the front end analogue electronics was similar for each of the channels and since the output of the A-to-D converters were proportional to their input, any deviation in the transfer function from a simple linear relationship was due to the analogue

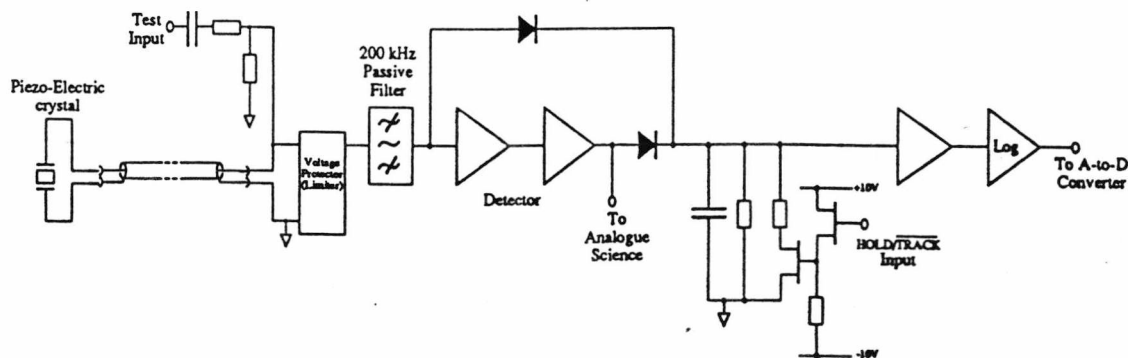


Figure 3.1: Block diagram of the front end electronics for one of the MSM sensors. Features to note are the voltage limiter and the logarithmic amplifier which both affect the shape of the signal transfer function.

front end. A block diagram of one of the MSM channels is shown in Figure 3.1. Based on this electrical design and the results obtained from the calibration tests a functional form for the response was produced, Equation 3.2 (Olearczyk, 1988).

$$D_v = (A \log_{10}[f(V)] + B) \cdot (1 - \left[\frac{C}{f(V)} \right]^D) \quad (3.2)$$

The constants A , B , C and D from Equation 3.2 were calculated from the calibration data which related the sensor output voltage, V , to the observed digital value D_v . The function, $f(V)$, took one of three forms (G.C. Evans, Personal communication, 1987) depending on the operating regime, i) normal operation (Equation 3.3), ii) over voltage protection (Equation 3.4) or iii) saturation (Equation 3.5).

$$f(V) = V \quad 0 \leq V \leq 10 \quad (3.3)$$

$$f(V) = 10 + [(V-10) \cdot 0.091] \quad 10 < V \leq 1000 \quad (3.4)$$

$$f(V) = 100 \quad 1000 < V \quad (3.5)$$

Sensor	A	B	C(Volts)	D
DID 2	28.004 (25.33)	176.66 (99.7)	0.03 (0.03)	1.760 (1.77)
DID 3	47.145 (50.21)	155.41 (16.01)	0.04 (0.04)	7.322 (5.59)
DID 4	30.718 (37.45)	174.51 (55.54)	0.03 (0.04)	2.112 (4.86)

Table 3.1: The new fitted values for the constants in Equation 3.2 (S.Nappo, personal communication, 1988). The values from the old fits (Olearczyk, 1988) are given in brackets.

Initial fits using Equation 3.2 were produced by R. Olearczyk of the University of Kent, (Olearczyk, 1988). During the post-mission reappraisal of available calibration data, some of the data sets used for the original fits were discarded either because they were of dubious quality or because they had been measured using the flight spare sensors or electronics. Using the rationalized data a new group of fits were produced using a non-linear least squares fitting technique and resulting in a new set of constants, Table 3.1 (S. Nappo, personal communication, 1988).

Equation 3.2 provides a relationship giving the digital value obtained for a particular voltage. In terms of the data analysis this is not the most useful form of the equation since in most instances the transformation from digital value to voltage output of the sensor is required. To obtain such a relationship, Equation 3.2 was solved numerically to provide the voltage at each digital value, D_V , between 0 and 255 and this information was stored in a look-up table. Figure 3.2 shows a plot of D_V against V produced using data from the look-up table for DID 3. The digital boundaries used by the on-board software to 'bin' the data are shown and also listed in Table 3.2. The digitisation of the transfer function in Figure 3.2 is hardly noticeable, indicating that the look-up table is a good approximation to the Equation 3.2. The digital thresholds corresponding to the 'Bin' boundaries are shown as dotted lines.

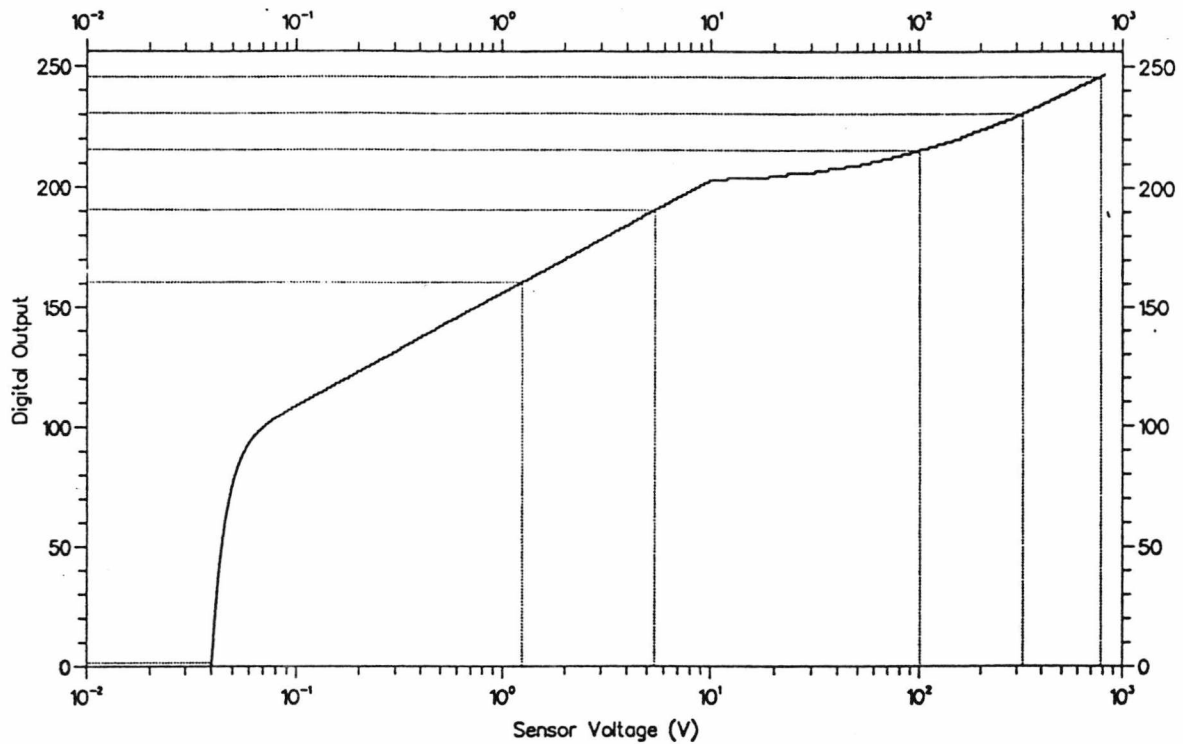


Figure 3.2: The signal transfer function for the DID 3 sensor. The resolution of the conversion is worst at low gradients, corresponding to the point where the voltage limiter starts to have an effect (Sensor Voltage > 10V).

During the reassessment of the calibration data, no changes were found necessary to the IPM-M or DID 5 calibration. However, neither the values for the constants in Equation 3.2, or the data from the original fits could be found. This was not important for the DID 5 rear shield sensor which detected the spall or debris from penetrating impacts on the front shield, since the amplitude information was not particularly meaningful and was not used in the data analysis. This was not the situation for the IPM-M transfer function which was required for the software simulation of the experiment and for the analysis of the 'discrete' data from this sensor. In the absence of the required fit parameters the less than ideal solution of digitising and then interpolating data from the calibration curve given in Evans, 1987 was used.

The main use for the transfer function is in the calculation of mass thresholds for the binned data, and individual masses for the 'discrete' data. In addition the functions were used by the software model of the experiment (see Chapter 4) to simplify the simulation of the front end electronics.

DID 2		DID 3		DID 4		IPM-M	
D _V	V						
1	3.01×10^{-3}	1	4.01×10^{-2}	1	3.01×10^{-2}	1	2.04×10^{-3}
160	3.14×10^{-1}	160	$1.24 \times 10^{+0}$	165	5.04×10^{-1}	181	7.33×10^{-3}
190	$3.05 \times 10^{+0}$	190	$5.41 \times 10^{+0}$	189	$2.96 \times 10^{+0}$	209	3.72×10^{-2}
215	$1.58 \times 10^{+2}$	215	$1.00 \times 10^{+2}$	213	$9.38 \times 10^{+1}$	250	2.01×10^{-1}
230	$7.78 \times 10^{+2}$	230	$3.21 \times 10^{+2}$	233	$7.79 \times 10^{+2}$	-	-
245	-*	245	$7.80 \times 10^{+2}$	243	-*	-	-

Table 3.2: The digital 'bin' boundaries used by the on board pulse height analysis software, with the corresponding sensor output voltages.

* The 'bin' threshold lies outside the calibration range of the sensor.

3.3 RELATIVE SHIELD SENSITIVITY

The relative shield sensitivity is only applicable to those sensors where the output is dependent, not only on the mass of the particle, but also on the distance of the impact from the sensor. For CIS and IPM-P, the sensitivity is constant over the full geometric area of the sensor, resulting in a well defined effective area (Section 3.4) and mass threshold (Section 3.5). A similar assumption is made for the IPM-M sensors by using an average, rather than absolute sensitivity (see Section 3.1.1). The same assumption cannot be made for the MSM sensors where the attenuation of the impact induced bending wave is dependent on the distance of the impact site from the sensor and can be very large. If the incident particles all had the same mass, the average sensitivity could be applied without any loss of accuracy. For a distribution containing a range of particle masses the problem arises that the experiment cannot distinguish small particles close to the sensor, from larger particles

further away. Hence, the detected impact rate is dependent both on the shape of the coma mass distribution and on the sensitivity variation with distance from the sensor. Therefore it is important to know the relative sensitivity of points around the shield. This information can then be combined with the absolute sensor sensitivity (Section 3.1) to calculate a correction term for use in the calculation of flux rates.

Since only limited access was available to the Flight Model (FM) shield, and because of the potentially damaging stimuli required to map the sensitivity, three structurally similar shields (Table 3.3) were constructed for the purpose of calibration (Evans, 1988).

SHEILD	COMMENT
Flight Model (FM)	Shield used on Giotto spacecraft. The underside was painted with PCB-Z conductive paint which had the effect of damping the acoustic transmission of the shield (Ridgeley, 1985)
Structural Model (SM)	Similar to the FM but without the conductive paint (Evans & Ridgeley, 1985).
Rutherford Appleton Lab Mock-Up (RAL)	Similar to FM except for a 1° offset in the rivet positioning. A CON-TACT plastic film was stuck to the underside of the shield to simulate the effect of the conductive paint.
University of Kent Mock-up (UKC)	Made at RAL and similar to the RAL shield except that it did not include the plastic coating.

Table 3.3: The four front bumper shields constructed for the Giotto spacecraft, engineering test and for calibration. The shield acronym is shown in brackets.

A number of calibration studies were carried out to map the sensitivity over the shields using four techniques:-

- i) A special purpose gas gun called the 'Bead Momentum Calibrator' (BMC) [FM, SM, RAL, UKC]
- ii) Bead drops [SM, UKC]
- iii) High energy laser stimulation [RAL]
- iv) Piezoelectric stimulation [FM, UKC]

These studies have been described in some detail in Evans, 1984; Evans & Ridgeley, 1985; Ridgeley, 1985 and Evans, 1988, and were summarized in Pankiewicz, 1989. The models were found to vary from one another, particularly in terms of the transmission across the isolating and non-isolating joints. Determination of which of the model shields most closely matched the response of the FM was made difficult by the limited amount of information available from the FM (only 11 BMC shots). Initial processing of the DIDSY data at the University of Kent made use of calibration data from the UKC shield using piezoelectric stimulation (Zarnecki *et al.*, 1986). During the reappraisal of calibration data, the decision was taken to switch to the laser calibration data from the RAL shield. The reasons for this change were threefold; firstly, the reliability of the piezoelectric measurements was questionable; secondly, the RAL mock-up shield was the only one to simulate the thermal paint of the FM shield, which was thought to increase the damping of bending wave; and finally, the RAL laser measurements provided the most detailed mapping. The data was taken from Ridgeley, 1985 and an area associated with each point, or averaged group of points. Figures 3.3 to 3.5 show the relative sensitivity map for each of the front shield momentum sensors. The data was normalised in each case to a peak of 10^5 on the sensor, equivalent to an absolute sensitivity of $50\text{kVN}^{-1}\text{s}^{-1}$ (Section 3.1.4). The data in the maps was averaged over small area elements which accounts for the lower peaks. The large attenuation in the sensitivity, caused by the isolating joints, is apparent in all three cases.

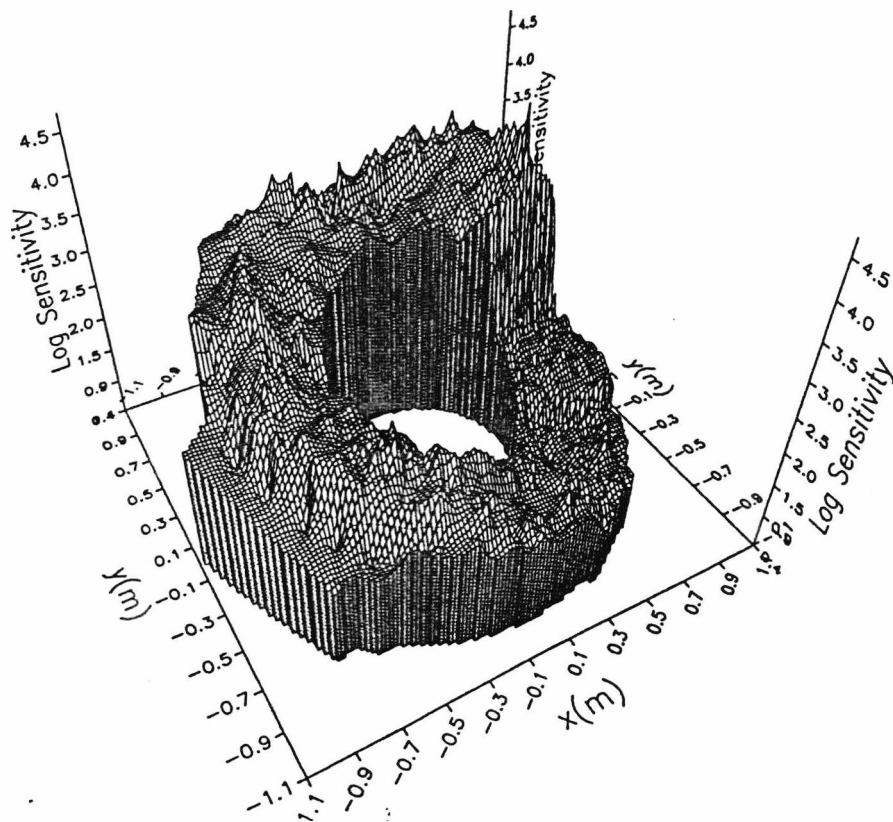


Figure 3.3: Shield sensitivity map the DID 2 sensor calculated from laser impact simulation on the RAL mock-up shield.

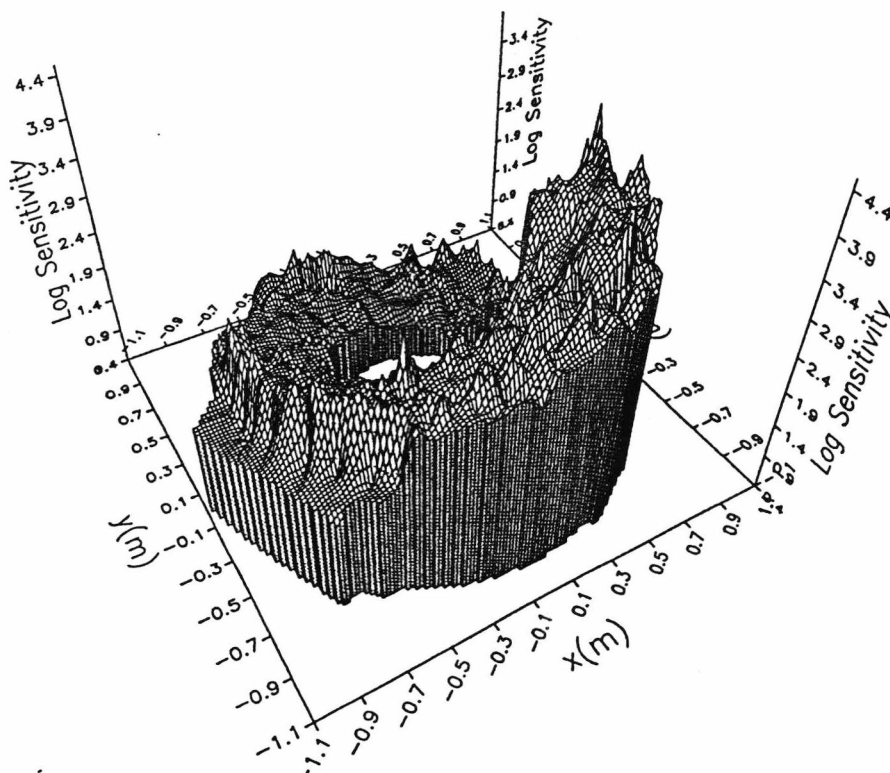


Figure 3.4: Shield sensitivity map the DID 3 sensor calculated from laser impact simulation on the RAL mock-up shield.

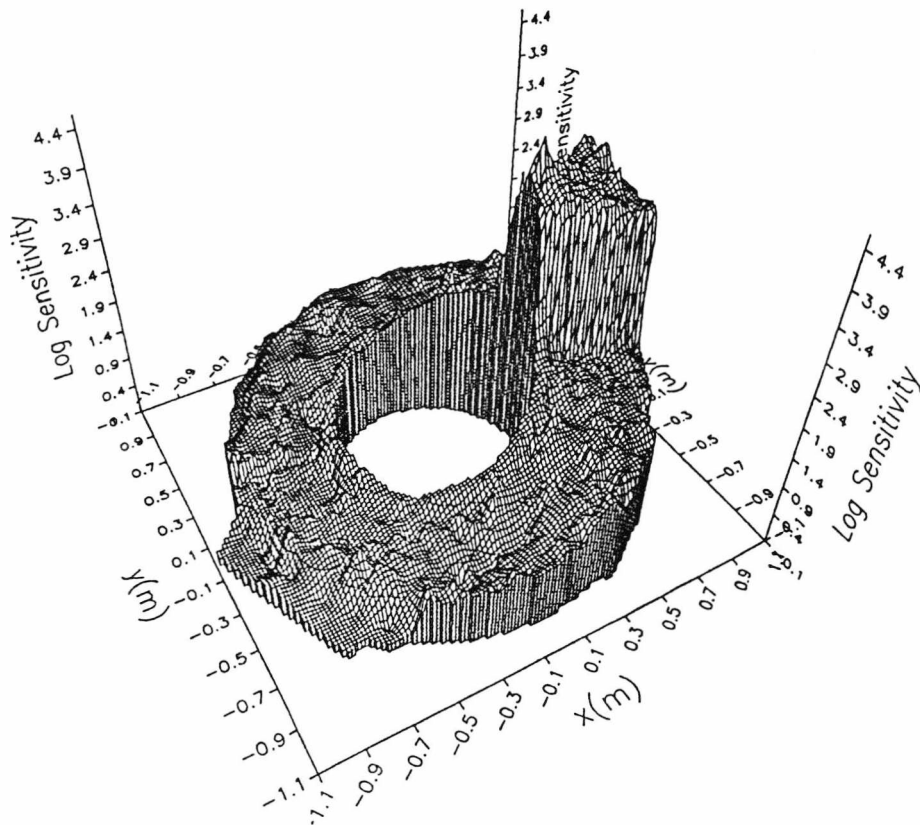


Figure 3.5: Shield sensitivity map the DID 4 sensor calculated from laser impact simulation on the RAL mock-up shield.

3.4 EFFECTIVE AREA CALCULATION

The effective area is the detecting area of a sensor for particles in a particular mass range, and includes a correction factor for the sensitivity variation across the geometric area of the sensor. In the case of CIS the sensitivity is constant which means that particles above the threshold mass can be detected anywhere on the sensor and results in a constant effective area, equal to its geometric area of 0.1m^2 . Similarly the IPM-P effective area is equal to $5.96 \times 10^{-3}\text{m}^2$ for each of the IPM-PA and IPM-PB sensors, although this value had to be revised because of the failure of the DID 8 cover to release.

In general, the effective area of the momentum sensors is calculated based on the sensitivity variation described in Section 3.3. However, in the case of the IPM-M and DID 5 sub-systems this effect has been accounted for in a

different way. For IPM-M the sensitivity variation was found to be small and a constant effective area equal to the geometric area of the target plate is used, equal to 0.0119m^2 , together with an average sensitivity, see Section 3.1. DID 5 is a special case since it does not directly measure the momentum of incident particles, but rather the spall or fragments produced by the impact of marginal or fully penetrating particles on the front bumper shield. The combination of mass and velocity required to penetrate the 1mm aluminium shield were unobtainable in the laboratory, instead, tests on the effects of penetration were carried out using a high energy pulsed laser (Evans, 1988). These tests indicated, that due to the high acoustic attenuation of the Kevlar rear shield, the fragments must impact on or near the DID 5 microphone for them to be detected. A somewhat arbitrary value of 0.02m^2 was used to represent the area of the front shield where sufficiently large impacts might be expected to also stimulate the rear shield.

As was shown in Section 3.3 the sensitivity variation of the MSM sensors with distance from the sensor is large, ~ 4 orders of magnitude from maximum to minimum sensitivity, hence, the area over which a particular sensor can detect an impact depends on the mass of the impacting particle. Equally for any individual particle there is no way to distinguish between a small impact close to the sensor and a larger impact some distance away, since both will produce the same signal on the sensor. However, if the size distribution of the particles is known, then the probability of occurrence may give some indication of which is more likely. By taking the results from an unbiased sample of impacts and assuming a form of the mass distribution then a statistically valid result can be obtained. In practice the form of the mass distribution is unknown and several iterations are required to obtain a solution; using the distribution calculated from the the first iteration for the next and so on. This effect can be conveniently incorporated into the area function for the sensor. Instead of the area being equal to the geometric area of

the sensor, it becomes a weighted mean of the area sensitivity product depending on the cumulative mass distribution index α , where the mass distribution is assumed to be of the form given in Equation 3.6

$$\varphi(\geq m) = k \cdot m^{-\alpha} \quad (3.6)$$

3.4.1 EFFECTIVE AREA CALCULATION FOR MSM

The remainder of this section will be concerned with how this method was used in practice to obtain the effective area functions for the DID 2, DID 3 and DID 4 sensors in each of the operating modes of the experiment.

A schematic representation of the analysis is shown in Figure 3.6. Using the shield calibration data, the mass of the particle required to just be detected in a particular sensor bin combination is calculated for every position on the shield. This is done in the following way. The digital threshold for the bin in question is converted to a voltage at the sensor using the experiment signal transfer function (Section 3.3). The attenuation between the sensor and the position on the shield being tested is known from the shield sensitivity map. Using this attenuation factor the voltage can be scaled to the value that would have been detected had the impact occurred directly on the sensor. Then using the absolute mass sensitivity of the sensor the mass of a particle needed to produce the required digital signal when impacting at the specified shield position is determined, Equation 3.7. for non-penetrating particles.

$$m = \frac{V(D_v) P_s}{\epsilon S v P(i)} \quad (3.7)$$

Where $V(D_v)$ is the signal transfer function, P_s the peak relative shield sensitivity, ϵ the momentum enhancement, S the absolute sensitivity, v the

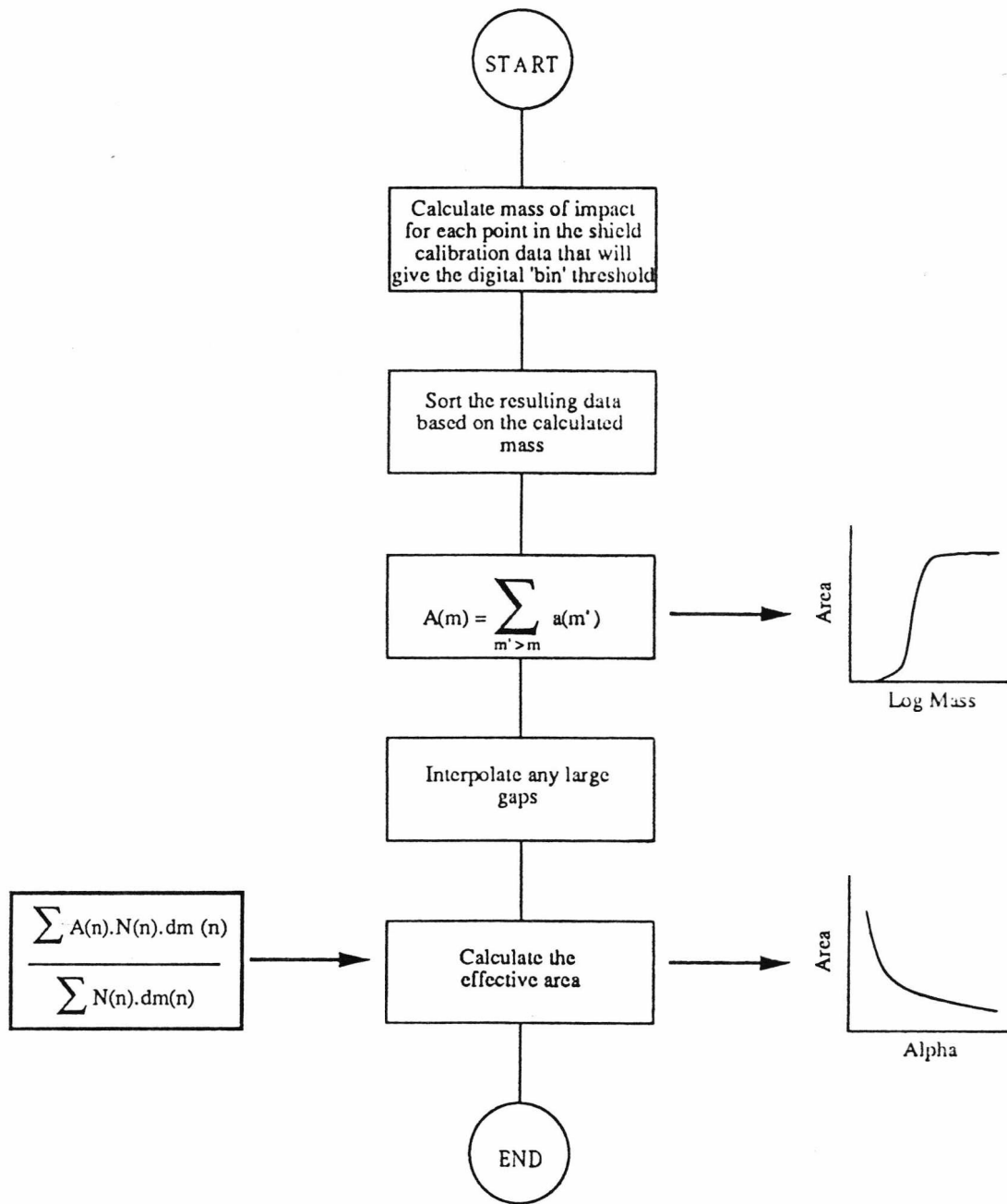


Figure 3.6: Flow diagram of the method used to calculate the MSM effective areas.

relative impact velocity and $P(i)$ the relative shield sensitivity at position i . If the calculated mass exceeds the penetration mass, m_{pen} of the shield, then a special correction term to take account of the momentum derating factor, γ must also be included (see Section 2.3.1; Section 7.3). This results in a list of mass and area values, the area corresponding to the pixel size of the associated sensitivity point in the shield map. The list must be sorted by mass, on the VAX/VMS computer used for the analysis, this is achieved using the operating system 'SORT' command. The area of the shield A over which a particular mass can be detected is given by the sum of all pixels areas a with mass thresholds M_T less than, or equal to, that mass Equation 3.8.

$$A(m) = \sum_{i=Whole\ shield} a(i) F(M_T(i)) \quad \text{Where } F(M_T(i)) = 0 \text{ if } m < M_T \\ = 1 \text{ if } m \geq M_T \quad (3.8)$$

A second area distribution is then produced using the same method but with a digital value equal to the threshold level of the next bin up and so on for each of the bins for that sensor. Figure 3.7 shows the area function for the DID 4 sensor. Each of the functions are open ended and simply represent the area of the shield over which a certain mass can be detected. The information returned by the experiment gives the number of counts in each differential amplitude 'bin'. Since, there is some overlap between the 'bins' in terms of particle mass it is more convenient to consider the data in cumulative 'bins'. A cumulative 'bin' is simply defined to contain all counts from the equivalent, and all higher, differential 'bins'. The limiting mass threshold of a cumulative 'bin' is well defined and the upper limit is open ended, therefore to determine an effective area, an assumed mass distribution must be used to weight the area function, Equation 3.9.

$$A_{Eff} = \frac{\sum_{m=M_T}^{M_{Max}} A(m) n(m) dm}{\sum_{m=M_T}^{M_{Max}} n(m) dm} \quad (3.9)$$

$$n(m) = k' m^{-(\alpha+1)} \quad (3.10)$$

Where $n(m)$ is the differential mass distribution of the form described in Equation 3.10. M_T is the threshold mass and M_{Max} is the maximum mass for the calculation and is taken to be 10kg. Before this calculation is done the area function must first be interpolated to ensure that the mass step dm is not too large. This is particularly important for the DID 4 area (Figure 3.7) since there is a substantial drop in the mass sensitivity across the isolating joints, which leads to a large dm where there are no area points.

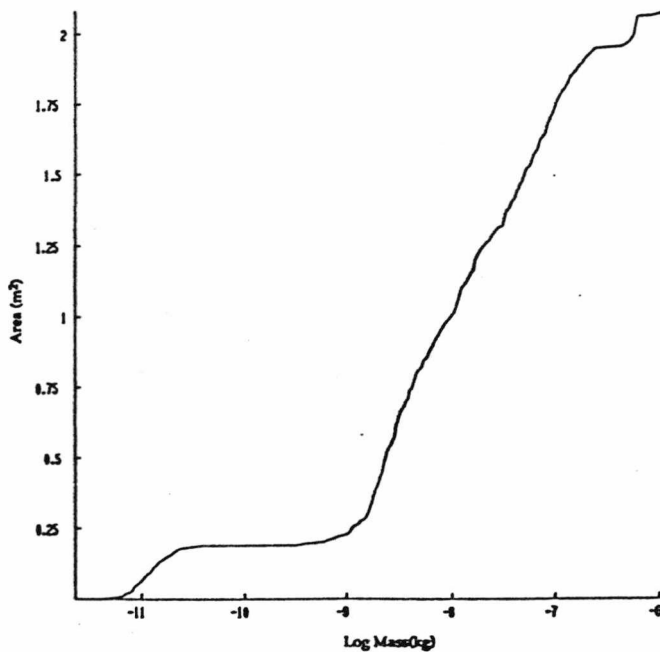


Figure 3.7: The area function for the DID 4 sensor 'Bin1'. For a given mass the area function gives the area of the shield over which the impact could be detected. The effect of the isolating joints is seen as a constant area between $\sim 2 \times 10^{-11}$ kg and 10^{-9} kg.

Using this method a set of effective area values have been obtained for each 'bin' of the MSM sensors, and in the case of DID 2/3 for each mode. The calculated effective area depends on the mass distribution index α . Since the value of α is not known until the fluxes are calculated an algorithm is used where an initial value of α is used to calculate a distribution from which a new value α' is obtained this in turn is used to determine a new set of areas and hence a new flux distribution. Since the process of calculating effective areas is time consuming, a set of look-up tables have been produced containing effective areas for a range of α between 0.3 and 2.0 at intervals of 0.1. These are listed in Table 3.4 and shown graphically for DID 4 in Figure 3.8, intermediate values were obtained by linear interpolation between the two closest points.

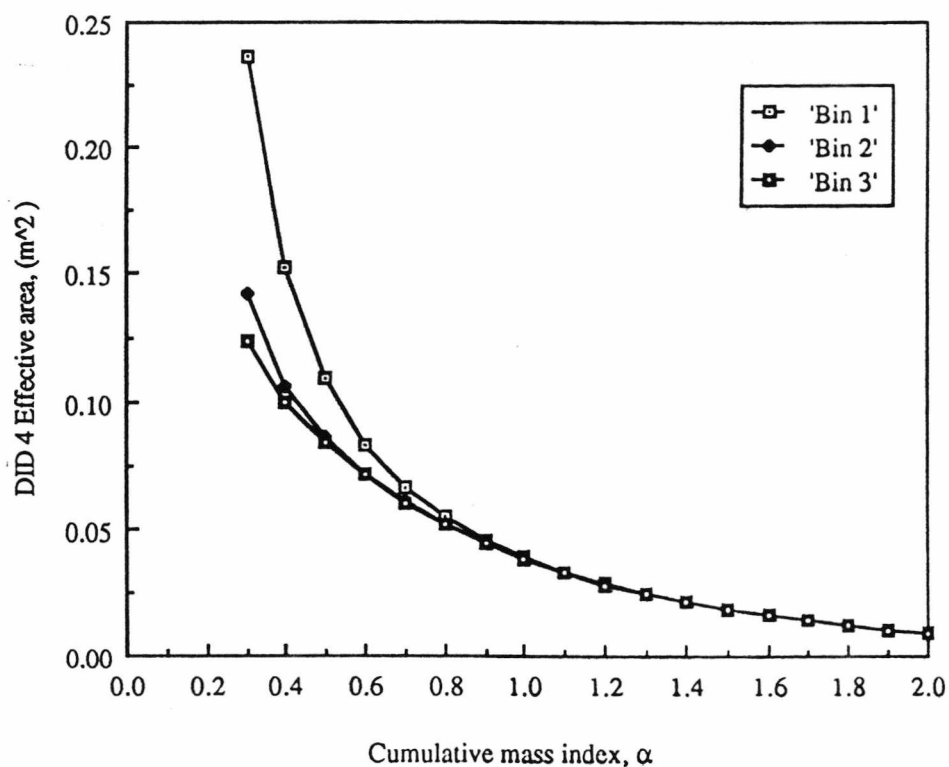


Figure 3.8 shows the effective area vs. alpha function for the MSM sensor DID 4.

DID 2

α	'Bin 1'	'Bin 2'	'Bin 3'
0.3	0.55	0.49	0.36
0.4	0.38	0.34	0.25
0.5	0.27	0.25	0.19
0.6	0.20	0.18	0.14
0.7	0.15	0.14	0.11
0.8	0.11	0.11	8.79E-02
0.9	8.77E-02	8.59E-02	6.98E-02
1.0	6.84E-02	6.74E-02	5.59E-02
1.1	5.40E-02	5.35E-02	4.52E-02
1.2	4.30E-02	4.27E-02	3.68E-02
1.3	3.46E-02	3.45E-02	3.02E-02
1.4	2.81E-02	2.80E-02	2.49E-02
1.5	2.30E-02	2.30E-02	2.07E-02
1.6	1.90E-02	1.90E-02	1.73E-02
1.7	1.58E-02	1.58E-02	1.46E-02
1.8	1.32E-02	1.32E-02	1.23E-02
1.9	1.11E-02	1.11E-02	1.05E-02
2.0	9.48E-03	9.47E-03	9.01E-03

DID 3

α	'Bin 1'	'Bin 2'	'Bin 3'
0.3	0.42	0.26	0.17
0.4	0.28	0.18	0.12
0.5	0.19	0.14	8.98E-02
0.6	0.14	0.10	7.00E-02
0.7	0.10	8.47E-02	5.62E-02
0.8	8.07E-02	6.76E-02	4.60E-02
0.9	6.28E-02	5.47E-02	3.81E-02
1.0	4.98E-02	4.47E-02	3.20E-02
1.1	4.00E-02	3.68E-02	2.70E-02
1.2	3.26E-02	3.05E-02	2.30E-02
1.3	2.68E-02	2.55E-02	1.97E-02
1.4	2.23E-02	2.14E-02	1.69E-02
1.5	1.87E-02	1.81E-02	1.46E-02
1.6	1.58E-02	1.54E-02	1.27E-02
1.7	1.34E-02	1.32E-02	1.10E-02
1.8	1.14E-02	1.13E-02	9.69E-03
1.9	9.88E-03	9.81E-03	8.49E-03
2.0	8.54E-03	8.51E-03	7.47E-03

DID 4

α	'Bin 1'	'Bin 2'	'Bin 3'
0.3	0.23	0.14	0.12
0.4	0.15	0.10	9.97E-02
0.5	0.10	8.60E-02	8.37E-02
0.6	8.33E-02	7.20E-02	7.10E-02
0.7	6.67E-02	6.11E-02	6.06E-02
0.8	5.50E-02	5.21E-02	5.19E-02
0.9	4.61E-02	4.46E-02	4.45E-02
1.0	3.91E-02	3.83E-02	3.82E-02
1.1	3.34E-02	3.30E-02	3.29E-02
1.2	2.87E-02	2.84E-02	2.84E-02
1.3	2.47E-02	2.46E-02	2.45E-02
1.4	2.14E-02	2.13E-02	2.12E-02
1.5	1.86E-02	1.85E-02	1.84E-02
1.6	1.61E-02	1.61E-02	1.60E-02
1.7	1.41E-02	1.40E-02	1.40E-02
1.8	1.23E-02	1.23E-02	1.22E-02
1.9	1.08E-02	1.07E-02	1.07E-02
2.0	9.52E-03	9.49E-03	9.46E-03

DID 2 OR DID 3

α	'Bin 1'	'Bin 2'	'Bin 3'
0.3	0.68	0.59	0.46
0.4	0.49	0.42	0.33
0.5	0.35	0.30	0.24
0.6	0.26	0.22	0.18
0.7	0.19	0.16	0.13
0.8	0.15	0.12	0.10
0.9	0.11	9.61E-02	8.46E-02
1.0	9.02E-02	7.44E-02	6.71E-02
1.1	7.07E-02	5.82E-02	5.37E-02
1.2	5.59E-02	4.61E-02	4.33E-02
1.3	4.45E-02	3.68E-02	3.52E-02
1.4	3.58E-02	2.96E-02	2.88E-02
1.5	2.90E-02	2.41E-02	2.37E-02
1.6	2.37E-02	1.97E-02	1.97E-02
1.7	1.94E-02	1.63E-02	1.64E-02
1.8	1.61E-02	1.36E-02	1.38E-02
1.9	1.34E-02	1.14E-02	1.16E-02
2.0	1.12E-02	9.67E-03	9.89E-03

DID 2 AND DID 3

α	'Bin 1'
0.3	0.81
0.4	0.63
0.5	0.50
0.6	0.40
0.7	0.33
0.8	0.27
0.9	0.23
1.0	0.19
1.1	0.17
1.2	0.14
1.3	0.12
1.4	0.11
1.5	0.10
1.6	8.99E-02
1.7	8.07E-02
1.8	7.27E-02
1.9	6.59E-02
2.0	6.01E-02

Table 3.4: The effective areas calculated for each 'Bin' of the MSM sensors and for each mode of DID 2/3. All areas are in m².

Several points should be made concerning the effective areas produced by this analysis. The fluxes calculated using these areas correspond to mass thresholds calculated from the most sensitive pixel area (see Section 3.5). Also, the areas were calculated assuming a constant mass index α for all masses $>10^{-13}$ kg. According to the analysis of the MSM 'discrete' data (Section 7.3) there is some evidence to suggest an increase in α at larger masses, if this is the case then it will effect the areas calculated for the upper 'bins'. There will be no discernible effect on the lower 'bins' where the smaller particles dominate those detected by the sensor.

3.5 MASS THRESHOLDS

The fixed effective areas for the CIS, IPM-P, IPM-M and DID 5 sensors, results in fixed mass thresholds for these sensors. For CIS a threshold based on the penetration limit of the thin foil is used, equal to 3×10^{-13} kg. The operation of IPM-P and IPM-M pre-encounter is dependent on the DID 8 cover and will be considered in Chapter 5. Post-encounter IPM-P became noisy, IPM-M was operational and mass thresholds based on an absolute sensitivity of $\sim 7 \text{ kVN}^{-1} \text{ s}^{-1}$ (Evans, 1988) and the IPM-M transfer function (Section 3.2) were combined to give the values listed in Table 3.5. DID 5 is assigned a threshold mass corresponding to the marginal penetration limit of the front shield of $\sim 10^{-9}$ kg.

The fluxes produced using the effective areas produced in the previous section for the MSM sensors, must have a corresponding mass at which they are plotted. This might initially be thought to be the threshold mass of the detector, derived from the peak sensitivity on the sensor, however this is not the case. This can be understood if the area against mass function calculated in Section 3.4 is considered. Although the peak sensitivity is at $50 \text{ kVN}^{-1} \text{ s}^{-1}$ the area corresponding to this threshold is infinitesimal and the probability of particles being detected at this point, is close to zero. For the effective areas to be

applied correctly the resultant fluxes should be plotted at the mass threshold derived from the most sensitive pixel used to calculate the areas. This means that if a different shield sensitivity data set is used, not only are a new set of areas produced but also a new set of mass thresholds for which the effective areas apply. This did in fact occur during the reappraisal of calibration data, which resulted in a change in the sensitivity map used to a higher resolution map, produced using laser impact simulation. This accounts for the small differences between the mass thresholds published in McDonnell *et al.*, 1987 and the majority of publications after this date (e.g. McDonnell *et al.*, 1989). The thresholds calculated for the RAL laser map using Equation 3.7 and voltage thresholds from Table 3.2, are given in Table 3.5.

Sensor	Mass threshold (kg)			
	Bin 1	Bin 2	Bin 3	Bin 4
IPM-M *	4.0×10^{-13}	1.0×10^{-12}	5.0×10^{-12}	4.0×10^{-11}
DID 2	1.7×10^{-12}	1.8×10^{-11}	1.7×10^{-10}	-
DID 3	3.4×10^{-12}	1.1×10^{-10}	4.6×10^{-10}	-
DID 2 OR DID 3	1.7×10^{-12}	1.8×10^{-11}	1.7×10^{-10}	-
DID 2 AND DID 3	1.5×10^{-10}	-	-	-
DID 4	2.2×10^{-12}	3.7×10^{-11}	2.2×10^{-10}	-
DID 5	$\sim 1 \times 10^{-9}$	-	-	-
CIS	3.0×10^{-13}	-	-	-

Table 3.5: Limiting mass thresholds for the DIDSY sensors. The values for the MSM sensors depend on the sensitivity map used to calculate the corresponding effective areas. These limiting masses were calculated using based on the RAL laser shield calibration (see text).

* The IPM-M mass threshold is only applicable post-encounter, after the protective cover has been released.

Due to the shape of the area function the probability of detecting particles at the threshold mass is quite low. In some cases it is useful to plot the calculated flux at a mass more representative of the 'Bin' distribution, rather than at the threshold mass. The representative mass is taken to be the mass above which 95% of the particles are detected. This is determined by weighting the area function given by Equation 3.8, with a differential mass distribution of the form given in Equation 3.10 and selecting the mass above which 95% of the area under the graph resides. The representative, or 'take-off' masses as they are sometimes known, are listed for the MSM sensors in Table 3.6. The fluxes plotted at the representative masses ϕ_R must be transformed from the 'threshold' fluxes ϕ_T . Thus assuming a cumulative mass distribution with index α the flux is scaled according to Equation 3.11.

$$\phi_R = \phi_T \left(\frac{m_T}{m_R} \right)^\alpha \quad (3.11)$$

Another mass definition, which will only be considered briefly here, is the masses at which differential 'bin' fluxes are plotted. These are calculated in

Sensor	Representative Mass (kg)		
	Bin 1	Bin 2	Bin 3
DID 2	6.0×10^{-12}	6.3×10^{-11}	6.0×10^{-10}
DID 3	1.2×10^{-11}	3.8×10^{-10}	1.6×10^{-9}
DID 2 OR DID 3	6.0×10^{-12}	6.3×10^{-11}	6.0×10^{-10}
DID 2 AND DID 3	5.3×10^{-10}	-	-
DID 4	7.7×10^{-12}	1.3×10^{-10}	7.7×10^{-10}

Table 3.6: Representative masses for the MSM sensors. These masses are only applicable when used in conjunction with modified flux rates.

a similar way to the cumulative mass thresholds described in Section 3.4, except that the area functions are not left open ended. Instead, at each mass point, the area from the current 'bin' plus one, is subtracted from the area for the current 'bin'. This only affects the area function for masses above the threshold of the current 'bin' plus one. The modified area function is weighted by a differential number distribution and the centroid of resulting distribution used to define the representative mass.

3.6 INTEGRATION TIMES AND CORRECTION FOR EXPERIMENTAL DEAD TIMES.

The integration time is the time during which a sub-system is able to detect and respond to, a new event. The data gathering interval of the DIDSY experiment was the same for all sensors and was directly linked to the operating mode of the spacecraft's telemetry control systems. All events detected by the DIDSY experiment on the night of encounter occurred while the spacecraft was in 'Format 2' and transmitting at 46kbits^{-1} which corresponded to a nominal time of 1.13s for a DIDSY Data Gathering Interval (DGI). During the period of operation just prior to closest approach, a number of spurious resets affected the operation of the experiment and resulted in DGI's which were either shorter or longer than this time, these will be considered in Section 5.4.3.

At low count rates the integration time and the length of a DGI are effectively equal and no correction to the observed count rates is required. However, as the number of events detected by the experiment increase, the fraction of DGI taken up by the system to service and reset the sensors becomes significant. During this time the sensor is unable to detect any new impacts, resulting in an integration time less than the length of a DGI. Assuming that the events are randomly distributed in time, the observed counts can be scaled

to take account of the 'missing' integration time (Equation 3.12).

$$N' = \frac{N}{\left(1 - \frac{\tau_d}{\tau_i}\right)} \quad (3.12)$$

Where τ_d is the total time during the DGI (of length τ_i) that the sensor was unable to detect new impacts and N is the number of impacts actually observed. The value of τ_d is different for each bin of each sensor and to a lesser extent also dependent on the activity of other sensors and of the experiment as a whole.

The calculation of τ_d is simplest for CIS since the sensor only has a single 'bin' and the use of a hardware counter means that the sensor is unaffected by the activity on the rest of the system. Hence, τ_d is only dependent on the fixed 1.19ms disable time during which the sensor is recharged after each event, resulting in a value for the 'dead' time of, $\tau_d = N * 1.19 \times 10^{-3}$ s.

Due to the failure of the IPM-P sensor to operate correctly (Section 5.3.1), dead time corrections are not applicable for this sensor. However, the effect of the post-encounter, noisy, IPM-P activity on the other sensors and in particular IPM-M is important (see Section 5.4.1).

The situation for the momentum sensors is slightly more complex since the operation of the electronics mean that the 'dead' times for each sensor 'bin' are different and related to the number of events in the other 'bins'. This can be understood by considering what happens when an event is detected by a single momentum sensors.

Prior to the impact the front end electronics of the sensor is in 'track' mode and the digital threshold level on the D-to-A converter is at some level, depending on the time since the last impact and its amplitude. If the signal from the impacting particle is larger than the threshold value set on the D-to-A, the front end electronics will switch to 'hold', and a flag will be set to inform

the CDF that an event has occurred. When the CDF next gets round to reading the event flags, it sees that an impact has occurred and branches to the appropriate event service routine. The time taken between the occurrence of the event and the CDF servicing the event is known as the 'hold time' τ_{Hold} . Once in the service routine, the CDF reads the signal level from the sensor and stores the information ready for the PHA routine. The CDF then takes the observed digital levels and adds a digital offset, D_{Offset} , to it and outputs the values to the D-to-A converters thus setting the new threshold levels. Before exiting the service routine, the CDF re-enables the sensor by switching it back into 'track' mode. The threshold value set on the D-to-A automatically starts to decrement at a rate τ_{Ramp} which is designed to mimic the decay of the acoustic signal on the shield. A new impact of the same amplitude as the original event can only be detected when the threshold has dropped to a value below this level, i.e. a time, $\tau_{\text{Hold}} + D_{\text{Offset}} \times \tau_{\text{Ramp}}$, after the original event. This is shown schematically in Figure 3.9. Since the level of each impact within a 'bin' is not known a digital amplitude, H , representative of the distribution of amplitudes expected within the 'bin', must be used.

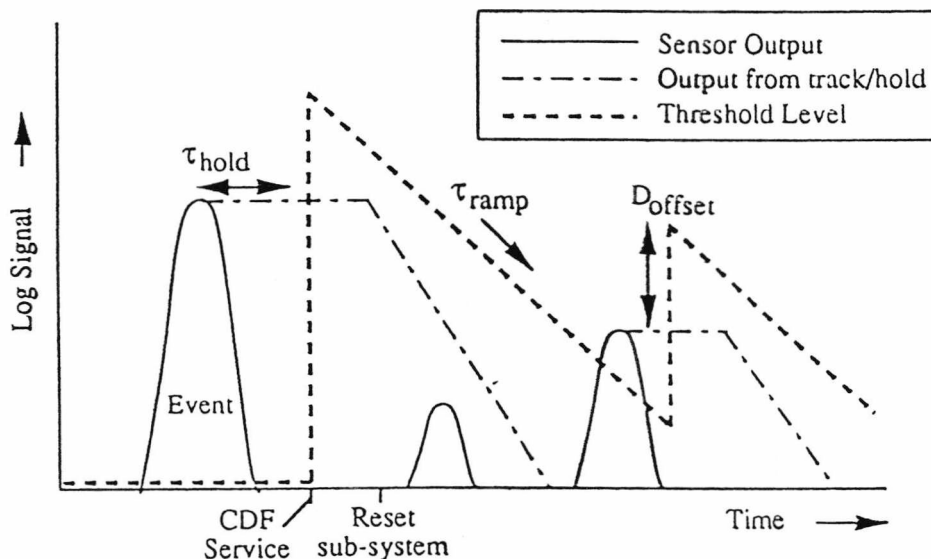


Figure 3.9: Schematic showing signal levels as a function of time. The dotted line represents the threshold level, the sensor is 'dead' to any impacts with amplitudes below this value.

A first order correction was proposed by S. Evans, of the University of Kent, (Evans, 1988) which consisted of two parts; a 'self' dead time and a correction based on the number of events in bins with higher mass thresholds. During the re-analysis of calibration techniques, the two terms were combined and the equation was modified so that it also took account of events in lower bins where the threshold level (because of the offset), could cause events in higher bins to be rejected. In addition a detailed examination of the operation of the hardware and software of the MSM sub-system showed that the 3ms hold time used in Evans, 1988, did not in fact occur. The actual hold time was found to be dependent on the sub-system, mode and how busy the CDF was at the time of the event. The improved dead time correction is shown in Equation 3.13 and the parameters for each of the MSM and IPM-M sensors are given in Table 3.7.

$$\tau_d(i) = \sum_{j=i}^{i_{Max}} \tau_{Hold} \cdot N(j) + \sum_{j=1}^{i_{Max}} \left[\left\{ \begin{array}{l} (H(j) + D_{Offset}) - H(i) \\ \leftarrow \text{If } > 255, = 255 \rightarrow \\ \text{If } < 0, = 0 \rightarrow \end{array} \right\} \cdot \tau_{Ramp} \cdot N(j) \right] \quad (3.13)$$

- Where:-
- $\tau_d(i)$ - Total 'dead' time for 'Bin i'
 - τ_{Hold} - Hold time
 - τ_{Ramp} - Ramp-down time per digital step
 - $H(i)$ - Representative value of 'Bin i'
 - D_{Offset} - Digital offset
 - $N(i)$ - Observed counts in 'Bin i'

Values for DID 5 have not been determined since the count rates on this sensor are low, however, the DID 5 electronics are identical to those of the MSM sensors and will result in a similar 'dead' time correction. This equation still only represented the dead time based on impacts on the same sensors, the second order effects caused by the CDF's processing of other sensors depends on

Sensor	τ_{Hold}	D _{Offset}	τ_{Ramp}	H(1)	H(2)	H(3)	H(4)	H(5)	H(6)
IPM-M	1.0	16	0.053	117	197	218	250	-	-
DID 2/3	0.3 *	64	0.160	100	169	199	217	224	245
DID 4	0.3	64	0.160	117	173	197	218	224	245

Table 3.7: Parameters for the calculation of 'dead' time corrections for the MSM and IPM-M sensors (see text). τ_{Hold} and τ_{Ramp} are in milliseconds, other parameters are in terms of digital values.

* This value is used for all DID 2/3 modes with the exception of DID 2 AND DID 3 where the hold time is longer, $\tau_{\text{Hold}}=0.75\text{ms}$

the run-time operation of the CDF. This could only be investigated by simulation of the experiment using realistic input data (see Chapter 4).

CHAPTER 4

A SOFTWARE MODEL OF THE GIOTTO DIDSY EXPERIMENT

As with all experiments destined for use in a harsh environment, the extensive ground testing of the Giotto payload was of prime importance. The European Space Agency (ESA) provided detailed design specifications and guide lines in the form of a series of PSS documents and these requirements had to be met before any experiment would be accepted for incorporation into the spacecraft. As with most space missions, correct operation of the experiments was clearly very important since few options were available after launch to remedy any problems should they occur. The majority of the testing requirements laid down by ESA related to the mechanical and electrical properties of experiments, to ensure that the experiments were able to survive the vibration of launch, the changes in temperature during the cruise phase and to ascertain their susceptibility to electromagnetic radiation. Of special relevance to the Giotto mission was the 16 minute round trip light travel time, which prevented the opportunity for real time command during encounter, to adjust to the needs of measurement in the inner coma. It was left to the designers to ensure that their individual experiments responded correctly to the rapidly changing environment they were to measure.

In the case of the DIDSY experiment, testing was achieved by stimulation of the sensors or front end channels using a variety of techniques, some of which have been described in relation with the experiment calibration (Chapter 3). The flight spare model (an exact replica of the flown experiment) was available for testing purposes after launch as were the dust shield models (Section 3.3), both proved to be invaluable in this context. While this type of testing was essential for determining the correct operation of the experiment, the range of inputs was limited and not representative in terms of the amplitude distributions, or multi-sensor activity, of encounter conditions.

In light of these limitations and as a response to some unexplained anomalies in the data returned during encounter (see Chapter 5), the need arose for a software model of the experiment which could be stimulated with a

realistic range of inputs. This section is principally concerned with a description of the design and operation of the simulation. The application of the model together with the appropriate data, is described in Chapter 5.

4.1 DIDSY: SYSTEM TESTING PRIOR TO ENCOUNTER

Due to limitations in terms of both computing facilities and available manpower, a software simulation approach was not considered during the design and development stage of the DIDSY experiment. Instead, testing of the system was limited to the actual hardware and the available test equipment. The tests involved the flight or flight spare electronics and used the Electrical Ground Support Equipment (EGSE) to collect and decode the data stream from the experiment. In the case of timing measurements which were used to verify the theoretical 'dead' times of the system, which had been derived from design considerations (Section 3.6), the output from a pulse generator was fed directly into the front end electronics of one of the channels and the count rates read from the EGSE display (Evans, 1987; Evans, 1988). An example transfer function (from Evans, 1987) is shown in Figure 4.1, for a regular impulse on the DID 5 (RSM) channel.

The output from the sensor shows a clear one-to-one relationship up to a frequency of about 80Hz after which the output frequency suddenly drops by a factor of two before again rising. The drop is an artifact of using regular pulses and occurs when the interval between two events just falls below the corresponding 'dead' time for that channel. At that point, every other event is lost, resulting in the factor of two decrease observed. While the regular output of the pulse generator does not represent a very realistic input, it is particularly useful for determining the operational 'dead' time for a single channel, since the input frequency at which the output rate drops, is easily ascertained. The 'dead' time is then given by the reciprocal of the input frequency at that point.

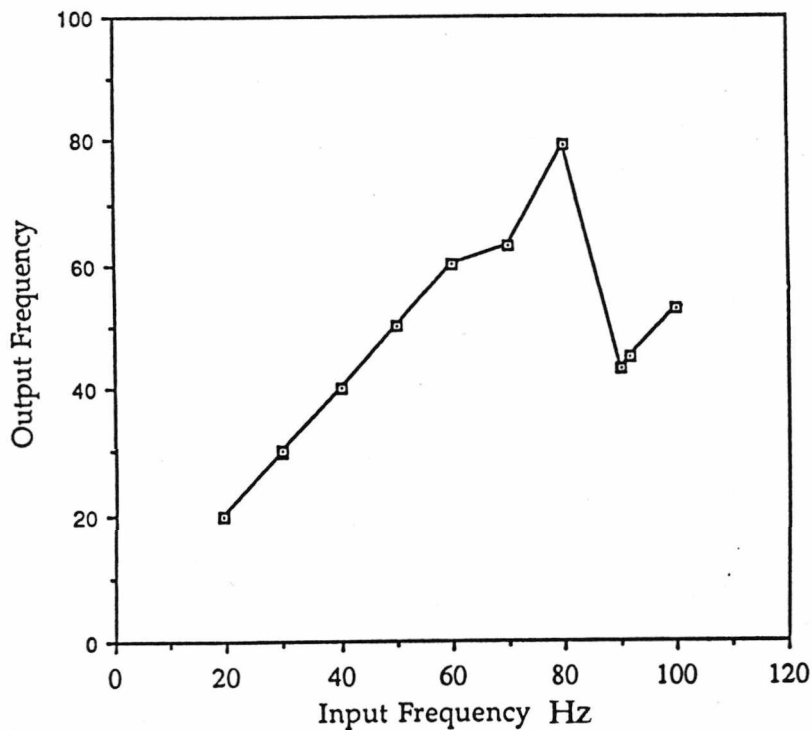


Figure 4.1: The event rate transfer function (from Evans 87) showing the response of the DID 5 channel to regular electrical stimuli.

Using this method a 'dead' time for the DID 5 channel of approximately 12.5 ms was obtained (Evans, 1987) which compared well with the calculated 'dead' time of 13ms (Evans, 1988).

In addition to the single channel tests, attempts were made to determine the effect of the activity on one channel by another channel. This was done by using several pulse generators simultaneously (Evans, 1988). Although the tests showed that the effect was significant at high rates, it was not possible to produce a quantitative relationship.

While the method described above was essential for hardware testing purposes and for confirming that there were no major deviations from the calculated 'dead' times, its use for the detailed analysis of the operation and timing of the experiment was limited in three major respects.

- i) The use of pulse generators to stimulate the channels was limited to regular pulses of constant amplitude and so was incapable of

producing a realistic input distribution consisting of randomly spaced impulses of varying amplitudes.

- ii) The system could only be run in real time, therefore looking for short term or irregular effects at high count rates was extremely difficult and tracing the cause of such effects, even more so.
- iii) The flight spare was an expensive and, with the departure from the group of the designer (G.C. Evans), a possibly irreplaceable piece of equipment. The idea of dismantling and "poking probes" into it was not greeted with enthusiasm!

These problems could be overcome using a software model of the experiment which could be stimulated by a set of calculated inputs which were comparable to those observed during the encounter with Halley.

4.2 SOFTWARE SIMULATION OF DIDSY

The design of the software simulation was divided into a number of individual parts. Figure 4.2 shows the modular approach used and how it was integrated with the VAX/VMS operating system and the FORTRAN programming environment under which the programs were developed. The complete simulation was split into two distinct areas, the simulation of the DIDSY hardware and software, and the data simulator used to provide the modelled input data. The interaction between these two programs being via an intermediate file.

4.2 .1 SIMULATION OF THE DIDSY HARDWARE.

The main reason for the simulation was to investigate the operation of the Central Data Formatter (CDF) for timing purposes and to help in the

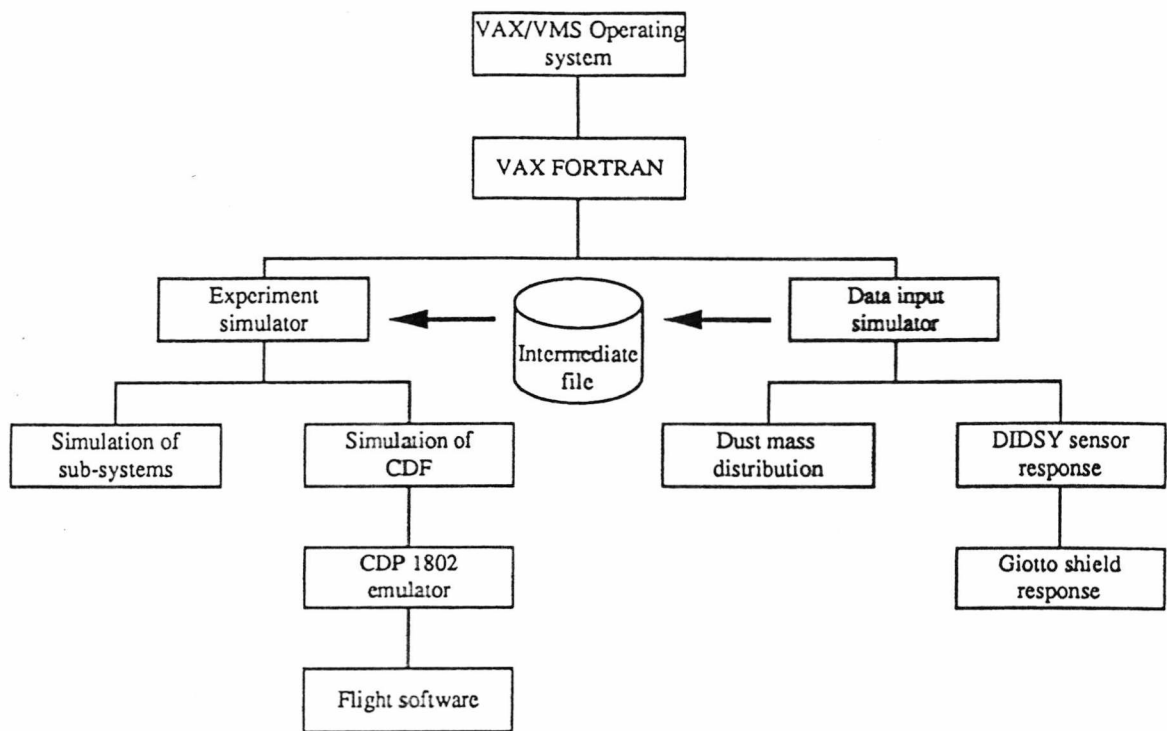


Figure 4.2: The modular approach used in the design of the DIDSY simulation and how it related to the computing environment.

interpretation of data anomalies in the returned telemetry. Therefore it was decided to limit the simulation of the front end analogue electronics, a brief description of which was given in Chapters 2 and 3. A full simulation at the individual component level would have been expensive in terms of the time taken to program it, and also the resources, time and memory, required at run time. It was also unnecessary for our purposes since the front end electronics did not introduce any significant time delays compared to the CDF processing time, and detailed work had already been carried out to determine the transfer function from sensor output to the output value of the analogue-to-digital converters (Section 3.2). This function was independent of activity for all channels and was simply implemented as a look up table.

The digital electronics represented another matter all together. An accurate simulation of the logical operation of the experiment was essential since it was this timing that dominated the 'dead' times. At the heart of the system was an RCA CDP 1802 microprocessor together with associated memory and interface circuitry and the simulation of this will be considered separately in Section 4.2.3; the simulation of the remaining digital electronics is described below.

4.2.2 SIMULATION OF THE DIGITAL SUB-SYSTEMS

4.2.2.1 SIMULATION OF THE IPM-P SUB-SYSTEM

The IPM-P sensor represented a particular problem due to its relatively complex operation compared to the other sensors, and the lack of a detailed description, calibration data or circuit diagrams. The unit and electronics were provided on an 'as is' basis from one of the co-investigator groups. In addition, operational problems arose with the sub-system during the encounter with P/Halley (see Section 5.3.1 & 5.4.2). In light of these problems it was decided that as with the front end analogue electronics, a full simulation would not be attempted, thus allowing more time to be spent on the other sub-systems. However, it was important that this sub-system appeared to be working from the point of view of the simulated CDF, so that any effects that its operation might have on the rest of the experiment could be gauged. The activity of IPM-P pre-encounter was low due to problems with the DID 8 cover (Section 5.3.1). This meant that the effect of IPM-P on the rest of the system was minimal and could be ignored when considering this period. Post-encounter, the output of the sub-system became dominated by a high level of noise (Section 5.4.2) and it was found that this could have a dramatic effect on other sub-systems and IPM-M in particular. The noisy operation was simulated in the model using actual

IPM-P data taken from the post-encounter period. The IPM-P data returned in a DIDSY data block (DDB) consists of three types:-

- i) Software Counters: These were updated by the CDF based on the amplitudes from the positive and negative charge sensitive amplifiers on the IPM-PA and IPM-PB sensors.
- ii) Discrete Data: These provided the actual amplitude information from the charge sensitive amplifiers for five different signal and sensor coincidence combinations for a sub-set of the total number of impacts.
- iii) Hardware Counters: These consisted of sixteen 16 bit counters that were updated internally by the IPM-P hardware to avoid CDF induced 'dead' time delays, and only read at the end of each DIDSY data gathering interval (DGI).

The hardware counter values, iii), had no effect on the operation of the system and fixed values were returned to the simulated CDF, when requested at the end of each DGI. The event data, i) and ii), was modelled by using the software counter and amplitude information from the discrete data taken during the post-encounter period, to reconstruct a realistic rate and set of output values which could then be inserted into the simulation at the sub-system I/O level. At this point the relevant co-incidence flags could be raised to ensure correct emulation of the CDF operation. Two flags were used, the first notified the CDF that an IPM-P event had occurred and remained 'on' until the CDF serviced the request, the second flag represented the IPM-P coincidence line and after an impact, was placed in the 'on' state for 1ms of experiment time, after which it was automatically reset without the intervention of the CDF. The noise on the IPM-P sub-system remained high for the entire post-encounter period and was at a rate close to the limit serviceable by the CDF. Therefore it was not necessary to change the data used by the simulation when

considering different times during the post-encounter period. The data file produced contained a list of times and amplitudes for each individual noise event that was to be simulated. This file was appended to the output of the shield model program (Section 4.4) and the resulting file sorted into time order. This allowed for comparison of the operation of the experiment with, and without IPM-P noise, while maintaining identical stimuli on the other sensors. In this way, any changes in the simulated output were known to be the result of the IPM-P activity.

4.2.2.2 SIMULATION OF THE CIS SUB-SYSTEM

The CIS operation and hence simulation was very straight forward, an impact on the sensor above its threshold mass would increment a hardware counter and the sensor would be disabled for 1.19ms, corresponding to the sensor 'dead' time. Any impacts occurring during this time were ignored. In the simulation, the decrementing variable used to represent the time left until the sensor became active, was also used to model the operation of the CIS co-incident line, which was in turn used by the MSM 'discrete' data categorisation routine. The co-incidence line was considered active while the value of the counter was greater than zero. As with the IPM-P hardware counters there was no requirement for the CDF to read the CIS counters every time an impact occurred. Since each impact only contained one bit of information this processing by the CDF would have required a disproportionate amount of the available CDF time and caused a detrimental effect to the operation of the system as a whole. Instead the counter was read four times during the course of a DGI and the values accumulated to a 16 bit counter by the on-board software. The intervals at which the hardware counter was read, are spread evenly throughout a DIDSY data gathering interval. The 4 reads allowed up to 1023 events to be detected, a level above the theoretical maximum of the experiment.

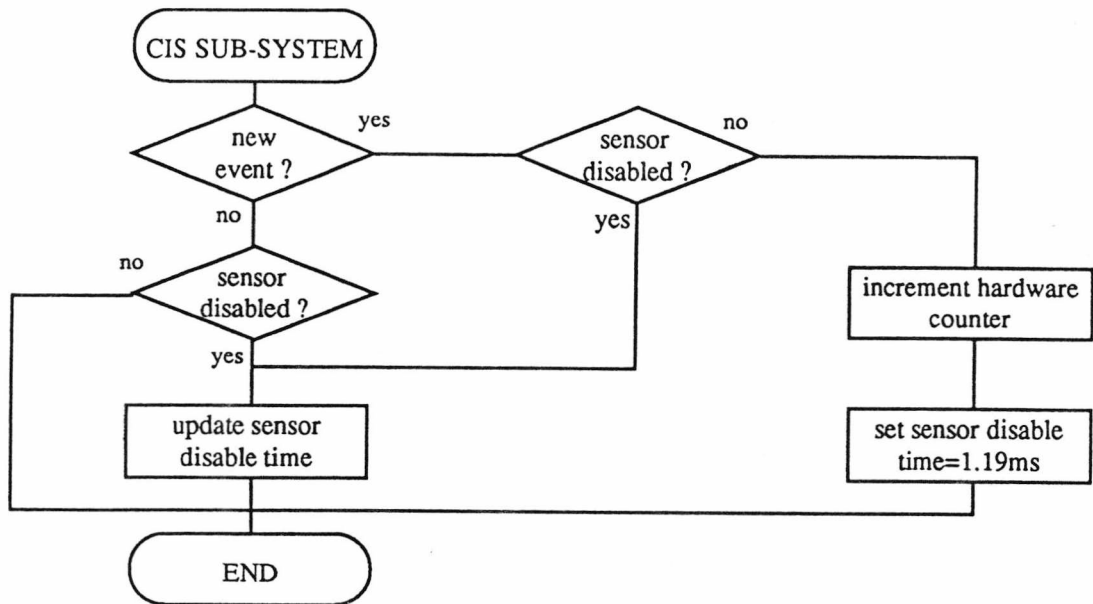


Figure 4.3: Schematic of CIS sub-system simulation.

Only the least significant 10 bits of the 16 bit software counter were actually used. The CIS hardware counter had to be read more frequently than in the case of IPM-P since it could only hold an 8 bit word (giving a maximum count of 255 events) and it was possible for this to result in a loss of information at high flux rates if only read once per DGI. Figure 4.3 shows the schematic operation of the simulated CIS sub-system.

4.2.2.3 SIMULATION OF THE MSM, RSM SUB-SYSTEMS

The four MSM, RSM channels (DID 2,3,4,5) represented the most difficult sub-systems to simulate since their operation is linked and also because the operation depends on the current mode setting. As was stated above the simulation of the front end channels was achieved simply by using the signal transfer function derived from pre-launch calibration measurements. By making this simplification any stimuli could be directly

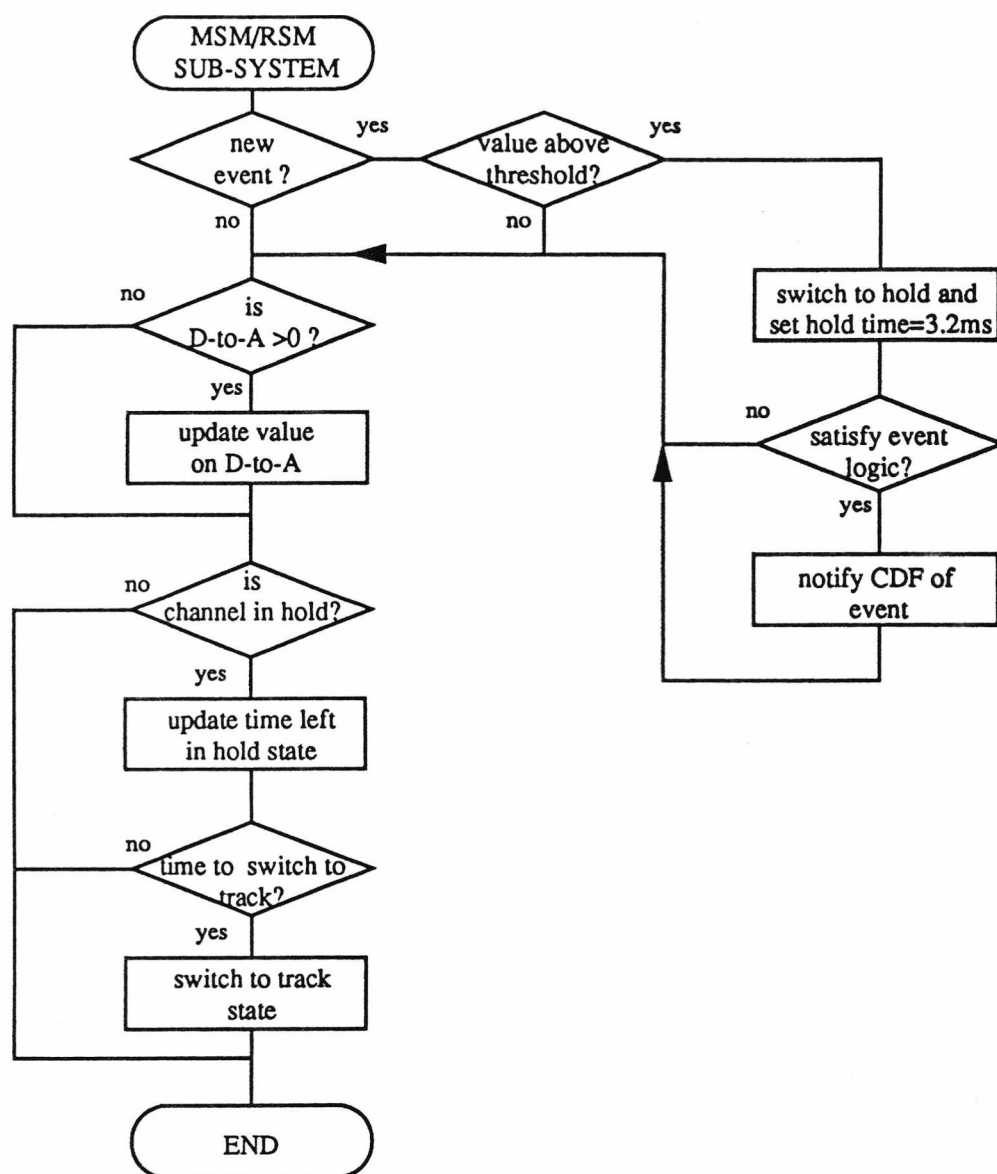


Figure 4.4: Schematic of the simulated operation of a single MSM or RSM channel.

represented by the digital output level which was produced by the A-to-D converter when the multiplexer was set up to measure that channel. The disadvantage of making such an assumption was that it did not take into account any design faults with the analogue section of the sub-system and certain assumptions had to be made about the input signal. Most important of

these was that the signal from a reflection on the shield would not be high enough to exceed the comparator level. This assumption was considered valid since this was the way that the experiment had been designed and there was no evidence from ground testing (Reading & Ridgeley, 1983), or in-flight data, to suggest otherwise. While there was no fundamental reason for not incorporating signal reflections into the shield simulation (see Section 4.4) it represented something of an unknown quantity and was considered beyond the scope and requirements of the project.

A schematic representation of the operation of the MSM/RSM simulation for a single channel is given in Figure 4.4, the other channels are identical. The amplitude of a new event was compared to the value representing the level of the Digital-to-Analogue (D-to-A) converter to determine if the event was sufficiently large to trigger the system. The result of the test was used to simulate two operations of the sub-system, firstly if the comparator level was high, indicating a threshold exceed on that channel, the hold circuitry on the input of the amplifiers was switched from 'tracking', to 'holding' the signal, corresponding to a change in the decay constant of the signal on the output of the log amplifier from 3ms to 30ms. 'Holding' the signal ensured that the level did not decay before the CDF had a chance to respond to the request. The sensor remained in the held state for a maximum of 3.2ms or until the hold circuitry was reset by a command from the CDF. The output of the comparators was also passed to a set of control logic which was used to flag the CDF when an appropriate event had occurred. The logic would immediately inform the CDF if a DID 4 or DID5 event occurred, however in the case of a DID2 or a DID 3 event the operation of the logic depended on the MSM mode of the experiment at that time as defined in Table 4.1. Once a request had been received by the CDF, it proceeded to read each of the channels in turn by means of a multiplexed Analogue to Digital (A-to-D) converter. In

MODE	ACTION
0	Inform CDF only when DID2 event ignore DID3
1	Inform CDF only when DID3 event, ignore DID2
2	Inform CDF when DID2 and DID3 events occur within 3.2ms of each other, ignore individual DID2 or DID3 events.
3	Inform CDF when either a DID2 or a DID3 event occurs.

Table 4.1: The rules used by the DID 2,3 logic to determine whether a particular event will be reported to the CDF

the simulation the signals were already in digital form and only the multiplexing required modelling.

When the level of each of the signals had been read, the CDF set the input of the D-to-A converters to the digital value read from the A-to-D for that channel, plus an additional value of 32. As soon as the the D-to-A was loaded, the value started to automatically decrement at a rate of 1 digital value per 126 μ s. This decay rate was designed to follow the decay of the acoustic signal on the shield with a suitable safety margin. This was to ensure that any reflections which might be of similar amplitude to the signal did not re-trigger the comparators. Initially this action may seem redundant in the simulation, since reflections were not being modelled in the input data and so the chance of secondary triggers was non-existent. However, this operation also had the potential of masking out any true impacts occurring a short time after the initial events. It was this recovery time, before a new impact could be detected, that dominated the 'dead' time for the MSM and RSM channels. As an additional safety measure the flight software waited for 3ms after setting the D-

to-A converters before allowing a new output from the comparators to re-trigger the system.

4.2.2.4 SIMULATION OF THE IPM-M SUB-SYSTEM

The operation and thus simulation of IPM-M was very similar to that of a single channel of the MSM and RSM sub-systems described above. If a new event occurred, it was compared to the current value on the D-to-A converter and if the signal exceeded the D-to-A value a flag was raised representing the CDF request line in the experiment. This trigger was also used to latch the current output on the A-to-D converter, since conversion took a finite amount of time, the signal latched on the output of the A-to-D converter corresponding to the pre-event level of the sensor (a useful diagnostic parameter). In addition to 'latching' the A-to-D, the event line also switched the track and hold circuitry on the input of the log amplifier into the hold state thus ensuring that the signal did not decay before the CDF had a chance to read the value. The sub-system remained in the hold state for a maximum period of 1ms or until switched back to the track state by intervention of the CDF. When the CDF serviced an IPM-M request, it first read the 'held' output of the A-to-D converter. The read operation automatically restarted the A-to-D converter and a subsequent read by the CDF measured the amplitude of the event. This value, plus 16, was loaded into the D-to-A converter which started decrementing at a rate of 1 digital value every 50 μ s to mimic the decay of the acoustic signal on the IPM baseplate.

4.2.3 SIMULATION OF THE CDF

The CDF or Central Data Formatter was the part of the experiment which controlled and collected data from the sub-systems, and converted the data into a suitable format (a DIDSY Data Block, DDB) for insertion into a telemetry

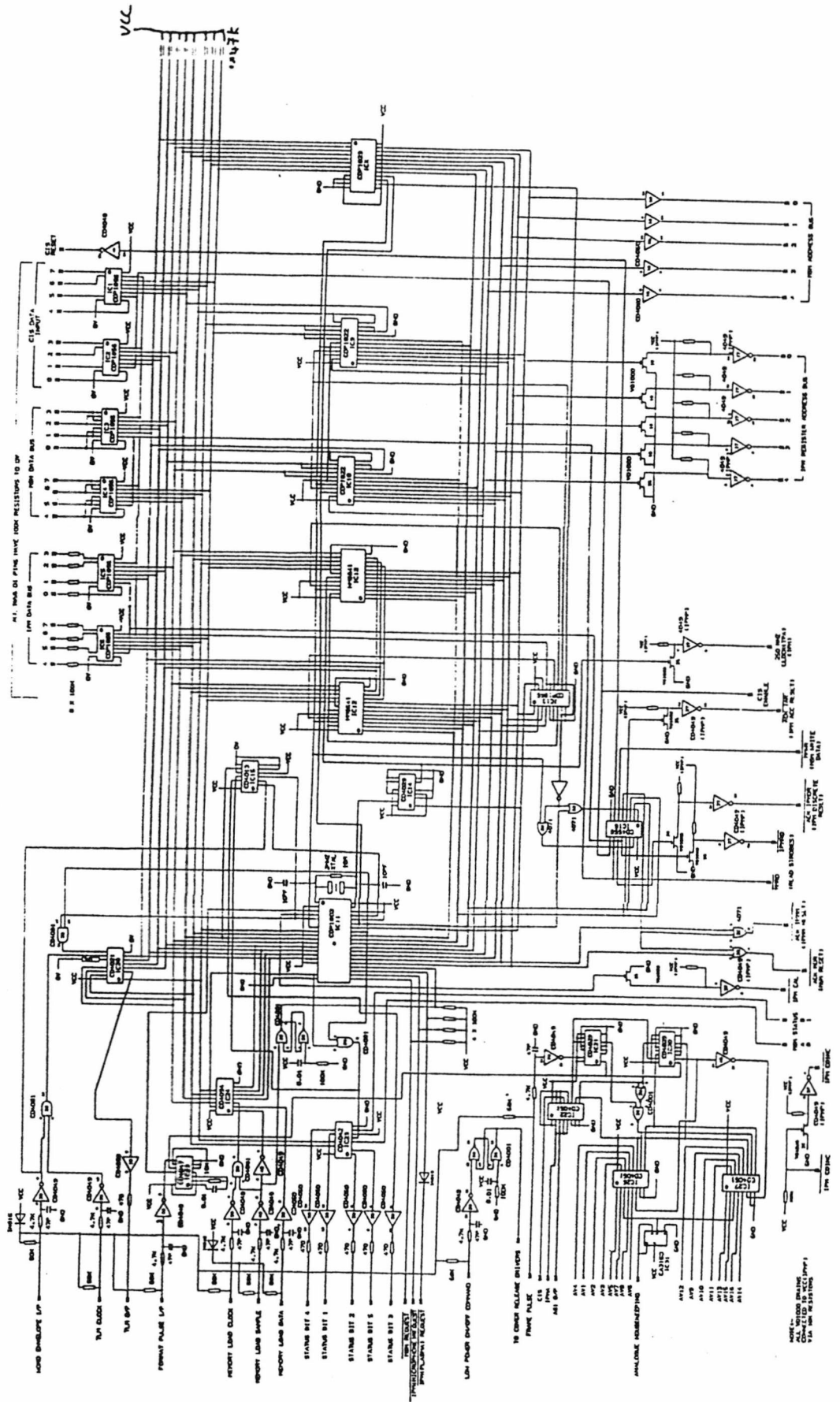


Figure 4.5: Circuit diagram of the Central Data Formatter (CDF) showing the CDP1802 processor (centre), the spacecraft interface (bottom left), the housekeeping multiplexing circuitry (bottom right) and the sub-system interfaces (top, left and right).

frame and subsequent transmission back to Earth. The CDF included the Experiment's micro-processor together with associated logic and interface circuitry for communicating with the DID sub-systems, housekeeping channels, and with the spacecrafts On Board Data Handler (OBDH). A complete circuit diagram of the CDF, which was designed at the Rutherford Appleton Lab. (RAL), is shown in Figure 4.5

The entire simulation of the DIDSY experiment was critically dependent on accurate modelling of the operation and timing of the CDF. This could be achieved in one of two ways. Either the operation of the flight software and electronics could be treated as a whole and modelled as such. Alternatively an emulator of the CDP 1802 microprocessor could be produced which was able to load and use the actual flight software. The first option had the advantage that the resultant code would run many times faster than an emulator based model and since the encounter had already taken place before the start of programming there was no possibility of a change in the flight software or electronic specifications. However, the first option also had disadvantages in terms of the time taken to program it since a full and very thorough knowledge of the experiment and software operation would be required to achieve an accurate simulation and in the case that a fault was found it might prove difficult to determine where the problem lay in the original experiment. Since execution time was not of major importance, a powerful VAX 8800 computer running VAX/VMS and FORTRAN being available, it was decided to adopt the second option. The simulation of the CDF can thus be split into two connected parts, the simulation of the interface circuitry and the simulation of the CDP1802 microprocessor itself.

4.2.3.1 SIMULATION OF THE CDF INTERFACE

The CDP1802 microprocessor communicated with the rest of the experiment and the spacecraft in three ways.

- i) Input/Output ports
- ii) Direct Memory Access (DMA)
- iii) Memory and Memory Mapped Input/Output

In the actual experiment the input port was used to read the MSM base mode from the spacecraft once every format and the output port used to return status information. Rather than trying to simulate the full functionality of the spacecrafts Remote Terminal Unit (RTU) only a minimum workable interface was designed. For the case of the input and output ports, they were simply implemented as two eight element arrays (corresponding to the eight input and eight output ports). On initialisation of the model, the program loaded the relevant element of the input port array with the base mode. No further change was required unless a tele-commanded change of mode operation needed to be simulated. In which case the value in the array was updated and read by the modelled CDF at the next simulated format pulse. The status information written to the output port array by the experiment was not used by the simulation and the data was overwritten by subsequent data from the processor.

The Direct Memory Access (DMA) function of the microprocessor was used to asynchronously extract data from the experiment for transmission back to Earth. Normally the spacecrafts on-board data handler (OBDH) would send a DMA request to the CDF, the CDF would then load an 8 bit parallel in, serial out buffer (IC28, Figure 4.5) with the data pointed to by the DMA pointer (Register 0), the data was then clocked out of the buffer by the OBDH allowing the processor to continue with its current operation. Again, to avoid having to simulate the OBDH, the process was simplified in the simulation. The main program control loop which kept track of the experiment time, and raised the appropriate flag when a DMA request would normally have been issued by the

OBDH. The control loop then issued the DMA request to the 1802 emulator and extracted the full data byte off the virtual data bus and sent the output to the data log file. The operation from the viewpoint of the processor was identical in both the real experiment and the simulation; it is simply seeing a DMA request, which it responded to, by putting the value of R(0) onto the address bus and waiting one machine cycle before continuing execution.

The final method of communication between the processor and its peripherals was by means of direct addressing using the processor address and data buses. Table 4.2 shows the memory map of the CDP1802. The ROM and RAM were simulated by a linear data array. Rather than allowing the CDP1802 emulator routine direct access to this array, all memory read and write functions were performed by two FORTRAN subroutine MAP_IO_R and MAP_IO_W. The routines checked the address of the memory location trying

Start Address	End Address	Description
0000H	03FFH	ROM - On board software and look-up tables
0400H	047FH	DDB 'Buffer A'
0480H	04FFH	DDB 'Buffer B'
0500H	057FH	Address copy of 'Buffer A'
0580H	05FFH	Address copy of 'Buffer B'
0600H	061FH	IPM-P Accumulators
0620H	067FH	Stack/Scratch pad RAM
1000H	102FH	IPM-P memory mapped I/O
1040H	104FH	MSM/RSM memory mapped I/O
105EH	105FH	IPM-M memory mapped I/O
1060H	1060H	CIS memory mapped I/O

Table 4.2: The memory map of the DIDSY experiment. Of particular importance is the address copy of the RAM buffers.

to be accessed and in the case of an I/O location (e.g. the setting of one of the D-to-A converters) the MAP_IO_W routine would write the data value directly into the variable designated to represent the input of the D-to-A converter. If instead the location being accessed was memory, then the address would be passed to one of two further routines, MR or MW, for reading or writing respectively. These checked that in the case of writing, the location being accessed was in RAM and also did the required address decoding for the memory map. The latter was extremely important since correct operation of the flight software was found to be dependent on the existence of an address copy of the RAM buffers at memory locations 0500H to 05FFH.

4.2.3.2 THE CDP1802 EMULATOR

The emulation of the CDP1802 microprocessor used in the DIDSY CDF was handled by a single FORTRAN subroutine, SIM1802, which controlled the execution of all instructions from the flight software, modifications of the registers and calculation of timing information. In addition the routine checked for DMA and INTERRUPT requests from the main control loop and took the appropriate action should such an event be detected. The operation of the CDP1802 emulation subroutine is shown schematically in Figure 4.6. The routine executes one instruction or one DMA, INTERRUPT event each time it is called. Instructions are executed by reading the memory location pointed to by the program counter variable from the array used to represent the system memory. The program counter is incremented and the instruction interpreted according to the specifications given in RCA, 1977. By only operating on a single instruction at a time the routines used to simulate the DID subsystems could be called after each command and this ensured that the operation of the simulation as a whole remained synchronized, any particular module never being more than 12 μ s (the time taken to execute the longest instruction) behind the CDF. To obtain the most accurate possible simulation, the emulator


```

0000 7B 7B 7B F8 0A A3 F8 00
0008 B3 D3 A0 A8 F8 28 A4 F8
0010 80 B8 14 F8 10 B9 F8 4C
0018 A9 F8 06 B2 F8 02 BA B1
0020 BB BC F8 90 AA F8 65 AB
0028 F8 78 AC F8 02 F9 80 A6
0030 F8 06 BD E6 3C 38 69 B8
0038 98 FE 3B 41 F8 04 A8 F4
0040 56 06 59 61 F8 6F A2 9E
0048 FC 01 AE E2 80 BE AF 2F
0050 F8 04 B0 B6 B7 BF F8 00
0058 5F 9E 52 8E F7 3A CD 24
0060 84 3A 68 F8 28 A4 30 72
0068 02 FA 1F 32 71 FA 07 CE
0070 C8 DB DC 02 FE 3A CD 94
0078 FC 70 A6 F8 20 AD F8 00
0080 AF ED F0 FE 73 F0 7E 5D
0088 60 32 A1 F0 C8 F0 76 FA
0090 F0 73 F0 F6 5D 32 9C 60
0098 1F 1F 30 8D 60 1F 8F F1
00A0 38 F0 56 F8 00 73 16 2D
00A8 8D 3A 7E E6 9E FB 80 B4
00B0 A6 95 56 16 85 56 16 FA
00B8 0F 3A BF F8 27 A9 09 15
00C0 98 56 88 32 C8 F4 56 28
00C8 F8 4C A9 F0 59 E2 F8 30
00D0 AD 0D CA 01 00 F8 01 5D
00D8 35 DD C0 01 00 C0 03 00
00E0 00 00 00 00 00 00 00
00E8 00 00 00 00 00 00 00
00F0 00 00 00 00 00 00 00
00F8 00 00 00 00 00 00 00
0100 F8 00 5D 37 08 C0 02 2D
0108 F8 40 A9 59 09 C4 C4 C4
0110 C4 49 73 89 FF 44 3A 0B
0118 F8 4E A9 09 52 12 F8 4B
0120 A9 F8 BE A1 E1 42 F4 60
0128 C7 F8 FF 59 29 89 FF 47
0130 3A 24 22 94 FC 02 A6 F8
0138 2E A9 F8 80 AF 2F 8F 3A
0140 3D 59 06 FA 03 32 7E FB
0148 03 32 7E FB 02 32 52 22
0150 02 C8 02 22 22 32 63 02
0158 22 22 32 6F 02 FA 01 32
0160 9A 30 90 02 22 22 32 76
0168 02 FA 01 32 AE 30 90 02
0170 FA 01 32 B8 30 90 02 FA
0178 02 C2 02 2D 30 A4 02 22
0180 32 88 02 22 32 8C 30 57
0188 02 22 32 63 22 22 30 6F
0190 94 FC 51 A6 94 FC 5A A7
0198 30 C2 94 FC 52 A6 94 FC
01A0 5F A7 30 C2 94 FC 53 A6
01A8 94 FC 64 A7 30 C2 94 FC
01B0 54 A6 94 FC 69 A7 30 C2
01B8 94 FC 55 A6 94 FC 6E A7
01C0 30 C2 06 FC 01 32 C8 56
01C8 94 FC 6F A6 F8 03 AF 02
01D0 FA 02 32 D8 94 FC 64 A7
01D8 E7 42 73 42 73 82 FF 03
01E0 AD ED 02 FA FC 5D 06 FA
01E8 FC F7 33 EF 8F F1 56 E7
01F0 42 73 2F 8F 3A E1 22 22
01F8 E2 94 FC 02 A6 06 FA 03
0200 C2 02 1A FB 03 CA 02 13
0208 72 F7 33 10 02 22 52 38
0210 22 30 1F FF 01 32 1F 12
0218 30 0C 72 F4 F6 22 52 DA
0220 04 AA 01 22 DA 0A B0 01
0228 22 DA 10 BA 01 3E 61 F8
0230 5F A9 F8 C2 A1 F8 FF 59
0238 29 09 73 F8 02 AF 2F 8F
0240 3A 3E F8 2D A9 59 E1 F8
0248 5E A9 49 52 F4 C7 F8 FF
0250 59 E2 DA 14 B6 01 94 FC
0258 50 A6 72 32 61 56 26 02
0260 56 C0 00 44 D3 F8 60 A9
0268 94 FC 04 A6 E6 09 59 F4
0270 73 F8 00 74 56 30 64 D3
0278 F8 20 AD F8 10 A9 ED 09
0280 59 F4 73 F8 00 74 73 19
0288 8D 3A 7F 30 77 13 E2 D3
0290 94 E3 F4 A6 60 72 A1 02
0298 F7 3B 8D F4 E1 F7 60 16
02A0 33 9D 06 FC 01 32 8D 56
02A8 30 8D A0 1E 19 14 0A 0B
02B0 A5 18 18 14 CA 0B B5 1C
02B8 29 06 95 2D 2B 13 40 40
02C0 40 40 10 20 28 38 80 00
02C8 00 00 00 00 00 00 00
02D0 00 00 00 00 00 00 00
02D8 00 00 00 00 00 00 00
02E0 00 00 00 00 00 00 00
02E8 00 00 00 00 00 00 00
02F0 00 00 00 00 00 00 00
02F8 00 00 00 00 00 00 00
0300 F8 40 AF 2F 8F 3A 03 F8
0308 04 A9 49 73 49 73 49 73
0310 49 73 F8 5F A9 F8 C2 A1
0318 F8 FF 59 29 09 73 F8 02
0320 AF 2F 8F 3A 21 F8 2D A9
0328 59 E1 F8 5E A9 49 52 F4
0330 C7 F8 FF 59 E2 DA 14 B6
0338 01 82 FC 04 A2 02 FA 03
0340 32 49 94 FC 36 A6 12 30
0348 CF 22 02 FA 03 FB 01 32
0350 79 FB 02 32 6F 22 72 F1
0358 FA FC 32 93 DA 2C C3 00
0360 94 FC 32 A6 06 FA 03 3A
0368 E8 86 FC 04 A6 30 81 DA
0370 24 C3 00 94 FC 4E A6 30
0378 81 DA 1C C3 00 94 FC 42
0380 A6 E6 22 22 22 42 73 42
0388 73 42 73 42 73 42 73 02
0390 56 30 95 12 12 E2 02 FA
0398 03 FB 01 32 C7 FB 02 32
03A0 BD 30 E8 22 72 F1 FA FC
03A8 32 E8 DA 28 C3 00 94 FC
03B0 32 A6 06 FA 03 3A E8 86
03B8 FC 04 A6 30 CF DA 20 C3
03C0 00 94 FC 48 A6 30 CF DA
03C8 18 C3 00 94 FC 3C A6 82
03D0 FF 05 A2 E6 42 73 42 73
03D8 42 73 42 73 42 73 02 73
03E0 E2 F8 27 A9 09 C0 00 44
03E8 82 FC 05 A2 30 E0 00 00
03F0 00 00 00 00 00 00 00
03F8 00 00 00 00 00 00 00

```

Figure 4.7: The hexadecimal representation of the flight software and look-up tables, used by the simulation to load the CDP1802 emulator.

was loaded with an exact replica of the software and data used in the flight experiment. The hexadecimal dump of the flight software which was read by the simulation program is given in Figure 4.7. The full, commented, assembly listing of the flight code which was developed at the Rutherford Appleton Laboratory is given in Appendix 1.

4.3 TESTING OF THE SIMULATION

The simulation program took its input from a standard ASCII file containing data on the amplitude of the events. The first record of the file contained the number of micro-seconds worth of data contained in the file. Once the simulation reached the end of the file it would start again from the beginning, this allowed for longer runs of the simulation at high event rates without the input file becoming too large. Each of the remaining records in the file contained information on the time (in μs), sensor and amplitude of a single stimulus. Hence, an impact that was detected by two sensors would have two entries in the input file, one for each sensor.

The major advantage of the software simulation over the previous testing of the hardware was the potential of being able to simulate the experiment with a representation of a realistic mass distribution. However before attempting this it was important to check that the model worked correctly, both in terms of its general response to stimuli and also in the time taken for the system to respond to and process an event. After all, one of the principle requirements of the model was for the checking of the first order 'dead' time correction algorithms at high event rates. The operation of the model CDF was easily checked by examining the telemetry stream produced, for correct positioning of the block counter and mode words within the DDB and also by confirming that the block counter was incrementing. These tests, while simple, were very susceptible to errors in the CDP1802 emulation or in

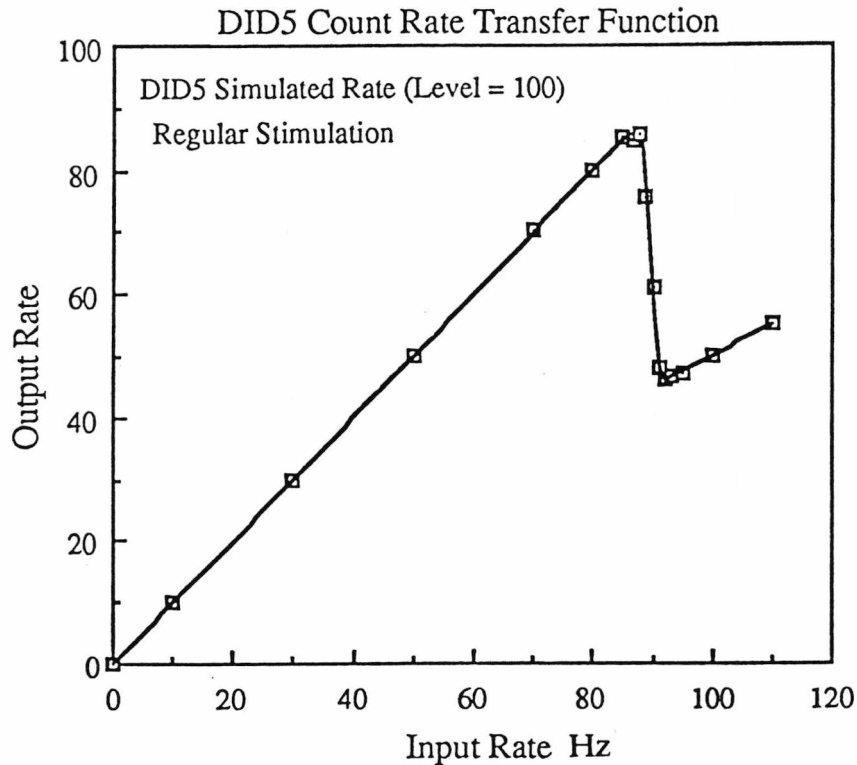


Figure 4.8: The frequency transmission characteristics for the simulated DID 5 channel. The simulated test was comparable to the hardware set-up used to produce Figure 4.1 .

faulty transcription of the relevant parts of the flight software. Although examination of the telemetry stream confirmed the operation of the modelled CDF; the sub-systems and the CDF, sub-system interface could only be checked while being stimulated. To achieve this a simple initial input data set was produced containing a regular, single amplitude pulse, on the DID5 channel. This was comparable to the hardware tests described in Section 4.1. Again, examination of the appropriate counter and magnitude bytes in the telemetry stream was used to ensure that the signal was being detected and that the input and measured signal levels matched. This was repeated for each of the other subsystems until all were known to be responding correctly.

The final and most important test in terms of accuracy of the modelling involved the timing of events and the speed at which the system could

respond to the detection of an event. This was checked by decreasing the interval between the regular pulses used to stimulate the channel until a sudden drop in the output rate was observed (see Section 4.1). This was done for DID5 so that the output could be directly compared with the equivalent hardware tests (Figure 4.1). The resultant output frequency against input frequency distribution from the model is shown in Figure 4.8. The correlation between the hardware tests (Figure 4.1) and the simulation results (Figure 4.8) was found to be very good. The frequency at which the drop in the output rate first occurred being almost identical for the two cases. The small deviations observed in the hardware tests were attributed to a slight drift in the pulse generator frequency during the measurements (Evans 1987).

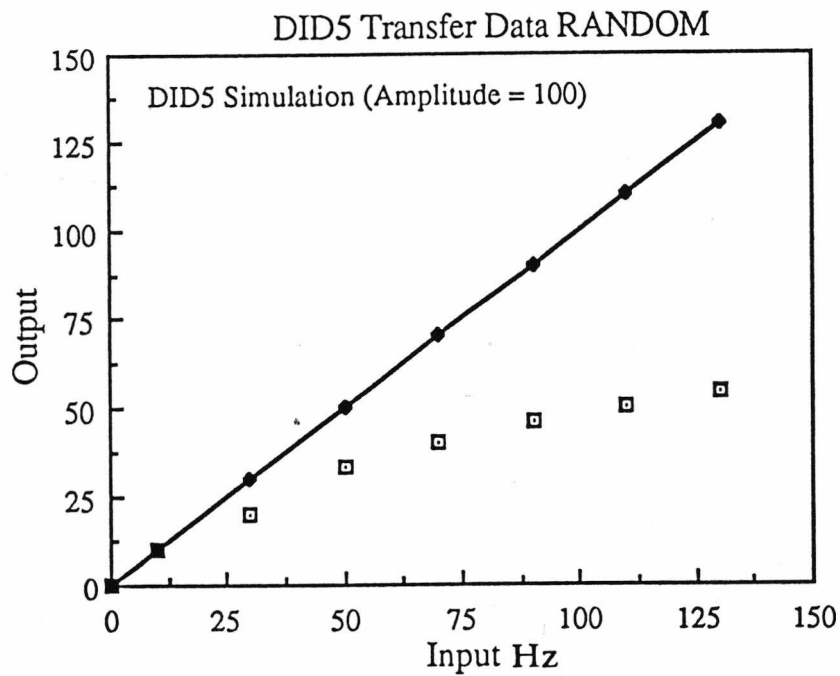


Figure 4.9: The simulated output from the DID 5 channel for a set of randomly spaced pulses of constant amplitude (\square). The solid line represents the modified output after correction for 'dead' times.

Once the initial comparison tests had been completed and the model was established to be working with a fair degree of accuracy, tests were started with input data that would have proved difficult to produce during the original hardware tests. An input distribution was produced which was similar to the DID 5 tests described above and in Section 4.1, except that instead of using regularly spaced data, the timing of the impacts was randomized. The result is shown in Figure 4.9 (□). The randomization smooths out the distribution, removing the the factor of two drop in the output frequency at 85Hz which was caused by the delay between the regular pulses just falling below the 'dead' time for the DID 5 channel. The simulated distribution provided a more realistic picture of the operation of the sensor. The solid line in Figure 4.9 shows the output rate after it had been modified using the theoretical 'dead' time correction presented in Section 3.6. The theoretical correction for this simple case, where only a single sensor was active, clearly worked very well!

4.4 SIMULATION OF REAL INPUT DATA

The tests described in the previous section were based on simple input data sets which bore little resemblance to the input stimuli that occurred during the Giotto flyby of comet P/Halley. At encounter the experiment had to deal with stimuli on all of its sub-systems, signals on different channels that were almost instantaneous (in the case of multiple detections of a single event) and a large range of amplitudes. To satisfy the requirement for data which could be used to simulate DIDSY operation at encounter a FORTRAN program, SSIM, was written.

The program calculated a fixed power law mass distribution, or a more complicated varying distribution could be constructed by the user. The number of events in each of a set of differential mass intervals, $d \log m$, was calculated based on the total area of the front shield and a random position was calculated

for each event. To reduce the size of the data file and the amount of processing required during the main simulation, the digital amplitudes of the signals were calculated at this stage and only those events which were likely to trigger the subsystems were stored. If the calculated position corresponded to one of the fixed effective area sensors (CIS or IPM-M) the appropriate signal value could easily be determined from the calibration data (Chapter 3). In the case of the microphone sensors where the effective area depended on mass and position, a look-up table was used based on the approximate position of the particle. The look-up table was in fact a very coarse representation of the full shield sensitivity maps. If the look-up table showed the event to be too small to be detected by any of the sensors, then it was discarded. Otherwise, the attenuation of the signal from the impact site was calculated using the full shield map data described in Section 3.3. The value of the attenuated signal was then converted using Equation 3.2 to give the digital output produced on the A-to-D converter of the experiment. In addition to calculating the magnitude of the signal, it was also important to calculate the propagation time of the signal from the impact site to each of the sensors. This was of particular significance for events which were detected by more than one sensor since the action of the CDF could depend on which was triggered first. Calibration tests on the UKC mock-up shield (Evans, 1988) showed that a signal took of the order of 3ms to completely traverse the shield. Matters were further complicated since the signal detected by the sensors was not always the one following the shortest route. For example, the signal of an impact near DID 3 could propagate to DID 2 via two paths, either ~300 degrees clockwise round the main sector or ~60 degrees anti-clockwise across the small sector (assuming the shield orientation and coordinate system shown in Figure 2.5). While the anti-clockwise route is undoubtedly the shorter, the bending wave would propagate across both isolating joints and would be attenuated to such a degree that it would be below the threshold of DID 2. In such a case it would be the signal

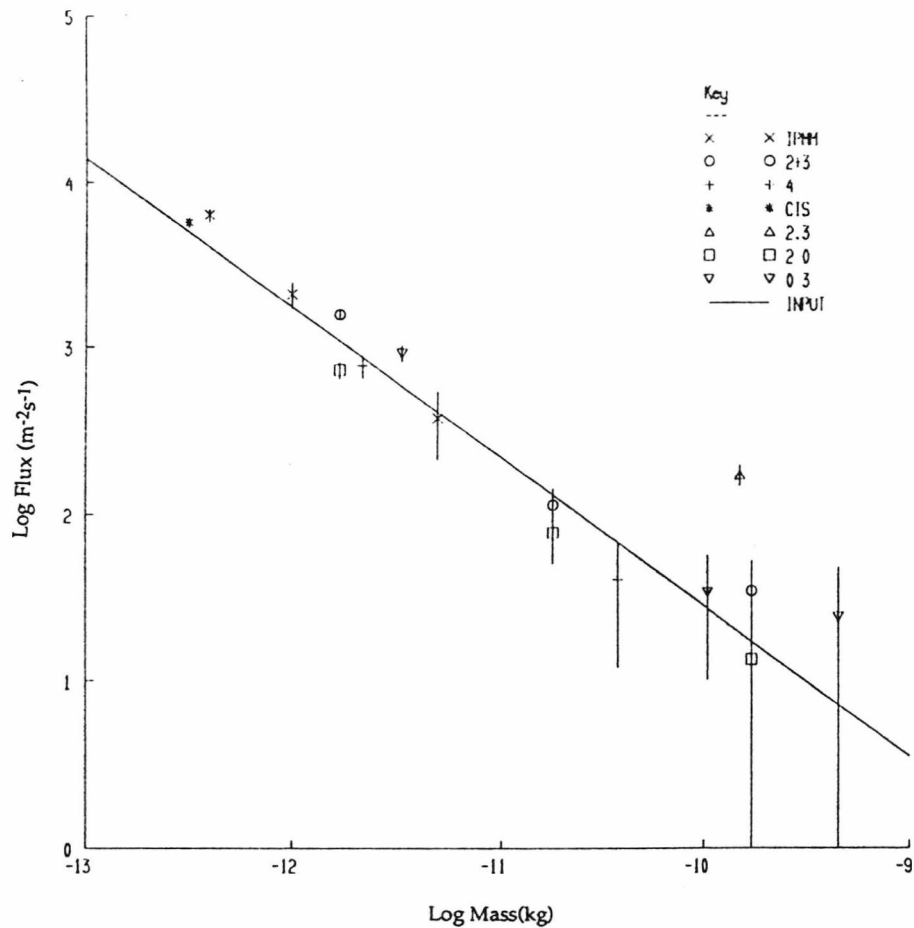


Figure 4.10: A mass distribution produced from the simulation of the DIDSY experiment. The solid line represents the fixed power law input distribution, the symbols mark the simulated fluxes derived from the PHA counters.

travelling in the clockwise direction which would be most likely to trigger DID 2, some 2ms to 2.5ms after the original impact occurred. After calculating the correct times for detection on each of the sensors the data is written to the output and the procedure repeated for the next event. The resulting data file is then used as the input for the main simulation program. For the simulation of high flux data, the intermediate data file could become very large, if the simulation is used to produce information for more than a couple of seconds of experiment time. To reduce this problem the simulation was operated such that once the program had reached the end of the data file, it started again from the beginning.

Figure 4.10 shows the output of the simulation compared to a constant power law input mass distribution. The error bars are based on Poissonian

statistics ($\pm\sqrt{N}$). The solid line represents the input distribution. The correlation is generally good with the exception of the DID 2 AND DID 3 point (Figure 4.10, Δ) which shows a considerable excess over the input value. The reason for this strange behaviour is involved with the interaction of sensors at high flux rates. Similar behaviour was observed in the flight data and is considered in Section 5.4.1.

4.5 DEAD TIMES

The idea of an instrumental dead time for the MSM sensors was discussed in Section 3.6, where a dead time algorithm was determined based on the operation of the sensors track/hold and threshold circuitry and making some assumptions on the value of τ_{Hold} from consideration of the operation of the on board software. To determine over what range these corrections were valid and to see if a second order correction term was required, the software simulation was used. The flux level was initially set low and then progressively increased, each step provided a single point on a correlation plot of output flux against input flux. To ensure that the effect of sensors upon each other was taken into consideration in a realistic manner, the input data was derived from a fixed slope cumulative mass distribution with $\alpha=0.9$ (consistent with the value used for the DIDSY flux analysis).

Initial thoughts were that the effect of other sensors would be to use up CDF processing time, resulting in longer dead times overall and lower counts. The simulation showed that this was not the case, instead a slightly higher count than expected was observed, which when corrected with the standard dead time routines became very much higher. The reason for this was quite straightforward; when a detection occurred on one of the MSM sensors, the CDF read the amplitude from all the other sensors within the sub-system. The read was carried out independently of any threshold checking so that a signal

that was still decaying from a previous impact could be read two or more times as if it were a new event. The effect became worse at higher flux rates due to the larger number of CDF service operations that were taking place. Using the simulation the flux at which a deviation from the nominal situation occurred, was determined. The simulation showed that the effect was limited almost exclusively to the highest sensitivity 'Bin' of the sensor and that it did not have a significant effect on the output until very high flux rates were reached ($>10^3\text{m}^{-2}\text{s}^{-1}$). Therefore the dead times that were already in use were left unchanged. Correction at higher impact rates was found to be possible by using a scaled exponential function, however, since such high rates were not observed, the additional correction term was not required.

CHAPTER 5

PERFORMANCE OF THE DIDSY EXPERIMENT

The Giotto spacecraft was successfully launched from the Centre Spatiale Guianaise, Kourou, French Guiana at 11:23:12 UT on 2nd July 1985. During the following eight month cruise phase of the mission, regular tracking, communication and testing of the spacecraft systems and scientific payload were carried out using ESA's 15m ground station at Carnarvon and the 64m dish at Parkes.

At 19:25UT Ground Receive Time (GRT) on March 13, 1986 the DIDSY experiment was switched on for the encounter with comet P/Halley. Over the subsequent 8 hours, DIDSY made measurements of the coma dust distribution for particles with masses in the range $10^{-13}\text{kg} \leq m \leq 10^{-5}\text{kg}$. While the performance of the experiment was generally good, several faults with individual parts of the hardware were observed and certain limitations of the system, particularly at high flux rates, became apparent. These are considered in Section 5.3 and Section 5.4.

5.1 CRUISE PHASE OPERATION

DIDSY was first switched on at 04:18UT on 8th October 1985. Housekeeping voltages and temperatures all showed nominal output values with the exception of the IPM-A ambient plasma monitor, which showed a lower than expected voltage (McDonnell, 1987). As predicted, with the exception of the once per format calibration pulses on the IPM-P sensor, no activity was seen on any of the DIDSY sensors. To ensure correct operation, several experiment check-out sequences were carried out during the cruise phase, these involved the switch on of each of the experiments and examination of the returned housekeeping data to ensure that all voltages and temperatures were within operating limits. In addition the check-outs included the transmission of telecommands to test the operation of the experiments making up the scientific payload. Correct reception and execution of each command was confirmed before continuing with the next step. In the case of DIDSY, the check-out consisted of cycling through each of the available MSM

modes (see Section 2.3.4) and checking the format of the returned science data stream for correct structure, including location and value of the mode word and synch counter bytes. No abnormalities with the operation of DIDSY were found during the initial, or any of the subsequent check-outs carried out prior to the encounter.

On the 10th February 1986 the first attempt was made to release the DID 8 cover, which was used for thermal control purposes and to protect the IPM-P sensor from contamination and damage during the firing of the solid rocket kick-motor (see Section 2.3.3). The cover was held in place by a thin wire and plastic retainer arrangement, to release the cover a 60kHz, 4V signal was applied to the wire which would heat up and melt the retainer, allowing the spring loaded cover roll back. The release mechanism was activated by a single telecommand, the release voltage remained in the on state until deactivated by switching the whole experiment off. The spacecraft confirmed correct reception of the command and indicated a high current drain. In addition, a noise signal was observed on both the IPM-M digital and analogue science channels (Figure 5.1). All these factors were taken to indicate that the release mechanism was operating correctly. The cover itself was a late addition to the experiment design and it did not include a facility to confirm successful release. The expected change in the temperature measured by the IPM mounted thermistor and marginal change in the ambient plasma monitor (IPM-A) due to photo-electrons, were not observed (Zarnecki, 1988). However both these changes were expected to be small and their absence was not unduly alarming. In an attempt to increase the likelihood of successful cover release, two further attempts were made during subsequent spacecraft passes. Neither provided any additional evidence to indicate that the cover had released. However, extensive ground testing of the release mechanism had not highlighted any problems and at the time, the operation was thought to have been successful. Examination of the encounter data showed that this optimism was unfounded and that the cover had not retracted during any of the cover release attempts.

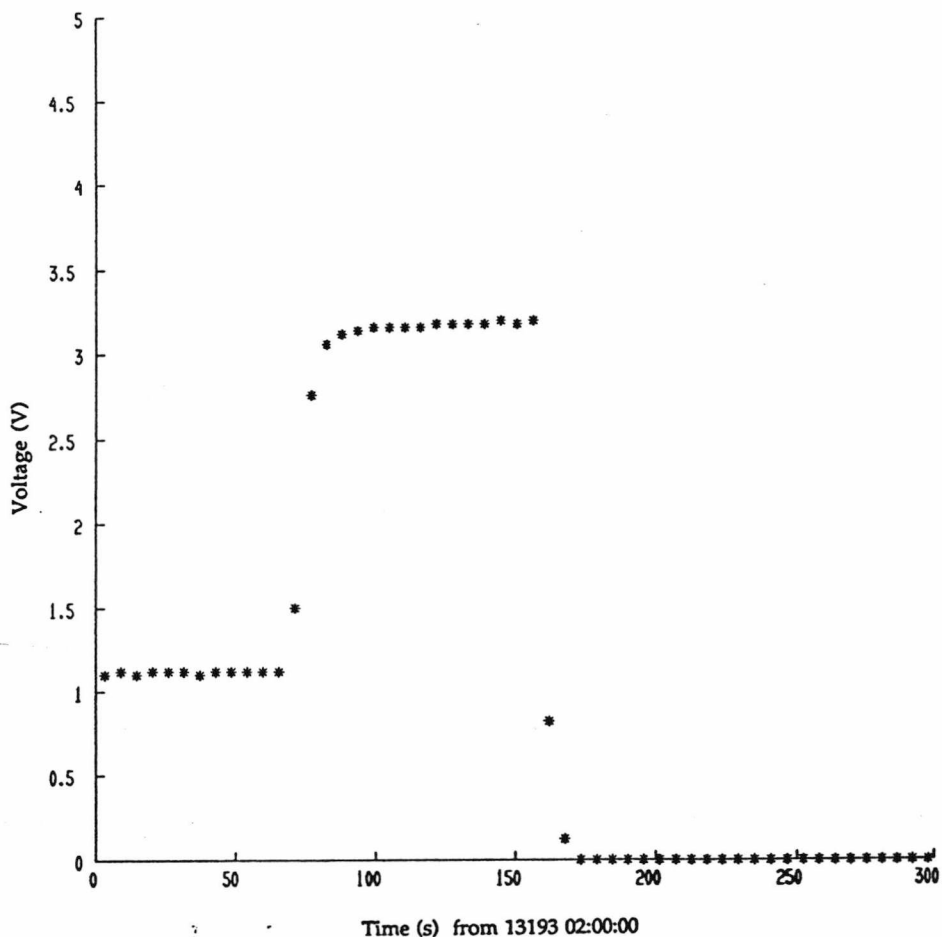


Figure 5.1: Output from the IPM-M analogue science channel during the cover release attempt. The activation of the cover release mechanism was seen as a sudden increase in the measured voltage due to electrical noise. The operation of the cover release mechanism was such that the current remained high until the experiment was turned off.

5.2 RAW DATA REDUCTION

5.2.1 REAL TIME ANALYSIS

On the night of encounter the real time analysis of DIDSY data was performed using the Electrical Ground Support Equipment (EGSE) and a set of BBC microcomputers which were installed at the European Space Operations Centre (ESOC) at Darmstadt. They provided a 'Quick Look' facility displaying information on the experiment status and the number of counts detected on each of the MSM, RSM and IPM-M sensors. A full description of the equipment and

software is given in Evans, 1987 and a frank appraisal of its operation is described in Olearczyk, 1988. The real time analysis of the CIS and IPM-P sub-systems was implemented separately by the co-investigator groups involved with those sub-systems. Neither the software or the results from the 'Quick Look' facility were used for the final data analysis and the system will not be considered further here.

5.2.2 REDUCTION OF THE FLIGHT EXPERIMENT TAPE

The initial Flight Experiment Tape (FET) provided by ESA a few weeks after the encounter contained nine files, covering the period from 19:20:22 UT Ground Receive Time (GRT) on the 13th March 1986 to 02:53:14 GRT on the 14th March and was the primary source for post mission data analysis. Each file contained a series of fixed length binary records, each record corresponding to a single spacecraft telemetry frame (Figure 5.2).

The initial FET provided by ESA only contained frames which were completely free from errors after Reed Solomon error correction. A second set of tapes containing partial and erroneous frames, recovered from the Parkes and NASA Deep Space

SYNC	BL	ST	TIME	ID	HK	DIDSY SCIENCE DATA	
---4---	-2-	-1-	---14---	-4-	---32---	----- 16(40) -----	-1-
----- 74(98) -----							

Record Length in bytes for Format 1(2) =

		4 x SYNCHRONISATION BYTES
		2 x BLOCK LENGTH
		1 x STATUS
		14 x TIME
		4 x ID
		32 x HOUSEKEEPING
		16(40) x DIDSY SCIENCE DATA
		<u>1 x SPARE</u>
TOTAL	=	<u>74(98) Bytes</u>

Figure 5.2 The contents and size of a DIDSY FET record in Format 1 and Format 2. Each record of the FET corresponds to a single Giotto telemetry frame.



Network (DSN) receiving stations, was made available some months after the encounter. These were used to produce a merged data set comprising of the good frames from the primary FET and, if not available, then the best quality frames from the other sources (Evans, 1987). To allow for easier inspection of the data, the files were converted from their original binary form to a tabular (ASCII) file format. This was done by producing a decimal listing of each byte from the digital science data together with some associated timing, format and block count information. In the process the housekeeping, analogue science and most of the header information was discarded. The initial conversion of the binary encoded FETs to the ASCII file format, was completed by J. Darby of the University of Kent's computing lab and G.C. Evans of the Space Science group using the university's ICL2960 computer. The ASCII files produced were given the name 'TEXTFILE#', where # was the number of the corresponding primary source file on the FET. The poor data frames which were now included in the 'TEXTFILE's were caused by the loss of the high gain antenna signal by the tracking stations. The loss of signal was due to an impact induced nutation of the spacecraft, which occurred just prior to closest approach (Section 5.3). The effect was periodic in nature and the transition from good data to noise could often be identified and the good data extracted by manually scanning through the files. This lengthy process was largely carried out by J.C. Zarnecki at University of Kent during the second half of 1986. A combination of the original 'TEXTFILE's and the 'HAND' reconstructed data, as the manually extracted data was known, were used to produce the most complete data set possible. To simplify the scientific analysis, the telemetry frames were reorganised into blocks containing information about individual Data Gathering Intervals (DGI). The original version of this data set, named 'COMPACT', was produced towards the end of 1987 (Pankiewicz, 1989) and was updated during the course of 1988 and 1989, based on a more detailed examination of the telemetry stream.

With the departure of J.Darby and G.C. Evans from the University, and the

replacement of the ICL machine with a cluster of three VAX/VMS computers, the Space Science group found itself in the awkward position of not being able to re-read the DIDSY FET's. This was not a significant problem for the encounter digital science data, since this had already been extracted, and was archived on tape in 'TEXTFILE' format which could be re-read on the new computers without problem. This was not the case for the analogue science or housekeeping data, which had only been stored as hardcopy output, or for the data taken during the cover release and experiment check-outs prior to encounter. With ESA's commitment to back the initial check-out stages of the Giotto Extended Mission (GEM) it became even more important to develop a piece of software which would enable processing direct from a FET file. To satisfy this requirement a data extraction program was written for the new computer system. Interactive user access to the tape drives on the University's VAX/VMS system was not supported and therefore the tape files had to be transferred to magnetic disk before any processing could take place. Although this situation was far from ideal, the use of disk files allowed for 'random' access to any part of the file, thus speeding up the data extraction process compared to the 'sequential' organisation of tape files. The final program, called 'DIDREAD', had the following specifications.

- i) Menu driven system with on-line help.
- ii) Little Knowledge of the Experiment or FET data formats was required to extract data.
- iii) Single program could be used to extract digital science, analogue science or housekeeping data.
- iv) Digital science data could be output in either 'TEXTFILE' or 'COMPACT' data formats for compatibility with existing analysis programs. (No error correction is provided for 'COMPACT' files).
- v) Automatic conversion of housekeeping data to voltages, temperatures and currents.

The program complemented the original 'TEXTFILE' to 'COMPACT' conversion

and error correction utility, 'RIWI', written by G.S. Pankiewicz (Pankiewicz, 1989), and was used to produce new versions of the input files used by 'RIWI', which had improved timing information. The program was also extensively used for the extraction of information from pre-encounter check-out and cover release tests, in preparation for comparison with the results obtained from the the GEM check-out.

5.3 DIDSY ENCOUNTER PERFORMANCE

Continuous telemetry reception during the encounter phase of the mission started approximately 70 hours before the time of closest approach and continued until 30 hours after the encounter; though the scientific payload was not active for this entire period. The spacecraft parameters for the encounter are given in Table 5.1. The spacecraft geocentric distance of 0.96AU at the time resulted in a signal travel time of 8 minutes. This meant that the operation of the spacecraft and its experiments had to be automated and this was indeed the case, with the exception of the change-over of telemetry format.

Parameter	Value
Giotto-Halley miss distance	596±2 km
Distance to Earth	1.44x10 ⁸ km (0.96 AU)
Distance to Sun	1.35x10 ⁸ km (0.9AU)
Distance below the ecliptic	3x10 ⁶ km (0.02AU)
Time of closest approach	00:03:01.84±0.2s (SCET) 00:11:01.94 (GRT)
Phase Angle	107.05°
Relative spacecraft velocity	68.373kms ⁻¹

Table 5.1: Parameters for the Giotto encounter with comet Halley on 14th March 1986 (Reinhard, 1987).

Two science telemetry formats were provided which distributed the available bandwidth differently. Providing the plasma experiments with a higher data rate, at the expense of the dust experiments, in the outer coma where the dust flux was low and the probability of a detectable impact occurring was small (Format 1). Then switching to give the dust experiments a higher data rate in the inner coma where detectable dust impacts were more frequent (Format 2). The switch-over was done from the ground via telecommand. Because of the 16 minute round trip time from transmission of experiment data to reception of the telecommand at the spacecraft, the decision to send the command could not be based on the returned data but had to be made in advance using predicted flux rates from computer models of the coma. The On Board Data Handler (OBDH) was switched from 'Format 1' to 'Format 2' at 22:46:38 GRT (~84.5 minutes before closest approach) and was switched back to 'Format 1' again at 01:11:42 GRT (+60.5 minutes after closest approach). All DIDSY events were detected while the experiment was in the preferential dust detector mode 'Format 2'.

Continuous telemetry was received from the spacecraft until 00:10:54.3 GRT at which time Giotto was hit by a large dust impact. The impact caused a shift in the angular momentum vector of 1° and resulted in a spacecraft nutation about this new axis of amplitude 1° and period 3.2s (Reinhard, 1987). Interpretation of the Doppler shift in the transmitted signal that was observed by the GRE at the same time (Edenhofer *et al.*, 1987), placed an upper limit on the mass of the impacting grain of $\sim 0.17\text{g}$ (Reinhard, 1987). At the same time the spin period of the spacecraft changed from 3.998s to 4.010s (Reinhard, 1987) which resulted in a loss of signal for 21.75s while the despun antenna automatically adjusted to the change in spacecraft spin and orientation. The spacecraft signal was recovered at 00:11:19 GRT but for the next 32 minutes telemetry reception was intermittent while the on board nutation dampers slowly reduced the amplitude of the nutation to a level where continuous telemetry was restored. Figure 5.3 indicates the loss of telemetry on the science data stream based on information from the FET, 'good' frames are

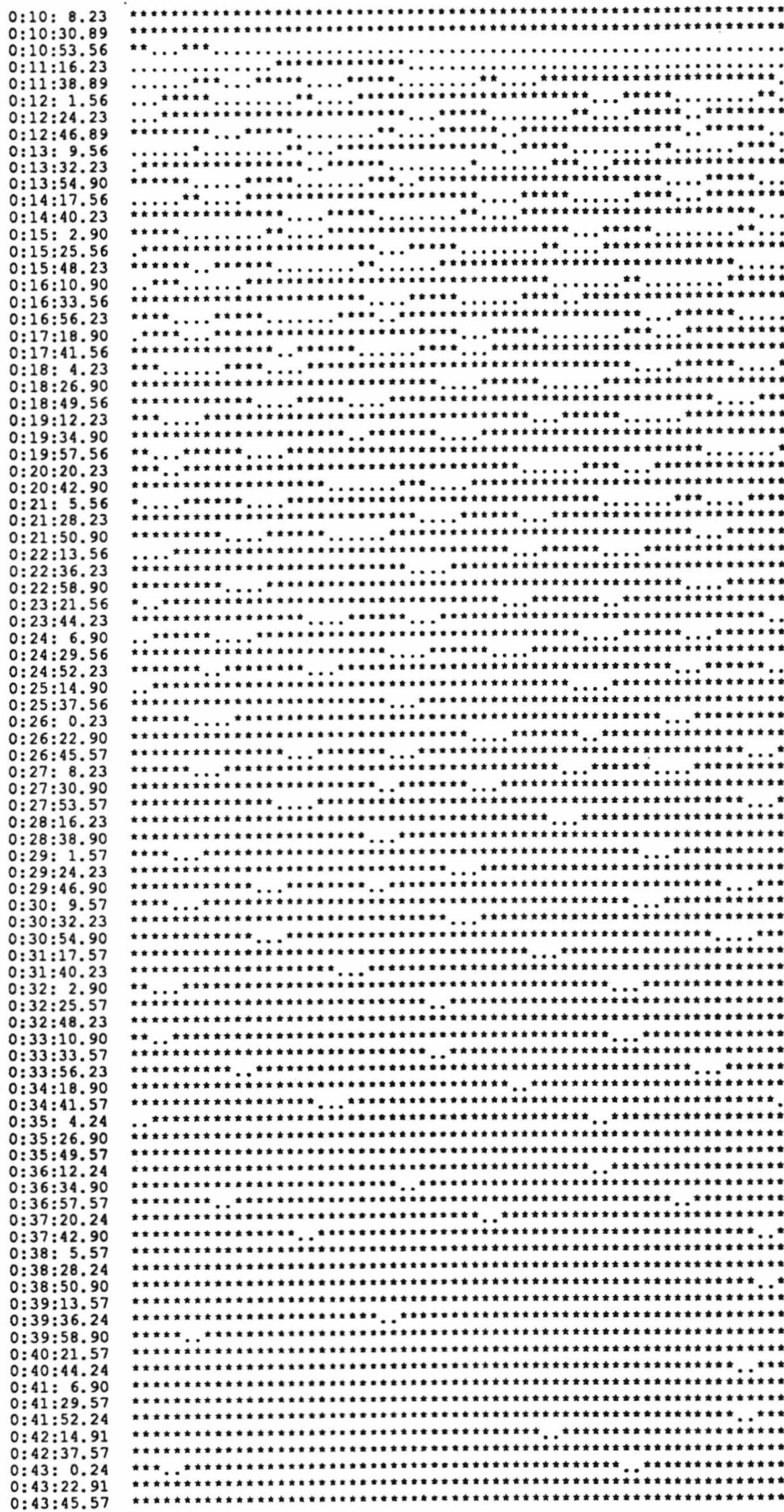


Figure 5.3 A telemetry map for Giotto during the encounter period. 'Good' frames are represented by '*' and bad frames by '.'. The effect of the nutation dampers to reduce the length of 'drop-outs' is apparent. In the case of DIDSY, analysis of the 'Bad' frames was able to provide additional data.

Voltage Rail	Pre-Encounter		Post-Encounter	
	MIN	MAX	MIN	MAX
CDF +5 Volts	5.00	5.04	5.00	5.04
IPM-P Analogue +10 Volts	9.34	9.41	9.34	9.41
IPM-P Analogue -10 Volts	-9.31	-9.31	-9.31	-9.31
IPM-P Digital +10 Volts	9.41	9.47	9.41	9.41
IPM-PA +30 Volts Bias	30.58	30.58	30.58	30.58
IPM-PA -30 Volts Bias	-30.42	-30.20	-30.20	-30.20
IPM-PB +30 Volts Bias	30.36	30.58	30.36	30.36
IPM-PB -30 Volts Bias	-29.98	-29.98	-30.20	-29.98
MSM Digital +5 Volts	5.08	5.08	5.08	5.08
MSM Analogue +10 Volts	9.41	9.47	9.41	9.47
MSM Analogue -10 Volts	-9.31	-9.21	-9.31	-9.21
CIS Digital +5 Volts	5.24	5.28	5.24	5.28
CIS +50 Volts	49.60	49.60	49.60	49.60
IPM-A +10 Volts	9.79	9.79	9.79	9.79
IPM-A -25 Volts	-24.26	-24.04	-24.26	-24.04

Table 5.2: The variation in housekeeping voltages for two periods are shown, Pre-Encounter (-2411s to -45s) and Post-Encounter (+45s to +3003s). The period between -45s and +45s has not been considered due to problems with the voltage multiplexer during this time (see Section 5.4.3). Most of the variations represent single bit transitions in the output of the A-to-D converters.

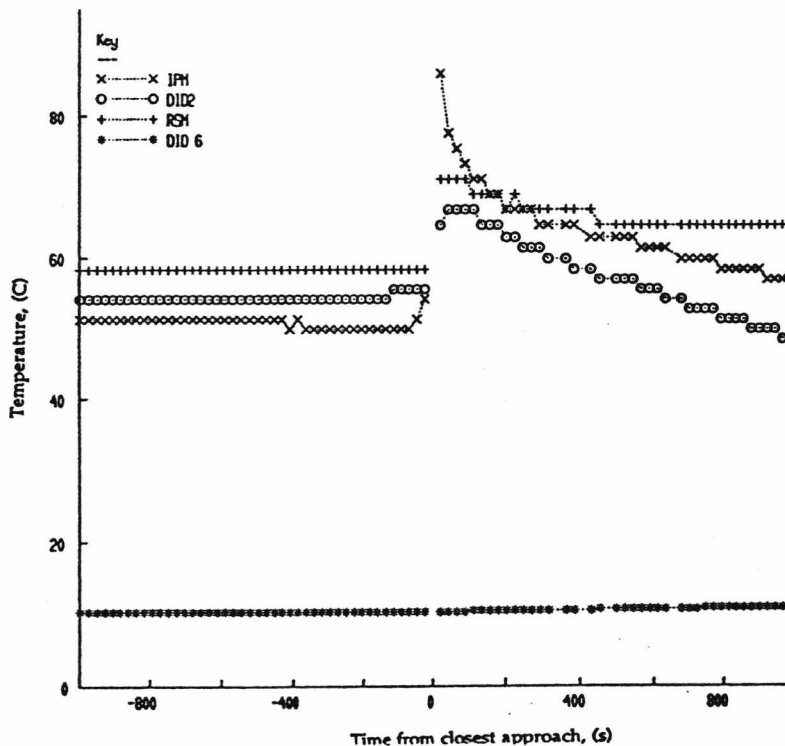


Figure 5.4 Temperatures over encounter measured by thermistors close to DIDSY sensors and attached to the DID 6 electronics box.

indicated by '*' and bad frames by '.', the DIDSY frames recovered by merging of all available data sets have been given in Evans, 1987.

The DIDSY experiment was switched on at 19:25:17 GRT on 13th March 1986. The housekeeping data indicated that all the monitored power supply rails were at their correct voltages and this remained the case throughout the encounter period until the experiment was turned off at 03:50:11 GRT, on 14th March 1986.

The temperature profiles taken from thermistors mounted, on the front shield near DID 2, on the IPM unit, on the rear shield near DID 5 and attached to the DIDSY electronics box in the scientific payload area, are shown in Figure 5.4. The temperature of the electronics box remained stable throughout the encounter period. The front shield thermistor showed a rise of $\sim 10^{\circ}\text{C}$ during the missing telemetry period at closest approach before slowly decaying back to its pre-encounter value. The IPM thermistor, which was expected to measure temperatures similar to those on the front shield, was initially some 4°C lower. Just prior to closest approach the temperature began to rise more rapidly than the front shield, the reason for this was linked to the operation of the IPM protective cover and will be discussed in Section 5.3.1.

Although the housekeeping voltages indicated correct operation of the experiment throughout encounter (Table 5.2), a detailed analysis of the analogue and digital science data highlighted a number of problems with both the operation of the sub-systems and of the DIDSY Central Data Formatter (CDF). An examination of the performance of each of the sub-systems is given in the following sections. The operation of the CDF is considered in Section 5.4

5.3.1 OPERATION OF THE IPM SUB-SYSTEM

The first impacts on the IPM-PA, IPM-PB and IPM-M sensors were detected at $-61^{\text{m}}45^{\text{s}}$, $-36^{\text{m}}09^{\text{s}}$ and $-24^{\text{m}}30^{\text{s}}$ from encounter, respectively. The IPM-P sensors became noisy just prior to closest approach, a state which they remained in until

the experiment was switched off. The IPM-M sensor detected its last event at +41^m49^s from closest approach.

As was stated in Section 5.1, prior to the night of encounter, the DID 8 cover, which was designed to protect the IPM unit from contamination during the firing of the the MAGE 1S kick motor, was thought to have been correctly released on the 10th February 1986. After the initial analysis of the data (McDonnell *et al.*, 1986b), a more detailed examination of the pre-encounter data was undertaken. It became clear that all was not well with the returned count rates from either the IPM-M momentum sensor, or the IPM-P impact plasma sensor (Lange *et al.*, 1986; McDonnell *et al.*, 1986c). The effect was most apparent on the IPM-P sensor due to its high mass sensitivity. The impact rate was lower than expected and was inconsistent with the rates being detected by PIA which had a similar mass sensitivity (Figure 5.5). In addition the number of high charge coincidence events, detected on the IPM-PA and IPM-PB sensors was much larger than expected (Lange *et al.*, 1986).

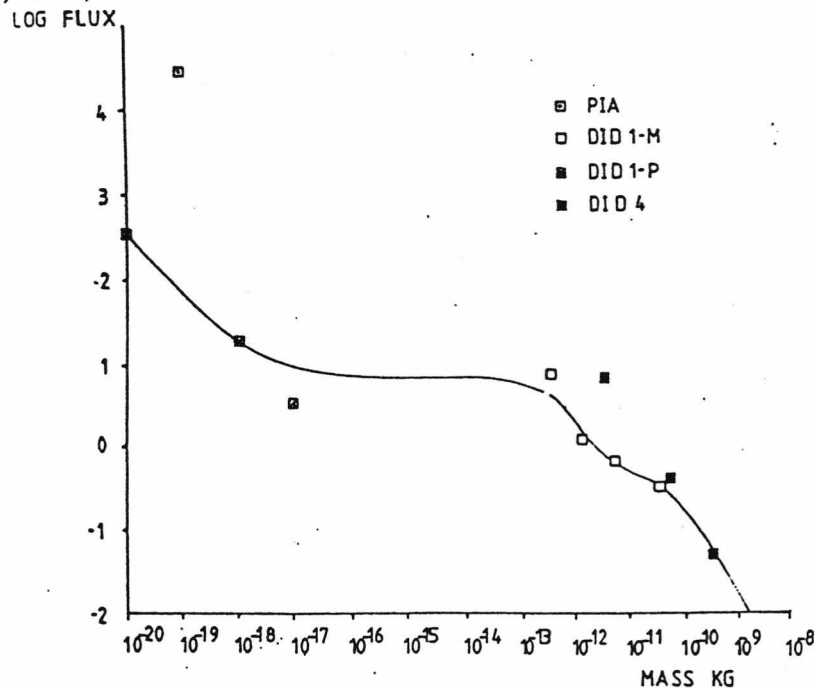


Figure 5.5: A mass distribution calculated for DIDSY and PIA data for the period -300s to -60s from closest approach (from Evans, 1988). Both IPM-P and IPM-M levels are lower than expected when compared to the fluxes rates determined from PIA and DID 4.

The likely explanation for these effects was that the DID 8 cover did not retract until the last minute prior to closest approach when the high flux rate caused the release of the cover (McDonnell *et al.*, 1986). Before the release only particles able to penetrate all, or part of, the cover were detected. The plasma and debris produced by these penetrating particles spread in the intervening space between the cover and the sensors, resulting in the higher than expected coincidence rate. There was considerable evidence for this scenario.

The IPM-A sensor, which was designed to measure the level of ambient plasma on the leading face of the spacecraft, showed a fairly constant output until ~70s before closest approach. It then measured a sudden increase in the secondary electron current of more than three orders of magnitude (Figure 5.6). This behaviour was totally inconsistent with results from similar sensors on the Vega spacecraft which had shown an approximately inverse square law dependence (Grard *et al.*, 1987). The output level dropped slightly post-encounter until ~40s after closest approach, after which time the average level remained constant; which has been attributed to impact damage sustained at closest approach (Grard *et al.*, 1987).

Comparison of the IPM-M sensor, with the most reliable of the front shield mounted piezoelectric sensors, DID 4, showed a substantial change in relative activity between pre- and post-encounter data. While part of this change was undoubtedly due to an instrumental effect on IPM-M (see Section 5.4.2), this cannot completely explain the observed difference.

The final evidence which indicated that the cover did retract during the close encounter period came from the temperature profile measured by the thermistor attached to the IPM unit, compared to that of the front shield (Figure 5.4). The IPM unit was initially ~5°C cooler but within the last minute before closest approach, the temperature increased rapidly, a change that was not matched by the front shield temperature.

The evidence would seem to support the idea that the cover did not release

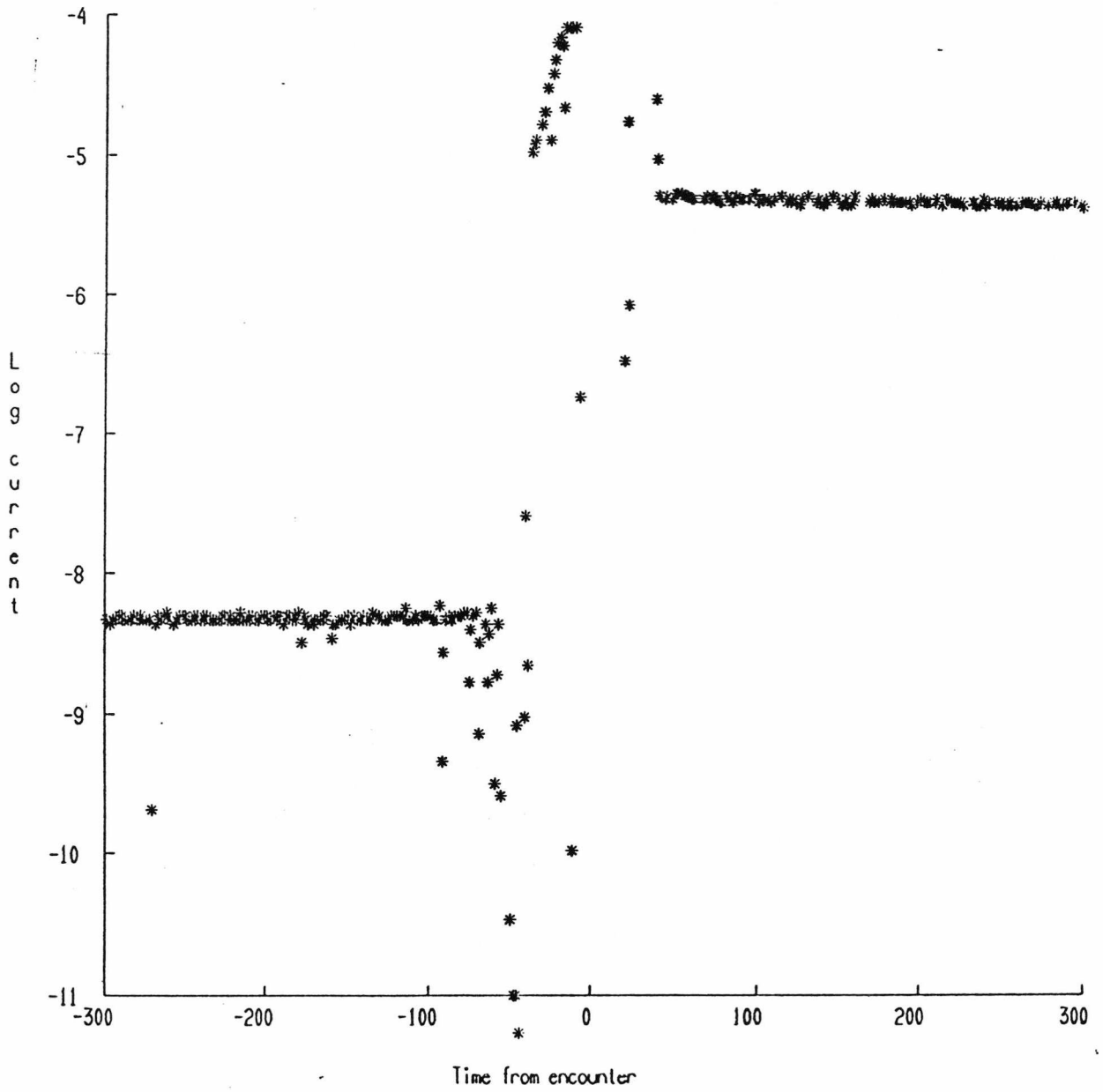


Figure 5.6: The secondary electron current measured by the IPM-A ambient plasma monitor during the encounter with Halley. The current remained constant until the last minute before closest approach when it underwent a sudden increase.

until some time within the last minute before closest approach, however, whether the cover was instantaneously released, or was eroded, is not clear. Calibration studies done after the encounter indicated that the penetration mass for a single foil of the DID 8 cover is 1.4×10^{-15} kg and that penetration of all three foils requires particles of mass $> 1 \times 10^{-12}$ kg (Maas *et al.*, 1989). From the calculated fluence up to 40s before closest approach (Section 7.4), $\sim 10^4$ and ~ 100 particles would have penetrated a single foil and the entire cover respectively. This was an insufficient number to completely erode the $\sim 2.2 \times 10^{-2} \text{m}^2$ cover. Therefore, an instantaneous release, or combined erosion and release appear to be more likely explanations.

It is possible to take account of the effect of the cover on the IPM sensors during the periods when the cover is known to be in place ($t \leq -70\text{s}$) or when released ($t \geq 0$). Tests by D. Maas at the Max Planck Institute, Heidelberg, have shown that impacts penetrating only two of the three foils that comprise the cover, can be detected on the IPM-PA sensor due to plasma leakage through the holes in the final foil. The thin foil over the IPM-PB sensor prevents the detection of such events. Hence new mass thresholds can be assigned to IPM-PA of 4×10^{-14} kg and to IPM-PB of 5×10^{-12} kg (Maas *et al.*, 1989) where penetration of all three foils is required.

In addition to the failure of the cover to release when originally commanded several other anomalies in the operation of the IPM sensors was discovered. Most important of these, was the multiple counting of IPM-M events during periods of high IPM-P activity. This was linked to the operation of the CDF and will be considered separately in Section 5.4.2. The operation of the CDF also accounted for the 0 pre- and post-event amplitudes in the IPM-M 'discrete' data (see Section 5.4.2 and Section 7.1) which had originally been attributed to marginal detections on the sensor. Examination of the DIDSY science telemetry stream also showed that during four periods pre-encounter (Table 5.3) all bytes returned from the IPM-P sensors were set to zero, this was inconsistent with the surrounding data and an explanation for this operation has not yet been found.

Start Time	Start Block	End Time	End Block
0:08:30	43329	0:08:46	43343
0:08:48	43345	0:09:03	43358
0:09:49	43399	0:09:59	43407
0:10:20	43426	0:10:37	43439

Table 5.3: Timings (GRT) and DIDSY block numbers for the periods when the IPM-P sub-system returned zeros for all counter and amplitude data (see text).

5.3.2 OPERATION OF THE CIS SUB-SYSTEM

The first impact on the CIS sensor was observed at 23:37:03.7±0.56 GRT. The sensor operated correctly until approximately 23:55 GRT detecting a total of 15 events during this period. At about this time, a fault occurred with the sensor which showed up as a drop in the output of the CIS analogue science channel (Figure 5.7). The cause of the fault is unknown, but was most probably due to a large impact which caused an electrical short between the two electrodes of the sensor. No further events were detected until 00:07:26 GRT. During the following 3 minutes a number of events were detected including a very high count of 637 in a single DGI. However, the rates did not match the activity on the other sensors and the analogue science data continued to indicate faulty operation of the sensor. The output became somewhat more consistent at 00:10:15 GRT and this was matched by a partial recovery of the analogue science data 5 to 10 seconds later. Although counts were recorded from this time until closest approach, the operation of the sensor was less reliable. This was confirmed both by the analogue science channel (Figure 5.8) and also by comparison of the count rates with those measured by the DID 4 sensor over the same period (Figure 5.9).

After closest approach, the CIS analogue science channel returned to a nominal level (Figure 5.8) indicating that normal sensor operation should have

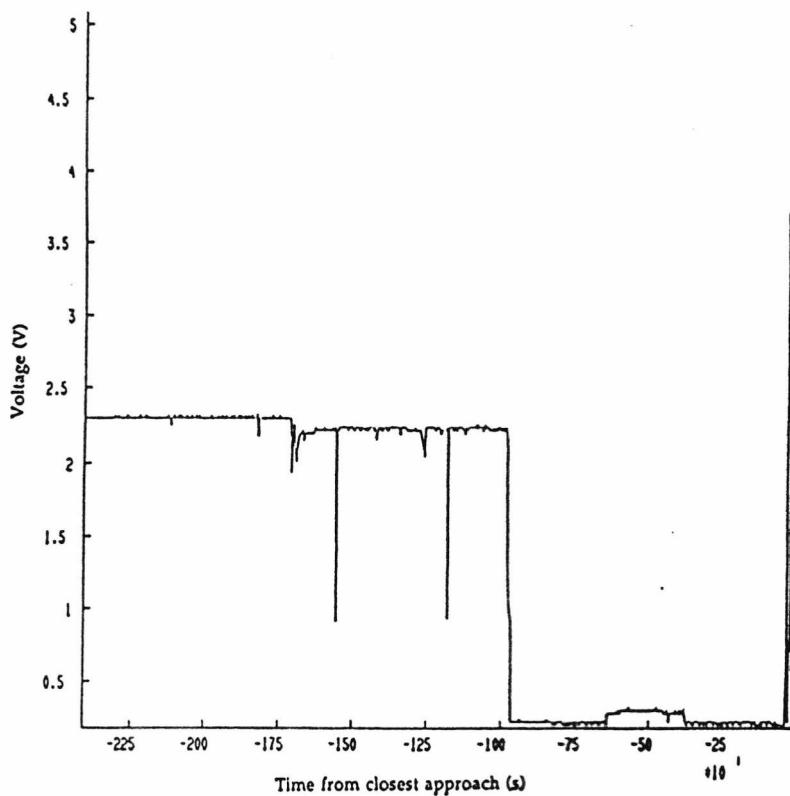


Figure 5.7: Analogue science data for the CIS sensor for the pre-encounter period, showing the fault at -960s (-16min) and partial recovery just before closest approach.

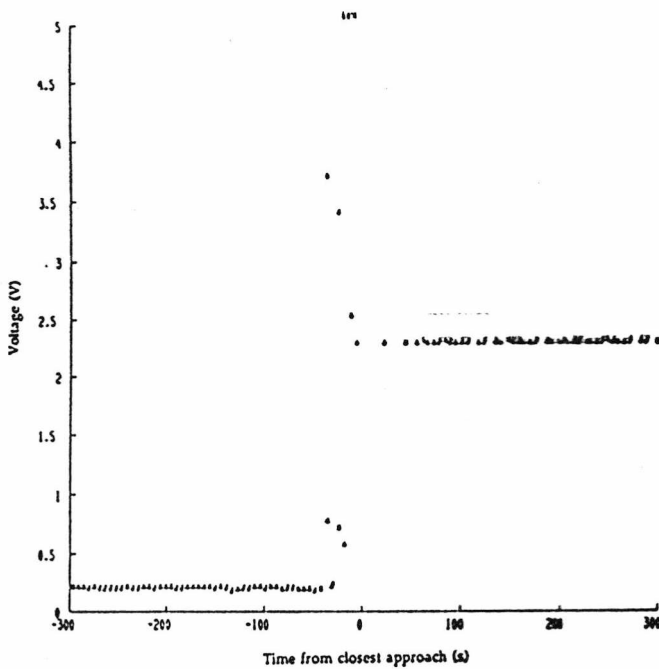


Figure 5.8: Analogue science data for CIS for the period -300s to 300s, showing the partial recovery of the sensor at -40s and then return to a nominal level post-encounter.

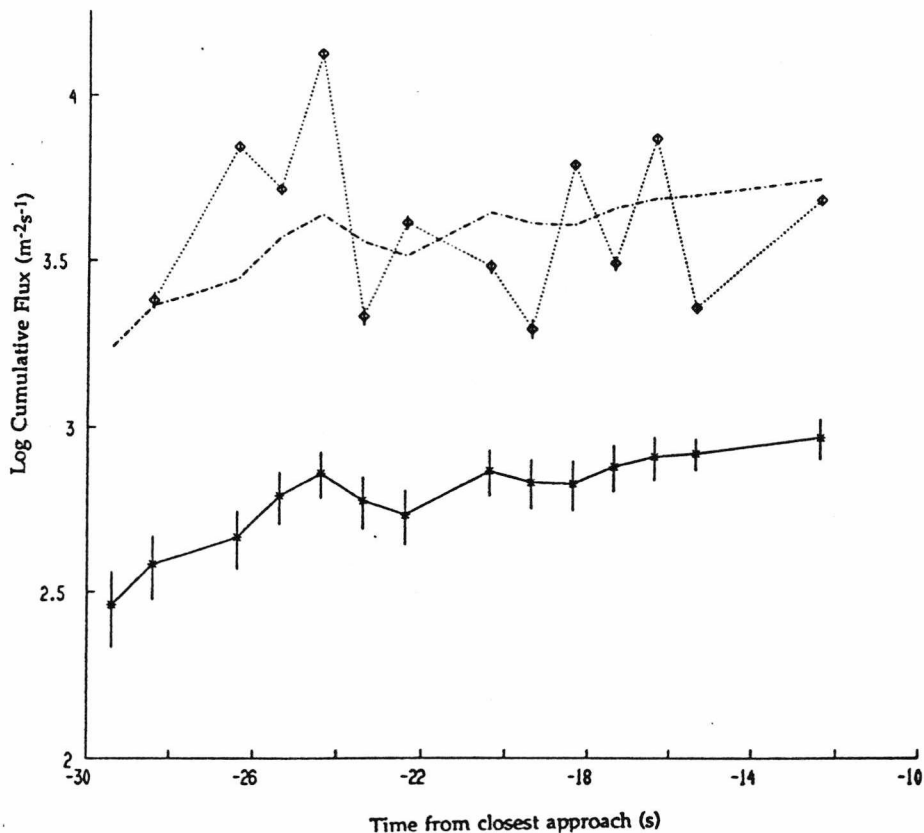


Figure 5.9: Comparison of CIS flux rates (dotted line) with the DID 4 'bin 1' flux rates (solid line) during the last 30s before closest approach. The 'chain' line represents the DID 4 flux scaled to the CIS mass assuming a mass distribution index $\alpha=0.9$.

resumed. However, no counts were detected post-encounter and it must be concluded that the sensor was irreparably damaged during closest approach.

5.3.3 OPERATION OF THE MSM/RSM SUB-SYSTEM

The first impacts detected by the DID 4 and DID 5 (RSM) sensors were at -70^m0^s and -3^m0^s from closest approach. The impact on DID 4 was also the first dust impact detected by any of the DIDSY sensors. The first DID 2 OR DID 3 impact occurred at -61^m41^s and the first DID 2 AND DID 3 event at -7^m14^s . The last impacts on DID 2 AND DID 3, DID 4 and DID 5 were at 7^m49^s , 49^m11^s and 1^m05^s respectively. DID 2 OR DID 3 mode was not active after closest approach.

During analysis of the MSM 'discrete' data, a minor problem was observed with the distribution of values produced by the analogue to digital converter. This

can be seen in Figure 5.10a which shows the pulse height analysis distribution, taken for all available data over encounter, for the DID 3 sensor. The number of events were 'binned' in steps of two amplitude values to reduce the overall noise level. Similar distributions are also obtained for the DID 2 and DID 4 sensors, the number of events on DID 5 is not large to determine the distribution. In each case, a large peak in the digital amplitude range 126-127 is observed, followed by a zero or low count in the 128-129 and 130-131 bins. This represents the transition from 01111111_B (127_D) to 10000000_B (128_D), and would appear to indicate some form of error in the analogue to digital conversion process. The reason for this is not clear although tests with the DIDSY flight spare electronics have shown similar effects. This indicates a design error rather than a fault peculiar to the operation of the flight electronics during encounter. Repeating the PHA analysis with larger amplitude bins, Figure 5.10b, yields the expected form of the distribution. Which implies that amplitude values missing from one digital level have been assigned a value close to their true value.

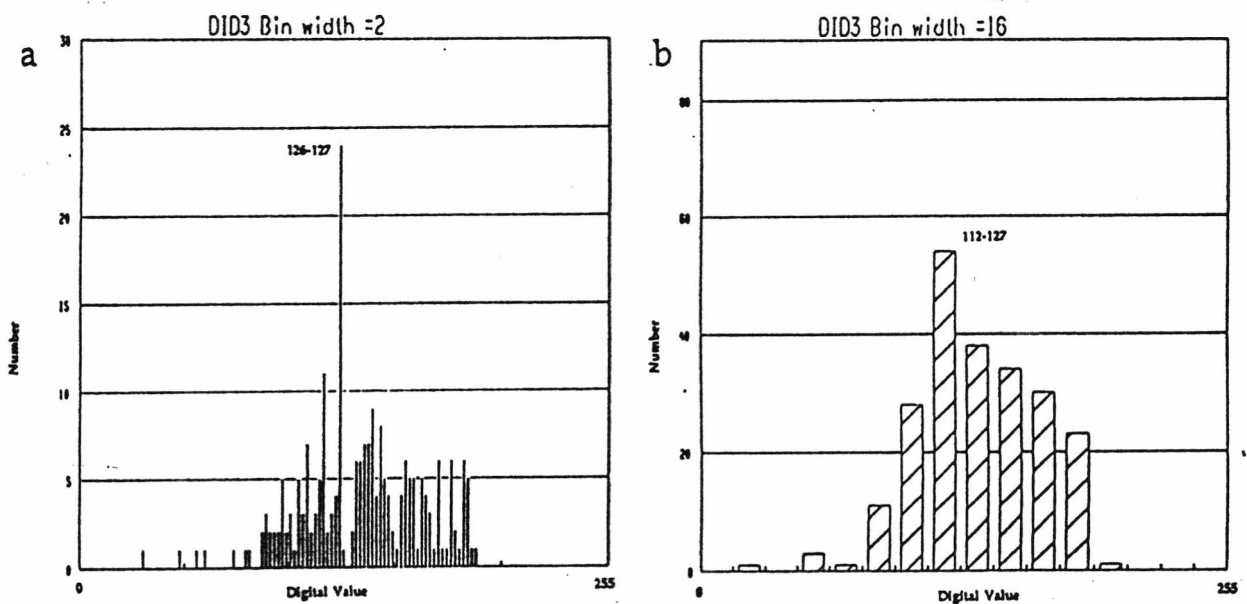


Figure 5.10: Pulse height analysis of DID 3 amplitudes taken over the whole encounter period. The amplitudes are obtained from the 'discrete' data which represents a sample of the amplitudes used by the on board PHA. The data has been plotted for two fixed amplitude steps, a) 2 digital steps, b) 16 digital steps.

Further tests with the flight spare electronics, indicated that the problem was limited to amplitude values around 128_D (although the test equipment available could not cover the full range of input levels). If this is the case, then there will be no effect on fluxes calculated from the 'binned' data since the range of digital values in question are contained within a single 'bin', any effect on the 'discrete' data analysis will also be minor.

Several other limitations were found with the MSM sub-system and in particular the the DID 2/3 mode operation. These were as a result of the operation of the CDF and will be considered separately in Section 5.4.1 and Section 5.4.3.

5.4 OPERATION OF THE CENTRAL DATA FORMATTER

During the course of the encounter with comet P/Halley a number of limitations in the design and operation of the DIDSY central data formatter were highlighted. The effects were particularly noticeable at high flux rates and tended to be the result of the interaction between several sensors. This represented the type of situation that it had not been possible to test prior to launch but for which the software simulation described in Chapter 4 was particularly well suited.

The first problem with the operation of the system became apparent with the re-emergence of CIS from a period of inactivity (Section 5.3.2) some 40s before closest approach. While the operation of CIS was independent of the other DIDSY sub-systems, a CIS coincidence line was used by the MSM/RSM sub-system as part of the categorisation procedure for the 'discrete' data. The category in question, 'Category 1', had the highest priority and was defined as CIS coincidence with detection on any of the MSM/RSM sensors. Each time a CIS event occurred the coincidence line was set for a period ~ 1 ms. When CIS started working again its' high count rate meant that the coincidence line was active for a significant proportion of each DGI. This resulted in a large number of MSM events being placed in 'Category 1' even though they were not CIS coincident events and should

GRT	Blk	CIS	C1	C2	C3	C4	C5
0:10:20	43426	0	0	0	0	6	23
0:10:21	43427	0	0	0	0	9	24
0:10:22	43428	40	13	0	0	5	17
0:10:23	43429	6	23	0	0	0	0
0:10:25	43430	235	26	0	0	0	0
0:10:26	43431	261	26	0	0	0	0
0:10:27	43432	273	24	0	0	0	0
0:10:29	43433	24	14	0	0	8	34
0:10:30	43434	0	0	3	0	21	21
0:10:31	43435	0	0	1	0	15	21
0:10:33	43436	211	18	1	0	10	19
0:10:35	43437	432	45	0	0	0	0
0:10:36	43438	363	44	0	0	0	0
0:10:37	43439	584	92	0	0	2	3
0:10:38	43440	193	52	0	0	0	0
0:10:39	43441	312	53	0	0	2	5
0:10:40	43442	252	53	2	0	2	3
0:10:41	43443	180	57	0	1	0	0
0:10:42	43444	402	54	0	0	1	4
0:10:44	43445	256	51	1	0	1	10
0:10:45	43446	446	38	2	0	8	21
0:10:46	43447	334	66	0	0	0	0
0:10:47	43448	0	43	7	0	3	9
0:10:48	43449	347	34	1	0	1	3

Table 5.4: Effect of CIS on the classification of MSM/RSM data. C1 to C5 are the category counters associated with each of the five categories defined in Section 2.3.4. When there is a high rate on CIS the majority of 'discrete' events are placed in 'Category 1'.

have been placed in one of the other modes. The effect is shown in Table 5.4, which lists the category counters (the number of events in a particular category) together with CIS count rate for the last 24 DGIs before encounter.

A similar effect was also found to occur between the sensors that make up the MSM/RSM sub-system. At high flux rates several independent events would appear to the system as a single, multi-sensor event. This was a particular problem when in the DID 2 AND DID 3 mode since the electronics waited for up to 3.4ms for events on both sensors. In other modes the CDF was notified immediately of an event. This effect is considered in more detail in Section 5.4.1.

In Section 5.3.1, the performance of the IPM sensors was described. Due to the cover pre-encounter, and the noisy operation post-encounter, little in the way of useful information was obtained from the IPM-P sensor. IPM-M pre-encounter data also suffered from the failure of the cover to release. Post-encounter the count rate was somewhat higher than expected, this was found to be a consequent of the IPM-P operation and is discussed in Section 5.4.2

In addition to the problems described above, the CDF also suffered from a number of spurious resets which caused a loss of synchronization with the spacecraft's OBDH. The effect of the resets on the CDF and the reconstruction of the data are described in section 5.4.3

5.4.1 OVER COUNTING IN DID 2 AND DID 3 MODE

Analysis of the mass distribution calculated from the 'binned' data over the period -30s to -14s indicated that the flux rate determined from the DID 2 AND DID 3 coincidence mode, was substantially higher than expected from comparison with other sensors. Since results from this mode were not inconsistent at greater distances from the comet (both pre- and post-encounter) it was clear that the problem was in some way related to the high rates being measured near closest approach. To investigate this phenomenon the software model of the DIDSY experiment (see Chapter 4) was used to simulate the operation of the experiment at high impact rates.

Using an input distribution with a fixed cumulative mass index of $\alpha = 0.9$, the dead time corrected flux was compared to the input flux (Figure 4.10). Exactly the same effect that had been observed in the real data was also seen in the output from the simulation, confirming that the high DID 2 AND DID 3 flux rate was a result of experiment design and not just a fault with the flight sensor or electronics. Examination of the electronic operation of the MSM sub-system showed that the discrepancy could be attributed to several small events hitting the shield within a

sufficiently short space of time (3.4ms), and thus appearing to the system as a single, larger, DID 2 AND DID 3 event. The effect was most apparent in the DID 2 AND DID 3 sensor due to the high mass threshold (1.5×10^{-10} kg) of the co-incident mode and because the electronics waited for up to 3.4ms for a coincidence signal before alerting the CDF of an event. Both of these factors increased the probability of false triggers due to smaller impacts, compared to DID 4, or DID 2 OR DID 3 mode events, which were reported to the CDF immediately.

Using the results from the simulation it was possible to calculate a correction factor that could be applied to the DID 2 AND DID 3 flux (Equation 5.1

$$F = 10^{\log(F) - 0.174(\log(F) + 1.5)} \quad \text{for } F > 10^{-1.5} \quad 5.1$$

If the DID 2 AND DID 3 flux rate was not sufficiently high to make this correction i.e. only one count per DGI then extrapolation from a more active channel was required. The correction algorithm was strictly only applicable for $\alpha=0.9$ and was used more to confirm the understanding of problem than as a correction for the observed flux rates. It was therefore decided, not to use DID 2 AND DID 3 data within ± 40 s of closest approach, where the effect was significant. This was unfortunate since a mode change meant that the experiment was in DID 2 AND DID 3 mode for the majority of this period.

5.4.2 OVER COUNTING OF IPM-M EVENTS

Analysis of the IPM-M data, post-encounter, after the cover had released, showed an apparent excess in the lowest bin compared to the flux rates calculated from the other DIDSY sensors. This was initially attributed to an indication that 'Bin 1' of the IPM-M sensors was more sensitive than originally thought (McDonnell *et al.*, 1987). Tests using the experiment software simulation indicated that this was not the case, instead an instrumental effect was found which

accounted for this observed excess.

The excess was due to the operation of the flight software which meant that the IPM-M sub-system was read every time an IPM-P trigger was serviced by the CDF. If a value was found on the output of the IPM-M A-to-D converter this value was passed directly to the data accumulation routine without first checking to see if the signal was above the comparator threshold level. Hence, a decaying signal from a previous IPM_M impact could be re-read as a new event, resulting in multiple detections of the event. The degree of over counting was linked to the level of activity on IPM-P and due to the cover (see Section 5.3.1) was small pre-encounter. However, the noisy operation of IPM-P post-encounter, led to almost continuous triggering of the sensor and meant that the IPM-P sub-system was being serviced by the CDF at its maximum possible rate. This caused particular problems just after closest approach when the IPM-M rate was also high, increasing the probability of multiple detections of a single event.

Using the software model an attempt was made to account for this effect. The over counting was predominantly in the lowest bin of the IPM-M sensor, the effect being negligible in the higher bins due to the relatively low numbers of true events. The simulation was run for two data sets which were identical with the exception of the IPMP activity which was zero in one case and noisy (see Section 4.2.2.1) in the other. The flux rates produced were plotted against one another (Figure 5.11) and a fit made to determine the deviation from a one to one relationship. Using this fit a simple expression to transform from observed counts N to corrected counts N' was derived, Equation 5.2.

$$N' = 10 \left(\frac{\log_{10}(N) - \log_{10}(2.88)}{0.91} \right) + 1 \quad (5.2)$$

The additional value of 1 is added to avoid digitisation effects at low count rates.

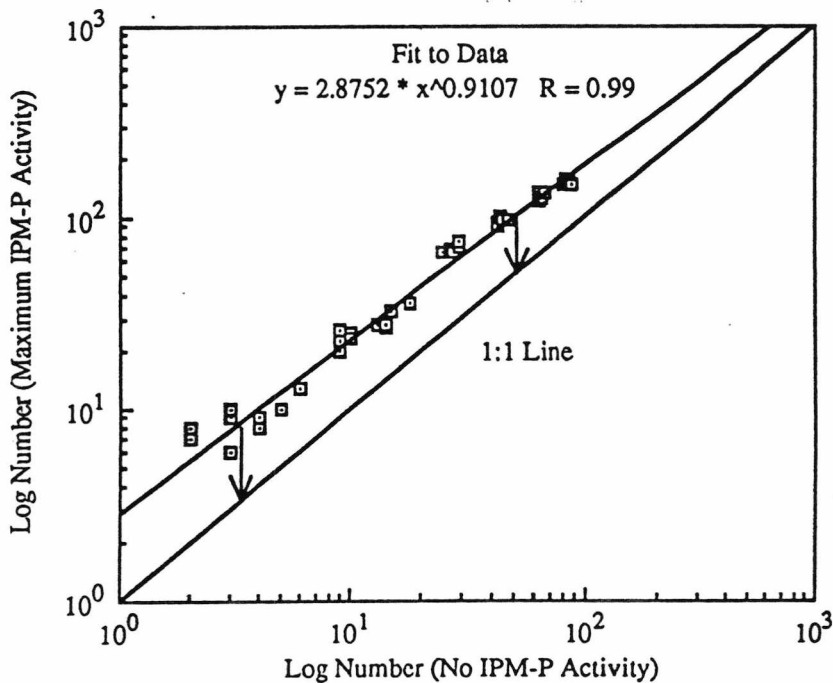


Figure 5.11: The effect of IPM-P noise on the IPM-M count rate. The deviation from a one-to-one relationship between the observed rate with, and without IPM-P noise, is clear.

In addition to the over counting of IPM-M events, the software path taken by CDF during an IPM-P service request was different from that taken by a normal IPM-M service operation. This meant that the IPM-M 'discrete' data was written to special locations in the IPM-P data 'discrete' data block instead of the IPM-M 'discrete' data area. Under certain circumstances this resulted in DGIs where the PHA counters for IPM-M were non-zero, but the corresponding IPM-M 'discrete' data was zero. These events had originally been interpreted as marginal detections on the sensor (Evans, 1988).

5.4.3 SPURIOUS RESETS OF THE DIDSY EXPERIMENT

Analysis of the DIDSY telemetry stream returned during the Giotto flyby of Comet P/Halley on 13/14 March 1986 showed evidence of a number of spurious resets of the CDF in the last minute before encounter. The first of the resets (at ~0:10:22 GRT) coincided with the re-emergence of CIS data after a time of inactivity and also to a deceleration of the spacecraft seen in the radio science data

(Feature 1, Edenhofer *et al.*, 1987) and attributed to passing through a jet. This was supported by a slight increase observed in the red, green and blue channels of the OPE data at the same time (S. Nappo, personal communication, 1989). No spurious resets were observed in the post encounter data, however proper synchronization with the telemetry handler was not recovered until the first format pulse after closest approach at 0:11:19 GRT.

When the experiment is powered up, and the spacecraft's on board data handler (OBDH) is in a suitable mode for handling data from the DIDSY experiment i.e. one of the science formats (format 1 or format 2) then digital science data is output to the OBDH using the built in direct memory access (DMA) facility of the RCA1802 processor. The use of DMA for transfer of data provides a reliable interface, the data being available to the OBDH within a matter of a few microseconds of the request, and also keeps software overheads to a minimum allowing greater scope for on-board processing of the incoming signals. The CDF handles digital science data via two buffers. Under normal operation data is output to the spacecraft OBDH from one buffer while data is accumulated in the other. The processor keeps track of the DMA pointer and after each byte transfer the corresponding byte in the buffer is set to zero by software, unlike the transfer to the OBDH this action is not time critical and there may be a delay of as much as a few 10s of milliseconds between DMA transfer and the byte being cleared. While this delay is perfectly acceptable under normal operation as will be shown later the effect may become important under certain circumstances. When a complete buffer (128 bytes) has been output, the action is swapped. Hence the time taken to accumulate a DGI is synchronized to the telemetry request line of the spacecraft and is dependant on the spacecraft telemetry format and data rate (ranging from 5.6s to the value of 1.13s used during encounter). To ensure that telemetry synchronization is maintained a CDF hardware reset is triggered on each format pulse (every 22.67s). After a hardware reset the DMA pointer is reset to the start of 'Buffer A' (memory 0400H), accumulation continues to the same buffer as before

the reset and if in MSM auto-sample mode, the auto-sampling is re-initialise. If normal synchronization is maintained the format pulse will occur just after the end of a DGI transmitted from 'Buffer B' and will have no apparent effect on the pointers. However if synchronization is lost or if a reset pulse unconnected with a format pulse is encountered then unusual but predictable effects will result. The effect depends on the state of the CDF before the reset and leads to two possible cases.

i) **On RESET : DMA from 'Buffer B', data accumulation to 'Buffer A'**

After RESET: The DGI being transmitted from 'Buffer B' will be truncated and DMA will resume from the start of 'Buffer A'. Additionally accumulation will continue to 'Buffer A' resulting in a DGI which is being accumulated and transmitted at the same time (blocks 43429,43448). After the whole of 'Buffer A' is transmitted DMA starts from 'Buffer B' , no further accumulation to this buffer has occurred since the reset and so the whole DGI being transmitted at the time of the reset can be reconstructed (blocks 43428,43447). During the transmission of 'Buffer B' data accumulation continues to 'Buffer A' resulting in a DGI accumulated over a time greater than 1.13 seconds, the actual integration time depends on the position of the byte within the 128 bytes of the DGI (blocks 43430,43449). The operation of the CDF then returns to normal although synchronization with the format pulse is lost.

ii) **On RESET : DMA from 'Buffer A', data accumulation to 'Buffer B'**

After RESET : The DGI being transmitted from 'Buffer A' will be truncated and DMA will resume from the start of 'Buffer A', i.e. the same DGI will be re-transmitted (blocks 43434,43436,43449). During this time data accumulation continues to 'Buffer B' resulting in a DGI accumulated over a time greater than 1.13 seconds (blocks 43435,43436,43450). The operation of the CDF then returns to normal, although again, synchronization with the

format pulse is lost.

In addition to the above mentioned effects, when a spurious reset occurred the MSM mode word was found to shift by one bit to the left, the LSB being replaced by a zero. The MSM mode word is stored in a serial-in, parallel-out buffer, during a mode command the spacecraft clocks the new mode word into the buffer which is then read by the CDF at the next format, or reset, pulse. The shift in value of the mode word indicates that in addition to spurious reset pulse there must also have been an unexpected pulse on the 'memory load sample' line. The effect of this mode change is that in two cases (blocks 43429,43437) the DGI was accumulated in two different modes, this invalidates the DID2/3 counts obtained, although further analysis may allow data from some bins to be recovered, since the DID 2 AND DID 3 only writes data to the lowest bin. The mode word in the last DGI pre encounter before telemetry was lost, was 0 thus indicating that at least eight resets occurred, the number of shifts to the original mode word of 247 required to get 0. This operation is shown schematically in Figure 5.12, the diagonal line maps the progress of the DMA pointer through the two buffers. The shaded areas represents the buffer to which data was being accumulated and the MSM mode. The integration time for any byte within a buffer can be inferred from the amount of shaded area between two successive DMA's and the software accumulators corrected (Appendix 2).

It should also be noted that the spurious resets were seen to have the effect of resetting the analogue multiplexers used to select the appropriate line for one of the Housekeeping, and one of the Analogue Science channels. Synchronization was restored at the next format pulse but during the intervening period, data was incorrectly assigned. This gave the appearance of wildly fluctuating voltages. In most cases corrections can be made for this effect and the source of the return voltage can be determined.

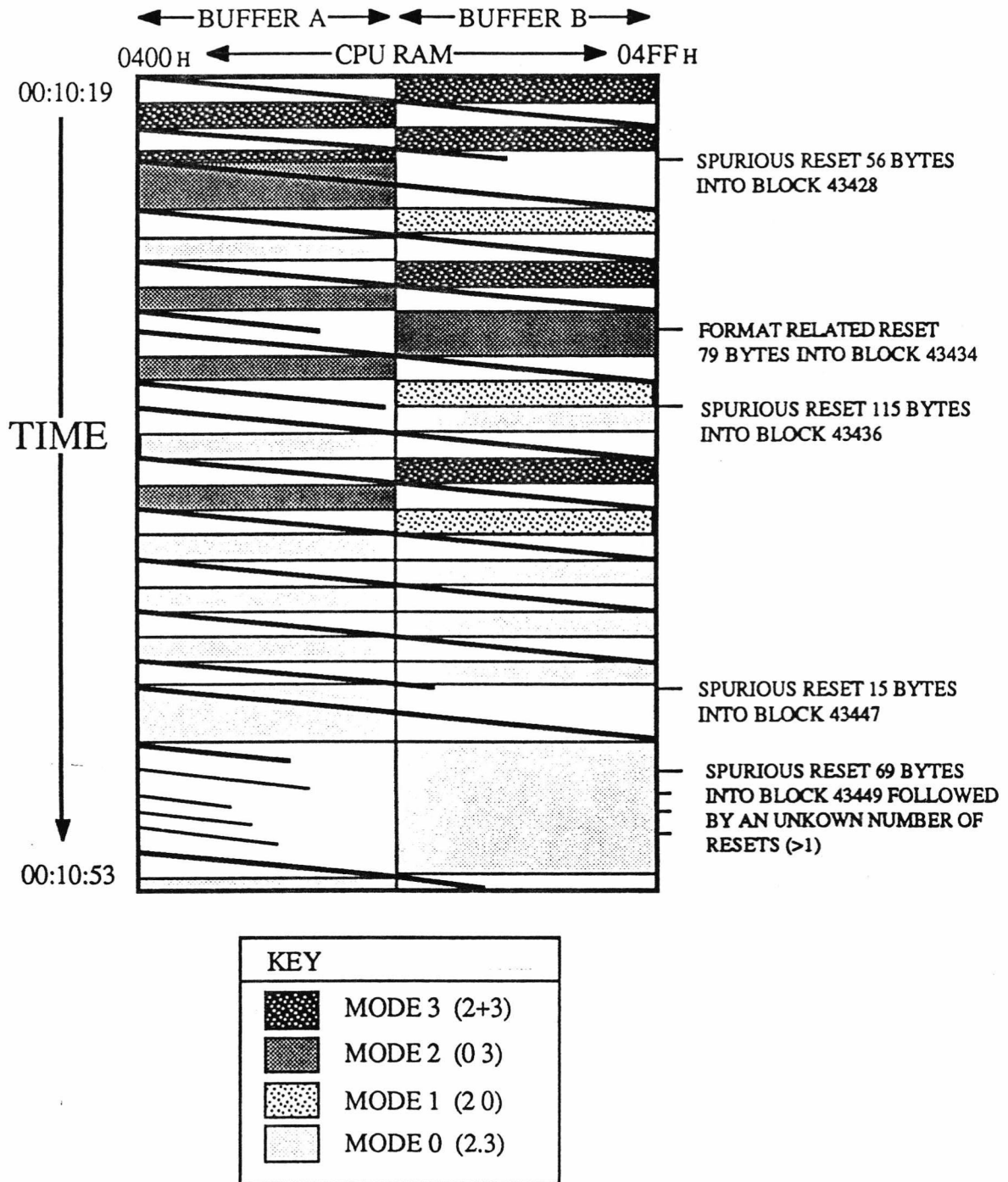


Figure 5.12: Shows a time line of the DMA pointer indicating its cyclic progression through the storage buffers (diagonal line), together with the current buffer to which data is being accumulated (shaded area). Spurious resets show up as a discontinuity of the DMA pointer in the middle of a buffer and a possible change in the DID 2/3 mode of accumulation.

5.5 DIDSY FLUX RATES

Using the results of the recalibration described in Chapter 3 and based on a better understanding of the operation and faults of the experiment, the most reliable data set possible was obtained. Figure 5.13 shows the flux rates obtained from the most reliable DIDSY sensor, DID 4, over the period -300s to +300s. Full flux rates for all the DIDSY sensors have been published in Pankiewicz (1989).

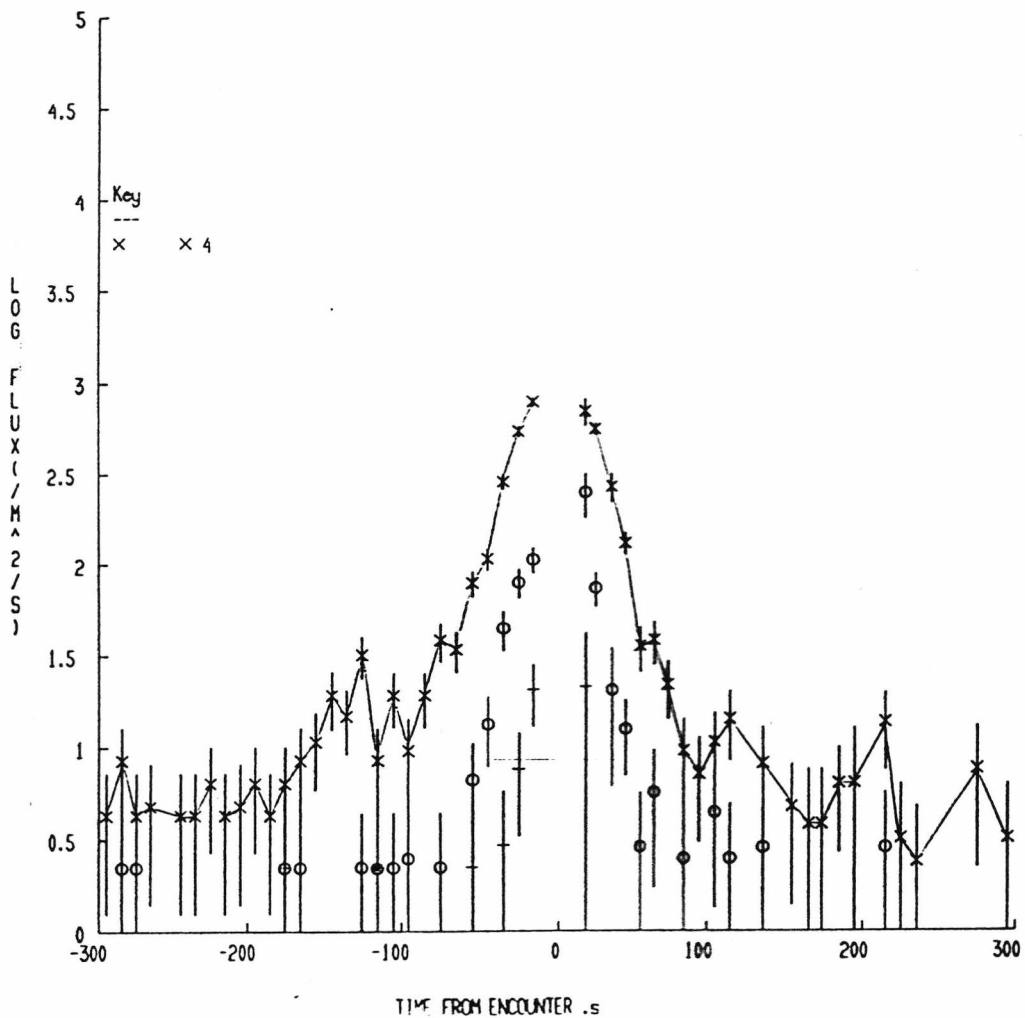


Figure 5.13: Flux rates for the DID 4 sensor during the period ± 300 s using 10s averaging. Fluxes are shown for 'Bin 1' (x), 'Bin 2' (o), 'Bin 3' (+) and for the single 'Bin 4' (*) event detected throughout the entire encounter period. Error bars are $\pm\sqrt{N}$ of the counts.

CHAPTER 6

PARTICULATE IMPACT ANALYSER

The failure of the DIDSY IPM cover to release before encounter (Section 5.3.1) and the subsequent noisy operation of the IPM-P sensor post encounter (Section 5.4.2) meant that the DIDSY experiment was only able to provide data on particles with mass, $m \geq 10^{-13}\text{kg}$ ($2.4\mu\text{m}$). Analysis of ground based cometary observations combined with pre-encounter modelling had indicated that the differential number distribution of dust grains in the coma would peak in the range $10^{-15}\text{kg} \leq m \leq 10^{-14}\text{kg}$ (Divine *et al.*, 1986). For this reason and for comparison with measurements both at, and below, these masses by the dust detectors on board the Vega 1 and Vega 2 spacecraft an investigation was made to see if data from the Giotto Particulate Impact Analyser (PIA, section 2.4) could be used to cover this gap.

PIA was known to have sufficient sensitivity to detect particles with masses of $\sim 10^{-19}\text{kg}$ and greater (Kissel, 1986), however, due to telemetry constraints the experiment could only return data on a subset of the total impacts measured. In addition the conversion from measured impactor and target ion yields back to the original mass and density of the impacting particle was poorly known, initial attempts resulting in unrealistically low particle densities in the range $0.002\text{gcm}^{-3} \leq \rho \leq 0.5\text{gcm}^{-3}$ (Kissel, personal communication, 1986). Using the spectral data for the calculation of absolute flux rates was not, therefore, a viable solution.

As part of its system, PIA included three simple detectors (known as the front end channels), these were used by the experiment to trigger the time of flight measurement and also to change the operating mode of the experiment at high impact rates, to avoid saturation. Count rate information from these channels was returned as part of the telemetry, but, they had not been intended for use as absolute flux detectors and little in the way of pre-launch calibration data was available. This chapter describes the work carried out to calibrate the

channels based on the operation of the experiment during encounter, and how the calibration data was used to obtain flux rates.

6.1 PIA OPERATION

A full description of the operation of the experiment has been given in Pockentrup, 1984 and Kissel, 1986 and only the details relevant to the analysis of the data from the front end channels is given below.

6.1.1 THE FRONT END CHANNELS

The three front end channels consist of charge sensitive amplifiers connected to the target and to the acceleration grid, which measure the positive ions produced by an impacting dust grain and a photomultiplier which was set up to detect the light flash from the impact (see Section 2.4). Depending on the mode of operation, a trigger on a single channel or combination of channels would alert the experiment to an impact which would start a measuring cycle on the time of flight part of the analyser. To ensure that a measuring cycle was not started by false triggers from interference or noise the photomultiplier was protected from stray light by a specially designed baffle and all three channels had an r.m.s. noise meter attached to their outputs. The outputs from the noise meters were used to adjust the limiting threshold of the most sensitive comparator on each of the channels. In addition, if the threshold level was raised above 3.2V the offending channel was disabled from initiating a measuring cycle, the channel being re-enabled only when the noise level had dropped to below 3.2V.

The output of the front end channels were each connected to a set of three comparators with relative thresholds of $\times 1$, $\times 10$ and $\times 100$ via an amplifier. The amplifier could be switched into one of two sensitivity modes

differing in gain by a factor of $\times 100$, hence, in the low sensitivity mode the relative thresholds of the three comparators were raised to $\times 100$, $\times 1000$ and $\times 10000$.

6.1.2 ON BOARD PROCESSING

To ensure that the system did not become saturated by events at high flux rates three methods were employed to limit the number of triggers from the front end channels. These were:-

- i) A shutter in front of the target which could be rapidly opened or closed to control the amount of target exposed to incident dust flux.
- ii) The number of front end channels required to simultaneously trigger before a measuring cycle was initiated, could be increased. This could be varied from co-incidence mode 1 where a detection on a single channel was sufficient, to co-incidence mode 3 where a signal on all three front end channels was required before a measuring cycle would be initiated. The higher co-incidence modes had the effect of increasing the mass thresholds since smaller impacts, which were less likely to be detected by multiple channels, would not start the cycle.
- iii) Finally, the gain of the front end amplifiers could be switched by a factor of $\times 100$, again resulting in a shift in the mass sensitivity of the detectors.

At low flux rates the shutter would be fully open, the co-incidence requirement would be set to mode 1 and the amplifiers switched to high sensitivity to allow the best chance of detecting and measuring a particle impact.

Action	When...
Increase co-incidence level by one	IMPRS > 10 and IMPR > 2 × IMPRS
Switch from HIGH to LOW sensitivity for 4s, open shutter and change to no coincidence required.	IMPRL > NEDF+3 and have been in HIGH sensitivity for ≥4s
Close shutter by 10 steps	IMPRS > 90
Close shutter by 20 steps	IMPRS >180
Close shutter by 30 steps	IMPRS > 254
Open shutter by 10 steps	IMPRS < 60
Open shutter by 20 steps	IMPRS < 30
Open shutter by 30 steps	IMPRS < 15

Table 6.1: Summary of PIA controls which affect the operation of, or the measurements made by, the front end channels.

Since the time taken, during encounter, to transmit data to the Earth and for a telecommand to be sent back to the spacecraft was approximately 16 minutes (Reinhard, 1987), the shutter and mode switching, all had to be controlled by the on board software. Three software counters were provided for this purpose; the 'IMPACT RATE' (IMPR) counter which measured the number of events which triggered a measuring cycle, the 'IMPACT RATE LARGE' (IMPRL) counter which recorded the number of events which triggered a measuring cycle and had a signal on the upper comparator ($\times 100$) of at least one of the front end channels, and the 'IMPACT RATE S' (IMPRS) counter which recorded the number of good spectra measured. The counters were integrated for a period of a 0.945s (P. Hisung, Personal communication, 1987). After each integration period the on board microprocessor adjusted the shutter position,

and the co-incidence and sensitivity modes based on the rules listed in Table 6.1 .

Due to the limited telemetry budget only a sub-set of the measured spectra could be transmitted back to Earth. To ensure the best use of this bandwidth, the experiment included thirteen data buffers. Each incoming spectra was classified based on various parameters such as the number of front end triggers, the number of mass lines and whether it was the result of a test pulse. When a spectrum was taken the data blocks were searched for a free block, (one which contained data which had already been transmitted) or a block which contained data of a lower classification than the current event. If a suitable block was found, the new data was stored and subsequently transmitted, or overwritten by new data of a higher class, whichever case happened first. To prevent obtaining a completely biased data set every second spectra measured was classed a statistical sample which could only be overwritten by data from the in-flight test sequence. Each of the thirteen data blocks was output in turn to the spacecrafts` On Board Data Handler (OBDH) by means of the direct memory access feature of the CDP1802 microprocessor used by the experiments data processing unit. Once all thirteen blocks had been transmitted transfer started again from the first block. The result of this on-board buffering was that the order of any consecutive set of thirteen Experiment Data Frames (EDF's) would not in general correspond to the order in which the events occurred. Each of the transmitted EDF's consisted of two parts, the data header, and the mass spectrum (see Table 6.1). The first stage of the analysis was to decode the data tape.

6.2 DECODING THE FLIGHT EXPERIMENT TAPE

The PIA data was provided for use by the group at Canterbury by the experiment principle investigator, J. Kissel, in the form of a standard flight

experiment tape (FET). The FET represents a standard format used by ESA to distribute the science data for the various experiments on board Giotto. The format, as might be expected, shares a lot in common with the raw telemetry stream described in Section 2.2. The files are written to tape, phase encoded at 1600bpi and corresponding to ISO recommendation 1001. Each data record (Figure 6.1) in the file contains data from a single telemetry frame and can be split into three specific sets of data. i) Header information comprising data from the telemetry frame header and additional information inserted by the ground station, such as ground receive time and quality of the data. ii) The Housekeeping data and iii), the science data. Parts i) and ii) are common for all experiments but iii) only contains the science data for a particular experiment. Since the telemetry allocation varies from experiment to experiment and depends on the telemetry format the overall length of each record might vary. To ensure that each file contains fixed length records a new file is written each time the format changed or if telemetry synch was lost. Due to the large number of telemetry 'dropouts' after closest approach a single file containing

SYNC	BL	ST	TIME	ID	HK	PIA SCIENCE DATA	
---4---	-2-	-1-	--14--	--4--	---32---	----- 128(256) -----	-1
----- 186(314) -----							

Record Length in bytes for Format 1(2) =

		4 x SYNCHRONISATION BYTES
		2 x BLOCK LENGTH
		1 x STATUS
		14 x TIME
		4 x ID
		32 x HOUSEKEEPING
		128(256) x PIA SCIENCE DATA
		<u>1 x SPARE</u>
TOTAL	=	<u>186(314) Bytes</u>

Figure 6.1: The contents and size of a PIA FET record in Format 1 (and Format 2). Each record of the FET corresponds to a single Giotto telemetry frame.

Word no. (8 bits each)	Contents	Remarks	
0	ID Field MSB	Experiment identifier	
1	ID Field LSB	Experiment identifier	
2	EDF Length MSB	Length of current EDF in bytes and data file section (high 4 bits)	
3	EDF Length LSB	Length of current EDF	
4	Shutter Status	Shutter position from pot.	
5	Target Status	Target position in motor steps	
6	HV Status	MM 1 HV control word	
7	Operation Status	Sens.- and TM.-status	Pattern A
8	EDL Status	EDL configuration word	Pattern B
9	Impact Rate	Impacts/s all events	
10	Impact Rate L	Impacts/s large events	
11	Impact Rate S	Impacts/s events with spectrum	
12	Event Counter 1	No coinc. events	
13	Event Counter 2	Dual coinc. events	
14	Class Counter 3	Triple coinc. events	
15	Class Counter 4	Events with spectrum	
16	Class Counter 5	Events class ≥ 5	
17	Event Number High	Number of current event, MSB	
18	Event Number Low	Number of current event, LSB	
19	Time High	Impact time, MSB	
20	Time Low	Impact time, LSB	
21	Sector	Solar aspect at impact	
22	Lightflash	Level of PM + IFT ID + Event class	Pattern C
23	Target + ACC.	Levels of TG and AC	Pattern D
24	Monitor	Amplitude monitor	
25	Catcher	Amplitude catcher	
26	IFT Type	IFT sequence counter	
27	Sequence No. MSB	Sequential count of EDFs from	
28	Sequence No. LSB	the experiment	
29	Time *	Mass spectrum	
30	Amplitude *	Mass spectrum	
.		Mass spectrum	
.		Mass spectrum	
E-1	Time *	Mass spectrum	
E	Amplitude *	Mass spectrum	

Bit	Pattern A	Pattern B	Pattern C	Pattern D
LSB	TG Sens. 1 = HI	Sp. mode 0-3	PM Level 0	TG Level 0
LSB +1	AC Sens. 1 = HI		PM Level 1	TG Level 1
LSB +2	PM Sens. 1 = HI	Coinc. 3 of 3	PM Level 2	TG Level 2
LSB +3	CA Sens. 1 = HI	Coinc. 2 of 3	IFT ID 1=IFT	AC Level 0
LSB +4	MO Sens. 1 = HI	Coinc. 1 of 3	LSB	Class of cur- rent event
LSB +5	TM OBDH code	PM 1 = ON	LSB +1	
LSB +6	TM OBDH code	TG 1 = ON	LSB +2	
MSB	TM OBDH code	AC 1 = ON	LSB +3	Unused

* No. of samples and EDF length changes with actual number of peaks in mass spectrum

Table 6.2: The data contained in one of the PIA Experiment Data Frames (EDF), taken from Kissel, 1986. The first 29 bytes are header information which describe the state of the experiment. Of particular interest for calculation of flux rates are the IMPR, IMPRL and to a lesser extent the IMPRS counters.

File Number	Start		End	
	OBT	GRT	OBT	GRT
1	15510400	19:20:22	15514288	20:52:29
2	15514304	20:52:33	15516144	21:36:14
3	15516160	21:36:22	15517184	22:00:38
4	15517200	22:00:56	15519120	22:46:37
5	15519136	22:46:38	15520992	23:30:41
6	15521008	23:30:50	15524816	01:01:05
7	15524832	01:01:08	15525264	01:11:41
8	15525280	01:11:42	15529568	02:53:14
9	15529584	02:53:20	15532144	03:53:27

Table 6.3: The On Board Time (OBT) and UT Ground Receive Time (GRT) for each of the nine data files contained on the PIA FET. Files 5, 6 and 7 were format 2 the remaining files being format 1 data. Each individual file is continuous with the exception of file 6 (which covers the time of closest approach) and file 9, which contain 192 frame jumps and 13 OBT jumps, and 3 frame jumps respectively.

all the good data frames over the near encounter period was constructed (File 6). A good frame was defined as a one that was complete and free from any bit errors after Reed Solomon Decoding. It should be noted that a telemetry frame is not equivalent to an EDF which is constructed from the science data from one or more telemetry frames. The FET for the night of encounter contained nine data files. The on board, and ground receive times covered by each file are given in Table 6.3

To extract the PIA data from the science data block requires an understanding of how the PIA data is arranged within the science data stream. Unlike the DIDSY data (Section 5.2.2) the PIA experiment did not use a fixed length data block, this was done to allow maximum use of the allocated telemetry rate in each of the experiments measuring modes. Instead, a variable length data block made up of a fixed length header followed by a variable number of bytes containing the time and amplitude information for the

measured spectra were used. This meant that the PIA data block was in no way synchronized to the start of a frame, or the start of a format. The algorithm used to extract the data is shown in Figure 6.2. A record, which is equivalent to a single telemetry frame was read and its validity was confirmed by checking that the initial four bytes matched the synch pattern (66H,50H,FBH,A5H), that the quality of the data was good (no bit errors) and that the telemetry format indicator was correct. If the frame failed any of these tests it was discarded and a new record read. Once a valid data frame had been located a search was made for the two identifier bytes of the PIA data block header (A8H,B2H), see Table 6.2. If the header bytes were not found, a new record was read and the procedure repeated. If the header bytes were correctly located the remaining 27 bytes of the header were read. If during this process the end of frame was reached a new record was read and in addition to the synch and telemetry checks described above, a test was made to ensure that the data frames were continuous. If this was not the case, which might occur if there had been a telemetry dropout, then the current data was discarded and a search for the next set of header identifier bytes initiated. The bytes from the header were then decoded based on the description given in Table 6.2, to reproduce the two byte counters and extract the bit fields and the resultant information output in a more tabular (ASCII) format. Included in the data header is a parameter giving the total length of the experiment data block, this was used to determine the length of the spectral information and the data was read using the same procedure as for the header. This information could then be output in ASCII format to a file, however, in the case of the flux analysis, the spectral data was not required and due to its large size, after the data had been read from the binary file it was discarded. The whole procedure was then repeated and the experiment header information extracted from all available frames.

As was described in the previous section the resulting data was not be in chronological order, due to on board buffering of the EDFs. However, each

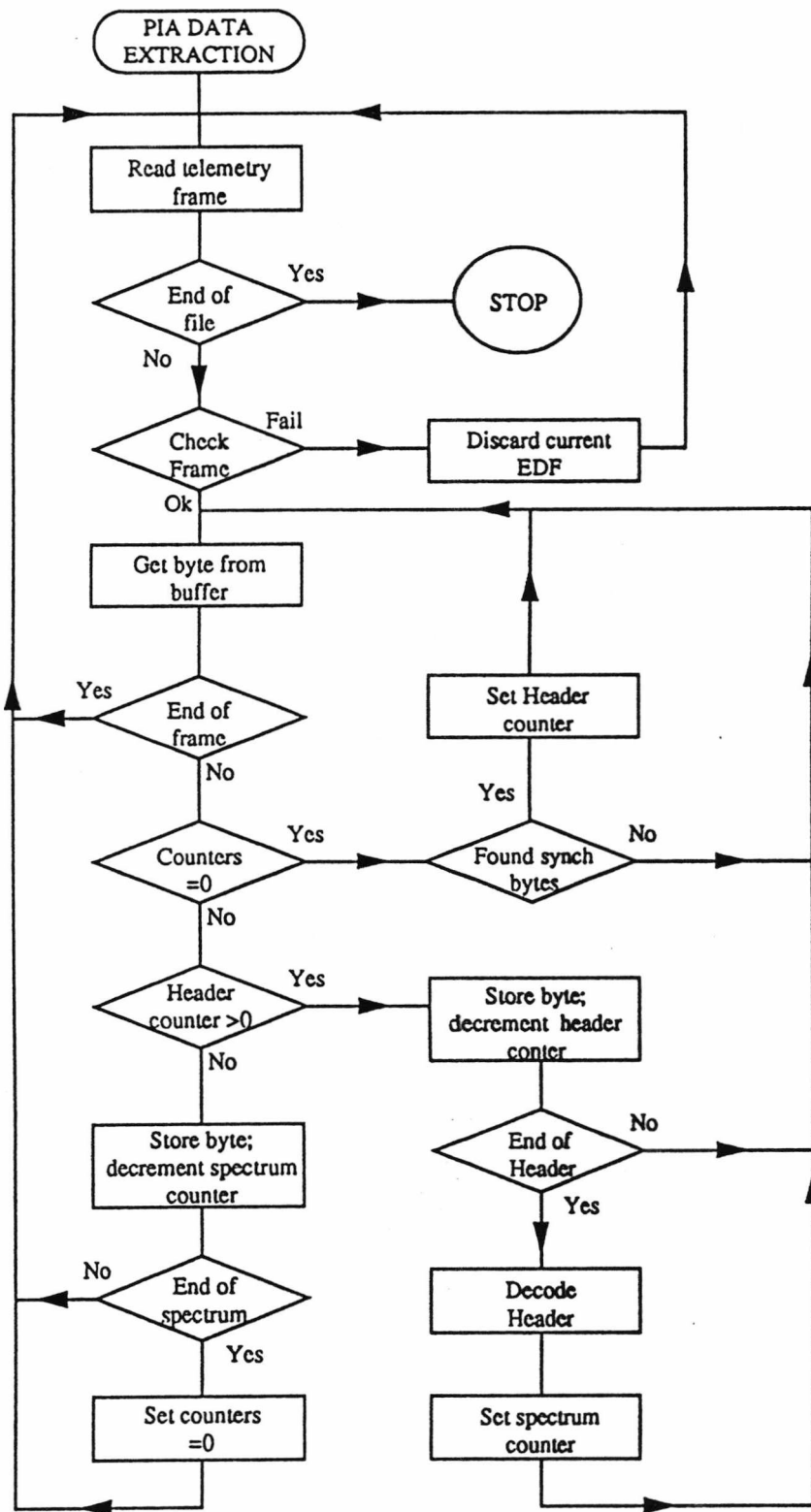


Figure 6.2: A flow diagram of the algorithm used to extract the PIA experiment data header from the Flight Experiment Tape.

spectrum was numbered and time tagged using the experiments internal clock so that the original order of the data could be reconstructed by sorting based on the time. In practice the file had to be edited and the sorting done in several stages since the clock overflowed and was reset during the encounter period. The final result was an formatted data file where each record corresponded to single EDF and contained only the information from the EDF header. An extract from the file is shown in Figure 6.3.

Sequence No.	Event No.	Exp. Time	Sun Angle	Lgth.	Data Blk.	Shutter	Target	HV	Sensitivity	Amplitude	Mode	Test	Test No.	Coin.	Cat. Counters	IMPR	IMPRL	IMPRS
31787	29506	32141	128	127	10	0	80	H40	HHHHH	0 1 1 6 0	...	36	1/ 2 8	195/ 11/	1/164/140	2	0	0
31788	29509	32143	113	169	11	0	80	H40	HHHHH	1 7 7 38 0	...	36	1/ 3 7	195/ 11/	1/164/142	2	0	0
31789	29522	32152	81	135	12	0	80	H40	HHHHH	1 0 0 1 0	...	35	1/ 1 5	195/ 11/	1/165/147	9	4	6
31790	29515	32149	137	63	13	0	80	H40	HHHHH	1 3 7 50 49	...	35	1/ 3 8	195/ 11/	1/165/143	9	4	6
31791	29520	32152	113	155	1	0	80	H40	HHHHH	1 7 7 25 0	...	35	1/ 3 7	195/ 11/	1/165/146	9	4	6
31792	29519	32152	129	129	2	0	80	H40	HHHHH	1 0 0 1 0	...	35	1/ 1 8	195/ 11/	1/165/145	9	4	6
31793	29531	32166	128	133	3	0	80	H40	HHHHH	0 0 1 2 0	...	35	1/ 1 8	198/ 11/	1/166/147	4	1	1
31794	29523	32156	129	123	4	0	80	H40	HHHHH	1 0 0 1 0	...	35	1/ 1 8	195/ 11/	1/165/147	9	4	6
31795	29525	32159	129	143	5	0	80	H40	HHHHH	1 7 7 41 0	...	35	1/ 3 8	196/ 11/	1/165/147	9	5	6
31796	29524	32158	17	121	6	0	80	H40	HHHHH	1 0 0 1 4	...	35	1/ 1 1	196/ 11/	1/165/147	9	5	6
31797	29543	32172	80	147	7	0	80	H40	HHHHH	0 3 3 18 0	...	35	1/ 2 5	200/ 11/	1/166/151	4	1	1
31798	29529	32165	129	139	8	0	80	H40	HHHHH	1 0 0 1 0	...	35	1/ 1 8	198/ 11/	1/165/147	4	1	1
31799	29527	32164	128	129	9	0	80	H40	HHHHH	0 1 3 19 0	...	35	1/ 2 8	197/ 11/	1/165/147	9	5	6
31800	29532	32166	113	153	10	0	80	H40	HHHHH	1 7 7 36 0	...	35	1/ 3 7	198/ 11/	1/166/148	4	1	1
31801	29533	32167	135	145	11	0	80	H40	HHHHH	7 7 7 63 0	...	35	1/ 3 8	198/ 11/	1/166/148	4	1	1
31802	29537	32169	129	119	12	0	80	H40	HHHHH	1 0 0 1 1	...	35	1/ 1 8	200/ 11/	1/166/148	4	1	1
31803	29538	32171	128	725	13	0	80	H40	HHHHH	0 3 3 11 0	...	35	1/ 2 8	200/ 11/	1/166/148	4	1	1
31804	29539	32171	113	169	1	0	80	H40	HHHHH	1 7 7 35 55	...	35	1/ 3 7	200/ 11/	1/166/149	4	1	1
31805	29544	32173	129	131	2	0	80	H40	HHHHH	1 7 7 44 0	...	35	1/ 3 8	200/ 11/	1/166/151	16	6	9
31806	29545	32174	113	129	3	0	80	H40	HHHHH	1 7 7 40 0	...	35	1/ 3 7	200/ 11/	1/166/152	16	6	9
31807	29555	32183	32	113	4	0	80	H40	HHHHH	0 1 3 19 0	...	35	1/ 2 2	202/ 12/	1/167/153	9	2	3
31808	29563	32191	65	119	5	0	80	H40	HHHHH	1 0 0 1 0	...	35	1/ 1 4	202/ 12/	1/168/156	10	4	7
31809	29550	32178	129	113	6	0	80	H40	HHHHH	1 0 0 1 2	...	35	1/ 1 8	202/ 11/	1/166/152	16	6	9
31810	29552	32180	129	117	7	0	80	H40	HHHHH	1 0 0 0 4	...	35	1/ 1 8	202/ 11/	1/167/152	16	6	9
31811	29561	32188	83	123	8	0	80	H40	HHHHH	3 7 7 0 0	...	35	1/ 3 5	202/ 12/	1/167/156	9	2	3
31812	29554	32183	129	121	9	0	80	H40	HHHHH	1 0 0 1 0	...	35	1/ 1 8	202/ 11/	1/167/153	9	2	3
31813	29567	32193	113	131	10	0	80	H40	HHHHH	1 7 7 26 0	...	35	1/ 3 7	202/ 12/	1/168/158	10	4	7
31814	29558	32186	128	119	11	0	80	H40	HHHHH	0 1 1 9 0	...	35	1/ 2 8	202/ 12/	1/167/154	9	2	3
31815	29570	32197	115	137	12	0	80	H40	HHHHH	3 7 7 0 63	...	34	1/ 3 7	202/ 12/	1/168/159	6	3	5
31816	29569	32197	143	69	13	0	80	H40	HHHHH	7 3 7 50 49	...	34	1/ 3 8	202/ 12/	1/168/158	6	3	5
31817	29571	32199	129	119	1	0	80	H40	HHHHH	1 0 0 1 0	...	34	1/ 1 8	202/ 12/	1/168/159	6	3	5
31818	29573	32202	129	135	2	0	80	H40	HHHHH	1 7 7 33 0	...	34	1/ 3 8	202/ 12/	1/168/160	6	3	5
31819	29572	32201	81	125	3	0	80	H40	HHHHH	1 0 0 0 0	...	34	1/ 1 5	202/ 12/	1/168/160	6	3	5
31820	29574	32203	65	121	4	0	80	H40	HHHHH	1 0 0 0 0	...	34	1/ 1 4	202/ 12/	1/169/160	6	3	5
31821	29577	32205	129	145	5	0	80	H40	HHHHH	1 0 0 1 0	...	34	1/ 1 8	203/ 12/	1/169/160	8	3	5
31822	29580	32206	80	145	6	0	80	H40	HHHHH	0 3 3 2 0	...	34	1/ 2 5	204/ 12/	1/169/161	8	3	5
31823	29581	32208	129	125	7	0	80	H40	HHHHH	1 0 0 1 3	...	34	1/ 1 8	204/ 12/	1/169/161	8	3	5
31824	29582	32209	113	153	8	0	80	H40	HHHHH	1 7 7 38 0	...	34	1/ 3 7	204/ 12/	1/169/162	8	3	5
31825	29583	32211	129	127	9	0	80	H40	HHHHH	1 0 0 1 4	...	34	1/ 1 8	204/ 12/	1/169/162	8	3	5
31826	29584	32212	32	129	10	0	80	H40	HHHHH	0 1 1 3 0	...	34	1/ 2 2	204/ 13/	1/169/162	8	3	5
31827	29585	32213	129	139	11	0	80	H40	HHHHH	1 0 0 1 0	...	34	1/ 1 8	204/ 13/	1/169/162	8	1	3
31828	29586	32216	65	137	12	0	80	H40	HHHHH	1 3 7 7 0	...	34	1/ 3 4	204/ 13/	1/170/162	8	1	3
31829	29587	32216	129	725	13	0	80	H40	HHHHH	1 0 0 3 3	...	34	1/ 1 8	204/ 13/	1/170/162	8	1	3
31830	29590	32220	128	133	1	0	80	H40	HHHHH	0 0 1 1 0	...	34	1/ 1 8	205/ 13/	1/170/162	8	1	3
31831	29588	32219	129	139	2	0	80	H40	HHHHH	1 0 0 1 0	...	34	1/ 1 8	204/ 13/	1/170/162	8	1	3
31832	29599	32226	32	125	3	0	80	H40	HHHHH	0 1 1 5 0	...	34	1/ 2 2	206/ 14/	1/172/163	6	1	4
31833	29591	32221	80	151	4	0	80	H40	HHHHH	0 1 0 1 0	...	34	1/ 1 5	205/ 13/	1/170/163	6	1	4
31834	29605	32231	65	139	5	0	80	H40	HHHHH	1 0 0 1 0	...	34	1/ 1 4	206/ 14/	1/174/164	11	3	6
31835	29596	32224	129	153	6	0	80	H40	HHHHH	1 7 7 41 0	...	34	1/ 3 8	206/ 13/	1/171/163	6	1	4
31836	29598	32226	135	135	7	0	80	H40	HHHHH	7 7 7 63 0	...	34	1/ 3 7	206/ 14/	1/172/163	6	1	4
31837	29601	32228	113	161	8	0	80	H40	HHHHH	1 7 7 28 0	...	34	1/ 3 7	206/ 14/	1/172/164	6	1	4
31838	29602	32229	129	137	9	0	80	H40	HHHHH	1 0 0 1 0	...	34	1/ 1 8	206/ 14/	1/172/164	11	3	6
31839	29604	32231	129	133	10	0	80	H40	HHHHH	1 0 0 1 0	...	34	1/ 1 8	206/ 14/	1/173/164	11	3	6
31840	29617	32238	81	147	11	0	80	H40	HHHHH	1 7 7 29 0	...	34	1/ 3 5	208/ 15/	1/176/165	10	0	8
31841	29622	32245	113	147	12	0	80	H40	HHHHH	1 7 7 28 0	...	33	1/ 3 7	208/ 15/	1/177/166	9	4	6
31842	29620	32243	137	57	13	0	80	H40	HHHHH	1 1 1 28 29	...	33	1/ 3 8	208/ 15/	1/177/165	10	0	8
31843	29621	32245	129	127	1	0	80	H40	HHHHH	1 1 3 0 0	...	33	1/ 3 8	208/ 15/	1/177/165	9	4	6
31844	29624	32246	65	131	2	0	80	H40	HHHHH	1 0 0 1 3	...	33	1/ 1 4	208/ 15/	1/178/166	9	4	6
31845	29626	32247	17	125	3	0	80	H40	HHHHH	1 0 0 1 0	...	33	1/ 1 1	209/ 15/	1/178/166	9	4	6
31846	29642	32262	55	129	4	0	80	H40	HHHHH	7 7 7 0 0	...	33	1/ 3 3	211/ 15/	2/181/168	6	1	5
31847	29632	32251	115	151	5	0	80	H40	HHHHH	3 7 7 36 0	...	33	1/ 3 7	211/ 15/	1/178/167	9	4	6
31848	29633	32252	129	127	6	0	80	H40	HHHHH	1 0 0 1 0	...	33	1/ 1 8	211/ 15/	1/178/167	9	4	6
31849	29638	32258	64	143	7	0	80	H40	HHHHH	0 0 1 0 0	...	33	1/ 1 4	211/ 15/	1/180/168	13	3	7
31950	29634	32256	113	171	8	0	80	H40	HHHHH	1 7 7 26 0	...	33	1/ 3 7	211/ 15/	1/178/168	13	3	7
31851	29635	32257	129	125	9	0	80	H40	HHHHH	1 0 0 1 0	...	33	1/ 1 8	211/ 15/	1/178/168	13	3	7

Figure 6.3: An example of the extracted header data from an EDF after the initial stage of decoding.

6.3 CALIBRATION

6.3.1 SHUTTER OPERATION (EFFECTIVE AREA)

The area of the target exposed to the dust coma was controlled by means of the shutter (Section 2.4). For all but 6 seconds of data taken during the encounter period, the shutter remained in its fully open position, resulting in an effective sensing area of 470mm^2 . Close to encounter the impact rate did rise sufficiently to cause the shutter to step down to apertures of 390 and 300mm^2 . The opening and closing of the shutter was not instantaneous, taking 36ms per step (P. Hisung, personal communication, 1989). Figure 6.4 shows the shutter area as a function of time for the period from -20s to -8s from closest approach, when telemetry was lost. Using this variation the average aperture size for each integration period was calculated, these values are listed in Table 6.4.

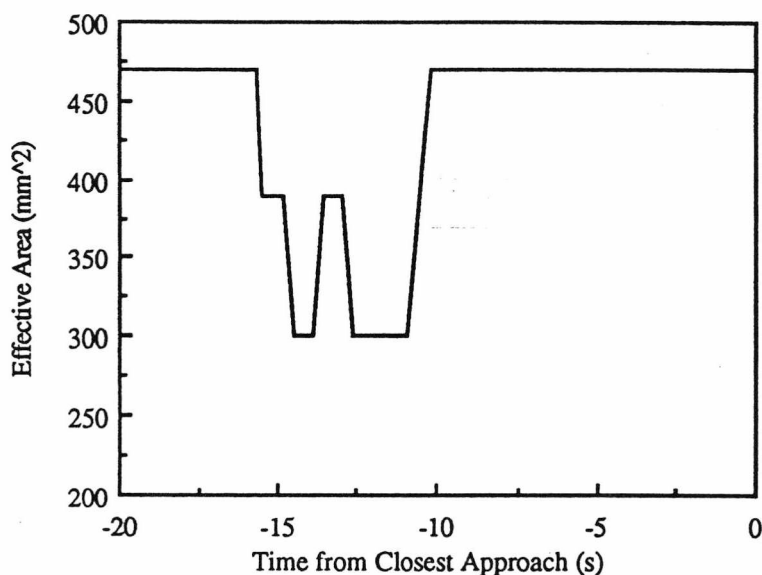


Figure 6.4: The time variation of the PIA shutter for the few seconds close to encounter when it is known to differ from its nominal value of 470mm^2

Time (s)	Area (mm) ²
-15.1	404
-14.2	315
-13.3	376
-12.4	315
-11.5	301
-10.6	404

Table 6.4: Average effective areas applicable for the 6 integration periods where the shutter was smaller than its nominal open value of 470mm². The time given is the mid-time of each integration period relative to closest approach.

6.3.2 SENSITIVITY AND NOISE CONSIDERATIONS FOR THE FRONT END CHANNELS

Initial results from the PIA experiment showed that the time of flight measurement was being triggered even at large distances, outside the modelled apex distances for particles of the sizes measured by the experiment. Some mass lines were seen in the spectra produced by the triggers (see Figure 6.5) and these were similar to the 'background' spectra from the PUMA experiments on board Vega 1 and Vega 2. These 'background' spectra have been attributed to very small particles of $\geq 10^{-23}$ kg (Sagdeev *et al.*, 1989). However, impacts from such small particles were not expected to trigger the front end channels and this was substantiated by the lack of correlation between the lines in the spectrum and the position of elemental lines produced by correctly triggered spectra (figure 6.5). Indeed, correlation between individual lines in the background spectra has not provided any conclusive evidence to the source or composition of the measured impact (M. Wright, personal communication, 1988).

In an attempt to see if the triggers were likely to be due to dust impacts an analysis of the sensitivity of the front end channels was considered. No pre-

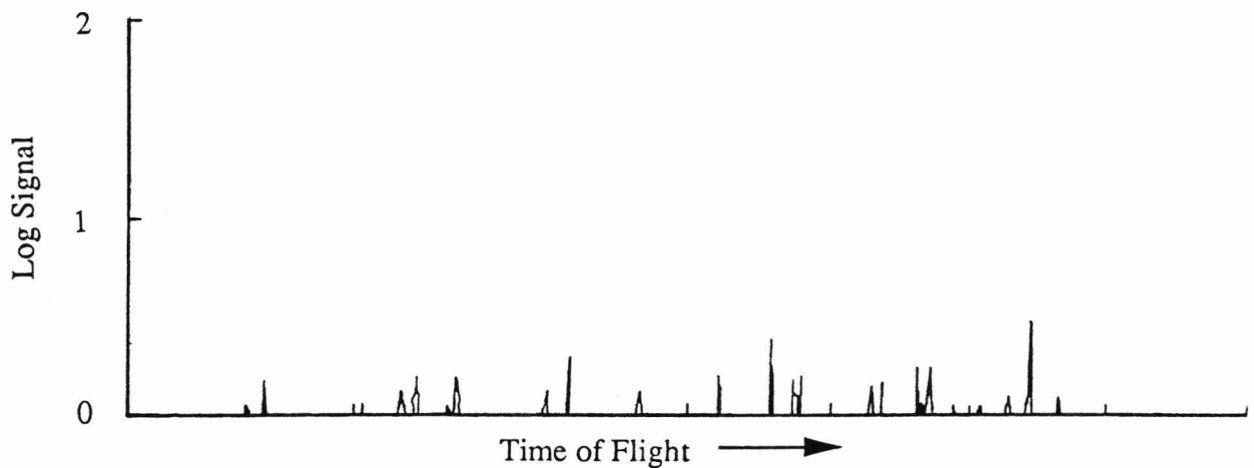


Figure 6.5: An example of a 'background' mass spectrum from PIA. The measuring cycle was triggered by an output of the most sensitive comparator connected to the photomultiplier. There appears to be no correlation between the lines in the spectra and either the position of lines from correctly triggered spectra or the other lines within the 'background' spectrum itself.

launch data was available so it was not possible to determine the absolute sensitivities, however, a qualitative result could be obtained by examination of the relative number of triggers caused by each front end channel , comparator combination. Initial investigation was limited to those events which were triggered by a single channel, (target, accelerator or photomultiplier) in the pre-encounter period -4200s to -1000s from closest approach this represents 99% of all events during this time. The results are shown in the first section of table 6.5. Over 98% of the single channel events were from the $\times 1$ comparator attached to the photomultiplier. Of course this would not be unreasonable if the photomultiplier channel was much more sensitive than the other channels. The study was then extended to include the double and triple channel triggers within this period. These results, Table 6.5, give a contradictory result to the single trigger analysis, for example, in the double channel case most events are detected by the $\times 1$ accelerator and $\times 1$ target channel combination indicating that both these channels were more sensitive than the photomultiplier and even the $\times 100$ accelerator, $\times 100$ target

combination detected more events than any combination which included the photomultiplier. A similar conclusion is reached from the triple channel events.

CO-IN	SEN	PM	TG	AC	FRACTION
1	HIGH	× 1	--	--	0.981
1	HIGH	--	× 1	--	0.011
1	HIGH	--	--	× 1	0.008
2	HIGH	--	× 1	× 1	0.368
2	HIGH	--	× 10	× 10	0.474
2	HIGH	--	× 1	× 10	0.105
2	HIGH	--	× 10	× 100	0.053
3	HIGH	× 1	× 10	× 100	0.300
3	HIGH	× 1	× 100	× 100	0.300
3	HIGH	× 100	× 100	× 100	0.200
3	HIGH	× 10	× 100	× 100	0.100
3	HIGH	× 1	× 1	× 1	0.100

Table 6.5: The fraction of triggers from each combination of discriminators for data taken during the period -4200s to -1000s. Data is shown separately for each of the three coincidence mode. Notice how in coincidence mode 1 the photomultiplier (PM) is the most frequently triggered while in the higher coincidence modes the target (TG) and acceleration grid (AC) channels seem to be more sensitive. The experiment remained in high sensitivity for the whole of this period hence the absence of any data in low sensitivity.

This combined with the 'good' spectra obtained from the coincidence events must lead to the suspicion that the single channel triggers caused by the × 1 photomultiplier output are the result of noise.

The two most likely sources of noise were either interference in the electronics or photometer itself, or alternatively it could be due to stray light. The latter could be checked, since any stray light effect would be related to the

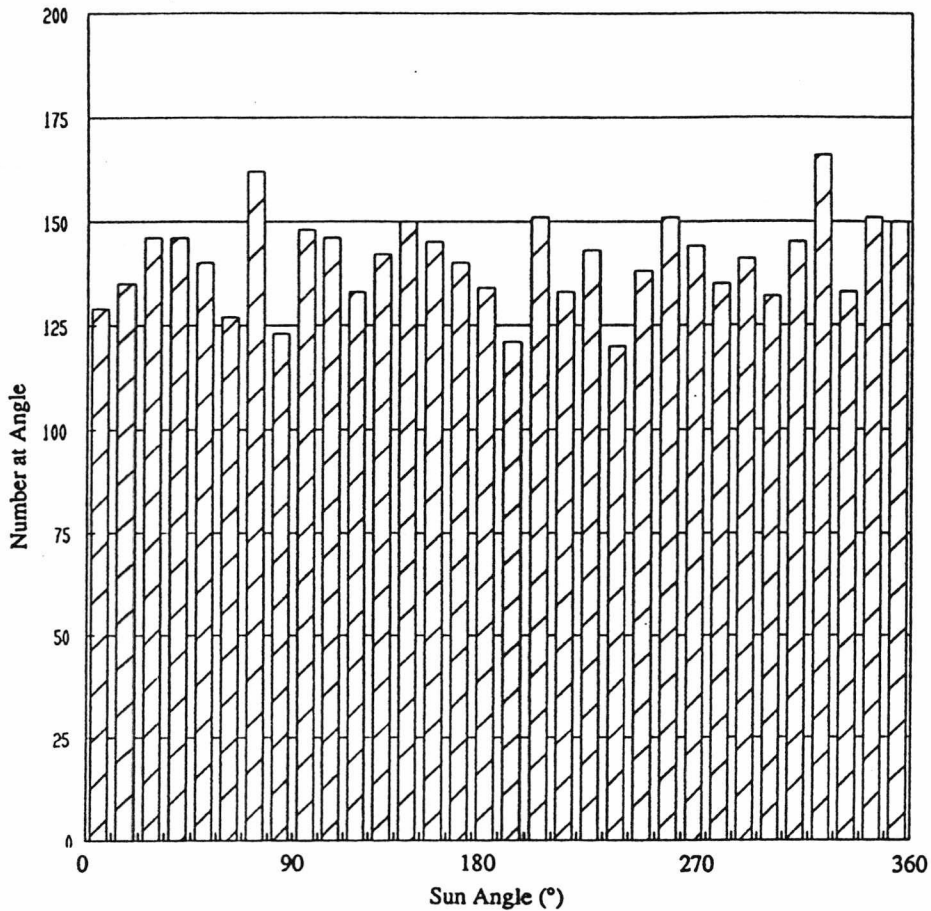


Figure 6.6: A histogram showing the variation in the number of $\times 1$ photomultiplier triggers with spacecraft solar aspect angle. No single angle predominates the distribution indicating that stray light is not the cause of these events.

rotation of the spacecraft and would appear preferentially for a particular rotation angle. Figure 6.6 shows a histogram of the number of single trigger events for a range of solar aspect angles. Although there is slight evidence for preferential angles, this is small and it would appear that the majority of the triggers during this period cannot be attributed to stray light. The background rate does not seem to vary significantly with time, having an average value of 3 counts per second which only affects the IMPR counter and then only when the experiment is in high sensitivity mode, the upper discriminator outputs are unaffected by the noise.

CO-IN	SEN	PM	TG	AC	FRACTION
1	LOW	--	×1	--	0.244
1	LOW	--	--	×1	0.659
1	LOW	×1	--	--	0.073
1	LOW	--	--	×10	0.024
1	HIGH	×1	--	--	0.855
1	HIGH	--	--	×1	0.118
1	HIGH	--	×1	--	0.017
1	HIGH	--	×10	--	0.007
1	HIGH	×10	--	--	0.002
2	LOW	--	×1	×1	0.535
2	LOW	--	×10	×10	0.406
2	LOW	--	×1	×10	0.032
2	LOW	--	×10	×1	0.019
2	LOW	--	×100	×10	0.006
2	LOW	--	×100	×100	0.002
2	HIGH	--	×1	×1	0.349
2	HIGH	--	×10	×10	0.316
2	HIGH	--	×1	×10	0.223
2	HIGH	--	×10	×100	0.063
2	HIGH	--	×100	×100	0.030
2	HIGH	--	×1	×100	0.004
2	HIGH	--	×100	×1	0.004
2	HIGH	--	×100	×10	0.004
2	HIGH	×1	×1	--	0.004
2	HIGH	×100	--	×1	0.004
3	LOW	×1	×100	×100	0.447
3	LOW	×1	×10	×10	0.304
3	LOW	×1	×100	×10	0.145
3	LOW	×10	×100	×100	0.094
3	LOW	×1	×1	×1	0.002
3	LOW	×1	×10	×1	0.002
3	HIGH	×10	×100	×100	0.390
3	HIGH	×1	×100	×100	0.333
3	HIGH	×100	×100	×100	0.209
3	HIGH	×1	×10	×100	0.038
3	HIGH	×1	×10	×10	0.014
3	HIGH	×1	×1	×10	0.011
3	HIGH	×10	×10	×100	0.004
3	HIGH	×10	×1	×1	0.001
3	HIGH	×10	×1	×10	0.001

Table 6.6: The fraction of triggers from each combination of discriminators for data taken during the period -300s to 300s. Data is shown separately for each of the three coincidence modes and for high and low sensitivity.

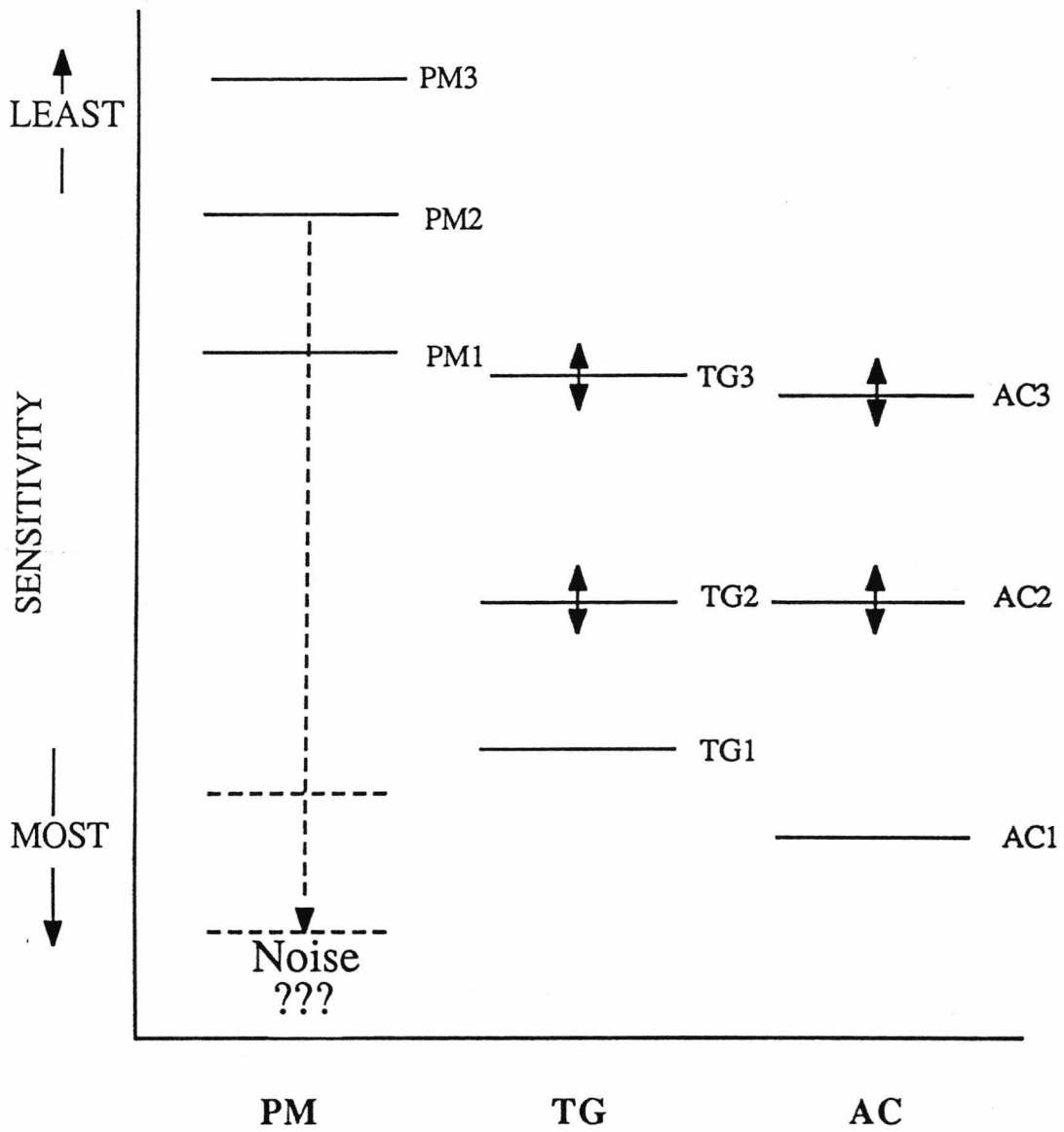


Figure 6.7: A possible solution for the relative sensitivities of the PIA front end channels to impacting grains. The target (TG) and accelerator grid (AC) are comparable in sensitivity, the output of the most sensitive comparator of the photomultiplier (PM1), is similar to the $\times 100$ comparator of TG and AC but is affected by noise.

The sensitivity analysis described above was further extended by considering the time from -300s to +300s. This covers the period when most of the coincidence and sensitivity mode switching took place. The higher impact rates would be expected to shift the ratio of single channel events as more real events were detected by the target and accelerator grid, relative to the constant noise level. Table 6.6 shows the fractional number of each type of trigger during this period, the photomultiplier rate in high sensitivity now being some 12% lower than in the -4200 to -1000 period, as expected. The remaining ratios were used to get a qualitative idea of the sensitivity of the channels relative to each other. Unfortunately the trigger levels on all of the front end channels are variable to some degree dependent on the output of the r.m.s. noise meter on each channel, so a unique solution cannot be derived. However, Figure 6.7 indicates one possible situation.

6.3.3 DEAD TIME EFFECTS

As with the whole of this analysis, the lack of calibration data has required that certain assumptions be made. While no absolute figure could be placed on the dead time of the front end channels, from consideration of the instrument operation the value was expected to exceed 1ms (J.Kissel, personal communication, 1987). In an attempt to narrow down the possible range of values for the dead time, an examination was made of the flux rates near closest approach, where any effect and therefore correction would be greatest. The analysis involved looking at the effect of different dead times on the radial power law dependence of the flux data. Each PIA mode was considered separately, the complete data set over this period is shown in Figure 6.8 (-120s to closest approach) and Figure 6.9 (closest approach to +120s). The data is plotted on a log flux against log cometocentric distance scale for three values of

the dead time, τ_d , ranging from 1ms to 3.5ms, using the formula given in Equation 6.1.

$$N' = \frac{N}{1 - \frac{N\tau_d}{0.945}} \quad (6.1)$$

Where N is the uncorrected count rate, N' is the corrected value and τ_d is the dead time. The variation from a fixed radial power law is clear in the example of the 1ms dead time, compared to the 3.5ms case which was calculated to give the smallest deviation from a constant power law expression by using a least squares fit. Since the point at which the flux deviates from a constant power law is the same for both the IMPR and IMPRL channels which have different mass sensitivities, it is likely that the effect is instrumental rather than a physical effect of the coma. The true dead time value cannot easily be ascertained from an analysis of the in-flight data, where true variations from a constant power law relation might be misinterpreted, however, the analysis described above offers considerable weight to a dead time of the order of 3.5ms and this value has been used throughout the remaining analysis. It is possible that further calibration work with the flight spare model of the PIA experiment at Heidelberg may provide a more accurate answer.

6.3.4 MASS CALIBRATION

No detailed mass calibration for the front end channels was undertaken before launch. Initial attempts to calculate mass and density of particles from their spectra, which could then be related to the front end signals were unsuccessful resulting in very low densities. Work is still under way by the group at Heidelberg concerning the theory of ion production in hypervelocity impacts. In this section a method is described for the calculation of PIA relative

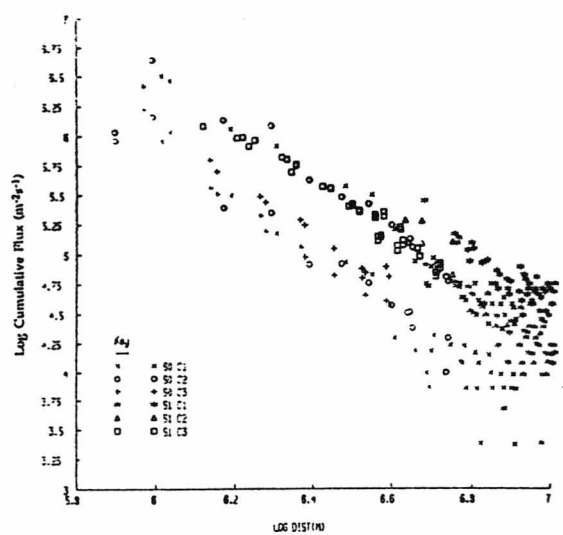
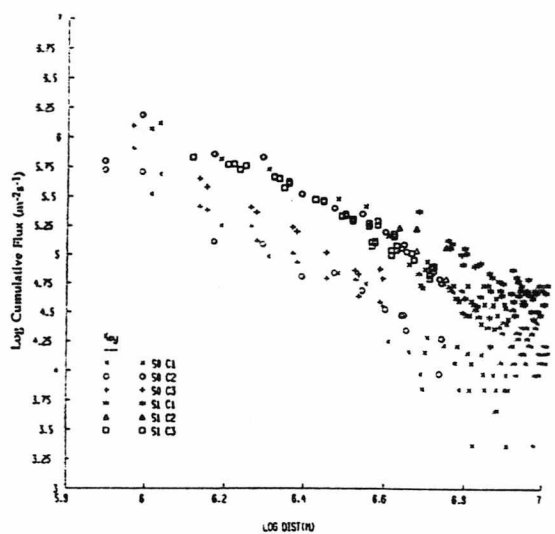
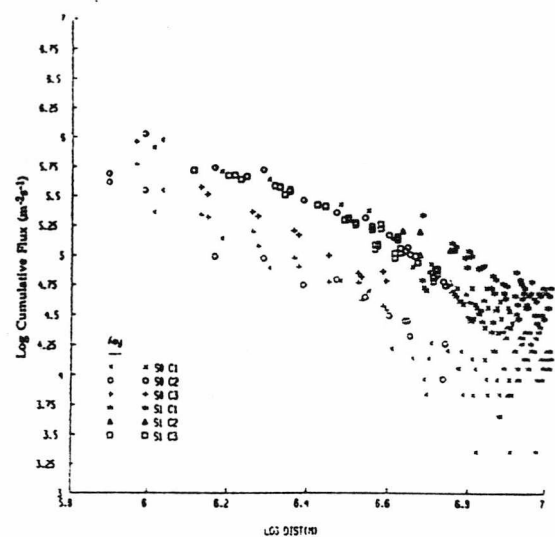


Figure 6.8: The effect of varying dead times on the PIA flux data from -120s to closest approach. This is shown for a) 1ms , b) 2ms and c) 3.5ms dead time.

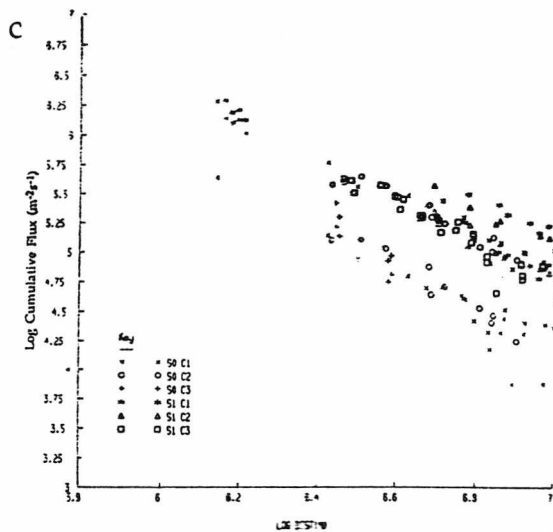
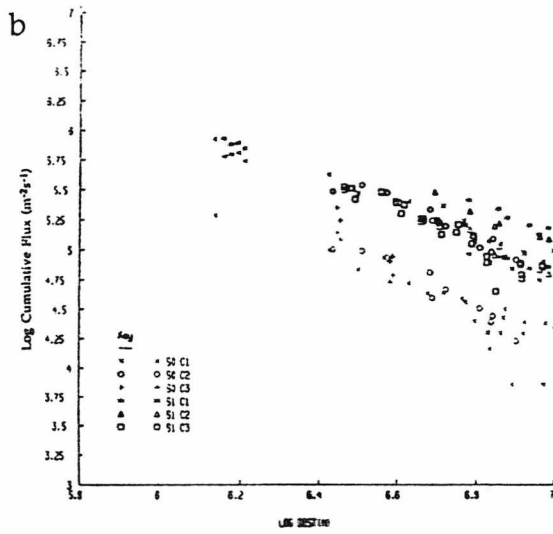
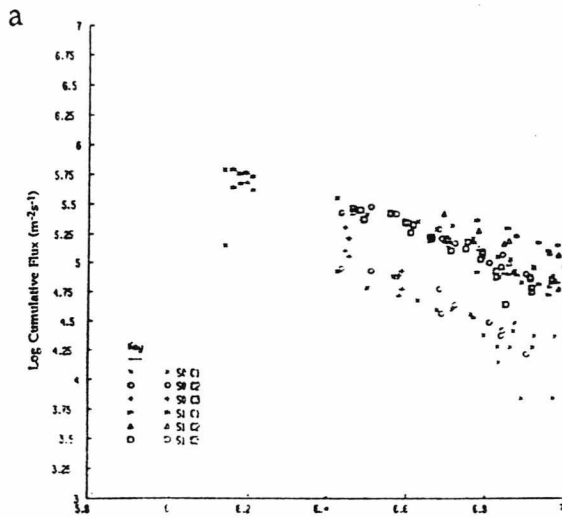


Figure 6.9: The effect of varying dead times on the PIA flux data from closest approach to +120s. This is shown for a) 1ms, b) 2ms and c) 3.5ms dead time.

mass thresholds with particular interest in the effect of changing channel sensitivity and co-incident requirements during the near encounter period, and possible systematic changes in sensitivity over encounter.

Using a dead time of 3.5ms results in two constant power law relations, one for pre and one for post encounter data. To determine the relative mass thresholds of all possible modes requires comparison of the flux rates obtained in each mode at some specific time. Since the experiment is only measuring in two of a possible twelve modes at any instance, the radial power law dependence is used to interpolate the data from modes not active at that time. Using the dead time specified above gives an average radial dependence for all modes of -2.3 pre- and -1.7 post-encounter. It is assumed that the output of the front end channels scales linearly with mass such that a change in the sensitivity mode which relates to a change in the gain of the front end channels by a factor of 100, results in a corresponding shift in the mass sensitivity by a similar factor. This is a reasonable assumption for the target and accelerator grid charge sensitive amplifiers, since the impact charge detected is almost directly proportional to mass (Section 2.3.3). The validity of this assumption for the light flash measured by the photomultiplier channel is less clear, however, the photomultiplier is the least sensitive of the front end channels (Section 6.3.2) and therefore its' importance is reduced. Using this assumption results in six pairs of data points, the individual data points in each pair being separated by a fixed relative mass. To determine the form of the mass distribution each of the data pairs are arranged in mass to produce a smooth continuous flux curve. This was achieved using a quadratic fit in log flux, log mass space (Equation 6.2). In theory a higher degree polynomial could have been used, however, due to computational constraints the quadratic was found most suitable.

$$A \log(m)^2 + B \log(m) + C = 0 \quad (6.2)$$

The mass of the centroid for each data pair was calculated, such that the flux was equal to that given by Equation 6.2, with an initial set of parameters based on the most sensitive point (highest flux) in the data set. A measure of the goodness of fit was then obtained from the sum of the squared deviation from the fit. The constants of the quadratic were varied independently and the data pairs re-aligned. The procedure was then repeated until the quadratic converged to the best fit solution at which point the relative masses of each of the data points was obtained from their final position. This method is shown schematically in Figure 6.10.

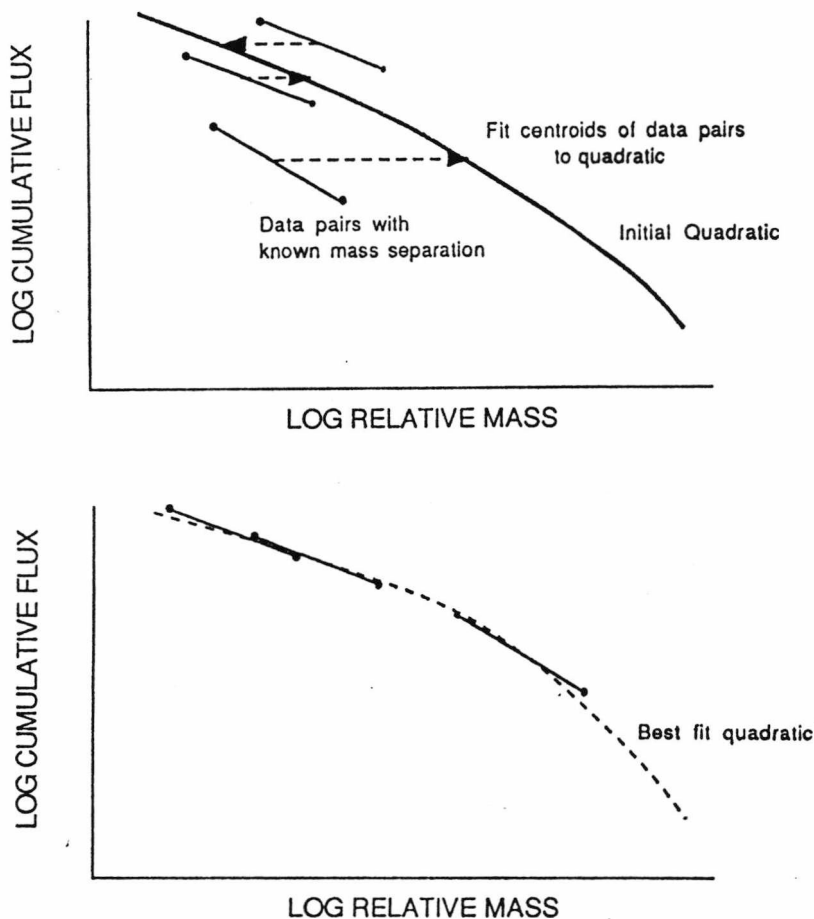


Figure 6.10: Schematic representation of the method used to obtain relative mass thresholds using pairs of data points with known relative sensitivities and fitting the best possible quadratic to the data.

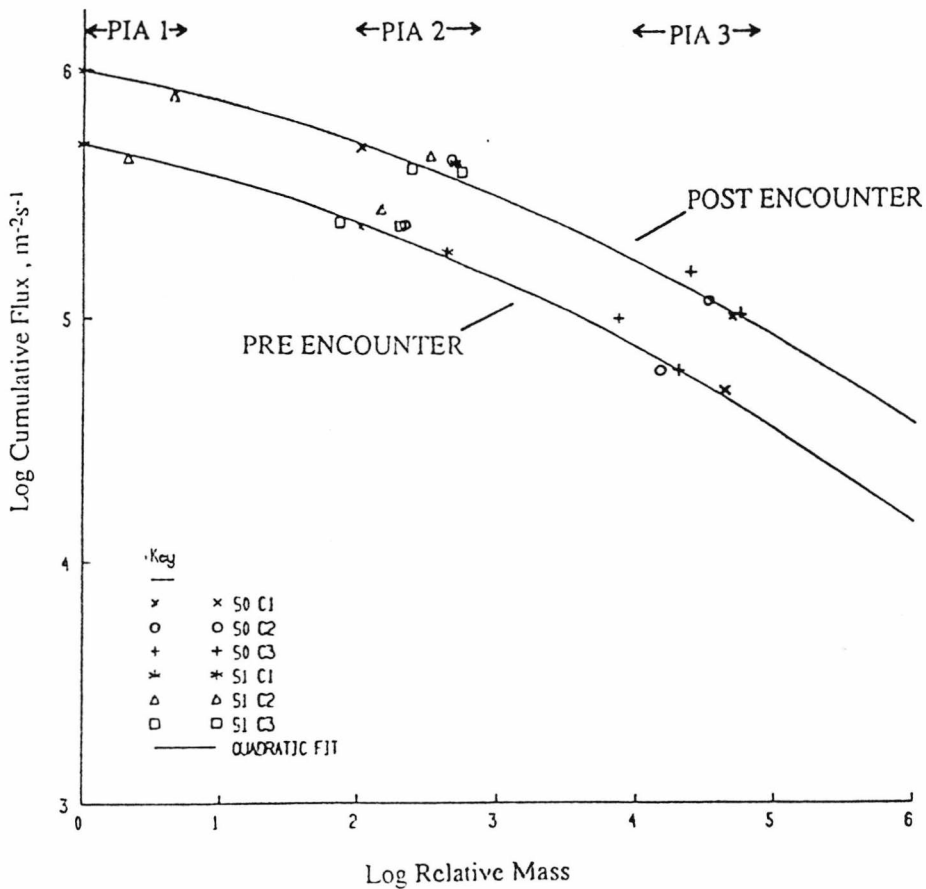


Figure 6.11: The pre and post encounter mass distributions derived from the PIA data assuming an absolute mass sensitivity for the most sensitive channel of 10^{-19}kg . The data can points can be divided into three groups with masses of $\text{PIA1}=5 \times 10^{-18}\text{kg}$, $\text{PIA2}=10^{-17}\text{kg}$ and $\text{PIA3}=5 \times 10^{-15}\text{kg}$

Using this method two distributions were obtained, one from the pre-encounter and one from the post encounter data, these are shown in Figure 6.11. If an absolute mass sensitivity of 10^{-19}kg is assumed for the most sensitive channel (J.Kissel , personal communication, 1987) then a set of absolute mass thresholds is obtained, Table 6.7.

In an attempt to look for major changes between the pre- and post-encounter mass thresholds obtained, the relative thresholds were plotted against each other, Figure 6.12. This shows a small but systematic decrease in sensitivity, although the errors involved in this analysis must be considered large this variation may indicate marginal damage or degrading of the target or front end channels during the high incident flux which must have been

Sensitivity mode	Coincidence mode	Counter	Log(Mass kg)	
			Pre-	Post-
HIGH	1	IMPR	-19.00	-19.00
HIGH	1	IMPRL	-16.39	-16.33
HIGH	2	IMPR	-18.65	-18.35
HIGH	2	IMPRL	-16.84	-16.51
HIGH	3	IMPR	-17.13	-16.64
HIGH	3	IMPRL	-16.70	-16.28
LOW	1	IMPR	-17.00	-17.00
LOW	1	IMPRL	-14.39	-14.33
LOW	2	IMPR	-16.65	-16.35
LOW	2	IMPRL	-14.88	-14.51
LOW	3	IMPR	-15.13	-14.64
LOW	3	IMPRL	-14.70	-14.28

Table 6.7: The absolute mass sensitivities of each of the twelve counter, coincidence, sensitivity combinations (see text).

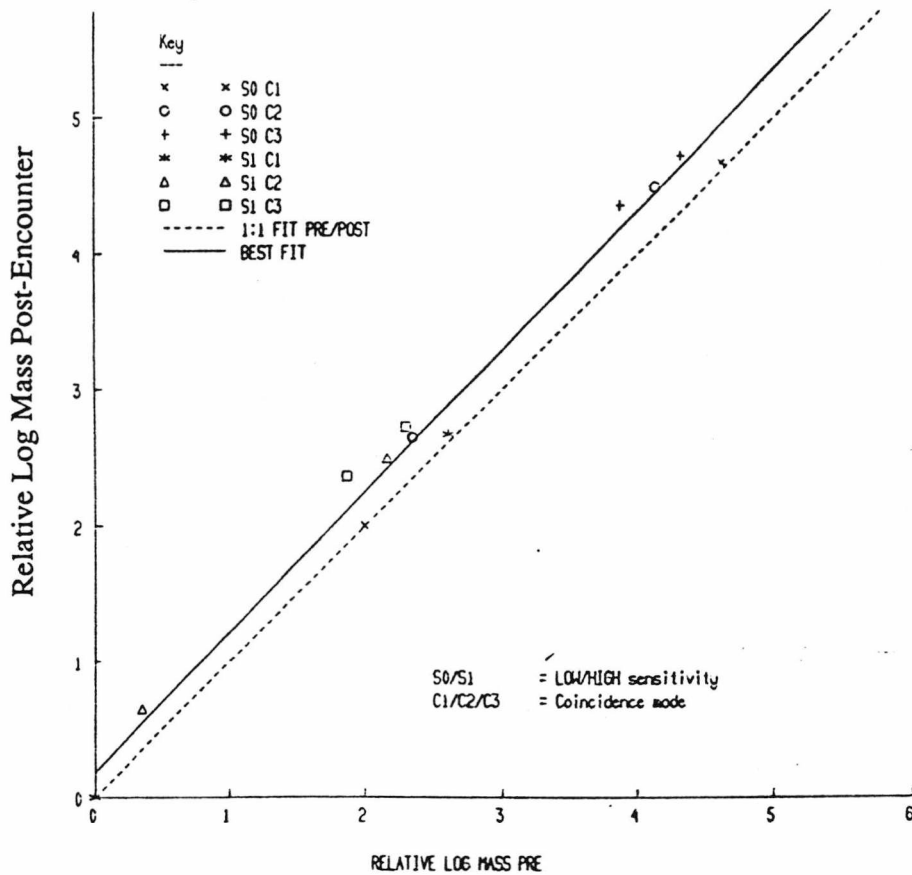


Figure 6.12: The correlation between the derived mass thresholds for the pre and post encounter data.

incident on the detector during the period of missing telemetry at closest approach.

Due to the possible errors involved and to try and improve the overall quality of the data, the mass points have been grouped together to reduce the twelve co-incident, sensitivity and counter combinations down to just three. This was possible due to the relatively close grouping of the data points. These three groupings are shown in Figure 6.11 and have average mass thresholds of 5×10^{-18} kg, 10^{-17} kg and 5×10^{-15} kg, and will be referred to as the PIA1, PIA2 and PIA3 channels. The error on these mass thresholds is considered to be of the same order as the spread of the data points which is about \pm half an order of magnitude.

6.4 PIA FLUX RATES

Using the calibration data described in the previous sections of this chapter it has been possible to obtain absolute flux levels using the impact rates from the front end channels. These results are presented here and are used elsewhere for the calculation of the mass distributions down to masses of 10^{-19} kg. Due to the mode changes only the PIA1 and PIA2 channels are available for the majority of the encounter period, the third less sensitive channel (PIA3) only being active during the high flux rate regime of the near encounter period.

Figures 6.13 to 6.24 show the PIA flux rates, plotted against time, during the near encounter period from -300s to +300s for each of the twelve different modes. Figure 6.25 shows the 180s time averaged flux for the most sensitive channel from -4200s to +4000s. Finally, Figure 6.26 shows the three combined channels (PIA1, PIA2, PIA3) for the -300s to +300s period together with the DIDSY results at two masses, the data is smoothed using a 10 point running mean.

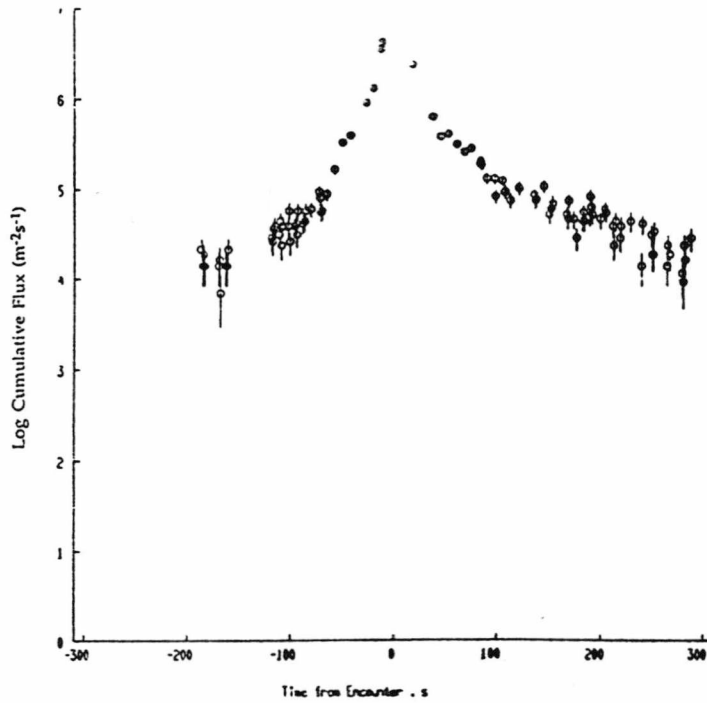


Figure 6.13: PIA flux rates for the period -300s to +300s from closest approach. The fluxes were recorded in LOW sensitivity mode on the IMPR counter and in coincidence mode 1.

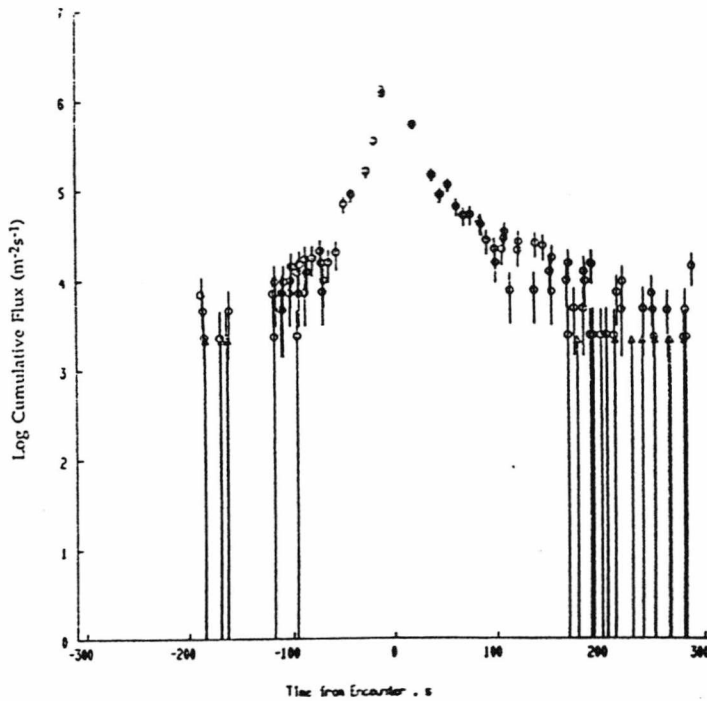


Figure 6.14: PIA flux rates for the period -300s to +300s from closest approach. The fluxes were recorded in LOW sensitivity mode on the IMPRL counter and in coincidence mode 1.

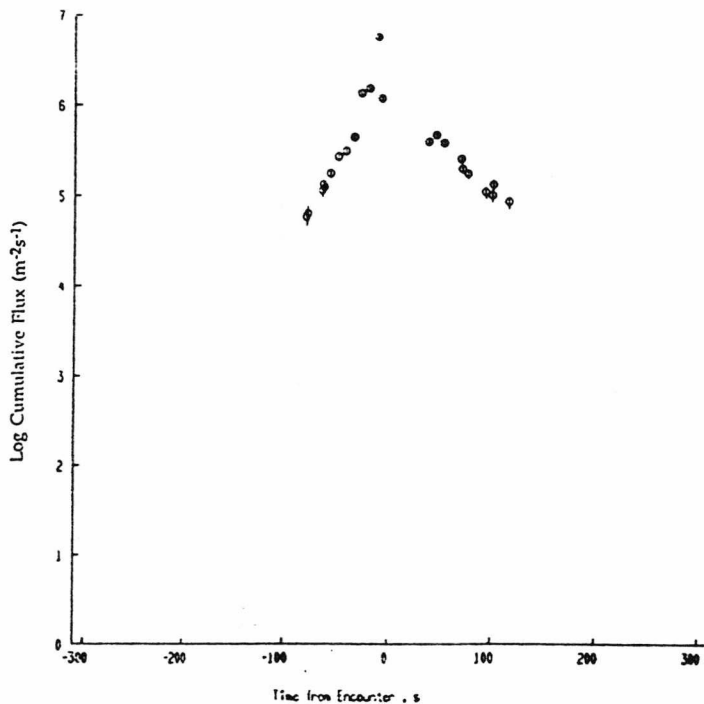


Figure 6.15: PIA flux rates for the period -300s to +300s from closest approach. The fluxes were recorded in LOW sensitivity mode on the IMPR counter and in coincidence mode 2.

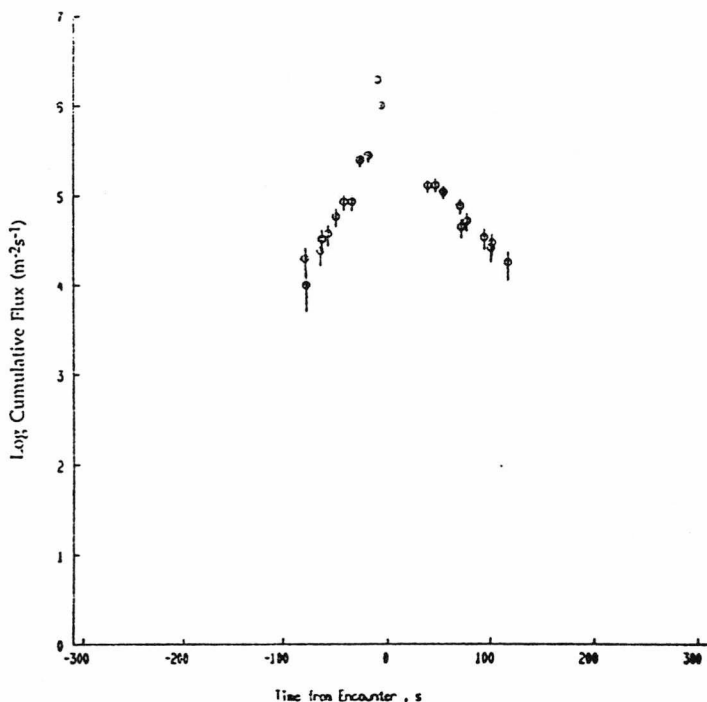


Figure 6.16: PIA flux rates for the period -300s to +300s from closest approach. The fluxes were recorded in LOW sensitivity mode on the IMPRL counter and in coincidence mode 2.

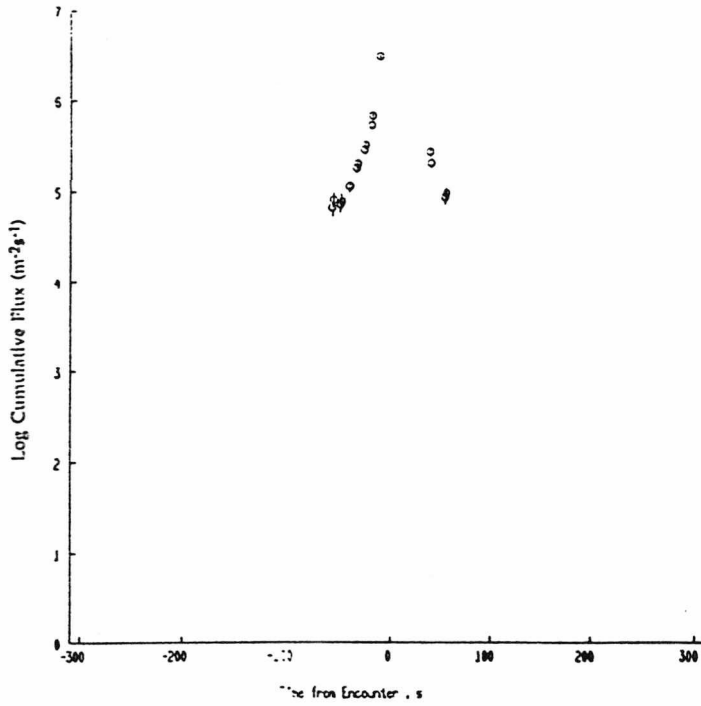


Figure 6.17: PIA flux rates for the period -300s to +300s from closest approach. The fluxes were recorded in LOW sensitivity mode on the IMPR counter and in coincidence mode 3.

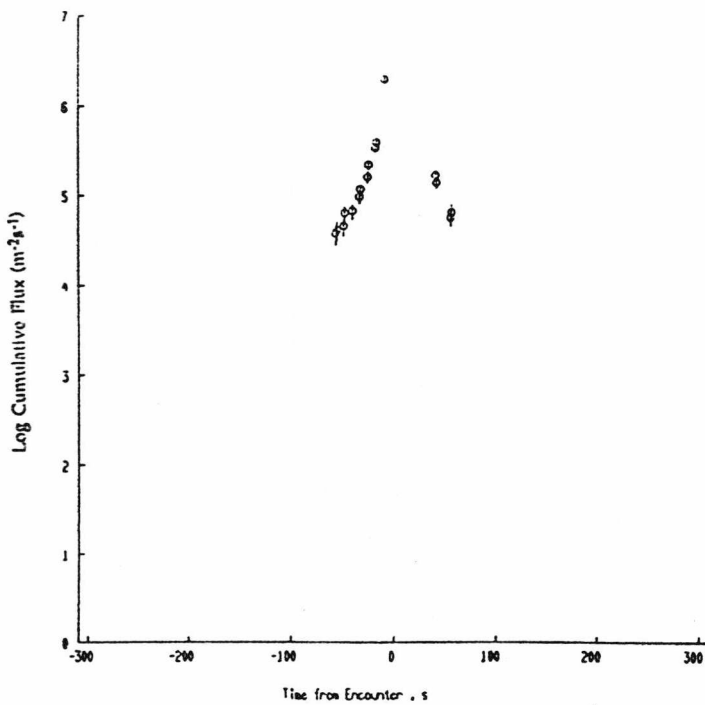


Figure 6.18: PIA flux rates for the period -300s to +300s from closest approach. The fluxes were recorded in LOW sensitivity mode on the IMPRL counter and in coincidence mode 3.

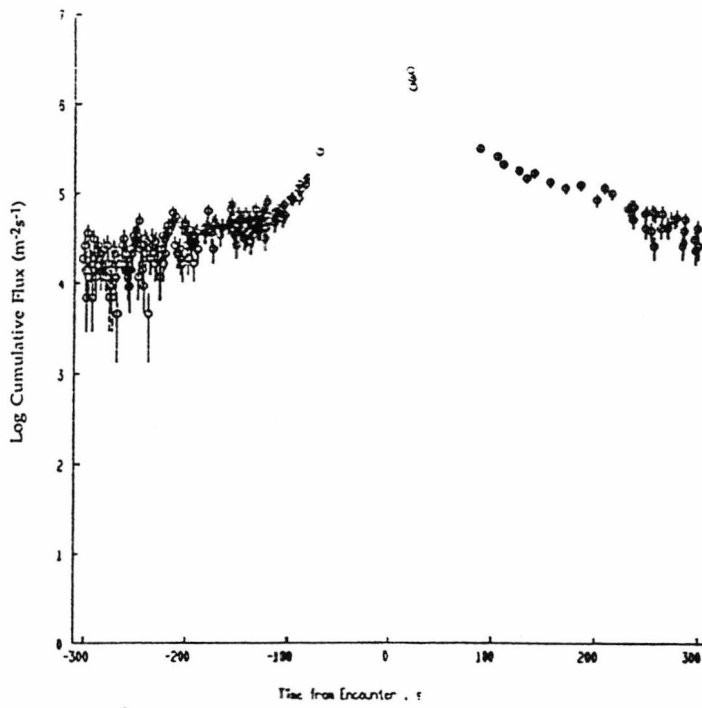


Figure 6.19: PIA flux rates for the period -300s to +300s from closest approach. The fluxes were recorded in HIGH sensitivity mode on the IMPR counter and in coincidence mode 1.

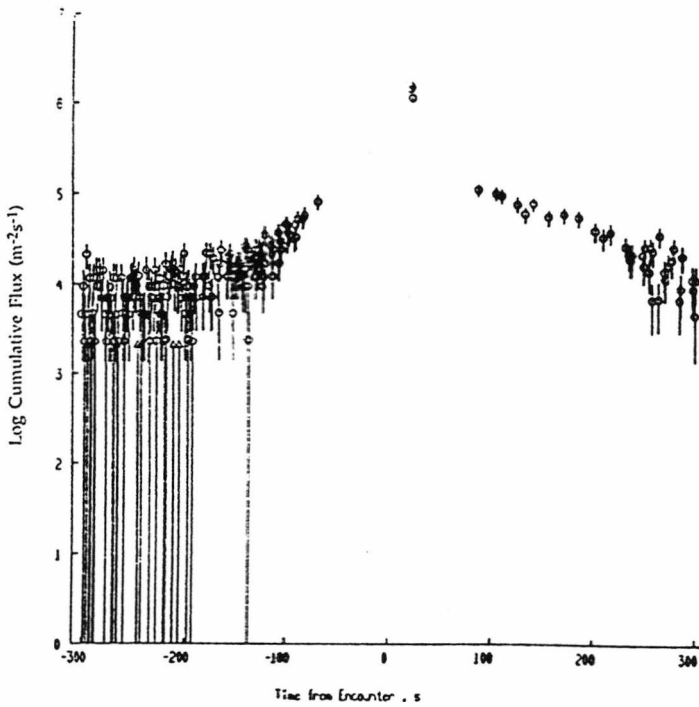


Figure 6.20: PIA flux rates for the period -300s to +300s from closest approach. The fluxes were recorded in HIGH sensitivity mode on the IMPRL counter and in coincidence mode 1.

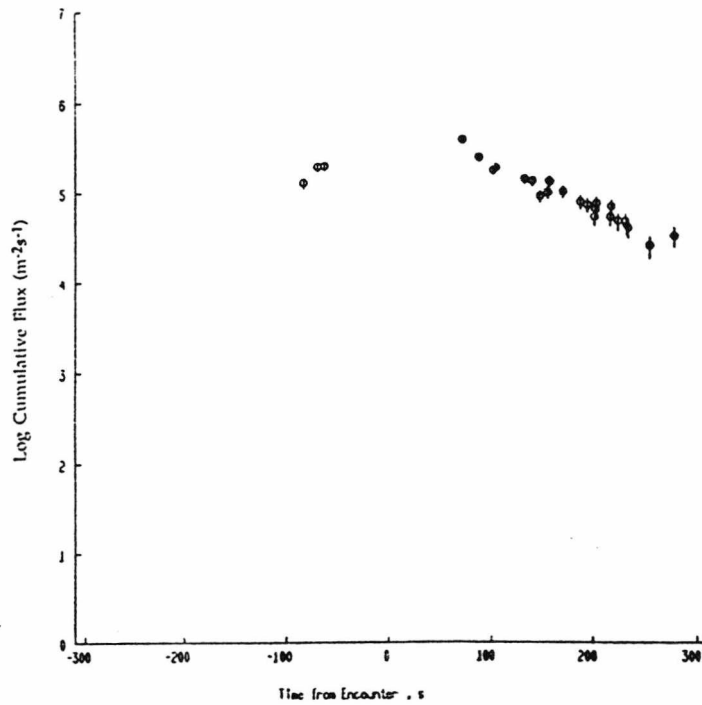


Figure 6.21: PIA flux rates for the period -300s to +300s from closest approach. The fluxes were recorded in HIGH sensitivity mode on the IMPR counter and in coincidence mode 2.

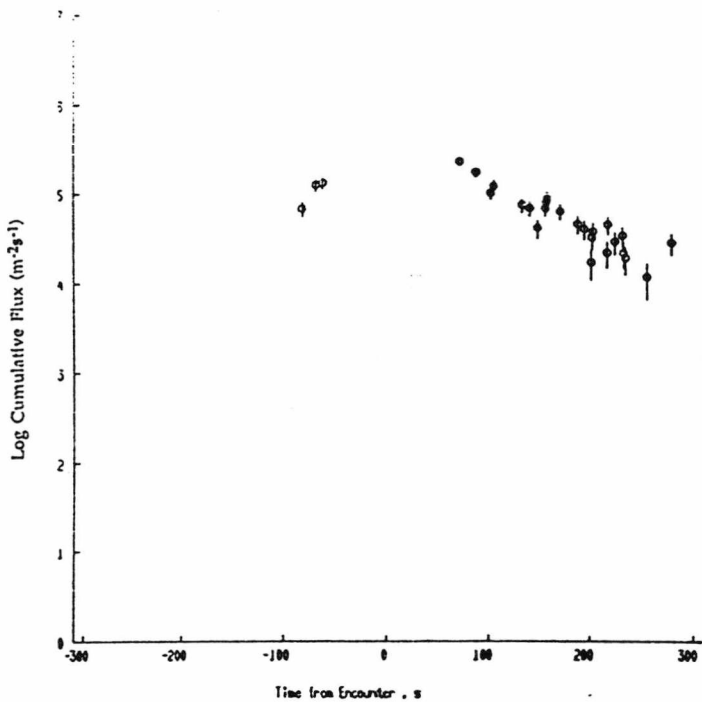


Figure 6.22: PIA flux rates for the period -300s to +300s from closest approach. The fluxes were recorded in HIGH sensitivity mode on the IMPRL counter and in coincidence mode 2.

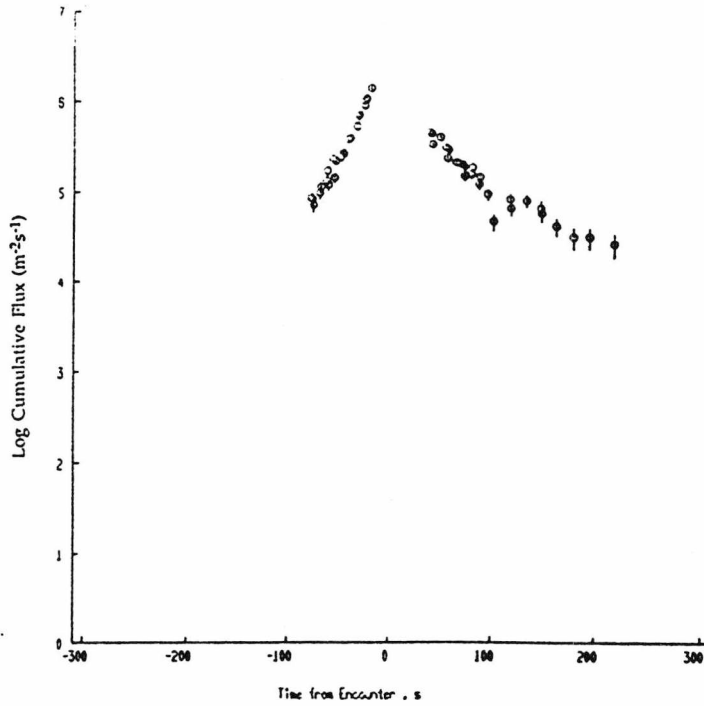


Figure 6.23: PIA flux rates for the period -300s to +300s from closest approach. The fluxes were recorded in HIGH sensitivity mode on the IMPR counter and in coincidence mode 3.

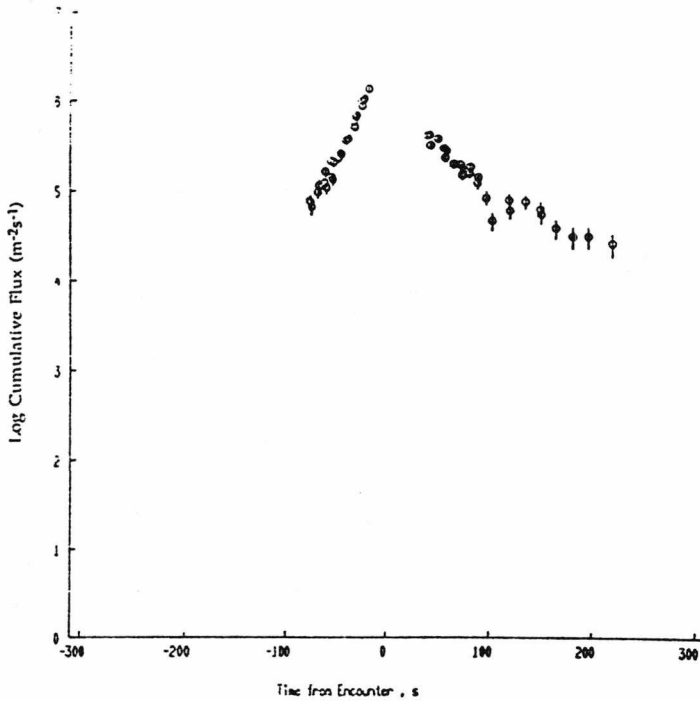


Figure 6.24: PIA flux rates for the period -300s to +300s from closest approach. The fluxes were recorded in HIGH sensitivity mode on the IMPRL counter and in coincidence mode 3.

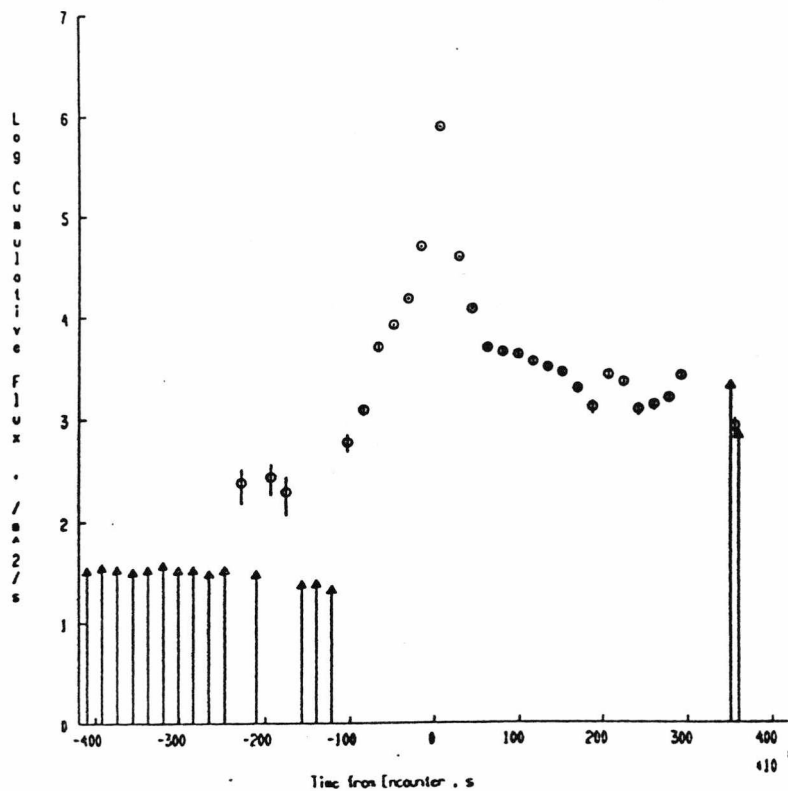


Figure 6.25: PIA flux rates for the period -4200s to +4000s from closest approach averaged over 180s intervals. The fluxes were recorded in HIGH sensitivity mode on the IMPR counter and in coincidence mode 1. The triangles represent upper limits.

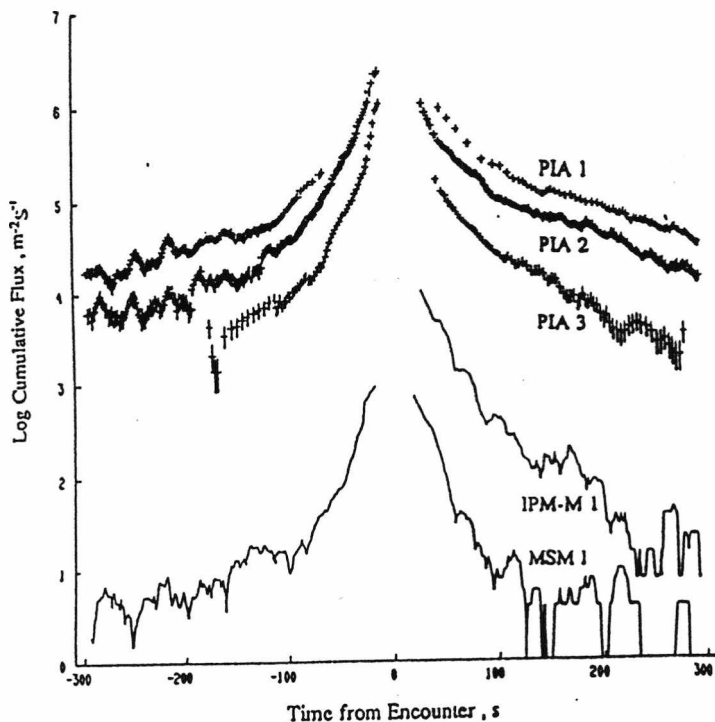


Figure 6.14: PIA flux rates for the period -300s to +300s from closest approach, using a 10 point running mean. The fluxes are shown for the PIA 1, PIA 2 and PIA 3 combined channels (see text) together with MSM and IPM-M data.

In all case the errors bars are given by \sqrt{N} of the counts and upper limits are shown as Δ . The $\pm 300s$ periods correspond to measurements out to a distance of $\sim 20500km$ and the $\pm 4000s$ period is corresponds to a distance out to $\sim 275000km$.

6.5 LIMITATIONS OF THE ANALYSIS

Once again it should be made clear that the front end channels were not designed for the quantitative measurement of the dust flux and had the DIDSY IPM-P sensor worked as intended such a detailed analysis of this data would not have been undertaken. Three major assumptions have been made in this analysis, they are:-

- i) That a simple dead time of 3.5ms correctly characterizes the operation of the experiment hardware/software.
- ii) That the sensitivity variation of the front end channels is approximately linear with mass.
- iii) That the limiting sensitivity of the most sensitive channel is $\sim 10^{-19}kg$.

The reasons for these assumptions have been described in the relevant sections and should, at sometime in the future, more accurate information become available it will be straight forward to make the appropriate adjustments. To represent the uncertainties involved the PIA fluxes used to calculate mass distributions have been assigned order of magnitude error bars both in mass and in flux.

CHAPTER 7

ANALYSIS OF THE DIDSY 'DISCRETE' DATA

'Discrete' data is the name given to the sub-set of DIDSY data which contains information on a selection of individual events (Section 2.3.4). All of the sub-systems with the exception of CIS (which only detects the number of events greater than its penetration mass) return some form of 'discrete' data. In the case of IPM-P, problems with the cover pre-encounter, and noisy operation post encounter prevent the use of pre-launch calibration data and analysis of this data set is not considered. The cover also affects the pre-encounter IPM-M data, since the relationship between the impacting particle, the debris formed as it passes through the cover and the digital output recorded by the sub-system, is unknown. The analysis of the remaining data sets is described below.

7.1 IPM-M DISCRETE DATA ANALYSIS

The IPM-M 'discrete' data is, in principle, the simplest to interpret since the sensitivity across the target plate is considered to be constant (Section 3.3). The mass corresponding to a digital signal is therefore given by Equation 2.1 where the momentum p is determined from the measured sensor output voltage $V(D_v)$ and the absolute sensor sensitivity S . Rearranging Equation 2.1 and making the substitution for p , gives Equation 7.1.

$$m = \frac{V(D_v)}{S \epsilon v} \quad (7.1)$$

Where D_v is the digital amplitude from the discrete data and V is the experiment transfer function described in Section 3.2. The values of S , ϵ and v are constant resulting in a mass relationship which is only dependent on the observed digital value.

Telemetry constraints meant that data on only one IPM-M discrete could be returned in each data gathering interval. For simplicity and to avoid

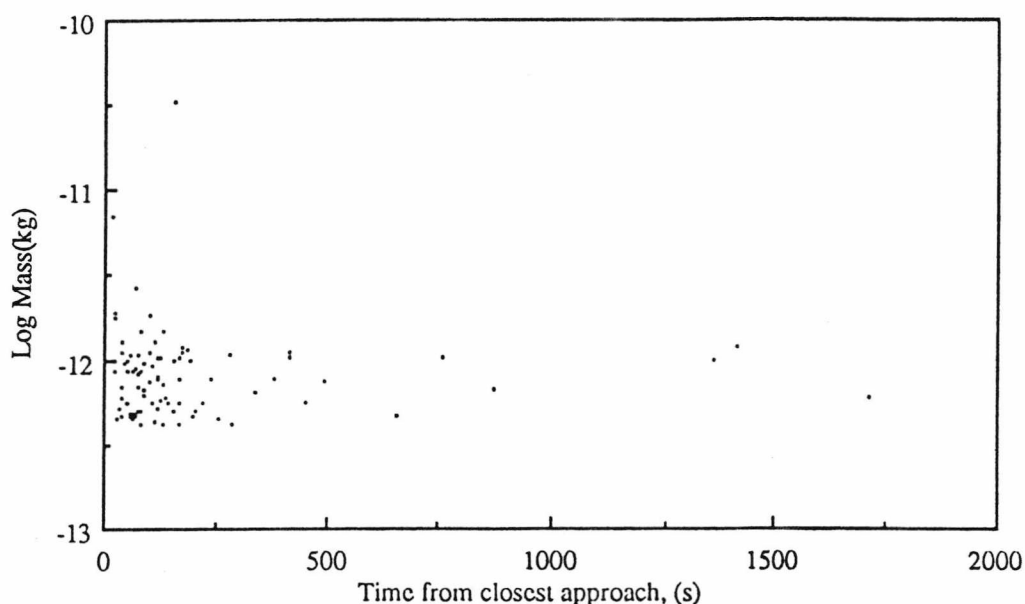


Figure 7.1: Scatter plot showing the mass of individual IPM-M impacts as a function of time. Events have only been plotted for the post-encounter period and then only if the 'pre-event' value was equal to zero.

selection effects, the event transmitted was the last event to be detected in the DGI. If no event occurred a zero amplitude was returned. In addition to the event amplitude, information on the sensor output level just prior to the event was also recorded. This 'pre-event' value is useful for diagnostic purposes, for example checking that the 'event' amplitude exceeds the 'pre-event' value.

An initial analysis of the IPM-M discrete data was presented in Evans, 1988. However, at that time it was assumed that DGIs which contained zero amplitude 'discrete' data but which had a non-zero count in the IPM-M PHA counters, were the result of marginal detections on the sensor. Subsequent work has shown that this is not the case and that the result can instead be attributed to an experimental effect which occurs during high activity on the IPM-P sensor (Section 5.4.2). A mass time scatter plot for the post-encounter period and for 'good' events is shown in Figure 7.1. Due to the problems

involving the DID 8 cover (pre-encounter) and the interaction between IPM-P and IPM-M (post-encounter) further analysis of this data set has not been attempted.

7.2 DID 4 DISCRETE DATA ANALYSIS

In Section 2.3.4 the method by which the DIDSY Central Data Formatter determines a category for MSM and RSM discrete data, based on sensor coincidence, was described. One of the category classes ('Category 4') contains events which are only detected by the DID 4 sensor. For an event to fall into this category the impact must occur on the acoustically isolated small sector of the front bumper shield. An impact elsewhere on the shield will always produce a signal on one of the other sensors and result in a different categorisation of the event. Since the exact position of the impact site within the small sector is unknown an average shield sensitivity, applicable over the whole sector, must be produced. This is done by calculating the mean, P' , of the shield sensitivity calibration data $P(i)$, weighted by the area of each calibration pixel $A(i)$ (Equation 7.2)

$$P' = \frac{\sum_{i = \text{small sector}} P(i) A(i)}{\sum_{i = \text{small sector}} A(i)} \quad (7.2)$$

Substituting P' for $P(i)$ in Equation 3.7 results in a mass relationship (Equation 7.3) which, as with the IPM-M 'discrete' data, is only dependent on the digital amplitude D_v returned by the experiment.

$$m = \frac{V(n) P_s}{\epsilon S v P'} \quad (7.3)$$

The effect of using a mean sensitivity is that the error in the calculated mass for any individual event is of the same order as the variation in the sensitivity. This is the same effect that applies to individual 'binned' data and is due to the ambiguity between the signal obtained from an impact at one position compared to a larger particle impacting at a position with lower relative sensitivity. Note that this is only important if an individual, or a small number of particles is being considered, in larger samples the errors of the individual events will tend to cancel. The ground receive time and mass of each 'Category 4' event over the whole encounter period are listed in Appendix 3.

By considering data over an extended time period a cumulative dust mass distribution in the range $10^{-11}\text{kg} \leq m \leq 10^{-9}\text{kg}$ can be produced. To obtain an absolute rather than relative measurement some correction must be made for the under-sampling of the discrete data. Although 'discrete' data on only one 'Category 4' event is produced per DGI, a counter which records the total number of such events per DGI is also maintained. If the shape of the mass distribution is assumed to remain constant over the period in question, a single multiplication factor k which applies at all masses is given by Equation 7.4.

$$k = \frac{\text{Number of 'category 4' events}}{\text{Number of 'discrete' data values}} \quad (7.4)$$

The use of a weighted mean sensitivity takes account of the effective area function which would otherwise be required and instead an area corresponding to the geometric area of the small sector of 0.18m^2 is used. The resulting distribution cannot be directly compared with other cumulative data unless some adjustment is made for the missing data with $m > 10^{-9}\text{kg}$, which occurs due to events above this mass being detected by another sensor in addition to DID 4 and being placed in a different category. In this analysis the missing data

is accounted for by using a calibration point derived from the DID 4 'binned' data which is cumulative.

Due to problems with the categorisation of events at high flux rates (Section 5.4) the calculation of fluence distributions is restricted to periods outside the range -42s to +40s from closest approach. Calculation of the total encounter fluence is achieved by extrapolation of the pre-encounter fluence up to -42s from closest approach and the post-encounter fluence from +40s relative to closest approach. Since insufficient discrete data is available to accurately define the radial trends required for this extrapolation, two multiplication factors (one for the pre- and one for the post-encounter fluences) have been calculated based on the radial dependence of the DID 4 binned data; both factors have been calculated to have a value of ~ 14 (S.F. Green, personal communication, 1989). The resulting DID 4 cumulative mass fluences for the periods -5064s to -42s and +40s to +3640s from to closest approach and for the total fluence over the whole encounter period, are shown as dotted lines in Figures 7.5, 7.6 and 7.7 respectively.

7.3 MULTI-SENSOR DISCRETE DATA ANALYSIS

The multi-sensor 'discrete' events represent a sub-set of the MSM 'discrete' data which only includes those events that are detected by two or more sensors. Such events are produced by particles with mass $m \geq 10^{-10}\text{kg}$, impacting at a position on the front shield where the bending wave induced by the impact can propagate to at least two sensors and still be detected. Particles with mass $m \geq 10^{-8}\text{kg}$ will result in multiple detection no matter where on the shield the impact occurs. A description of the categorisation process for the MSM data was given in section 2.3.4 and shows that all of the five categories with the exception of 'category 4' (see Section 7.2) can contain data from a multi-sensor event.

The method used to analyse multi-sensor events is similar to that described for the IPM-M and DID 4 'discrete' data. However, in this case it is not appropriate to calculate an average shield sensitivity, since the variation in sensitivity over the whole shield is very large (Section 3.3). Instead, the ratio of signals from two sensors is used to determine an approximate position for the event, and the sensitivity from this position used to calculate the mass. In the case of detection by two sensors there is only a single ratio, while detection by all three MSM sensors results in three ratios. In addition a signal from the rear shield microphone (RSM) is used to indicate that the impact occurred on the small sector. To obtain an impact position, the ratio of signals is compared to the ratio of corresponding shield sensitivities taken at each of calibration points around the shield. A fit parameter $K(i)$ being calculated for each calibration position, i . The location at which the best match between event and calibration ratios is obtained, indicated by the smallest value of $K(i)$, is taken to be the impact position. The shield sensitivity calibration data is far from smooth (see Section 3.3) and in the case of detection on only two sensors in particular, there can be some level of ambiguity as to the location of the most probable impact position. This problem is countered to some extent by using the null value on the remaining sensor as an anti-coincidence signal, to indicate the region of the shield where the impact is un-likely to have occurred. Equation 7.5 shows the definition of $K(i)$ for an event detected by DID 2 and DID 3 but not DID 4.

$$K(i) = \left[\left(\frac{V_2(D_2)}{V_3(D_3)} - \frac{P_2(i)}{P_3(i)} \right)^2 + F_4(i)^2 \right] F_5(D_5, i) \quad (7.5)$$

Where $V_2(D_2)$ and $V_3(D_3)$ are the sensor signals corresponding to the digital amplitudes D_2 and D_3 on DID 2 and DID 3 respectively. $P_2(i)$ and $P_3(i)$ are the shield sensitivity values for a given calibration point, i . $F_4(i)$ is the anti-

coincidence parameter and $F_5(D_5, i)$ the DID 5 coincidence flag for a DID 5 digital amplitude of D_5 . To calculate a value for the anti-coincidence parameter the signals from one of the two detecting sensors is combined with the shield sensitivity data to calculate the signal that is expected on the non-detecting sensor if the position in question were the impact site. If the resulting signal is below the non-detecting sensor threshold then the anti-coincidence parameter is assigned a value of zero. If the signal is greater than the threshold, the anti-coincidence parameter is set to a value corresponding to the level above the threshold. The logic for the DID 5 coincidence flag $F_5(D_5, i)$ is somewhat simpler, it taking a value of 1 if either D_5 is equal to 0, or if D_5 is greater than 0 and the position of the calibration point i is within the small sector, and being set to a large number (10^{32}) otherwise. The definition for $K(i)$ in the case of detection by all three MSM sensors is shown in Equation 7.6.

$$K(i) = \left[\left(\frac{V_2(D_2)}{V_3(D_3)} - \frac{P_2(i)}{P_3(i)} \right)^2 + \left(\frac{V_2(D_2)}{V_4(D_4)} - \frac{P_2(i)}{P_4(i)} \right)^2 + \left(\frac{V_3(D_3)}{V_4(D_4)} - \frac{P_3(i)}{P_4(i)} \right)^2 \right] F_5(D_5, i) \quad (7.6)$$

The shield sensitivities corresponding to the approximate impact position obtained from this technique, are then used to calculate a particle mass. In addition to the sensor amplitudes, the MSM also returned a byte of information called the 'timing' word. It contains information on the order in which signals were detected, which is potentially useful in determining an impact position. However, even before launch, the 'timing' word was found to be unreliable and it has not been used in this analysis. Unlike the IPM-M and DID-4 'discrete' data, the masses of particles which produce detections may exceed the penetration mass m_{pen} of the 1mm aluminium front bumper shield. In such cases some of the particles momentum passes through the

shield and is not captured. This can be accounted for by the addition of a momentum derating term to Equation 3.7 (Wallis, 1986), Equation 7.7.

$$m = \frac{1}{\sqrt{1-\gamma}} \sqrt{\frac{V(D_v) P_s}{\epsilon S v P(i) m_{pen}^\gamma}} \quad (7.7)$$

Where γ is called the momentum derating factor and is assigned a nominal value of 0.67 (Wallis, 1986) and m_{pen} is the penetration mass limit for the front shield, taken to be 3×10^{-9} kg for this analysis (Section 2.3.1). The mass of a particle is first calculated with Equation 3.7 and then only if found to be greater than m_{pen} , is it recalculated using the momentum derating factor.

A mass calculation is done for each of the sensors on which a signal is detected. In theory the mass obtained from each calculation should be identical. The comparison is generally good in the case of double sensor events (where position determination is only dependent on the comparison of a single ratio) and the resultant mass is taken to be the average of the two values. The same is not true of the triple detection events, where it is sometimes found that one of the three calculated masses is several orders of magnitude larger, or smaller than the other two values. This is caused by impacts which occur at a position corresponding to the trough in one of the shield sensitivity maps. The ratio of the shield sensitivity at the sensor to that at the impact site, $P_s/P(i)$, becomes very large for that sensor, which, when combined with small errors and digitisation effects, results in the observed discrepancy in the calculated masses. In such cases the mass is rejected and an average of the remaining two masses is taken, otherwise the average of all three masses is used.

The positions and masses for each of the 100 multi-sensor discrete events for which data was returned are split into three time periods:-

- i) Experiment switch on to -43s (Table 7.1).

- ii) -42s to +39s from closest approach (Table 7.2). Data from this period is considered less reliable due to the possibility, at high flux rates, of multiple single events being seen by the CDF as single multi-sensor events. The period from -42s to closest approach has the additional problem of categorisation discussed in Section 5.4, which prevents calculation of an absolute fluence level.
- iii) +40s to experiment switch off (Table 7.3)

Masses are listed for $\gamma = 0.67, 0.4$ and 0.0 representing the nominal, preferred and 'no derating' cases respectively (see Section 7.4). Where not explicitly stated, the preferred value of $\gamma = 0.4$ has been used for subsequent calculations. The location on the front shield of events from all three periods is shown in Figure 7.2. Due to the shape of the shield calibration data, which has similar sensitivities at the inner and outer edges, the determined radial distances at angular positions some distance from a sensor are unreliable.

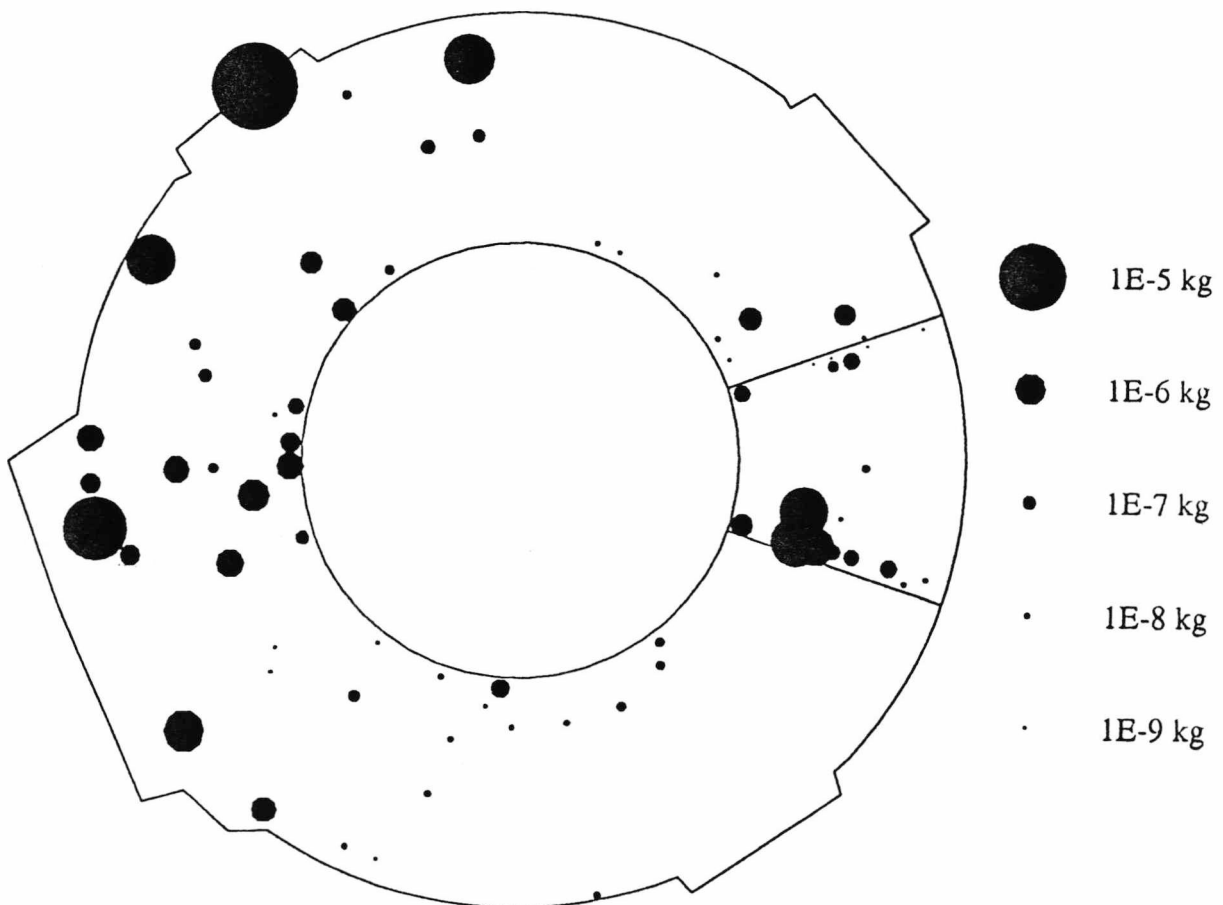


Figure 7.2: Locations on the Giotto front bumper shield determined for each of the MSM multi-sensor 'discrete' data events observed during the encounter.

Time (s) from c.a.	Block No.	Angle (°)	Rad. Dist (m)	Mass associated with event (kg)		
				$\gamma=0.0$	$\gamma=0.4$	$\gamma=0.67$
-2595	41173	109.5	0.48	6.2E-09	1.0E-08	2.8E-08
-1713	41951	184.5	0.48	4.7E-08	2.9E-07	1.2E-05
-1288	42326	16.5	0.48	5.3E-08	3.6E-07	1.8E-05
-1260	42351	342.0	0.68	2.1E-10	2.1E-10	2.1E-10
-1117	42477	171.0	0.90	1.6E-07	2.3E-06	5.6E-04
-655	42885	160.5	0.64	8.4E-08	7.7E-07	7.3E-05
-631	42906	178.5	0.48	7.8E-08	6.9E-07	5.9E-05
-569	42961	103.5	0.60	5.0E-09	7.0E-09	1.4E-08
-551	42977	142.5	0.64	1.4E-09	1.4E-09	1.4E-09
-434	43080	91.5	0.56	4.1E-09	5.2E-09	8.1E-09
-364	43142	183.0	0.90	4.5E-08	2.7E-07	1.1E-05
-281	43215	193.5	0.48	3.1E-08	1.5E-07	3.6E-06
-223	43266	223.5	0.60	5.6E-08	4.0E-07	2.2E-05
-216	43272	16.5	0.88	3.9E-09	4.8E-09	4.8E-09
-180	43304	16.5	0.64	1.1E-07	1.2E-06	1.7E-04
-170	43313	328.5	0.56	6.0E-08	4.4E-07	2.6E-05
-169	43314	18.0	0.48	2.0E-09	2.0E-09	2.0E-09
-156	43325	183.0	0.90	7.7E-08	6.7E-07	5.7E-05
-153	43328	220.5	0.48	6.5E-08	5.1E-07	3.4E-05
-135	43344	183.0	0.90	5.7E-08	4.1E-07	2.3E-05
-123	43354	141.0	0.90	3.6E-08	1.9E-07	5.7E-06
-114	43362	10.5	0.60	2.2E-07	3.8E-06	1.3E-03
-109	43367	114.0	0.88	5.0E-09	7.1E-09	1.4E-08
-103	43372	234.5	0.95	5.9E-07	2.0E-05	2.8E-02
-95	43379	79.5	0.92	8.0E-09	1.5E-08	6.0E-08
-78	43394	16.5	0.72	5.6E-09	8.7E-09	2.0E-08
-75	43397	160.5	0.48	2.1E-08	7.8E-08	1.1E-06
-75	43397	79.5	0.56	4.8E-09	6.6E-09	1.2E-08
-73	43398	126.0	0.90	6.7E-08	5.3E-07	3.6E-05
-72	43399	343.5	0.72	3.4E-08	1.7E-07	4.8E-06
-64	43406	328.5	0.48	1.7E-09	1.7E-09	1.7E-09
-59	43411	16.5	0.80	2.2E-08	8.7E-08	1.3E-06
-58	43412	141.0	0.90	1.6E-07	2.4E-06	5.7E-04
-53	43416	171.0	0.90	5.8E-08	4.2E-07	2.4E-05
-51	43418	16.5	0.60	2.3E-07	4.3E-06	1.6E-03
-50	43419	160.5	0.48	2.0E-08	7.2E-08	9.7E-07
-49	43420	336.0	0.74	5.3E-08	3.5E-07	1.8E-05
-46	43422	183.0	0.90	6.2E-08	4.7E-07	2.9E-05
-46	43422	342.0	0.76	1.0E-10	1.0E-10	1.0E-10
-45	43423	160.5	0.48	2.3E-08	9.1E-08	1.5E-06
-43	43425	171.0	0.90	1.6E-07	2.4E-06	5.7E-04

Table 7.1: Time, location and calculated mass for all MSM multi-sensor events in the period from experiment switch on to -43s from closest approach. Masses are shown for three values of the momentum derating factor, γ . Angles measured clockwise from DID 4.

Time (s) from c.a.	Block No.	Angle (°)	Rad. Dist (m)	Mass associated with event (kg)		
				$\gamma=0.0$	$\gamma=0.4$	$\gamma=0.67$
-34	43432	244.5	0.84	1.1E-08	3.0E-08	1.9E-07
-32	43434	262.5	0.84	2.2E-07	4.1E-06	1.5E-03
-30	43435	16.5	0.48	6.0E-09	9.7E-09	2.5E-08
-30	43435	139.5	0.68	1.7E-09	1.7E-09	1.7E-09
-29	43436	114.0	0.88	3.3E-09	3.5E-09	4.0E-09
-29	43436	223.5	0.60	2.8E-08	1.2E-07	2.7E-06
-29	43436	342.0	0.64	1.0E-10	1.0E-10	1.0E-10
-29	43436	127.5	0.48	2.0E-09	2.0E-09	2.0E-09
-26	43438	342.0	0.76	6.8E-11	6.8E-11	6.8E-11
-25	43439	334.5	0.48	7.8E-10	7.8E-10	7.8E-10
-21	43442	262.5	0.68	2.4E-08	6.8E-08	8.9E-07
-21	43442	195.0	0.68	2.3E-08	8.9E-08	1.4E-06
-20	43443	178.5	0.64	1.4E-08	4.1E-08	3.5E-07
-20	43443	16.5	0.64	1.4E-07	2.0E-06	4.2E-04
-19	43444	178.5	0.48	2.7E-08	1.2E-07	2.5E-06
-18	43445	18.0	0.48	1.1E-08	2.7E-08	1.6E-07
-18	43445	177.0	0.90	4.5E-08	2.8E-07	1.1E-05
-18	43445	16.5	0.68	2.6E-08	1.2E-07	3.1E-06
-18	43445	208.5	0.88	2.2E-07	4.0E-06	1.5E-03
-17	43446	342.0	0.76	7.7E-11	7.7E-11	7.7E-11
-17	43446	16.5	0.88	5.4E-09	4.6E-09	8.0E-09
-17	43446	16.5	0.72	3.0E-08	1.4E-07	3.3E-06
-17	43446	172.5	0.56	1.0E-07	1.1E-06	1.4E-04
-16	43448	235.5	0.48	1.3E-08	3.8E-08	3.1E-07
-16	43448	18.0	0.48	7.4E-10	7.4E-10	7.4E-10
-16	43448	16.5	0.68	8.7E-09	1.7E-08	7.6E-08
-16	43448	105.0	0.72	7.8E-09	1.4E-08	5.4E-08
18	43458	16.5	0.80	3.3E-08	1.6E-07	4.6E-06
18	43458	253.5	0.68	2.5E-08	1.0E-07	1.8E-06
20	43459	343.5	0.68	1.6E-08	5.0E-08	5.0E-07
20	43459	171.0	0.90	3.4E-07	8.2E-06	5.4E-03
21	43460	18.0	0.48	1.3E-09	1.3E-09	1.3E-09
21	43460	94.5	0.48	4.1E-08	2.3E-07	8.5E-06
22	43461	10.5	0.68	2.6E-09	2.6E-09	2.6E-09
22	43461	316.5	0.56	3.8E-09	4.6E-09	6.5E-09
25	43464	52.5	0.48	1.2E-08	3.2E-08	1.6E-07
25	43464	16.5	0.72	1.2E-09	1.2E-09	1.2E-09
29	43467	1.5	0.72	8.9E-09	1.8E-08	8.1E-08
32	43470	16.5	0.68	1.9E-09	1.9E-09	1.9E-09
35	43473	178.5	0.48	1.6E-08	5.0E-08	5.0E-07
35	43473	289.5	0.48	3.9E-09	4.7E-09	6.8E-09
39	43475	343.5	0.48	3.2E-08	1.5E-07	4.0E-06

Table 7.2: Time, location and calculated mass for all MSM multi-sensor events in the period from -42s to +39s from closest approach. Masses are shown for three values of the momentum derating factor, γ .

Time (s) from c.a.	Block No.	Angle (°)	Rad. Dist (m)	Mass associated with event (kg)		
				$\gamma=0.0$	$\gamma=0.4$	$\gamma=0.67$
40	43476	97.5	0.52	2.8E-09	2.8E-09	2.8E-09
41	43477	16.5	0.88	2.1E-09	2.1E-09	2.1E-09
43	43479	328.5	0.48	4.5E-09	5.9E-09	1.0E-08
44	43480	190.5	0.52	2.5E-09	2.5E-09	2.5E-09
51	43486	109.5	0.88	1.2E-09	1.2E-09	1.2E-09
53	43488	18.0	0.84	4.3E-09	5.6E-09	9.3E-09
67	43500	166.5	0.84	4.7E-08	3.0E-07	1.3E-05
68	43501	55.5	0.52	1.1E-08	2.7E-08	1.6E-07
93	43523	124.5	0.60	1.9E-08	6.6E-08	8.3E-07
106	43534	199.5	0.72	1.8E-08	5.9E-08	6.8E-07
108	43536	178.5	0.72	7.7E-08	6.7E-07	5.7E-05
112	43540	340.5	0.76	2.4E-09	2.4E-09	2.4E-09
172	43593	67.5	0.56	1.3E-08	3.6E-08	2.8E-07
216	43631	342.0	0.88	3.7E-10	3.7E-10	3.7E-10
354	43753	235.5	0.92	2.5E-08	1.0E-07	2.0E-06
393	43788	295.5	0.48	3.1E-09	3.3E-09	3.6E-09
469	43855	342.0	0.64	1.1E-10	1.1E-10	1.1E-10

Table 7.3: Time, location and calculated mass for all MSM multi-sensor events in the period from +40s to experiment switch off. Masses are shown for three values of the momentum derating factor, γ .

The 'discrete' data is a limited sample of all events detected by DIDSY and the multi-sensor events are only a sub-set of the whole MSM/RSM 'discrete' data. To obtain an absolute cumulative flux distribution from these events, a multiplication factor must be calculated which accounts for the under sampling. At large cometocentric distances where the count rate is low, information on all impacts is returned and the multiplication factor k is equal to unity. At higher count rates, k can only be accurately determined if data over a sufficiently long period to calculate the ratio between the number of multi-sensor events, to the number of single sensor events, in each category is used. In addition, the assumption must be made that the shape of the mass distribution does not change significantly within the time period. The value of k is given by Equation 7.8 where, N_c is the number of coincidence events in

category cat within the period and N_s the number of single sensor events. N_T is the total number of events within the category, obtained from the sum of the category counter (Section 2.3.4) over the period.

$$k = \frac{\sum_{cat=1}^5 \frac{N_T(cat) N_c(cat)}{N_s(cat) + N_c(cat)}}{\sum_{cat=1}^5 N_c(cat)} \quad (7.8)$$

An accurate value for k cannot be calculated for the period $-42s \leq t \leq 11s$ due to the operation of the CIS sub-system during this time (Section 5.4). When CIS activity is high, the CIS activity flag is almost continuously active which leads to all MSM events being assigned to 'Category 1'. The result of this is that 'Category 1' data is dominated by the more numerous single sensor events and there is insufficient data within the period to calculate an accurate value for the ratio of single to coincidence events. An additional problem caused by the possibility of two single sensor events being recorded by the experiment as a single multi-sensor event, means that data within the period $-40s \leq t \leq 40s$ from closest approach is considered of lower reliability.

In the case of the multi-sensor 'discrete' data the sensitivity used to calculate the mass of a particle is not constant, instead it is dependent on the calculated position of the event. It is therefore not appropriate to use the geometric area of the shield to calculate flux or fluence values. Instead a mass dependent area function is required which corresponds to the area of the shield over which a dust grain of particular mass can be detected. The method to derive the area function is similar to that used to calculate the effective area for each of the MSM PHA counters (Section 3.4) but since the data is not 'binned', the last stage of multiplying by a mass distribution function is not required. For each calibration pixel in the shield sensitivity map, the minimum mass of

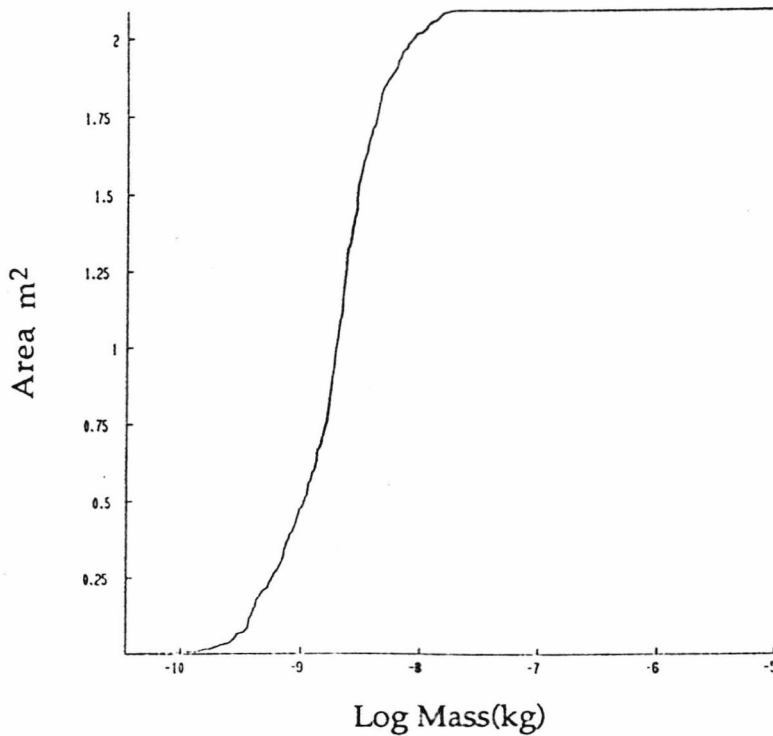


Figure 7.3: The area function for MSM multi-sensor 'discrete' data. Above $\sim 10^{-8}$ kg an impact anywhere on the shield will stimulate at least two of the sensors.

particle required to stimulate at least two of the MSM sensors is calculated. The resultant list of mass and pixel areas is sorted on mass and the total area for a particular mass is calculated from the sum of all pixel areas corresponding to an equivalent or lower mass. The resultant mass dependent area function (Figure 7.3) indicates that any particle with mass $m \geq 10^{-8}$ kg will produce a coincidence event no matter where on the shield the event occurs.

Figure 7.4 shows fluence distributions for two periods pre-encounter ($-4500s \leq t \leq -135s$ and $-134s \leq t \leq -42s$ from closest approach) and one period post-encounter ($+40s \leq t \leq +3200$ from closest approach). The error bars are based on the Poissonian uncertainty ($\pm\sqrt{N}$ of the count rate), and will be an underestimate at lower masses where the small effective area and corresponding small number of events combine to produce a less well defined distribution. The indication from the data is of a large mass distribution which varies in shape with position in the coma. The excess of large grains has

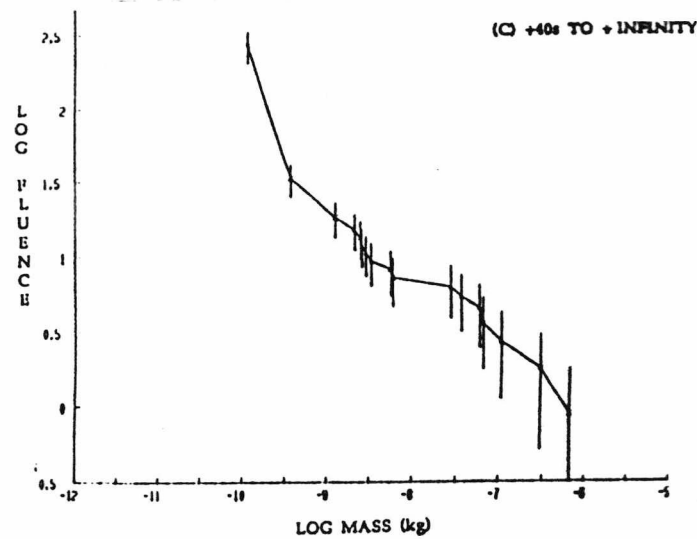
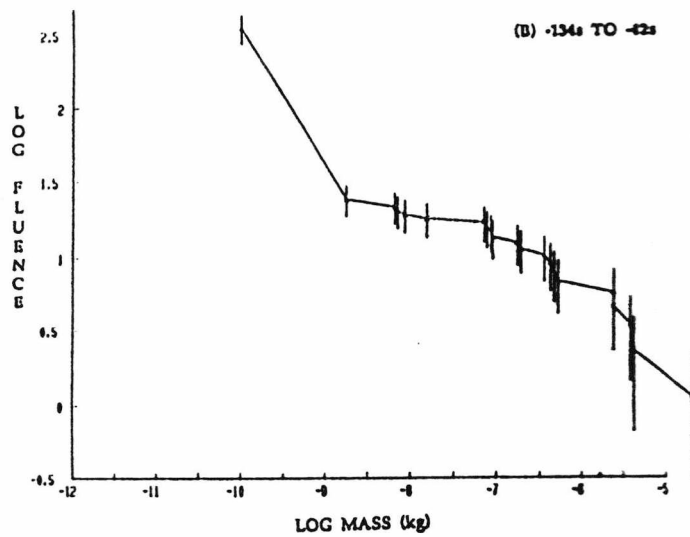
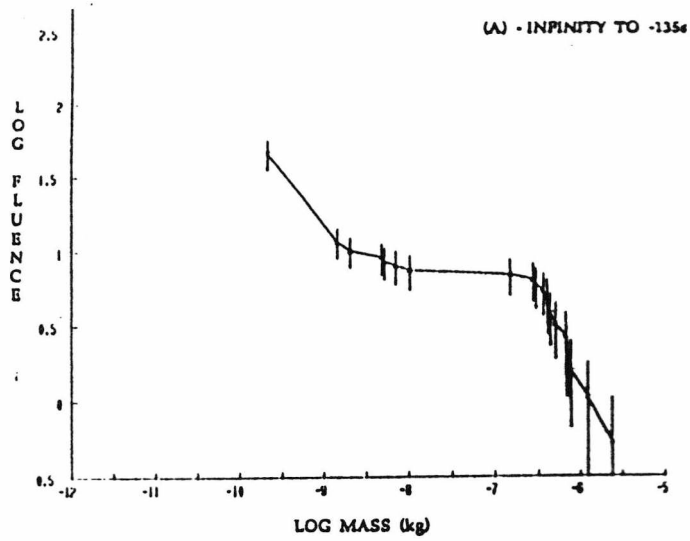


Figure 7.4: Three multi-sensor fluence distributions for A) $-4500s \leq t \leq -135s$, B) $-134s \leq t \leq -42s$, C) $+40s \leq t \leq +3200s$, showing the variation of the large mass excess. A higher resolution time analysis is not possible due to the small number of events.

important consequences for remote observations due to its large contribution to the total scattering area.

7.4 TOTAL ENCOUNTER FLUENCE

The total fluence $F(\geq m)$ is given by the integration of the cumulative flux data $\phi(\geq m, t)$ over the entire encounter period (Equation 7.9) and represents the best measure of the overall coma dust mass distribution. Clearly this is only true if the Giotto trajectory is a representative sample of the coma. By combining PIA (see Chapter 6), DIDSY 'binned' (see Chapter 5) and DIDSY 'discrete' data the calculated fluence covers a mass range from $\sim 10^{-19}$ kg to $\sim 10^{-5}$ kg.

$$F(\geq m) = \int_{-\infty}^{+\infty} \phi(\geq m, t) dt \quad (7.9)$$

To obtain an absolute level for the fluence, some correction must be made for telemetry drop-outs and in particular the missing period from -5s to +19s from closest approach. This is done by the extrapolation of data using the radial gradients derived from data surrounding the telemetry gap. The full method has been described in Pankiewicz, 1989. In the case of the multi-sensor 'discrete' data, an insufficient number of events are available to calculate radial gradients and the correction factor calculated for the DID 4 'discrete' data (Section 7.2) is used. The factor is applied to data integrated over two periods (see Figure 7.5 and 7.6) which contain the most reliable data, and the results combined to produce the total fluence. Correction for the periodic telemetry drop-outs post-encounter, caused by the nutation of the spacecraft, is achieved by linear scaling based on the time 'lost'.

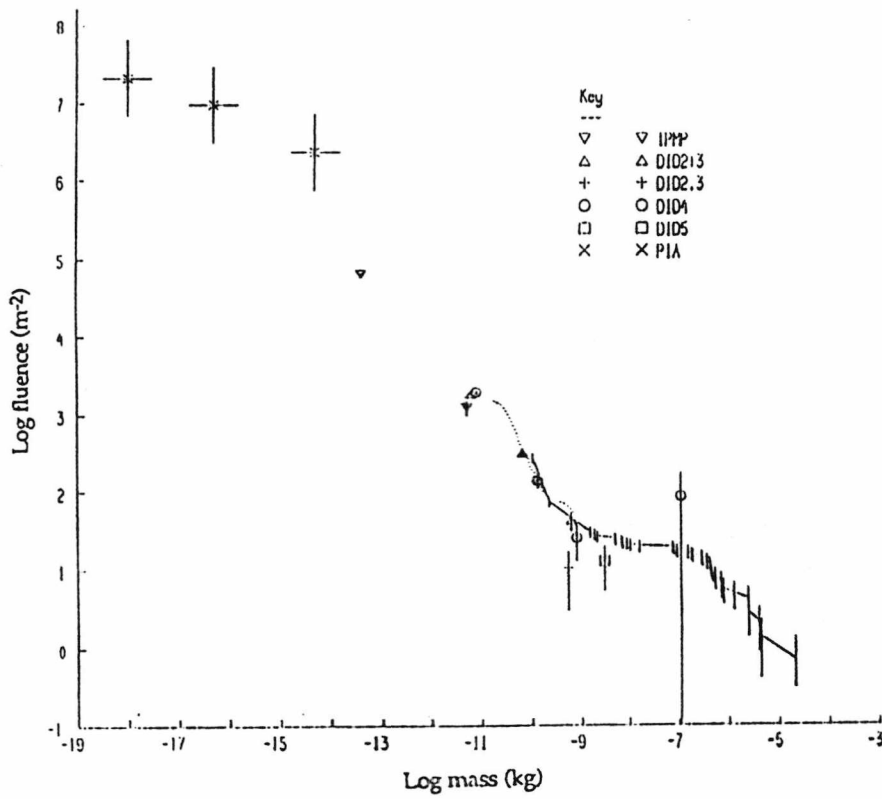


Figure 7.5: The DIDSY and PIA fluence distribution for the pre-encounter period from -4500s to -43s.

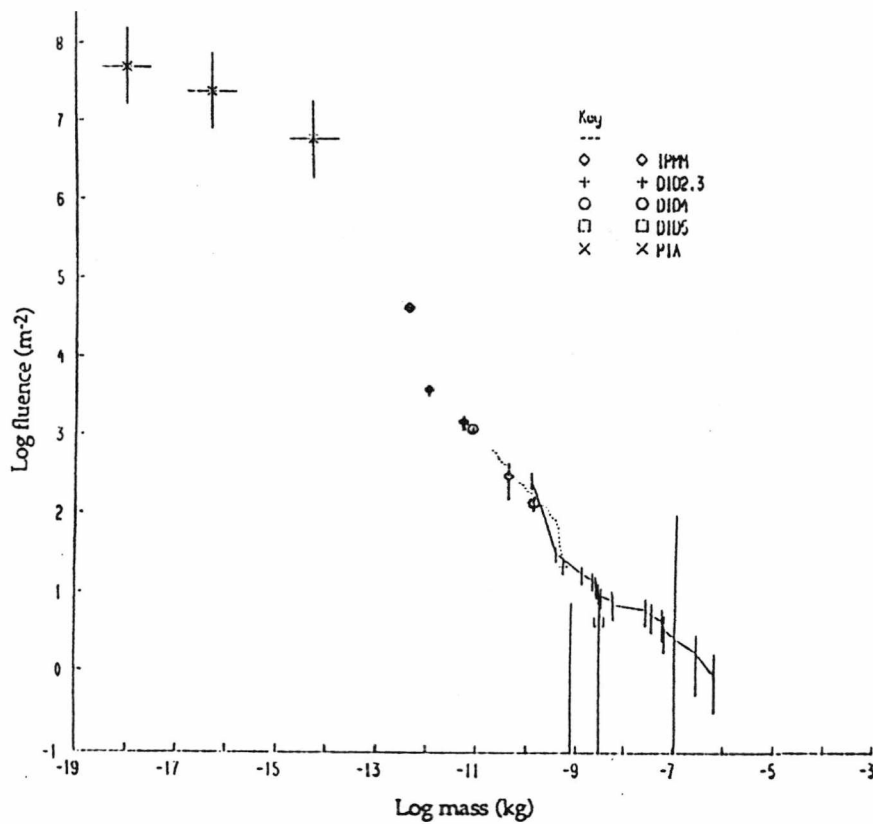


Figure 7.6: The DIDSY and PIA fluence distribution for the post encounter period from +40s to +3200s.

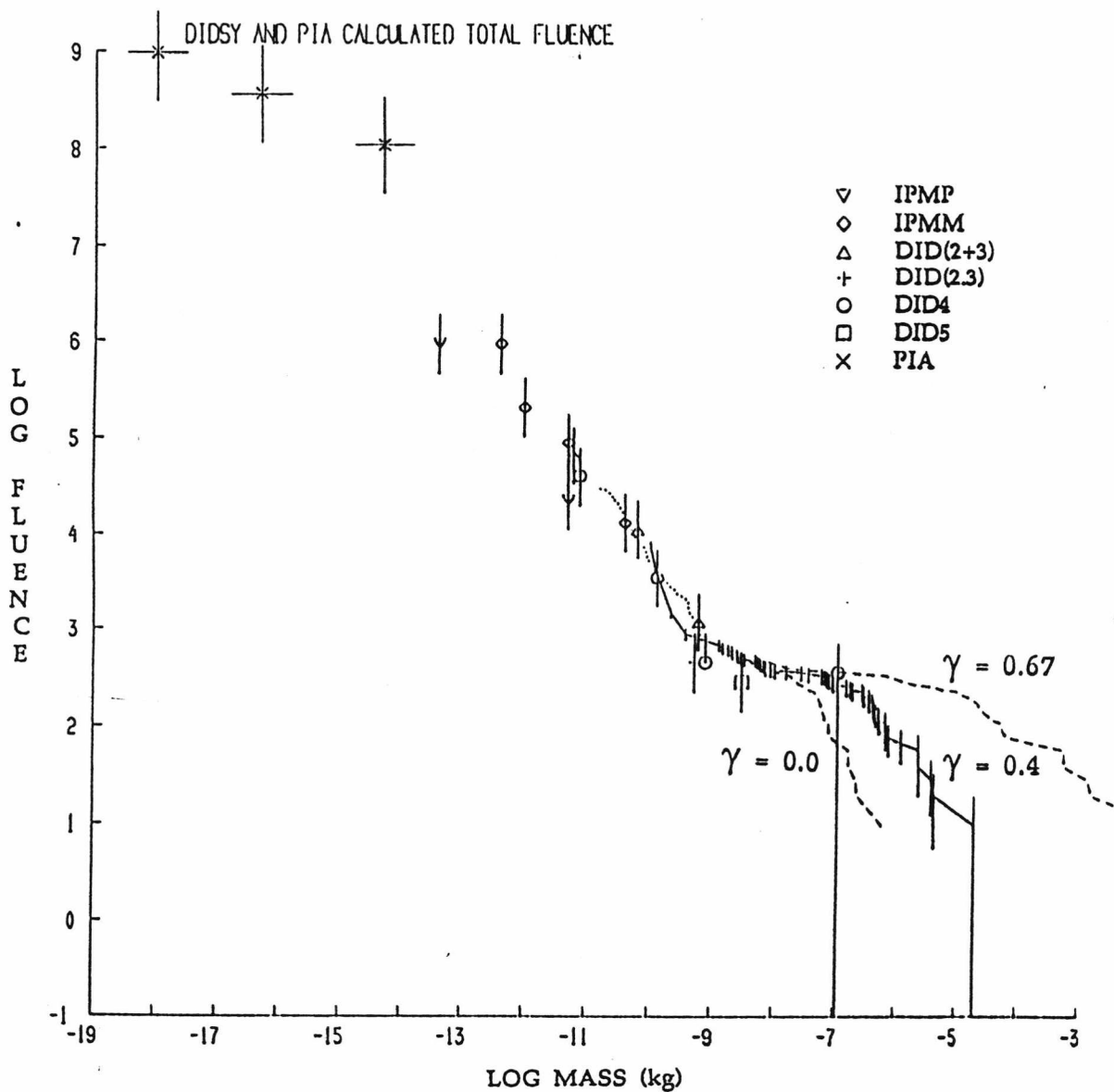


Figure 7.7: The total encounter DIDSY and PIA fluence, after correction for missing telemetry. The multi-sensor 'discrete' data is shown for three values of the momentum derating factor γ (solid and dashed lines). DID 4 'discrete' data is plotted as a dotted line.

The total encounter fluence is shown in Figure 7.7 where the dotted line indicates the DID 4 'discrete' data, and the two dashed and one solid line represent the multi-sensor 'discrete' data calculated using three different values of the momentum derating factor, γ .

7.4.1 CALCULATION OF THE MOMENTUM DERATING FACTOR

The nominal value of $\gamma=0.67$ (Wallis, 1986) was based on the impact contact circumference and penetration time of compact spherical particles. Large fluffy or conglomerate grains will therefore lead to a reduction in γ corresponding to higher proportion of the particles momentum being transferred to the front shield. To obtain a more realistic value for γ , a comparison between the total mass fluence inferred from the Giotto dust experiments and the total deceleration of the spacecraft determined from the Doppler shift of the radio signal is considered.

To determine the total deceleration due to impacting dust grains the momentum transferred to the spacecraft is required. For non-penetrating particles the momentum exchange is given by Equation 2.1. For penetrating grains the momentum imparted to the front shield is given by Equation 2.2 but in addition, some account must be made for the momentum which is not captured by the front shield. The momentum p' carried by the material which passes through the front bumper shield to impact on the rear Kevlar shield is given by Equation 7.10.

$$p' = m v \left[1 - \left(\frac{m_{pen}}{m} \right)^\gamma \right] \quad (7.10)$$

Combining Equations 2.2 and 7.10 results in the total momentum imparted to the spacecraft by a penetrating impact (Equation 7.11). Any ejecta thrown off by the impact of material on the rear shield is confined to the space between the two shields and therefore does not effect the total momentum calculation.

$$p_{Total} = m v \left[1 + (\epsilon - 1) \left(\frac{m_{pen}}{m} \right)^\gamma \right] \quad (7.11)$$

The momentum imparted to 1m^2 of the spacecraft over the encounter period due to particles in the range m to $m+dm$, for a particular value of γ , is given by the differential of the cumulative fluence $F(\geq m)$ multiplied by the momentum of a particle of mass m . Integrating over the whole mass range gives the total momentum imparted to the 1m^2 (Equation 7.12). Where p_{Total} is given by Equation 7.11 for penetrating particles and Equation 2.1 for non-penetrating particles. The value for the lower mass limit m_1 is not too important and is normally taken to be 10^{-19}kg . The value of m_2 , the upper mass limit, is critical since the largest mass dominates the coma distribution. It is assigned a value equal to the maximum mass expected to hit the spacecraft, which is determined by extrapolating the fluence curve and finding the mass corresponding to a fluence of 1 event over the cross-sectional area of the spacecraft (2.9m^2). The fluence distribution is poorly defined at these large masses and hence only an approximate result can be obtained from Equation 7.12.

$$p_{\text{Enc}} = \int_{m_1}^{m_2} \frac{dF(\geq m)}{dm} p_{\text{Total}}(m) dm \quad (7.12)$$

The momentum per m^2 is then multiplied by 2.9m^2 to yield the total momentum imparted to the spacecraft over the entire encounter period. In scaling up to the cross-sectional area of the spacecraft, it is assumed that impacts on the nozzle closure shells covering the kick motor impart a momentum equal to a similar size particle hitting the bumper shield.

In addition to the dust, some account must be made for the deceleration due to the gas. Assuming a gas production rate of $2.55 \times 10^4 \text{kg s}^{-1}$, mean molecular mass of $3.7 \times 10^{-26} \text{kg}$ and outflow velocity of 900m s^{-1} (Krankowsky *et al.* 1986) and a mean radius of 5.2km (Section 8.3.1) the total mass of gas

encountered per m^2 spacecraft, over encounter, is $\sim 1.2 \times 10^{-5} \text{kg}$. The gas impacts are considered to be elastic resulting in an momentum enhancement factor ϵ of 2. This gives a total momentum due to gas of 4.7kgms^{-1} . The total velocity change of the spacecraft measured by ESOC was 0.232ms^{-1} (Morley & Fertig, 1986) and the mass of the spacecraft at encounter was 550kg (Reinhard, 1986) resulting in a change in velocity due to dust of 0.223ms^{-1} equal to a momentum of 123kgms^{-1} .

The momentum derived from the spacecraft deceleration is compared with the result from the dust measurements given by Equation 7.12 and γ is varied until the two values match. Hence a value for γ in the range 0.3 to 0.5 is obtained, somewhat lower than the nominal value of 0.67 (Wallis, 1986). For the analysis of the multi-sensor 'discrete' data a preferred value of $\gamma=0.4$ has been used. This results in a maximum particle mass expected to hit the spacecraft during the encounter period of between 0.2g and 1.3g.

7.5 ADDITIONAL IN-SITU EVIDENCE FOR LARGE GRAINS

The analysis of the multi-sensor 'discrete' data shows an excess of grains with mass $m > 10^{-9} \text{kg}$, compared to levels predicted by pre-encounter models (e.g. Divine *et al.*, 1986). It is important to check that this result is not an artifact of the experiment's operation or processing. One possible test is the comparison of the 'binned' and 'discrete' data. Unfortunately, the statistical nature of the 'binned' data means that it is dominated by smaller masses, while in the case of the 'discrete' data the rapid fall off of the area function with decreasing mass below $\sim 10^{-8} \text{kg}$ (Figure 7.3) results in a corresponding fall in the observed number of multi-sensor events. However, in the small region of overlap between $10^{-10} \text{kg} < m < 10^{-9} \text{kg}$ the comparison between the two independently processed data sets is good.

To test the operation and processing of the experiment for effects which might provide an explanation for the observed excess on instrumental grounds, the software simulation described in Chapter 4 was used. The results of one such simulation are shown in Figure 7.8, for a distribution with a constant value of $\alpha=0.9$ at all masses,. The '*' represent the distribution from the shield simulation (Section 4.4) which was used as input for the experiment simulation. The excess at low masses was caused by use of experiment data analysis software on unprocessed input data. The ' Δ ' represent the distribution produced by the simulation, the level has not been adjusted for under sampling. Although only 10 events were available to form the distribution, the comparison between input and output data sets is still good.

Given that the excess of large grains along the Giotto trajectory was real the next question has to be whether there is any supporting evidence from other experiments on board the spacecraft. In Section 7.4 it was shown that the deceleration observed by the Radio Science experiment was consistent with the excess if a momentum derating factor of $\gamma=0.4$ is assumed. The same would not be true if the mass distribution continued with a slope of $\alpha=0.9$ for $m>10^{-9}\text{kg}$ (unless the interpolation over the missing telemetry gap is wrong). Similarly the probability of hitting the $\sim 0.17\text{g}$ particle required to cause the observed spacecraft nutation would be less than 0.01 in the case of a constant mass distribution index of $\alpha=0.9$.

In addition to the particle that caused the spacecraft nutation, analysis of HMC images for discontinuities caused by changes in the spacecraft attitude, have shown evidence for at least 7 impacts with effective masses ($\epsilon.m$) in the range $5 \times 10^{-7}\text{kg}$ to $3 \times 10^{-5}\text{kg}$ (Curdt & Keller, 1988). They conclude "*...a significant part of the mass of the comet dust is contained in rather large particles (1-100mg).*" (Curdt & Keller, 1988).

Additional evidence, both for and against the large mass excess, based on remote observations of comet Halley, together with three possible models for the excess, are given in Section 8.2.

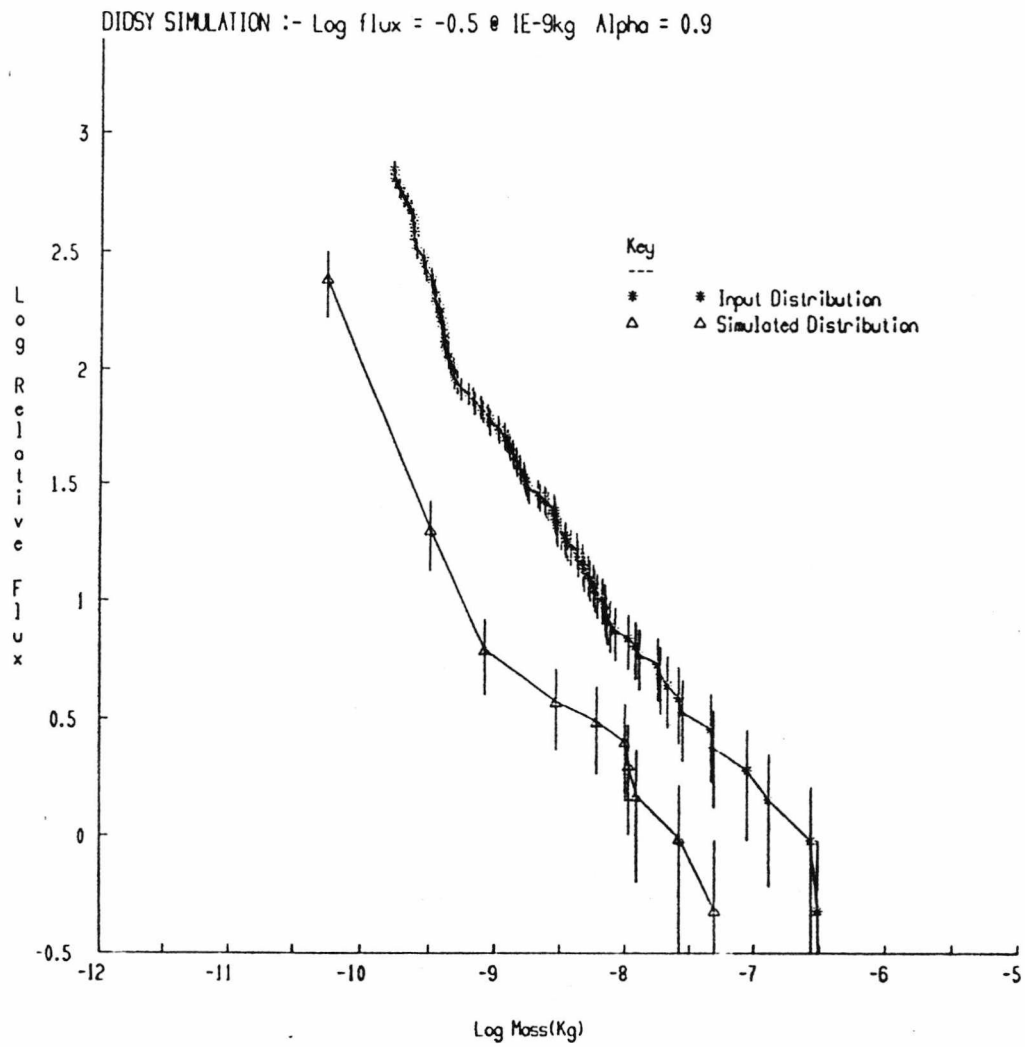


Figure 7.8: Comparison of input '*' and output 'Δ' distributions from a typical run of the DIDSY experiment simulation described in Chapter 4 (see text).

CHAPTER 8

THE DUST ENVIRONMENT OF COMET P/HALLEY

Previous chapters have primarily been concerned with the operation and measurements made by dust experiments on-board the Giotto spacecraft. The results have been viewed in the context of the position along the Giotto trajectory, which was only a single column through the coma. In this chapter the measurements are considered in more general terms of what information they can provide on the mass distribution in the coma as a whole and at the nucleus. Of particular interest is the distribution of small grains ($m < 10^{-17}$ kg) and large grains ($m > 10^{-9}$ kg) which are not readily measured by remote observations. It is perhaps not surprising therefore, that the observed mass distribution in both of these ranges differed significantly from pre-encounter models.

8.1 THE COMA MASS DISTRIBUTION AT SMALL AND INTERMEDIATE MASSES

One of the major differences between the observed distribution and pre-encounter models was in the number of small grains observed. Pre-encounter models (e.g. Divine et al., 1986) did not predict any particles with masses $< 10^{-15}$ kg. However, PIA (Chapter 6) saw high flux rates for particles down to the limiting mass threshold of the experiment ($\sim 10^{-19}$ kg). This discrepancy is perhaps understandable since pre-encounter models were based largely on infrared remote observations and the contribution to the scattering cross section of these small particles is small (Section 8.3.3) despite their large number.

As significant as the excess of small grains was their spatial distribution. Particles in this size range should be strongly affected by radiation pressure resulting in small apex distances. Simple 'fountain' model predictions indicated that Giotto should not see particles further out than 21900km

pre-encounter (Pankiewicz, personal communication, 1989). PIA measured particles well beyond this, and similar results were obtained from the SP-1 detectors on Vega 1 and Vega 2 (Vaisberg *et al.*, 1986). A possible explanation for these observations is that the small particles are the result of fragmentation of larger grains within the coma (Boehnhardt & Fechtig, 1987). Analysis of the time intervals between events, (the 'gap width' distribution) from the DUCMA and SP-1 experiments, which have limiting mass thresholds similar to that of PIA, has shown evidence of the particle clustering associated with fragmentation of larger grains (Simpson *et al.*, 1987).

Despite evidence from images taken by HMC that emission was largely confined to the sunlit side of the nucleus (Keller *et al.*, 1986), there was no sign in the PIA data of a sharp terminator, which would be expected to result in a large drop in the observed flux rate at ~27s before closest approach (McDonnell *et al.*, 1987). The pre-encounter radial gradient at -2.3 was somewhat steeper than the expected inverse square law, which may be an indication of non-radial outflow from the nucleus, leading to particles from the sunlit hemisphere being swept round into the night side. The post-encounter gradient was found to be shallower than an inverse square, which supports the idea of additional small particles being formed by the fragmentation of larger grains. However, some care must be taken when considering these radial gradients since to some extent they are dependent on the calibration parameters derived from the calibration work (Section 6.3) and in particular the value used for the dead time.

At intermediate masses the correspondence between the cardioid source function model (Divine *et al.*, 1986) and observed flux rates was generally good as shown by Figure 8.1. As with the smaller particles there was no evidence for a strong terminator. Although there was no sign of a terminator, enhancements in the observed count rates, caused by the traversal of jets, were observed (Pankiewicz *et al.*, 1989). Comparison of the observed gap widths to a

Poisson distribution modified to take account of the radial power law dependence of the average flux, for IPM-P cover penetration events and DID 4 'Bin 1' events showed no evidence for the excess at smaller gap widths which would have been indicative of fragmentation (Perry & Nappo, 1989). Instead a relative depletion at smaller gap widths was observed with the possible implication that particles in the size range 10^{-14} kg to 10^{-11} kg were fragmenting to smaller grains. Insufficient numbers of events were available to determine the situation at higher masses.

One of the most unexpected findings from the dust experiments was the existence of an excess of large grains along the spacecraft trajectory, compared to pre-encounter modelling. This excess will be considered in more detail in the next section.

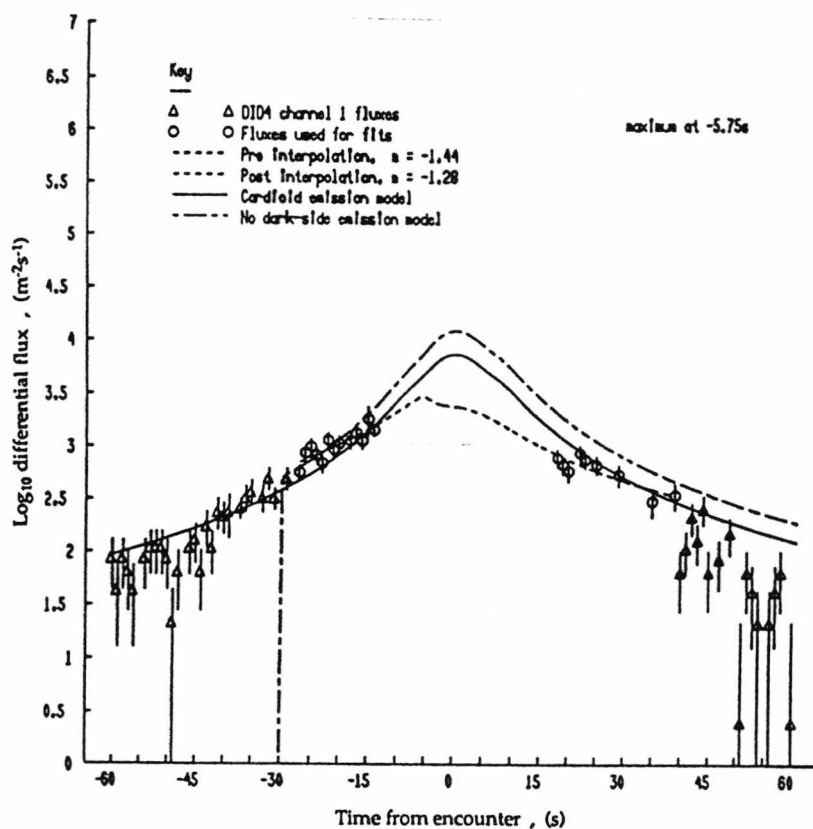


Figure 8.1: The differential flux-time plot for DID 4 'Bin 1' over the time period -60s to +60s from encounter (from Pankiewicz *et al.*, 1989). The expected flux rates from two modelled nucleus functions are also shown, cardioid distribution (solid line) and no dark-side emission (chain line).

8.2 POSSIBLE EXPLANATIONS FOR EXCESS OF LARGE GRAINS

Given that there was an excess of large grains compared to pre-encounter models, how might this come about, and how is it possible to reconcile the in-situ measurements with ground base infrared observations?

Infrared measurements made around the time of encounter indicated from both the mean grain temperature, which was higher than the equilibrium blackbody temperature, and from the existence of a silicate emission feature at $10\mu\text{m}$ and $20\mu\text{m}$, that grains $<20\mu\text{m}$ in size dominated the coma (Hanner *et al.*, 1987). However, other remote observations have indicated that there is an abundance of millimeter- to centimeter-sized grains in cometary coma. Radar measurements of comet IRAS Araki-Alcock by Harmon *et al.* (1989) showed a radar cross-section that was larger than could be accounted for by the nucleus alone and was attributed to a large number of grains in excess of 1cm. A similar excess in the radar cross section was also observed in measurements of comet Halley (Campbell *et al.*, 1989) although in this case the result was less clear since the signal to noise was poor. In addition to the radar measurements, a number of comets observed with the IRAS infrared satellite showed trails of grains close to their orbits (Eaton *et al.*, 1984; Sykes *et al.*, 1986), where the lower limit placed on the size of grains from which the trails were comprised, was in the sub-millimeter range.

Three possible models for the excess of large mass particles detected by Giotto are considered below.

8.2.1 MODEL 1 - OUTBURSTS

One model, which also provides an explanation for the apparent inconsistency between the Giotto dust mass distribution and ground based observations, is based on the variation of dust emission level with time (Perry

et al., 1987; Pankiewicz *et al.*, 1988). During the encounter the Giotto spacecraft passed through the coma in a matter of minutes, but the grains that were detected had taken times ranging from hours to days to arrive from the nucleus, depending on the velocity distribution (Gombosi, 1986). Hence grains of different masses, measured at the same point in the coma, had been emitted from the nucleus at different times. If the level of activity from the region of the nucleus surface that was sampled changed during this period, the observed mass distribution would not be representative of that near the nucleus.

It is therefore possible to envisage a situation where the activity of a region on the nucleus dropped by a factor of ~ 30 some 5-6 hours before encounter. At ~ 5 hours from encounter, the drop in activity would not have significantly changed the coma distribution and this would be consistent with infrared measurements made at the time, which indicated a dominant grain size in the micron size range (Hanner *et al.*, 1987). By the time of the Giotto encounter the small, fast, grains from the region of lower activity would have travelled more than 10000km out into the coma while the larger, slower, grains would still be within ~ 2000 km of the nucleus. Therefore the particles measured by Giotto would be a combination of the small grains from the inactive region and the large grains from the active region and would result in a pre-encounter fluence similar to that observed (Figure 7.5). If the change in activity was limited to a small region of the nucleus, then it would have no effect on the post-encounter data and a large mass excess would not be expected. This model satisfies both the observed DIDSY 'discrete' data and the ground-based observations, however, it would also be expected to effect the shape of the mass distribution at smaller masses and greater distances from the comet; this was not observed. A similar explanation was suggested by Sekanina (1987) to account for variations in the shape of the observed flux distribution measured by the Kuiper Airborne Observatory (Harvey *et al.*, 1986) during mid-March and which coincided with a variation in the absolute flux level by a factor of two.

8.2.2 MODEL 2 - LARGE MASS EXCESS THROUGHOUT THE COMA

Another possible explanation is that the excess of large grains measured by Giotto, was representative of the coma as a whole and therefore that a similar excess was to be found at the nucleus. The source distribution would not conform to those used in pre-encounter modelling. This model would fit the radar measurements which indicated a larger cross section than could be accounted for by the nucleus itself but would conflict with the optical and infrared observations where the excess would be expected to contribute substantially to the scattering area within the coma. This would have the effect of suppressing the silicate emission feature of smaller grains observed in infrared measurements. A model where the nucleus source distribution varied in shape as a function of time would have to be invoked to satisfy both in-situ and ground based measurements.

8.2.3 MODEL 3 - ASYMMETRIC TRAJECTORIES OF LARGE GRAINS

Pre-encounter models were largely based on the 'fountain' (Finson & Probstein, 1968) where particles follow parabolic trajectories in a fixed heliocentric and cometocentric coordinate system, their motion being defined by the ratio of solar gravitational attraction to solar radiation pressure. The 'fountain' model is only strictly applicable to small grains ($<10^{-12}$ kg) which are strongly affected by the solar radiation pressure and rapidly ejected from the vicinity of nucleus. For larger particles, with lower emission velocities and smaller acceleration from solar radiation pressure, particles spend a longer time close to the nucleus and the relative motion of the particles and comet in the heliocentric coordinate system must be considered. A dust coma model, using

trajectories of large particles was developed for ESOC (Massonne, 1985; Fertig and Schwehm, 1984). Figure 8.2 shows the effect of the heliocentric motion for particles of three different sizes. Particles with mass equal to $9.94 \times 10^{-16} \text{ kg}$ (Figure 8.2a) travel with approximately parabolic trajectories representative of a 'fountain' model type calculation, but the deviation from parabolic trajectories for the particles of $6.79 \times 10^{-11} \text{ kg}$ and $1.92 \times 10^{-6} \text{ kg}$ (Figure 8.2b and 8.2c) is clear. However, the dynamics alone do not result in a significant change in the shape of the mass distribution unless combined with a large peak-to-low emission ratio (Pankiewicz, 1989) such as a large day-to-night side emission ratio, or excess emission of large grains from active regions.

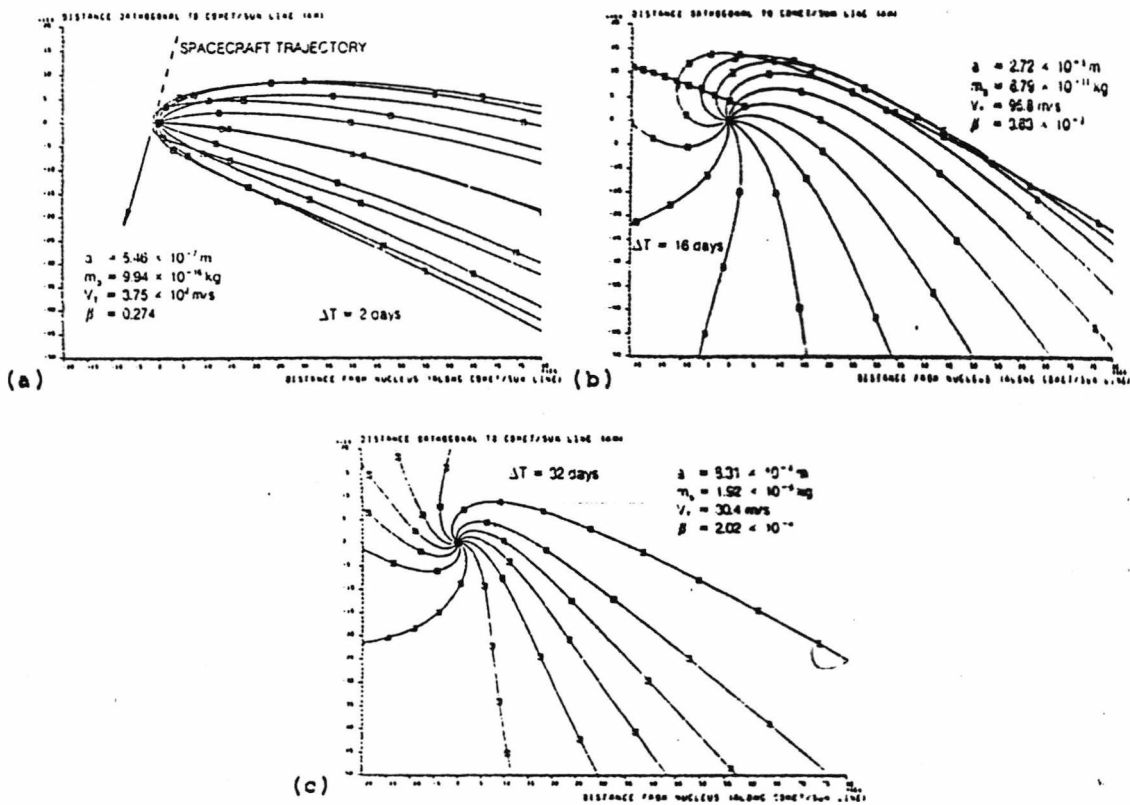


Figure 8.2: A full dynamical treatment of particle trajectories (from Fertig & Schwehm, 1986). For three particle masses a) $9.94 \times 10^{-16} \text{ kg}$, b) $6.79 \times 10^{-11} \text{ kg}$ and c) $1.92 \times 10^{-6} \text{ kg}$. The fountain model assumption of parabolic trajectories is only good for case a).

8.3 THE NUCLEUS DUST MASS DISTRIBUTION

It is not clear from the available data which individual, or combination of the models described above represents the true situation. In this section a simple model is used to transform the observed coma distribution back to the nucleus and values calculated for total dust emission and dust to gas ratio. To take account of the uncertainty in the mechanism resulting in the observed large mass excess, the analysis has been completed for two coma distributions, one corresponding to that observed by Giotto, and one with constant mass index at large masses more in keeping with pre-encounter models (Divine *et al.*, 1986). Models of this form have been assumed from the interpretation of remote observations and were used for pre-flight modelling with a differential size distribution index in the coma of $U=3.7$ (where $N(A)da = Ca^{-U}da$, Green *et al* 1987) in the coma (corresponding to the cumulative mass distribution index $\alpha=0.9$ where $N(\geq m) = Cm^{-\alpha}$). It is assumed that the in-situ observations and model distributions represent the two limiting cases.

8.3.1 THE DUST MASS DISTRIBUTION AT THE NUCLEUS

In order to smooth out any short term variations and to obtain from the in-situ measurements the mass distribution most representative of the coma, the fluence measured over the whole encounter period was used. A curve was fitted to the data to produce a smooth continuous distribution which could be used for the calculation (Figure 8.3, solid line). Another mass distribution, identical at masses less than 10^{-9} kg but continuing with constant slope above this mass was used to represent the model case (Figure 8.3, dotted line). As was stated in Section 8.2 the model is not consistent with the observed excess at large masses and would only be appropriate if it were shown that Giotto data were not representative of the average properties of the coma. To transform the

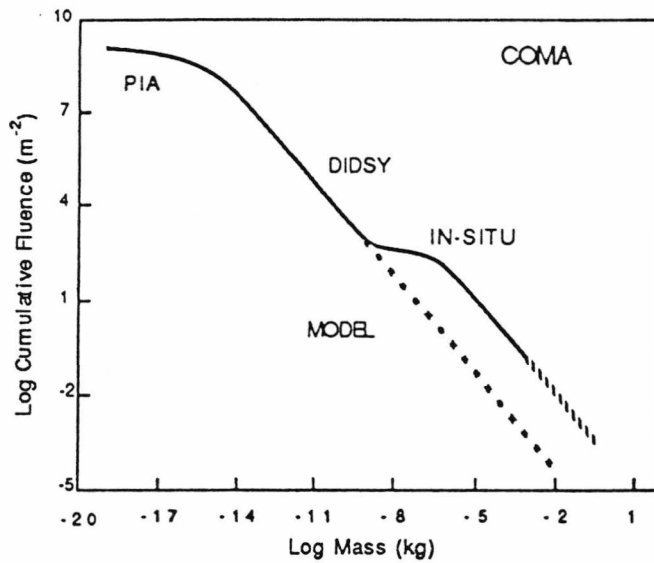


Figure 8.3: Cumulative fluence distribution function derived from the observed total fluence (Figure 7.7) solid line. The model distribution, without the large mass excess is shown as a dotted line above 10^{-9}kg .

coma distribution to the nucleus the fluence (representing a column density) must be converted to the spatial dust mass number density at a known distance from the nucleus. The definition of fluence as an integration over time was given in Equation 7.9 but it is equally valid to represent $F(\geq m)$ as an integral of the flux $\phi(\geq m, d)$ with respect to distance, taking $\pm\infty$ as the limits. If spherical symmetry, constant terminal velocities and radial trajectories are assumed, the flux will be related to distance from the comet by an inverse square law. Therefore the total fluence can be written in the form given by Equation 8.1.

$$F(m) = 2 \int_0^{\infty} \phi(m, R_{\text{Miss}}) \left(\frac{R_{\text{Miss}}}{R} \right)^2 dd \quad (8.1)$$

$$R = \sqrt{(d^2 + R_{\text{Miss}}^2)} \quad (8.2)$$

Where d is the distance along the trajectory from the point of closest approach and is given by vt (v is the Giotto velocity and t the time from closest approach). R is the cometocentric distance (related to distance d by Equation 8.2) and R_{Miss} is the Giotto miss distance of 600km. Substituting Equation 8.2 into

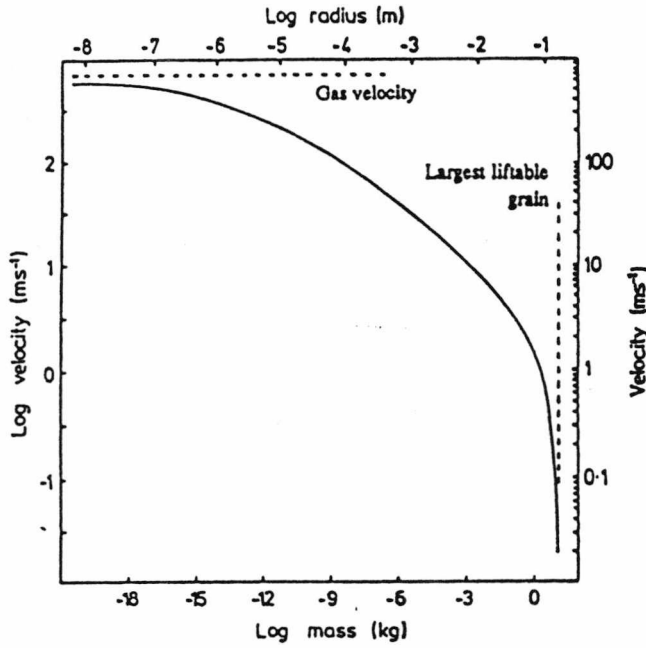


Figure 8.4: Dust terminal velocity distribution from Divine, 1981.

8.1 and taking the R_{Miss}^2 term out of the integral results in a standard form of integral which gives an arctan result, substituting in the limits yields the simple result shown in Equation 8.3.

$$F(m) = \varphi(m, R_{Miss}) R_{Miss} \pi \quad (8.3)$$

Rearranging this equation gives the average space flux density at the Giotto miss distance as a function of the calculated total fluence. By again assuming an inverse square scaling with distance and constant particle velocities the calculated flux can be scaled to a flux density just above the surface of the nucleus. To map back onto the surface of the nucleus itself a particle emission velocity is required. In this simple model acceleration of the grains is ignored and they are assumed to be ejected at their terminal velocity. Using the terminal velocity $v(a)$ given by Divine, 1981 (Figure 8.4), the cumulative dust flux $\varphi_n(m)$ (the number of particles with mass $\geq m$ leaving $1m^2$ of the nucleus per second) is given by Equation 8.4.

$$\begin{aligned}
\phi_n(m) &= \int_m^{m_{\text{Max}}} n_n(m') \, d\log m' \\
&= \int_m^{m_{\text{Max}}} \frac{F'(m')}{\pi R_{\text{Miss}}} v(a) \left(\frac{R_{\text{Miss}}}{R_n} \right)^2 \, d\log m'
\end{aligned}
\tag{8.4}$$

Where F' is the differential fluence $dF(m)/d\log(m)$ and R_n is the effective nucleus radius. A value for R_n of 5.2km is used, corresponding to the radius of a sphere with the same surface area as that given by the model of Sagdeev *et al.*, 1986. Using this relation a cumulative flux distribution at the nucleus is derived (Figure 8.5). The size of the maximum liftable mass m_{Max} , is derived by equating the gas drag forces on the grain to the gravitational attraction of the nucleus, a value of 15cm (~11kg) is used (Pankiewicz, personal communication, 1989) based on a nucleus density of 800kgm^{-3} and an active fraction of the total nucleus surface of 10% (Keller *et al.*, 1987). The mass m and radius a of a particle are assumed to be related by a density function of the form given by Divine *et al.*, 1986, (Equation 8.5) where $a_0=2 \times 10^{-6}\text{m}$.

$$\rho(a) = 3000 - 2200 \left(\frac{a}{a + a_0} \right)
\tag{8.5}$$

8.3.2 THE NUCLEUS DUST PRODUCTION RATE AND DUST TO GAS RATIO

Since the fluence used to calculate the nucleus distribution was derived from data taken over the whole Giotto trajectory, it will include the contribution from both active and inactive areas of the nucleus. If it is assumed

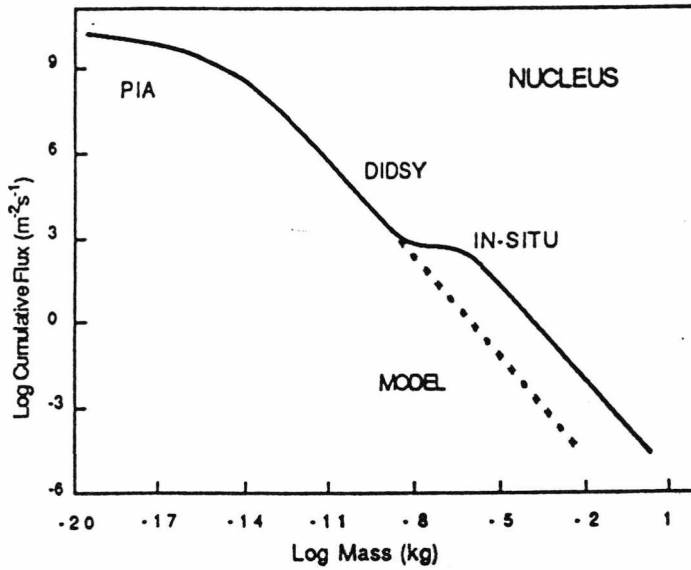


Figure 8.5: Cumulative flux distribution at the nucleus surface, calculated from the total encounter fluence (solid line) and for a model distribution (dashed line).

that the spacecraft track, mapped back to the nucleus, crossed over a region of the nucleus which when averaged was representative of the nucleus activity as a whole, then the total dust production rate of the nucleus can be determined by integrating the nucleus mass distribution over all masses up to the maximum liftable grain, and over the whole surface area of the nucleus. This results in dust production rates of $\sim 6 \times 10^4 \text{ kgs}^{-1}$ and $\sim 4 \times 10^3 \text{ kgs}^{-1}$ for the measured and modelled distributions respectively (compared with $\sim 1.5 \times 10^4 \text{ kgs}^{-1}$ from ground based observations, Hanner *et al.*, 1987). These production rates can be directly compared to the gas production rate of $2.55 \times 10^4 \text{ kgs}^{-1}$ (Krankowsky *et al.*, 1986) to yield a dust-to-gas ratio $\mu(m)$, Equation 8.6, as a function of mass.

$$\mu(m) = \frac{4\pi R^2}{Q_g M} \int_0^m n_n(m') m' d\log m' \quad (8.6)$$

Where Q_g is the gas production rate = $6.9 \times 10^{29} \text{ mol s}^{-1}$ (Krankowsky *et al.*, 1986) and M is the mean molecular mass = $3.7 \times 10^{-26} \text{ kg}$ (Divine *et al.*, 1986). The gas production rate is an average value for the data measured during the whole

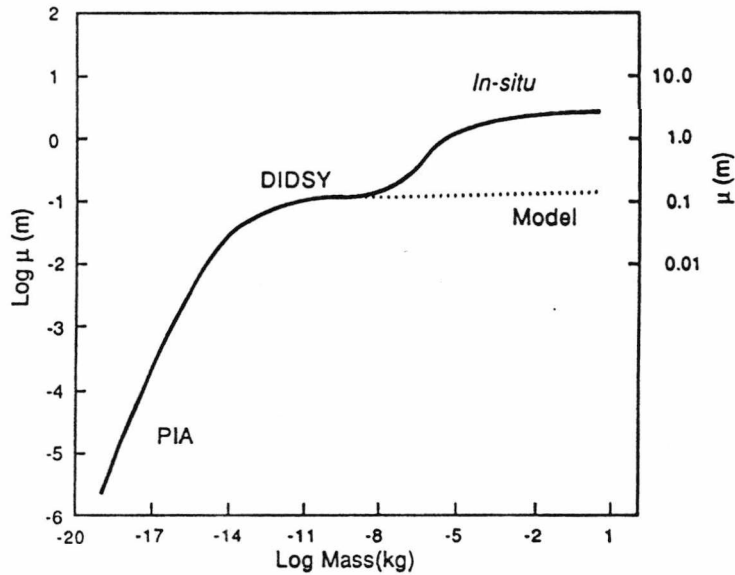


Figure 8.6: Dust-to-gas mass ratios μ as a function of the largest particle included (m).

encounter and as such is directly comparable to the dust production rate. Since the value of $\mu(m)$ is the ratio of these two production rates it is largely independent of the actual active area. Figure 8.6 shows the dust-to-gas ratio as a function of mass for the case of the measured distribution (solid line) and the model distribution (dotted line). If a maximum liftable mass of $\sim 11\text{kg}$ is again assumed, values for the total dust-to-gas ratio, $\mu(m_{\text{Max}})$, of ~ 0.2 for the model distribution and ~ 2.5 for the measured distributions are obtained. In both cases the high slope for masses $> 10^{-5}\text{kg}$ means that only a weak dependence on the maximum mass is found.

8.3.3 COMPARISON OF COMA AND NUCLEUS, MASS AND AREA DISTRIBUTIONS

Using the coma and nucleus distributions described in Section 8.3.2, the differential number, area and mass of particles within a 1m^3 volume of the

coma at 600km (corresponding to the Giotto miss distance), and at the surface of the nucleus can be calculated.

The coma differential distributions $n_c(m)$, $A_c(m)$ and $m_c(m)$ per log mass interval (Figure 8.7) are shown for the measured distribution (solid line) and the model distribution (dotted line) and are defined by Equations 8.7, 8.8 and 8.9.

$$n_c(m) \, d\log m = (n_c(m) / v_s) \, d\log m \quad (8.7)$$

$$A_c(m) \, d\log m = (n_c(m) \pi a^2 / v_s) \, d\log m \quad (8.8)$$

$$M_c(m) \, d\log m = (n_c(m) m / v_s) \, d\log m \quad (8.9)$$

Where v_s is the velocity of the spacecraft relative to the comet, and n_c is the differential flux (number of particles impacting the spacecraft per m^2 per second). From Figure 8.7, it can be seen that the total grain mass is dominated by the largest grains. Remote-sensing observations, which are dependent on the cross-sectional area, indicate dominant grain have masses $\sim 10^{-14}$ kg. The in-situ Giotto dust impact data indicate, however, that a significant contribution to the cross-sectional area could come from large grains.

Similar differential distributions for $1m^3$ of 'average' nucleus material are shown in Figure 8.8, where the number $n_n(m)$, area $A_n(m)$ and mass $m_n(m)$ per log mass interval are given by equations 8.10, 8.11 and 8.12 respectively.

$$n_n(m) \, d\log m = (n_n(m) / V) \, d\log m \quad (8.10)$$

$$A_n(m) \, d\log m = (n_n(m) \pi a^2 / V) \, d\log m \quad (8.11)$$

$$m_n(m) \, d\log m = (n_n(m) m / V) \, d\log m \quad (8.12)$$

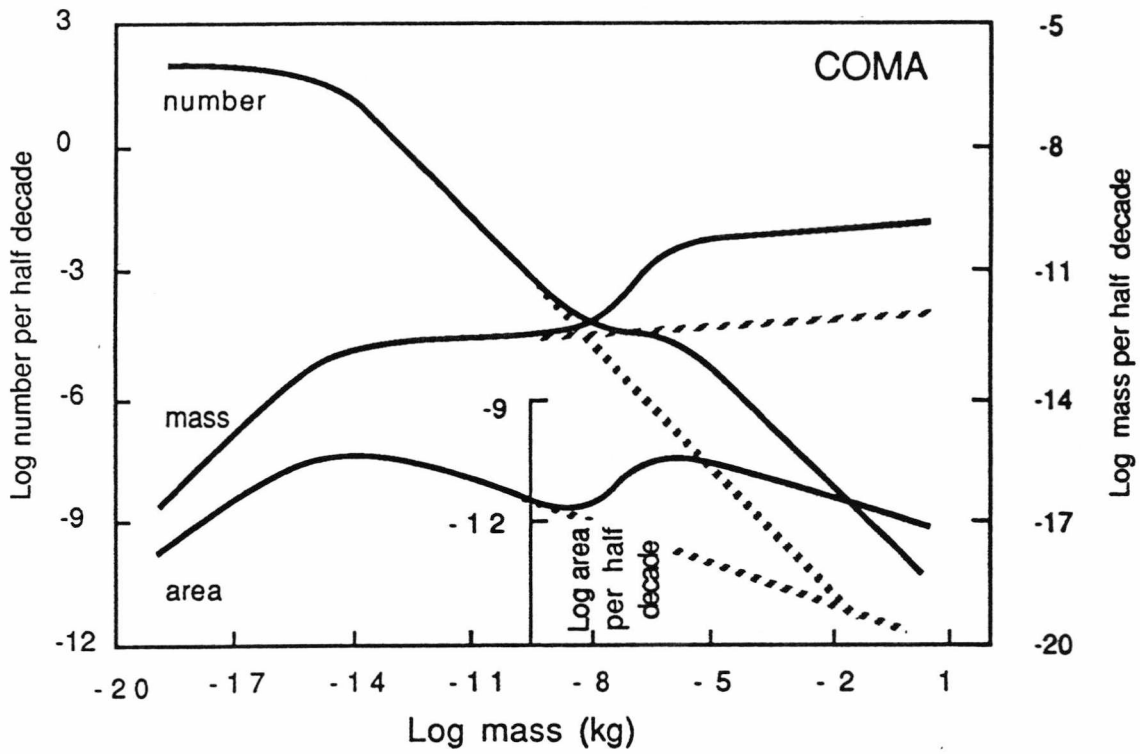


Figure 8.7: Differential number, cross-sectional area, and mass distributions in the coma, for measured (Solid line) and model (Dashed line) distributions.

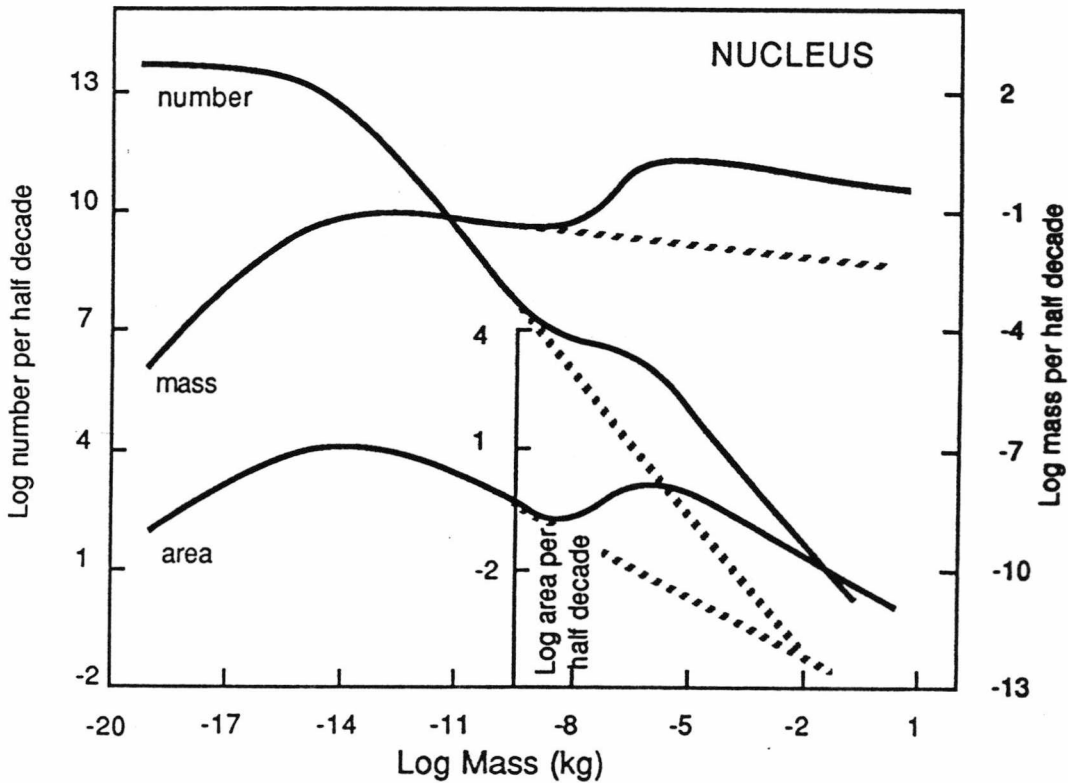


Figure 8.8: Differential number, cross-sectional area, and mass distributions on the nucleus, for measured (Solid line) and model (Dashed line) distributions.

Where V is the total volume of ice (in the form of gas) and dust ejected per m^2 per second from the nucleus and is given by Equation 8.13.

$$V = \int_0^{m_{Max}} n_n(m) \left(\frac{m}{\rho(m)_{Dust}} + \frac{m}{\mu(m_{Max}) \rho_{Ice}} \right) d \log m \quad (8.13)$$

The dust-to-gas ratio $\mu(m_{Max})$ is taken from Figure 8.6 at $m=11\text{kg}$ and ρ_{Ice} assumed to be 200kgm^{-3} for this work. The true value of ρ_{Ice} may be as high as 800kgm^{-3} resulting in an increase in $n_n(m)$ by factors of 2 and 3.5 for the measured and model distributions respectively. From Figure 8.8 it is seen that unlike the coma, the nucleus distribution of mass is not dominated by the largest grain; instead the distribution peaks at $\sim 10^{-14}\text{kg}$ for the model and $\sim 10^{-6}\text{kg}$ for the measured distributions respectively. The difference between model and measured distributions has important implications on the nature of the surface, where the relative excess of large grains in the observed distribution, leads to a less opaque surface than that predicted by the model distribution (McDonnell *et al.*, 1990), thus allowing radiation to penetrate further into the surface. In practice, no matter which distribution is most representative at smaller masses, the nature of the comet surface is likely to be affected significantly by grains which are too large to be lifted from the surface and will therefore not be observed by either in-situ or remote observations.

CHAPTER 9

CONCLUSIONS

The Giotto mission was a great success, returning information from within 1000km of the nucleus of comet P/Halley before telemetry was temporarily lost. Part of this success was undoubtedly due to the high degree of international cooperation that took place between the space agencies and between the experimenters. An example of this collaboration was the use of the Vega spacecraft as 'Pathfinders' for Giotto.

Despite the harsh environment, Giotto's dust detectors successfully measured the dust coma and returned information on a mass range covering more than 12 orders of magnitude. The performance of the DIDSY dust experiment was not without its faults, most important of which was the failure of the cover in front of the high sensitivity IPM-P sensor to retract before the encounter. This resulted in an increase in the experiments limiting threshold by more than a factor of a million, a serious limitation! In an attempt to regain at least some of the lost information at small masses, use was made of the PIA experiment. The lack of pre-launch calibration data meant that knowledge of the operation of the system combined with the observed flux rates had to be used in an attempt to obtain relative mass thresholds and dead time corrections. In future a similar analysis of the essentially identical PUMA mass spectrometers which flew on the Vega spacecraft would be most useful. These results could be compared to measurements from other dust detectors on the Vega spacecraft to better gauge the reliability of the PIA calibration analysis used.

A complete reassessment of DIDSY calibration data and techniques was undertaken by the data analysis team at UKC. These resulted in both a better understanding of the operation and calibration of the experiment and also a more rigorous treatment of the data. Certain aspects of the experiment were dependent on its operation at high flux rates. To understand these effects a software simulation of the experiment and its input were produced. This

provided an essential tool both in confirming flux calculation algorithms and in understanding anomalies in the returned telemetry. Many of the problems with interpreting the high flux data would have been foreseen if such a simulation had been available during the development stages of the experiment. Even at a fairly late stage minor changes in the on board software, for example to change the priority of 'discrete' data categorisation, would have resulted in an improved data set. This highlights the importance in future to test a fully integrated system, whether it be hardware or a software model, with a realistic range of inputs

In terms of the results, Halley provided surprises both at small and large masses; intermediate masses, which generally dominated the remote observations were closer to predictions (Section 8.1). At small masses both the number and the spatial extent were larger than expected possibly as a result of fragmentation which was almost certainly observed by the Vega dust detectors (Simpson et al., 1987). An examination of PIA data for non-randomness may yield additional information, however, some care would be required in the treatment of the data due to the high level of noise observed.

The most unexpected result from the dust measurements came at large masses ($>10^{-9}$ kg), where several experiments DIDSY, HMC and GRE saw an excess of large particles compared to predictions from pre-encounter models. In the case of DIDSY the large mass distribution is dependent on the momentum derating factor used, which is poorly defined and future investigation should attempt to better quantify the transfer of momentum for marginally and fully penetrating hypervelocity impacts. The poor temporal and spatial resolution of the large mass data means that any of two or three models can explain the excess. Further dynamical modelling along the lines of Fertig & Schwehm, 1986 is required for varying source location and emission functions to determine the distribution of these large grains over extended periods of time. Any theory must explain not only the Giotto measurements, but also those made by

infrared remote observations which indicate that particles with masses $\sim 10^{-14}$ kg dominated the scattering cross section only a few hours before Giotto encounter (Hanner et al., 1987).

The best overall measure of dust distribution along the Giotto trajectory has been obtained from the total fluence. Assuming a simple model this was transformed to the nucleus to obtain a dust production rate of 6×10^4 kgs⁻¹ and dust to gas ratio of 2.5. If instead the large mass excess was a dynamical or temporal effect then a distribution more in line with pre-encounter models resulted in a lower dust production rate of 4×10^3 kgs⁻¹ and a corresponding reduction in the dust to gas ratio to 0.2. Clarification of which situation best fits the comet must await improved modelling and will probably not be known until a cometary rendezvous mission takes place, where the spacecraft will be able to spend an extended period in the coma.

After the encounter, the Giotto spacecraft was placed in a state of hibernation. The orbital corrections required for the Halley encounter left more than 25kg of the original 69kg of hydrazine fuel, sufficient when combined with an Earth flyby, to allow for the possibility of retargeting to another comet. A number of the experiments were known to have failed during the encounter, but the status of others, and in particular the camera (HMC) were less certain. In February 1990, four years after the initial encounter, as Giotto's orbit brought it on a course back towards the Earth, the spacecraft was successfully located and its attitude changed so that communication via the high gain antenna was regained. Over the following months the spacecraft system and experiments were checked out. Unfortunately, suspicions that the camera was damaged were confirmed. The status of DIDSY was much as it had been when the spacecraft was put into hibernation, with the exception of the lowest channel of IPM-M which was observed to be noisy (R Beard, personal communication, 1990). IPM-P and CIS were both damaged by the encounter with Halley. This leaves the front shield MSM and rear shield RSM sensors as

the main source of dust detection in a future encounter. During the check-out the CDF was found to be operating normally and successful switching of the DID 2/3 mode was achieved.

On 2nd July 1990 Giotto passed within 20000km of the Earth, the necessary orbital manoeuvres were made for an intercept orbit, to encounter comet Grigg-Skjellerup in July 1992. The comet is in a prograde orbit (5.6 year period) resulting in a considerably lower encounter velocity ($\sim 15\text{kms}^{-1}$) than was the case with Halley. This is important for the dust experiments where output is proportional to momentum, the lower velocity together with a corresponding drop in the momentum enhancement will lead to a reduction in the mass sensitivity by a factor of ~ 10 . The requirement to point the high gain antenna towards the Earth means that the spacecraft will not encounter the comet 'head-on' instead a minimum offset of $\sim 25^\circ$ between the spacecraft spin axis and relative velocity vector. At this angle, dust will not be able to enter the PIA experiment and so no information on the smaller masses will be obtained. Nevertheless the GEM mission provides the opportunity of providing a valuable comparison to Halley, at a fraction of the cost of another dedicated mission

Further in the future is the Rosetta (formally CNSR) comet nucleus sample return mission, planned for around the turn of the century. The mission scenario involves a cometary encounter at a heliocentric distance of $\sim 6\text{AU}$, the spacecraft will land on the comet take samples and then return to Earth over a time period of 6-8 years (Bonnet, 1990). In addition to providing an actual sample of cometary material, the spacecraft will provide an insight into the gas and dust release mechanisms at large distances where sublimation of water ice, the driving force for emission at smaller heliocentric distances, is not thought to be dominant.

REFERENCES

- Berg O.E. and Richardson F.F., 1969, 'The Pioneer 8 cosmic dust experiment', *Rev. Sci. Instrum.*, **40**, pp.333
- Boehnhardt H., and Fethig H., 1987, 'Electrostatic charging and fragmentation of dust near P/Giacobini-Zinner and P/Halley', *Astron. Astrophys.*, **187**, pp.824-828.
- Bohn J.L. and Nadig F.H., 1950, 'Acoustical studies with V2 rockets', *Research Institute of Temple University, Report 8*.
- Bonnet R.M., 1990, 'ESA Plans for Planetary Exploraation', *Adv. Space Res.*, **10**, 3, pp.337-339.
- Brandt J.C., Farquhar R.W., Maran S.P. Niedner M.B. Jr., and von Roseninge T.T., 1988, 'The International Cometary Explorer', in '*Exploration of Halley's Comet*', Springer-Verlag, pp.969-980.
- Burton W.M., 1983, 'Cometary particle impact simulation using pulsed lasers', *Adv. Space Res.*, **2**, 12, pp.255-258.
- Campbell D.B., Harmon J.K., and Shapiro I.I., 1989, 'Radar observations of comet Halley', *Astrophys. J.*, **338**, pp.1094-1105.
- Curdt W., and Keller H.U., 1988, 'Collisions with Cometary Dust Recorded by the Giotto HMC Camera', *ESA Journal*, **12**, pp.189-208.
- Delsemme A.H., 1987, 'Diversity and similarity of comet', *ESA SP-278*, pp.19-30.
- Dietzel H., Eichorn G, Fechtig H., Hoffman H.J. and Kissel J., 1973, 'The Heos 2 and Helios micrometeoroid experiments', *J. Phys. E. Sci. Instrum.*, **6**, pp.209
- Divine N., 1981, 'Numerical models for Halley dust environments', *ESA SP-174*, pp.25-30.
- Divine N., and Newburn R.L. jr., 1987, 'Modeling Halley before and after the encounters', *Astron. Astrophys.*, **187**, pp.867-872.
- Divine N., Fechtig H., Gombosi T.I., Hanner M.S., Keller H.U., Larson S.M., Mendis D.A., Newburn R.L. Jr., Reinhard R., Sekanina Z. and Yeomans D.K., 1986, 'The comet Halley dust and gas environment', *Space Sci. rev.*, **43**, pp.1-104.
- Eaton N., Davies J.K., and Green S.F., 1984, 'The anomalous dust tail of comet P/Temple 2', *Mon. Not. R. Astr. Soc.*, **211**, pp.15-19.

- Edenhofer P., Bird M.K., Brenkle J.P., Buschert H., Kursinski E.R., Mottinger N.A., Porsche H., Stelzried C.T., and Volland H., 1987, 'Dust distribution of comet P/Halley's inner coma determined from the Giotto Radio-Science Experiment', *Astron. Astrophys.*, **187**, pp.712-718.
- Evans G.C., 1987, 'Dust detection systems for cometary encounter', *Ph.D. Thesis, Unit for Space Sciences, Physics Laboratory, University of Kent at Canterbury*.
- Evans S.T., 1984, 'Giotto DIDSY Comet Halley Mission: Development of piezo-electric Dust Detection System', *M.Sc. Thesis, Unit for Space Sciences, Physics Laboratory, University of Kent at Caanterbury*.
- Evans S.T., 1988, 'Hypervelocity impact studies on the Giotto comet Halley mission', *Ph.D. Thesis, Unit for Space Sciences, Physics Laboratory, University of Kent at Canterbury*.
- Evans S.T. and Ridgeley A., 1985, 'An analysis of the structure, calibration and system test data obtained from the Giotto structural model spacecraft at ESTEC, Noordwijk, 22nd October to 5 November 1983', *Rutherford Appleton Laboratory, Report RL-85-019*.
- Fertig J., and Schwehm G.H., 1984, 'Dust environment models for comet P/Halley: Support for targeting of the GIOTTO S/C', *Adv. Space Res.*, **4**, pp.213-216
- Finson M.L., and Probst R.F., 1968, 'A theory of dust comets. I. Model and equations', *Ap. J.*, **154**, pp.327-352.
- Friichtenicht J.F., 1964, 'Micrometeoroid simulation using nuclear accelerator techniques', *Nucl. Instrum. Meth.*, **28**, pp.70-78.
- Göller J.R., Grün E., Maas D., 1987, 'Calibration of the DIDSY - IPM dust detector and application to other impact ionisation detectors on board the P/Halley probes', *Astron. Astrophys.*, **187**, pp.693-698.
- Gombosi T.I., 1986, 'A heuristic model of the comet Halley dust size distribution.', *ESA SP-250, II*, pp.167-172.
- Grard R.J.L., Gombosi T.I. and Sagdeev R.Z., 1986, 'The Vega Missions', *ESA SP-1066*, pp.49-70.
- Grard R.J.L., McDonnell, J.A.M., Grün E., and Gringauz K.I., 1987, 'Secondary electron emission induced by gas and dust impacts on Giotto, Vega 1 and Vega 2 in the environment of comet P/Halley.', *Astron. Astrophys.*, **187**, pp.785-788.

- Green S.F., McDonnell J.A.M., Perry C.H., Nappo S., and Zarnecki J.C., **1987**, 'P/Halley dust coma: Grains or Rocks?', *ESA SP-278*, pp.379-384.
- Green S.F., Clarke C.D., and Stevenson T.J., **1988**, 'A 2MV Van de Graaf accelerator for cosmic dust impact simulation', *JBIS*, **41**, pp.393-396.
- Hanner M.S., 1983, 'The nature of cometary dust from remote sensing', in 'Cometary exploration II', conference on cometary exploration Budapest, 1982, pp.1-22.
- Hanner M.S., Tokunaga A.T., Golisch W.E., Griep D.M., and Kaminski C.D., **1987**, 'Infrared emission from P/Halley's dust coma during March 1986', *Astron. Astrophys.*, **187**, pp.653-660.
- Harmon J.K., Campbell D.B., Hine A.A., Shapiro I.I., and Marsden B.G., **1989**, 'Radar observations of comet IRAS-Araki-Alcock(1983d)', *Astrophys. J.*, **338**, pp.1071-1093.
- Hill D.C., **1988**, 'Laser simulation of micrometeoroid impacts', *JBIS*, **41**, pp.397-402.
- Hirao K., **1986**, 'The Suisei/Sakigake (Planet-A/MS-T5) Missions', *ESA SP-1066*, pp.71-84.
- Hirao K., Itoh T., **1987**, 'The Sakigake/Suisei encounter with comet P/Halley', *Astron. Astrophys.*, **187**, pp.39-46.
- Hughes D.W., **1979**, 'The micrometeoroid hazard to a space probe in the vicinity of the nucleus of Halley's Comet', *ESA SP-153*, pp.51-56.
- Keller H.U., Arpigny C., Barbieri C., Bonnet R.M., Cazes S., Coradini M., Cosmovici C.B., Delamere W.A., Huebner W.F., Hughes D.W., Jamar C., Malaise D., Reitsema H.J., Schmidt H.U., Schmidt W.K.H., Seige P., Whipple F.L., and Wilhelm K., **1986**, 'First Halley Multicolour Camera imaging results from Giotto', *Nature*, **321**, pp.320-326.
- Keller H.U., Delamere W.A., Huebner W.E., Reitsema H.J., Kramm R., Thomas N., Arpigny C., Barbieri C., Bonnet R.M., Cazes S., Coradini M., Cosmovici C.B., Hughes D.W., Jamar C., Malaise D., Schmidt K., Schmidt W.K.H., and Siege P., **1987**, 'Comet P/Halley's nucleus and its activity', *Astron. Astrophys.*, **187**, pp.807-823.
- Kissel J., **1986**, 'The Giotto Particulate Impact Analyser', *ESA SP-1077*, pp.67-83.
- Kissel J., and Krueger F.R., **1986**, 'Ion Formation by Impact of Fast Dust Particles and Comparison with Related Techniques', *Appl. Phys.*, **A 41**, pp.1-17.

- Kissel J., Brownlee D.E., Büchler K., Clark B.C., Fechtig H., Grün E., Hornung K., Igenbergs E.B., Jessberger E.K., Krueger F.R., Kuczera H., McDonnell J.A.M., Morfill G.M., Rahe J., Schwehm G.H., Sekanina Z., Utterback N.G., Völk H.J. and Zook H.A., 1986, 'Composition of comet Halley dust particles from Giotto observations', *Nature*, **321**, pp.336-337.
- Krankowsky D., Lammerzahl P., Herrwerth I., Woweries J., Eberhardt P., Dolder U., Hermann U., Schulte W., Berthellier J.J., Iliano J.M., Hodges R.R., and Hoffman J.H., 1986, 'In situ gas and ion measurements of comet Halley', *Nature*, **321**, pp.326-330.
- Laakso H, Grard R., Pedersen A. and Schwehm G., 1989, 'Impacts of large dust particles on the Vega spacecraft', *Adv. Space Res.*, **9**, 3, pp.269-272.
- Lange G., Grün E., Maas D., Göller J.R., Kissel J., McDonnell J.A.M., Zarnecki J.C., Bussoletti E. and Grard R.J.L., 1986, 'Performance of the impact plasma and momentum detector (DIDSY-IPM) before closest approach to comet Halley', *ESA SP-250*, II, pp.191-193.
- Maas D., Göller J.R., Grün E., Lange G., McDonnell J.A.M., Nappo S., Perry C., and Zarnecki J.C., 1989, 'Cometary dust particles detected by the DIDSY - IPM-P sensor on board Giotto', *Adv. Space Res.*, **9**, 3, pp.247-252.
- Mandeville J.C., McDonnell J.A.M., Alexander W.M., 1983, 'A Capacitor Impact Sensor (CIS) on board Giotto for detection of cometary dust particles', *Adv. Space Res.*, **2**, 12, pp.189-191.
- Massonne L., 1985, 'Coma morphology and dust emission pattern of comet Halley', *Adv. Space Res.*, **5**, 12, pp.187-196.
- Mazets E.P., Sagdeev R.Z., Aptekar R.C., Golenetskii S.V., Guryan Yu. A., Dyachkov A.V., Ilyinskii V.N., Panov V.N., Petrov G.G., Savvin A.V., Sokolov I.A., Frederiks D.D., Khavenson N.G., Shapiro V.D. and Schevchenko V.I., 1987, 'Dust in comet P/Halley from Vega observations', *Astron. Astrophys.*, **187**, pp.699-706.
- McDonnell J.A.M., 1969, 'Calibration studies on a piezoelectric sensing diaphragm for the detection of micrometeorites in space', *J. Phys. E.*, **2**, pp.1026-1030.
- McDonnell J.A.M., 1979, 'Marginal hypervelocity penetration studies of single and double foil structures: Experimental measurements and the possibilities of a 2MV microparticle accelerator for comet meteoroid probe design explored', *ESA SP-153*, pp. 93-97.

- McDonnell J.A.M., 1987, 'The Giotto dust impact detection system', *J. Phys. E.*, **20**, pp. 741-758.
- McDonnell J.A.M., Alexander M., Lyons D., Tanner W., Anz P., Hyde T., Chen A.L., Stevenson T.J. & Evans S.T., 1984, 'The impact of dust grains on fast fly-by spacecraft: momentum multiplication, measurements and theory', *Adv. Space Res.*, **4**, 9, pp. 297-301.
- McDonnell J.A.M., Alexander W.M., Burton W.M., Bussoletti E., Clark D.H., Evans G.C., Evans S.T., Firth J.G., Grard R.J.L., Grün E., Hanner M.S., Hughes D.W., Igenbergs E., Kuczera H., Lindblad B.A., Mandeville J.C., Minafra A., Reading D., Ridgeley A., Schwehm G.H., Stevenson T.J., Sekanina Z., Turner R.F., Wallis M.K. & Zarnecki J.C., 1986a, 'The Giotto dust impact detection system', *ESA SP-1077*, pp. 85-107.
- McDonnell J.A.M., Alexander W.M., Buurton W.M., Bussoletti E., Clark D.H., Grard R.J.L., Grün E., Hanner M.S., Hughes D.W., Igenbergs E., Kuczera H., Lindblad B.A., Mandeville J.C., Minafra A., Schwehm G.H., Sekanina Z., Turner R.F., Wallis M.K., Zarnecki J.C., Chakaveh S.C., Evans G.C., Evans S.T., Firth J.G., Littler A.N., Massone L., Olearczyk R.E., Pankiewicz G.S., Stevenson T.J. and Turner R.F., 1986b, 'Dust density and mass distribution near comet Halley from Giotto observations', *Nature*, **321**, pp.338-341.
- McDonnell J.A.M., Kissel J., Grün E., Grard R.J., Langevin Y., Olearczyk R.E., Perry C.H., and Zarnecki J.C., 1986c, 'Giotto's dust impact detections system DIDSY and particulate impact analyser PIA: interim assessment of the dust distribution and properties within the coma', *ESA SP-250, II*, pp.25-38.
- McDonnell J.A.M., Alexander W.M., Burton W.M., Bussoletti E., Evans G.C., Evans S.T., Firt J.G., Grard R.J.L., Grrn S.F., Grün E., Hanner M.S., Hughes D.W., Igenbergs E., Kissel J., Kuczera H., Lindblad B.A., Langevin Y., Mandeville J.C., Nappo S., Pankiewicz G.S., Perry C.H., Schwehm G.H., Sekanina Z., Stevenson T.J., Turner R.F., Weishaupt U., Wallis M.K., and Zarnecki J.C., 1987, 'The dust distribution within the inner coma of comet P/Halley 1982i: Encounter by Giotto's impact detectors', *Astron. Astrophys.*, **187**, pp.719-741.
- McDonnell J.A.M., Pankiewicz G.S., Birchley P.N.W., Green S.F., and Perry C.H., 1990, 'The Comet Nucleus: Ice and Dust Morphological Balances in a Production Surface of Comet P/Halley', *Proceedings of the 20th Lunar and Planetary Science Conference*, pp.373-378.

- Morley T.A. and Fertig J., **1986**, 'Giotto's encounter with comet Halley: a braking and shaking experience', *ESA Bull.*, **46**, pp.71-73.
- Naumann R.J., **1966**, 'The Pegasus micrometeoroid satellite', *NASA, Report TN-D 3717*.
- Olearczyk R.E., **1988**, 'A real-time data analysis system and a scientific database for the Dust Impact Detection System experiment on the European Space Agency's Halley Comet probe Giotto', *M.Sc. Thesis, Unit for Space Sciences, Physics Laboratory, University of Kent at Canterbury*.
- Pankiewicz G.S., Nappo S. and Perry C.H., **1988**, 'The Giotto - Halley encounter: Dust impact analysis at Kent', *JBIS*, **41**, pp.411-419
- Pankiewicz G.S., **1989**, 'Dust Environment Modelling from Encounters with Comet P/Halley', *Ph.D. Thesis, Unit for Space Sciences, Physics Laboratory, University of Kent at Canterbury*.
- Pankiewicz G.S., McDonnell J.A.M., and Perry C.H., **1989**, 'In-situ exploration of the dusty coma of comet P/Halley at Giotto's encounter: Nucleus emission and production rates from temporal variability', *Adv. Space Res.*, **9**, 3, pp.273-276.
- Perry C.H., Green S.F. & McDonnell J.A.M., **1987**, 'A possible explanation for the inconsistency between the Giotto grain mass distribution and groundbased observations', in '*Infrared observations of comets Halley and Wilson and properties of the grains*', *NASA conference publication 3004*, pp. 178-180.
- Perry C.H. and Nappo S., 'A Search for non-random effects in Giotto dust impact data', *Poster paper presented at Comets, Asteroids, Meteors III, Uppsala, June 12-15, 1989*.
- Pockentrup, 1984 PIA Software design manual, Dornier Systems.
- Probstein R.F., 1969, 'The dusty gas dynamics of comet heads', in '*Problems of hydrodynamics and continuum mechanics*', Philadelphia, pp.568-583.
- RCA, 1977, 'User Manual for the CDP1802 COSMAC Microprocessor'
- Reading D.H. and Ridgeley A., **1983**, 'Design optimisation studies for the Giotto spacecraft front shield using pulsed laser energy to initiate a flexural wave motion', *Rutherford Appleton Laboratory, Report RL-83-024*.

- Reinhard R., **1979**, 'Preliminary design concepts for the Halley probe shield', *ESA SP-153*, pp.7-15.
- Reinhard R., **1981**, in 'Scientific and experimental aspects of the Giotto mission', *ESA SP-169*, pp.ix-xix.
- Reinhard R., **1986**, 'Halley's Comet as an Outstanding Target', *ESA SP-1066*, pp.vii-xvi.
- Reinhard R., **1988**, 'The Giotto mission to Halley's Comet', in '*Exploration of Halley's Comet*', Springer-Verlag, pp.949-958.
- Ridgeley A., **1985**, 'A report on the mapping of the DIDSY sensor responses as a function of micro-meteorite impact position on the Giotto bumper shield', *Rutherford Appleton Laboratory, Report RL-85-108*.
- Sagdeev R.Z., Linkin V.M., Kezhanovich V.V., Lipatov A.N., Shurupov A.A., Blamont J.E., Crisp D., Ingersoll A.P., Elson C.S., Preston R.A., Hildebrand C.E., Ragent B., Seiff A., Young R.E., Petit G., Boloh L., Alexandrov Yu. N., Armand N.A., Bakitko R.V. and Selivanov A.S., **1986a**, 'Overview of Vega Venus balloon in-situ meteorological measurements', *Science*, **231**, pp.1411-1414.
- Sagdeev R.Z., Krasikov V.A., Shamis V.A., Tarnopolski V.I., Szego K., Toth I., Smith B., Larson S., and Merenyi E., **1986b**, 'Rotation period and spin axis of comet Halley', *ESA SP-250, II*, pp.335-338.
- Sagdeev R.Z., Evlanov E.N., Fomenkova M.N., Prilutskii O.F. and Zubkov B.V., **1989**, 'Small-size dust particles near Halley's Comet', *Adv. Space Res.*, **9**, 3, pp.263-267.
- Simpson J.A., Rabinowitz D., Tuzzolino A.J., Ksanfomality L.V. Ksanfomality, and Sagdeev R.Z., **1987**, 'The dust coma of comet P/Halley: measurements on the Vega-1 and Vega-2 spacecraft', *Astron. Astrophys.*, **187**, pp.742-752.
- Sykes M.V., Lebofsky L.A., Hunten D.M., and Low F., **1986**, 'The discovery of dust trails in the orbits of periodic comets', *Science*, **232**, pp.1115-1117.
- Trotignon J.G., Béghin C., Grard R., Pedersen A., Formisano V., Mogilevsky M., and Mikhailov Y., **1987**, 'Dust observations of comet P/Halley by the plasma-wave analyser', *Astron. Astrophys.*, **187**, pp.83-88.
- Vaisberg O.L., Smirnov V.N., Gorn L.S., Iovlev M.V., Balichkin M.A., Klimov S.I., Savin S.P., Shapiro V.D., and Schevchenko V.I., **1986**, 'Dust coma

- structure of comet Halley from SP-1 detector measurements', *Nature*, **321**, pp.274-276.
- Vaisberg O.L., Smirnov V., Omelchenko A. Gorn L. and Iovlev M., **1987**, 'Spatial and mass distribution of low mass dust particles ($m < 10^{-10}g$) in comet P/Halley's coma', *Astron. Astrophys.*, **187**, pp.753-760.
- Wallis M.K., **1986**, 'Hypervelocity dust impulses on the comet Halley probes', *Planet. Space Sci.*, **34**, 11, pp.1087-1089.
- Whipple F.L., **1950**, 'A comet model. I. The acceleration of comet Encke', *Ap. J.*, **111**, pp.375-394.
- Zarnecki J.C., **1988**, 'Giotto dust impact detection system: instrument and in-flight performance', *JBIS*, **41**, pp.403-409.
- Zarnecki J.C., McDonnell J.A.M., Alexander W.M., Burton W.M., and Hanner M.S., **1986**, 'Mass distribution of particulates measured by Giotto's dust impact detection system (DIDSY) in the close encounter period', *ESA SP-250, II*, pp.185-190.

APPENDIX 1

The DIDSY flight software.

```

0000 | 0001          ..VERSION 0016.A01      20-MAY-84
0000 | 0002          ..
0000 | 0003          .. MAJOR CHANGE (V16) BECAUSE OF TOTAL TIME TO
0000 | 0004          .. SERVICE NRM AND IPWP FLASB UNOLS DATA BLOCKS ON
0000 | 0005          .. ME MERGED. EXTRA TEST INSERTED AFTER IPWP EVENT
0000 | 0006          .. TO PREVENT PROBLEMS. SOF (NRM FLASB) INCORPORATED
0000 | 0007          .. TO CHANGE NO LOCKOUT OF IPWP OR NRM WHEN NRM
0000 | 0008          .. DATA RATE EXCEEDED. (20-MAY-84)
0000 | 0009          .. CHANGED IDEAS. CAL PALSE AT HYDRAONE RESET AT FORMAT
0000 | 0010          .. START. OCCASIONAL IPWP RESET (IPWPACK) WHEN LOW 6 BITS
0000 | 0011          .. OF BLOCK COUNTER GO TO ZERO ("EVERY 17 BLOCKS")
0000 | 0012          .. ACQUISITION OF OFFER CAPABILITY TO IPWP
0000 | 0013          .. NRM AND IPWP OFFSETS SET TO FLIGHT VALUE (20/3/84)
0000 | 0014          ..
0000 | 0015          ..-----
0000 | 0016          .. ADDRESS ALLOCATIONS
0000 | 0017          ..-----
0000 | 0018          ..IPWP  PRG0+1000H+101FH INCLUSIVE
0000 | 0019          ..IPWP  HARDWARE ACCUMULATOR RESET      LHM 1000H+101FH
0000 | 0020          ..IPWP  DISCRETE DATA RESET              LHM 1023H
0000 | 0021          ..NRM/NRM  HEAD  PRG0+(1040H+1.5*8H)
0000 | 0022          ..NRM  COINCIDENCE CONTROL REGISTER(CCR) PRG0+(1040H)
0000 | 0023          ..NRM/NRM  TIRING MGRD PRG0+(1048H)
0000 | 0024          ..NRM/NRM  THRESHOLD SETTING PRG0+(1048H+P.A.*8H)
0000 | 0025          ..NRM/NRM  ACKNOWLEDGE PRG0+1020H (WITH NAO=0)
0000 | 0026          ..IPWP  READ  WRITE PRG0+102FH
0000 | 0027          ..IPWP  ACKNOWLEDGE PRG0+102FH (WITH NAO=0)
0000 | 0028          ..CIS  PRG0+1040H
0000 | 0029          ..AND IPWP ACCUMULATORS ARE AT PRG0+100H+61FH
0000 | 0030          ..STACK/SCRATCHPAD RAM PRG0+630H+67FH
0000 | 0031          ..-----
0000 | 0032          .. REGISTER ALLOCATIONS
0000 | 0033          ..-----
0000 | 0034          ..R0 = DMA POINTER
0000 | 0035          ..R1 = LOOKUP TABLE POINTER
0000 | 0036          ..R2 = STACK POINTER-STACK ADDRESS PRG0+600
0000 | 0037          ..R3 = NRM PROGRAM COUNTER
0000 | 0038          ..R4.0 = WORD/FRAME COUNTER
0000 | 0039          ..R4.1 = DATA UPDATE BLOCK SELECT
0000 | 0040          ..R5 = BLOCK COUNTER
0000 | 0041          ..R6 = DATA UPDATE POINTER
0000 | 0042          ..R7 = NRM MAGNITUDE BUFFER POINTER
0000 | 0043          ..R8.0 = NRM HOSE COUNTER
0000 | 0044          ..R8.1 = NRM HOSE STORE
0000 | 0045          ..R9 = DATA GATHER POINTER
0000 | 0046          ..RA = PC FOR EVENT MAGNITUDE COMPUTING ROUTINE
0000 | 0047          ..RB = PC FOR CIS READ
0000 | 0048          ..RC = PC FOR IPWP ACCUMULATOR READ
0000 | 0049          ..RD = IPWP SCRATCHPAD POINTER
0000 | 0050          ..RE.0 = DATA BLOCK UPDATE SWITCH
0000 | 0051          ..RE.1 = DATA BLOCK FOLLOWER
0000 | 0052          ..RF = GENERAL POINTER/COUNTER
0000 | 0053          ..
0000 | 0054          ..FLAG 1 = NRM HOSE INPUT
0000 | 0055          ..FLAG 2 = IPWP EVENT FLAG
0000 | 0056          ..
0000 | 0057          ..FLAG 3 = IPWP EVENT FLAG
0000 | 0058          ..FLAG 4 = NRM EVENT FLAG
0000 | 0059          ..
0000 | 0060          ..-----
0000 | 0061          .. POWER-UP AND FORMAT START ROUTINE
0000 | 0062          ..-----

0000 | 0063  PRG0    EQU 0H
0000 | 0064  INDATA EQU PRG0+1000H
0000 | 0065  LOOK    EQU 01H
0000 | 0066  COMPJ   EQU 02H
0000 | 0067  COUNT   EQU 03H
0000 | 0068  CIBRD   EQU 04H
0000 | 0069  IPWPAD  EQU 05H
0000 | 0070  IPWPAC EQU 07H
0000 | 0071  IPWPOR EQU 08H
0000 | 0072          ..
0000 | 0073          .. MINIMUM DELAY BETWEEN IPWP
0000 | 0074          .. REQUEST (RFP2) AND IPWP DATA READ
0000 | 0075          .. (ABOUT 1MS)
0000 | 0076  STACK  EQU PRG0+67FH
0000 | 0077  ACCET  EQU PRG0+630H
0000 | 0078  HOSEUB EQU INDATA+0CH
0000 | 0079  TMDL   EQU 4
0000 | 0080          ..
0000 | 0081          .. DELAY BETWEEN NRM REQUEST AND
0000 | 0082          .. TIRING WORD READ
0000 | 0083          .. DELAY BETWEEN NRM WRITES AND ACK
0000 | 0084          .. START UP HOSE AS PER TABLE
0000 | 0085          ..-----
0000 | 0086          .. VALUE      HOSE
0000 | 0087          .. 00H      0 STATIC
0000 | 0088          .. 01H      1 STATIC
0000 | 0089          .. 02H      2 STATIC
0000 | 0090          .. 03H      3 STATIC
0000 | 0091          .. 04H      0 AUTO
0000 | 0092          .. 05H      1 AUTO
0000 | 0093          .. 06H      2 AUTO
0000 | 0094          .. 07H      3 AUTO
0000 | 0095          ..-----
0000 | 0096          ORG PRG0
0000 | 0097          ..
0000 | 0098          .. CLEAR OUT ANY PENDING DMA'S
0000 | 0099          .. AND IPWP TEST PALSE GOES OFF
0000 | 0100          .. SET UP R0 SO THAT DMA'S DMA
0000 | 0101          .. CAN CO MEND
0000 | 0102          ..
0000 | 0103  START  SEI  REGI  REG
0000 | 0104          ..
0000 | 0105  LD  A,0(PC3)
0000 | 0106  PL0 R0
0000 | 0107  LD  A,1(PC3)
0000 | 0108  PL0 R0
0000 | 0109  SEP R0
0000 | 0110  PC3    PL0 R01 PL0 R8
0000 | 0111  LD  COUNT1 PL0 R8
0000 | 0112  LD  SNOOZE1 PH1 R8
0000 | 0113  INC R4
0000 | 0114          .. SET RA.1 TO STARTING HOSE
0000 | 0115          .. SET RA.0 READY FOR IPWP ACC READ
0000 | 0116          .. DATA INPUT POINTER
0000 | 0117          ..
0000 | 0118          .. SET UP STACK POINTER
0000 | 0119          .. AND BUS ROUTINE POINTERS
0000 | 0120          ..
0000 | 0121  LD  A,1(INDATA); PH1 R9
0000 | 0122  LD  A,0(INDATA); PH1 R9
0000 | 0123  LD  A,1(STACK); PH1 R2
0000 | 0124  LD  A,1(COMP);
0000 | 0125  PH1 LOOK
0000 | 0126  PH1 CIBRD
0000 | 0127  PH1 IPWPAC
0000 | 0128  LD  A,0(COMP);
0000 | 0129  PL0 COMPJ
0000 | 0130  LD  A,0(CIBRD);
0000 | 0131  PL0 CIBRD
0000 | 0132  LD  A,0(IPWPAC);
0000 | 0133  LD  A,0(IPWPAC);
0000 | 0134  LD  A,0(IPWPAC);
0000 | 0135  LD  A,0(IPWPAC);
0000 | 0136  LD  A,0(IPWPAC);
0000 | 0137  LD  A,0(IPWPAC);
0000 | 0138  LD  A,0(IPWPAC);
0000 | 0139  LD  A,0(IPWPAC);
0000 | 0140  LD  A,0(IPWPAC);
0000 | 0141  LD  A,0(IPWPAC);
0000 | 0142  LD  A,0(IPWPAC);
0000 | 0143  LD  A,0(IPWPAC);
0000 | 0144  LD  A,0(IPWPAC);
0000 | 0145  LD  A,0(IPWPAC);
0000 | 0146  LD  A,0(IPWPAC);
0000 | 0147  LD  A,0(IPWPAC);
0000 | 0148  LD  A,0(IPWPAC);
0000 | 0149  LD  A,0(IPWPAC);
0000 | 0150  LD  A,0(IPWPAC);
0000 | 0151  LD  A,0(IPWPAC);
0000 | 0152  LD  A,0(IPWPAC);
0000 | 0153  LD  A,0(IPWPAC);
0000 | 0154  LD  A,0(IPWPAC);
0000 | 0155  LD  A,0(IPWPAC);
0000 | 0156  LD  A,0(IPWPAC);
0000 | 0157  LD  A,0(IPWPAC);
0000 | 0158  LD  A,0(IPWPAC);
0000 | 0159  LD  A,0(IPWPAC);
0000 | 0160  LD  A,0(IPWPAC);
0000 | 0161  LD  A,0(IPWPAC);
0000 | 0162  LD  A,0(IPWPAC);
0000 | 0163  LD  A,0(IPWPAC);
0000 | 0164  LD  A,0(IPWPAC);
0000 | 0165  LD  A,0(IPWPAC);
0000 | 0166  LD  A,0(IPWPAC);
0000 | 0167  LD  A,0(IPWPAC);
0000 | 0168  LD  A,0(IPWPAC);
0000 | 0169  LD  A,0(IPWPAC);
0000 | 0170  LD  A,0(IPWPAC);
0000 | 0171  LD  A,0(IPWPAC);
0000 | 0172  LD  A,0(IPWPAC);
0000 | 0173  LD  A,0(IPWPAC);
0000 | 0174  LD  A,0(IPWPAC);
0000 | 0175  LD  A,0(IPWPAC);
0000 | 0176  LD  A,0(IPWPAC);
0000 | 0177  LD  A,0(IPWPAC);
0000 | 0178  LD  A,0(IPWPAC);
0000 | 0179  LD  A,0(IPWPAC);
0000 | 0180  LD  A,0(IPWPAC);
0000 | 0181  LD  A,0(IPWPAC);
0000 | 0182  LD  A,0(IPWPAC);
0000 | 0183  LD  A,0(IPWPAC);
0000 | 0184  LD  A,0(IPWPAC);
0000 | 0185  LD  A,0(IPWPAC);
0000 | 0186  LD  A,0(IPWPAC);
0000 | 0187  LD  A,0(IPWPAC);
0000 | 0188  LD  A,0(IPWPAC);
0000 | 0189  LD  A,0(IPWPAC);
0000 | 0190  LD  A,0(IPWPAC);
0000 | 0191  LD  A,0(IPWPAC);
0000 | 0192  LD  A,0(IPWPAC);
0000 | 0193  LD  A,0(IPWPAC);
0000 | 0194  LD  A,0(IPWPAC);
0000 | 0195  LD  A,0(IPWPAC);
0000 | 0196  LD  A,0(IPWPAC);
0000 | 0197  LD  A,0(IPWPAC);
0000 | 0198  LD  A,0(IPWPAC);
0000 | 0199  LD  A,0(IPWPAC);
0000 | 0200  LD  A,0(IPWPAC);
0000 | 0201  LD  A,0(IPWPAC);
0000 | 0202  LD  A,0(IPWPAC);
0000 | 0203  LD  A,0(IPWPAC);
0000 | 0204  LD  A,0(IPWPAC);
0000 | 0205  LD  A,0(IPWPAC);
0000 | 0206  LD  A,0(IPWPAC);
0000 | 0207  LD  A,0(IPWPAC);
0000 | 0208  LD  A,0(IPWPAC);
0000 | 0209  LD  A,0(IPWPAC);
0000 | 0210  LD  A,0(IPWPAC);
0000 | 0211  LD  A,0(IPWPAC);
0000 | 0212  LD  A,0(IPWPAC);
0000 | 0213  LD  A,0(IPWPAC);
0000 | 0214  LD  A,0(IPWPAC);
0000 | 0215  LD  A,0(IPWPAC);
0000 | 0216  LD  A,0(IPWPAC);
0000 | 0217  LD  A,0(IPWPAC);
0000 | 0218  LD  A,0(IPWPAC);
0000 | 0219  LD  A,0(IPWPAC);
0000 | 0220  LD  A,0(IPWPAC);
0000 | 0221  LD  A,0(IPWPAC);
0000 | 0222  LD  A,0(IPWPAC);
0000 | 0223  LD  A,0(IPWPAC);
0000 | 0224  LD  A,0(IPWPAC);
0000 | 0225  LD  A,0(IPWPAC);
0000 | 0226  LD  A,0(IPWPAC);
0000 | 0227  LD  A,0(IPWPAC);
0000 | 0228  LD  A,0(IPWPAC);
0000 | 0229  LD  A,0(IPWPAC);
0000 | 0230  LD  A,0(IPWPAC);
0000 | 0231  LD  A,0(IPWPAC);
0000 | 0232  LD  A,0(IPWPAC);
0000 | 0233  LD  A,0(IPWPAC);
0000 | 0234  LD  A,0(IPWPAC);
0000 | 0235  LD  A,0(IPWPAC);
0000 | 0236  LD  A,0(IPWPAC);
0000 | 0237  LD  A,0(IPWPAC);
0000 | 0238  LD  A,0(IPWPAC);
0000 | 0239  LD  A,0(IPWPAC);
0000 | 0240  LD  A,0(IPWPAC);
0000 | 0241  LD  A,0(IPWPAC);
0000 | 0242  LD  A,0(IPWPAC);
0000 | 0243  LD  A,0(IPWPAC);
0000 | 0244  LD  A,0(IPWPAC);
0000 | 0245  LD  A,0(IPWPAC);
0000 | 0246  LD  A,0(IPWPAC);
0000 | 0247  LD  A,0(IPWPAC);
0000 | 0248  LD  A,0(IPWPAC);
0000 | 0249  LD  A,0(IPWPAC);
0000 | 0250  LD  A,0(IPWPAC);
0000 | 0251  LD  A,0(IPWPAC);
0000 | 0252  LD  A,0(IPWPAC);
0000 | 0253  LD  A,0(IPWPAC);
0000 | 0254  LD  A,0(IPWPAC);
0000 | 0255  LD  A,0(IPWPAC);
0000 | 0256  LD  A,0(IPWPAC);
0000 | 0257  LD  A,0(IPWPAC);
0000 | 0258  LD  A,0(IPWPAC);
0000 | 0259  LD  A,0(IPWPAC);
0000 | 0260  LD  A,0(IPWPAC);
0000 | 0261  LD  A,0(IPWPAC);
0000 | 0262  LD  A,0(IPWPAC);
0000 | 0263  LD  A,0(IPWPAC);
0000 | 0264  LD  A,0(IPWPAC);
0000 | 0265  LD  A,0(IPWPAC);
0000 | 0266  LD  A,0(IPWPAC);
0000 | 0267  LD  A,0(IPWPAC);
0000 | 0268  LD  A,0(IPWPAC);
0000 | 0269  LD  A,0(IPWPAC);
0000 | 0270  LD  A,0(IPWPAC);
0000 | 0271  LD  A,0(IPWPAC);
0000 | 0272  LD  A,0(IPWPAC);
0000 | 0273  LD  A,0(IPWPAC);
0000 | 0274  LD  A,0(IPWPAC);
0000 | 0275  LD  A,0(IPWPAC);
0000 | 0276  LD  A,0(IPWPAC);
0000 | 0277  LD  A,0(IPWPAC);
0000 | 0278  LD  A,0(IPWPAC);
0000 | 0279  LD  A,0(IPWPAC);
0000 | 0280  LD  A,0(IPWPAC);
0000 | 0281  LD  A,0(IPWPAC);
0000 | 0282  LD  A,0(IPWPAC);
0000 | 0283  LD  A,0(IPWPAC);
0000 | 0284  LD  A,0(IPWPAC);
0000 | 0285  LD  A,0(IPWPAC);
0000 | 0286  LD  A,0(IPWPAC);
0000 | 0287  LD  A,0(IPWPAC);
0000 | 0288  LD  A,0(IPWPAC);
0000 | 0289  LD  A,0(IPWPAC);
0000 | 0290  LD  A,0(IPWPAC);
0000 | 0291  LD  A,0(IPWPAC);
0000 | 0292  LD  A,0(IPWPAC);
0000 | 0293  LD  A,0(IPWPAC);
0000 | 0294  LD  A,0(IPWPAC);
0000 | 0295  LD  A,0(IPWPAC);
0000 | 0296  LD  A,0(IPWPAC);
0000 | 0297  LD  A,0(IPWPAC);
0000 | 0298  LD  A,0(IPWPAC);
0000 | 0299  LD  A,0(IPWPAC);
0000 | 0300  LD  A,0(IPWPAC);
0000 | 0301  LD  A,0(IPWPAC);
0000 | 0302  LD  A,0(IPWPAC);
0000 | 0303  LD  A,0(IPWPAC);
0000 | 0304  LD  A,0(IPWPAC);
0000 | 0305  LD  A,0(IPWPAC);
0000 | 0306  LD  A,0(IPWPAC);
0000 | 0307  LD  A,0(IPWPAC);
0000 | 0308  LD  A,0(IPWPAC);
0000 | 0309  LD  A,0(IPWPAC);
0000 | 0310  LD  A,0(IPWPAC);
0000 | 0311  LD  A,0(IPWPAC);
0000 | 0312  LD  A,0(IPWPAC);
0000 | 0313  LD  A,0(IPWPAC);
0000 | 0314  LD  A,0(IPWPAC);
0000 | 0315  LD  A,0(IPWPAC);
0000 | 0316  LD  A,0(IPWPAC);
0000 | 0317  LD  A,0(IPWPAC);
0000 | 0318  LD  A,0(IPWPAC);
0000 | 0319  LD  A,0(IPWPAC);
0000 | 0320  LD  A,0(IPWPAC);
0000 | 0321  LD  A,0(IPWPAC);
0000 | 0322  LD  A,0(IPWPAC);
0000 | 0323  LD  A,0(IPWPAC);
0000 | 0324  LD  A,0(IPWPAC);
0000 | 0325  LD  A,0(IPWPAC);
0000 | 0326  LD  A,0(IPWPAC);
0000 | 0327  LD  A,0(IPWPAC);
0000 | 0328  LD  A,0(IPWPAC);
0000 | 0329  LD  A,0(IPWPAC);
0000 | 0330  LD  A,0(IPWPAC);
0000 | 0331  LD  A,0(IPWPAC);
0000 | 0332  LD  A,0(IPWPAC);
0000 | 0333  LD  A,0(IPWPAC);
0000 | 0334  LD  A,0(IPWPAC);
0000 | 0335  LD  A,0(IPWPAC);
0000 | 0336  LD  A,0(IPWPAC);
0000 | 0337  LD  A,0(IPWPAC);
0000 | 0338  LD  A,0(IPWPAC);
0000 | 0339  LD  A,0(IPWPAC);
0000 | 0340  LD  A,0(IPWPAC);
0000 | 0341  LD  A,0(IPWPAC);
0000 | 0342  LD  A,0(IPWPAC);
0000 | 0343  LD  A,0(IPWPAC);
0000 | 0344  LD  A,0(IPWPAC);
0000 | 0345  LD  A,0(IPWPAC);
0000 | 0346  LD  A,0(IPWPAC);
0000 | 0347  LD  A,0(IPWPAC);
0000 | 0348  LD  A,0(IPWPAC);
0000 | 0349  LD  A,0(IPWPAC);
0000 | 0350  LD  A,0(IPWPAC);
0000 | 0351  LD  A,0(IPWPAC);
0000 | 0352  LD  A,0(IPWPAC);
0000 | 0353  LD  A,0(IPWPAC);
0000 | 0354  LD  A,0(IPWPAC);
0000 | 0355  LD  A,0(IPWPAC);
0000 | 0356  LD  A,0(IPWPAC);
0000 | 0357  LD  A,0(IPWPAC);
0000 | 0358  LD  A,0(IPWPAC);
0000 | 0359  LD  A,0(IPWPAC);
0000 | 0360  LD  A,0(IPWPAC);
0000 | 0361  LD  A,0(IPWPAC);
0000 | 0362  LD  A,0(IPWPAC);
0000 | 0363  LD  A,0(IPWPAC);
0000 | 0364  LD  A,0(IPWPAC);
0000 | 0365  LD  A,0(IPWPAC);
0000 | 0366  LD  A,0(IPWPAC);
0000 | 0367  LD  A,0(IPWPAC);
0000 | 0368  LD  A,0(IPWPAC);
0000 | 0369  LD  A,0(IPWPAC);
0000 | 0370  LD  A,0(IPWPAC);
0000 | 0371  LD  A,0(IPWPAC);
0000 | 0372  LD  A,0(IPWPAC);
0000 | 0373  LD  A,0(IPWPAC);
0000 | 0374  LD  A,0(IPWPAC);
0000 | 0375  LD  A,0(IPWPAC);
0000 | 0376  LD  A,0(IPWPAC);
0000 | 0377  LD  A,0(IPWPAC);
0000 | 0378  LD  A,0(IPWPAC);
0000 | 0379  LD  A,0(IPWPAC);
0000 | 0380  LD  A,0(IPWPAC);
0000 | 0381  LD  A,0(IPWPAC);
0000 | 0382  LD  A,0(IPWPAC);
0000 | 0383  LD  A,0(IPWPAC);
0000 | 0384  LD  A,0(IPWPAC);
0000 | 0385  LD  A,0(IPWPAC);
0000 | 0386  LD  A,0(IPWPAC);
0000 | 0387  LD  A,0(IPWPAC);
0000 | 0388  LD  A,0(IPWPAC);
0000 | 0389  LD  A,0(IPWPAC);
0000 | 0390  LD  A,0(IPWPAC);
0000 | 0391  LD  A,0(IPWPAC);
0000 | 0392  LD  A,0(IPWPAC);
0000 | 0393  LD  A,0(IPWPAC);
0000 | 0394  LD  A,0(IPWPAC);
0000 | 0395  LD  A,0(IPWPAC);
0000 | 0396  LD  A,0(IPWPAC);
0000 | 0397  LD  A,0(IPWPAC);
0000 | 0398  LD  A,0(IPWPAC);
0000 | 0399  LD  A,0(IPWPAC);
0000 | 0400  LD  A,0(IPWPAC);
0000 | 0401  LD  A,0(IPWPAC);
0000 | 0402  LD  A,0(IPWPAC);
0000 | 0403  LD  A,0(IPWPAC);
0000 | 0404  LD  A,0(IPWPAC);
0000 | 0405  LD  A,0(IPWPAC);
0000 | 0406  LD  A,0(IPWPAC);
0000 | 0407  LD  A,0(IPWPAC);
0000 | 0408  LD  A,0(IPWPAC);
0000 | 0409  LD  A,0(IPWPAC);
0000 | 0410  LD  A,0(IPWPAC);
0000 | 0411  LD  A,0(IPWPAC);
0000 | 0412  LD  A,0(IPWPAC);
0000 | 0413  LD  A,0(IPWPAC);
0000 | 0414  LD  A,0(IPWPAC);
0000 | 0415  LD  A,0(IPWPAC);
0000 | 0416  LD  A,0(IPWPAC);
0000 | 0417  LD  A,0(IPWPAC);
0000 | 0418  LD  A,0(IPWPAC);
0000 | 0419  LD  A,0(IPWPAC);
0000 | 0420  LD  A,0(IPWPAC);
0000 | 0421  LD  A,0(IPWPAC);
0000 | 0422  LD  A,0(IPWPAC);
0000 | 0423  LD  A,0(IPWPAC);
0000 | 0424  LD  A,0(IPWPAC);
0000 | 0425  LD  A,0(IPWPAC);
0000 | 0426  LD  A,0(IPWPAC);
0000 | 0427  LD  A,0(IPWPAC);
0000 | 0428  LD  A,0(IPWPAC);
0000 | 0429  LD  A,0(IPWPAC);
0000 | 0430  LD  A,0(IPWPAC);
0000 | 0431  LD  A,0(IPWPAC);
0000 | 0432  LD  A,0(IPWPAC);
0000 | 0433  LD  A,0(IPWPAC);
0000 | 0434  LD  A,0(IPWPAC);
0000 | 0435  LD  A,0(IPWPAC);
0000 | 0436  LD  A,0(IPWPAC);
0000 | 0437  LD  A,0(IPWPAC);
0000 | 0438  LD  A,0(IPWPAC);
0000 | 0439  LD  A,0(IPWPAC);
0000 | 0440  LD  A,0(IPWPAC);
0000 | 0441  LD  A,0(IPWPAC);
0000 | 0442  LD  A,0(IPWPAC);
0000 | 0443  LD  A,0(IPWPAC);
0000 | 0444  LD  A,0(IPWPAC);
0000 | 0445  LD  A,0(IPWPAC);
0000 | 0446  LD  A,0(IPWPAC);
0000 | 0447  LD  A,0(IPWPAC);
0000 | 0448  LD  A,0(IPWPAC);
0000 | 0449  LD  A,0(IPWPAC);
0000 | 0450  LD  A,0(IPWPAC);
0000 | 0451  LD  A,0(IPWPAC);
0000 | 0452  LD  A,0(IPWPAC);
0000 | 0453  LD  A,0(IPWPAC);
0000 | 0454  LD  A,0(IPWPAC);
0000 | 0455  LD  A,0(IPWPAC);
0000 | 0456  LD  A,0(IPWPAC);
0000 | 0457  LD  A,0(IPWPAC);
0000 | 0458  LD  A,0(IPWPAC);
0000 | 0459  LD  A,0(IPWPAC);
0000 | 0460  LD  A,0(IPWPAC);
0000 | 0461  LD  A,0(IPWPAC);
0000 | 0462  LD  A,0(IPWPAC);
0000 | 0463  LD  A,0(IPWPAC);
0000 | 0464  LD  A,0(IPWPAC);
0000 | 0465  LD  A,0(IPWPAC);
0000 | 0466  LD  A,0(IPWPAC);
0000 | 0467  LD  A,0(IPWPAC);
0000 | 0468  LD  A,0(IPWPAC);
0000 | 0469  LD  A,0(IPWPAC);
0000 | 0470  LD  A,0(IPWPAC);
0000 | 0471  LD  A,0(IPWPAC);
0000 | 0472  LD  A,0(IPWPAC);
0000 | 0473  LD  A,0(IPWPAC);
0000 | 0474  LD  A,0(IPWPAC);
0000 | 0475  LD  A,0(IPWPAC);
0000 | 0476  LD  A,0(IPWPAC);
0000 | 0477  LD  A,0(IPWPAC);
0000 | 0478  LD  A,0(IPWPAC);
0000 | 0479  LD  A,0(IPWPAC);
0000 | 0480  LD  A,0(IPWPAC);
0000 | 0481  LD  A,0(IPWPAC);
0000 | 0482  LD  A,0(IPWPAC);
0000 | 0483  LD  A,0(IPWPAC);
0000 | 0484  LD  A,0(IPWPAC);
0000 | 0485  LD  A,0(IPWPAC);
0000 | 0486  LD  A,0(IPWPAC);
0000 | 0487  LD  A,0(IPWPAC);
0000 | 0488  LD  A,0(IPWPAC);
0000 | 0489  LD  A,0(IPWPAC);
0000 | 0490  LD  A,0(IPWPAC);
0000 | 0491  LD  A,0(IPWPAC);
0000 | 0492  LD  A,0(IPWPAC);
0000 | 0493  LD  A,0(IPWPAC);
0000 | 0494  LD  A,0(IPWPAC);
0000 | 0495  LD  A,0(IPWPAC);
0000 | 0496  LD  A,0(IPWPAC);
0000 | 0497  LD  A,0(IPWPAC);
0000 | 0498  LD  A,0(IPWPAC);
0000 | 0499  LD  A,0(IPWPAC);
0000 | 0500  LD  A,0(IPWPAC);
0000 | 0501  LD  A,0(IPWPAC);
0000 | 0502  LD  A,0(IPWPAC);
0000 | 0503  LD  A,0(IPWPAC);
0000 | 0504  LD  A,0(IPWPAC);
0000 | 0505  LD  A,0(IPWPAC);
0000 | 0506  LD  A,0(IPWPAC);
0000 | 0507  LD  A,0(IPWPAC);
0000 | 0508  LD  A,0(IPWPAC);
0000 | 0509  LD  A,0(IPWPAC);
0000 | 0510  LD  A,0(IPWPAC);
0000 | 0511  LD  A,0(IPWPAC);
0000 | 0512  LD  A,0(IPWPAC);
0000 | 0513  LD  A,0(IPWPAC);
0000 | 0514  LD  A,0(IPWPAC);
0000 | 0515  LD  A,0(IPWPAC);
0000 | 0516  LD  A,0(IPWPAC);
0000 | 0517  LD  A,0(IPWPAC);
0000 | 0518  LD  A,0(IPWPAC);
0000 | 0519  LD  A,0(IPWPAC);
0000 | 0520  LD  A,0(IPWPAC);
0000 | 0521  LD  A,0(IPWPAC);
0000 | 0522  LD  A,0(IPWPAC);
0000 | 0523  LD  A,0(IPWPAC);
0000 | 0524  LD  A,0(IPWPAC);
0000 | 0525  LD  A,0(IPWPAC);
0000 | 0526  LD  A,0(IPWPAC);
0000 | 0527  LD  A,0(IPWPAC);
0000 | 0528  LD  A,0(IPWPAC);
0000 | 0529  LD  A,0(IPWPAC);
0000 | 0530  LD  A,0(IPWPAC);
0000 | 0531  LD  A,0(IPWPAC);
0000 | 0532  LD  A,0(IPWPAC);
0000 | 0533  LD  A,0(IPWPAC);
0000 | 0534  LD  A,0(IPWPAC);
0000 | 0535  LD  A,0(IPWPAC);
0000 | 0536  LD  A,0(IPWPAC);
0000 | 0537  LD  A,0(IPWPAC);
0000 | 0538  LD  A,0(IPWPAC);
0000 | 0539  LD  A,0(IPWPAC);
0000 | 0540  LD  A,0(IPWPAC);
0000 | 0541  LD  A,0(IPWPAC);
0000 | 0542  LD  A,0(IPWPAC);
0000 | 0543  LD  A,0(IPWPAC);
0000 | 0544  LD  A,0(IPWPAC);
0000 | 0545  LD  A,0(IPWPAC);
0000 | 0546  LD  A,0(IPWPAC);
0000 | 0547  LD  A,0(IPWPAC);
0000 | 0548  LD  A,0(IPWPAC);
0000 | 0549  LD  A,0(IPWPAC);
0000 | 0550  LD  A,0(IPWPAC);
0000 | 0551  LD  A,0(IPWPAC);
0000 | 0552  LD  A,0(IPWPAC);
0000 | 0553  LD  A,0(IPWPAC);
0000 | 0554  LD  A,0(IPWPAC);
0000 | 0555  LD  A,0(IPWPAC);
0000 | 0556  LD  A,0(IPWPAC);
0000 | 0557  LD  A,0(IPWPAC);
0000 | 0558  LD  A,0(IPWPAC);
0000 | 0559  LD  A,0(IPWPAC);
0000 | 0560  LD  A,0(IPWPAC);
0000 | 0561  LD  A,0(IPWPAC);
0000 | 0562  LD  A,0(IPWPAC);
0000 | 0563  LD  A,0(IPWPAC);
0000 | 0564  LD  A,0(IPWPAC);
0000 | 0565  LD  A,0(IPWPAC);
0000 | 0566  LD  A,0(IPWPAC);
0000 | 0567  LD  A,0(IPWPAC);
0000 | 0568  LD  A,0(IPWPAC);
0000 | 0569  LD  A,0(IPWPAC);
0000 | 0570  LD  A,0(IPWPAC);
0000 | 0571  LD  A,0(IPWPAC);
0000 | 0572  LD  A,0(IPWPAC);
0000 | 0573  LD  A,0(IPWPAC);
0000 | 0574  LD  A,0(IPWPAC);
0000 | 0575  LD  A,0(IPWPAC);
0000 | 0576  LD  A,0(IPWPAC);
0000 | 0577  LD  A,0(IPWPAC);
0000 | 0578  LD  A,0(IPWPAC);
0000 | 0579  LD  A,0(IPWPAC);
0000 | 0580  LD  A,0(IPWPAC);
0000 | 0581  LD  A,0(IPWPAC);
0000 | 0582  LD  A,0(IPWPAC);
0000 | 0583  LD  A,
```



```

0200 0505 ..R2 POINTING AT INPUT DATA
0201 0506 ..R4 IS PROGRAM COUNTER FOR ROUTINE
0202 0507 ..R7 IS LOOP COUNTER IN ROUTINE
0203 0508
0204 0509 ..ROUTINE IS CALLED AS FOLLOWS:-
0205 0510

0206 0611 ..SEP RA
0207 0612 ..PARAMETER 1 = ACCUMULATOR START-1
0208 0613 ..PARAMETER 2 = LOOKUP TABLE START
0209 0614 ..PARAMETER 3 = 0 INCLUDE 5 MAGNITUDE VALUES IN BOTTOM 51M
0210 0615 .. 1 EXCLUDE 5 MAGNITUDE VALUES FROM 51M
0211 0616
0212 0617
0213 0618 CONVE1 INC R01 REX R01 SEP R0 ..RETURN
0214 0619 CONP ONI R41 REX R0 ..SET R4 TO ACCUMULATOR SECTION
0215 0620 ADU ..PARAMETER 1
0216 0621 PLO R4
0217 0622 IRI
0218 0623 LDIA ..PARAMETER 2
0219 0624 PLO R1 ..LOOKUP TABLE POINTER
0220 0625 LDM R21 5H ..CHECK DATA AGAINST PARAMETER 3
0221 0626 5H CONVE1 ..NEGATIVE HEAVE DATA IS 1280 AND
0222 0627 ADG ..IS TO BE DISCARDED
0223 0628 SEE R1
0224 0629 CONCI 5H ..ABSTRACT 1ST TABLE VALUE.
0225 0630 IRI ..LOOP TABLE POINTER
0226 0631 INC R4 ..ACCUMULATOR POINTER
0227 0632 5H1 CONCI ..AND KEEP GOING UNTIL ONE FITS
0228 0633 LDM R4 ..THEN GET ACCUMULATED NUMBER
0229 0634 ADI 1
0230 0635 5I CONVE1 ..CHECK FOR POTENTIAL OVERFLOW
0231 0636 STR R4 ..IF OK STORE INCREMENTED VALUE
0232 0637 5H CONVE1
0233 0638
0234 0639
0235 0640
0236 0641
0237 0642
0238 0643
0239 0644
0240 0645
0241 0646
0242 0647
0243 0648
0244 0649
0245 0650
0246 0651
0247 0652
0248 0653
0249 0654
0250 0655
0251 0656
0252 0657
0253 0658
0254 0659
0255 0660
0256 0661
0257 0662
0258 0663
0259 0664
0260 0665
0261 0666
0262 0667
0263 0668
0264 0669
0265 0670
0266 0671
0267 0672
0268 0673
0269 0674
0270 0675
0271 0676
0272 0677
0273 0678
0274 0679
0275 0680
0276 0681
0277 0682
0278 0683
0279 0684
0280 0685
0281 0686
0282 0687
0283 0688
0284 0689
0285 0690
0286 0691
0287 0692
0288 0693
0289 0694
0290 0695
0291 0696
0292 0697
0293 0698
0294 0699
0295 0700
0296 0701
0297 0702
0298 0703
0299 0704
0300 0705
0301 0706
0302 0707
0303 0708
0304 0709
0305 0710
0306 0711
0307 0712
0308 0713
0309 0714
0310 0715
0311 0716
0312 0717

0313 F85F91 0548 LDI A.011P91M11 PLO R9
0314 F85F92 0549 STR R9
0315 F85F93 0550 STR R1
0316 F85F94 0551 LDI 0FFH STR R01 DEC R0 ..SET DAC TO FF
0317 F85F95 0552 LDM R01 STR R01 DEC R0 ..THEN READ PWR-EVENT VALUE
0318 F85F96 0553 LDM R01 STR R0 ..WAIT FOR 2-D CONVERSION
0319 F85F97 0554 LDI 1P91M11 PLO R9
0320 F85F98 0555 DEC R01 DLO R01 5H1 1P9DEL

0321 F85F99 0556 LDI A.011P91M11 PLO R9
0322 F85FA0 0557 STR R9
0323 F85FA1 0558 STR R1
0324 F85FA2 0559 LDI A.011P91M11 PLO R9 ..SEND 1P9WKE
0325 F85FA3 0560 LDM R01 STR R01 ADD ..SO OFFSET CAN BE ADDED
0326 F85FA4 0561 LDM R01 STR R01 ADD ..READ VALUE AND ADD OFFSET
0327 F85FA5 0562 LDM R01 STR R01 ADD ..TOTAL C18M
0328 F85FA6 0563 LDI 0FFH ..OTHERWISE FORCE TO 0FFH
0329 F85FA7 0564 STR R01 DEC R0 ..AND STUFF INTO DAC
0330 F85FA8 0565 SEP COMPU
0331 F85FA9 0566 DC A.011P9AC-111, A.011P9TAB, 1
0332 F85FAB 0567 OLO R21 ADI 4 ..START COMPUTATION BY TESTING
0333 F85FAC 0568 PLO R21 LDM R2 ..ENL SIGNAL BITS IN WORD 5
0334 F85FAD 0569 ANI 3H1 5I NOCAL
0335 F85FAE 0570 5H1 R41 ADI A.011P9CA1-511 PLO R4 ..AND OUTPUT DATA TO BLOCK
0336 F85FAF 0571 INC R21 BR 1P9P3 ..GO TO WORD 4
0337 F85FB0 0572 DEC R2 ..NEW WORD 4 BITS 0 AND 1
0338 F85FB1 0573 LDM R2
0339 F85FB2 0574 ANI 3 ..CATEGORY 3 EVENT
0340 F85FB3 0575 XRI 11 5I 1P9CAT3 ..CATEGORY 5 EVENT
0341 F85FB4 0576 XRI 31 5I 1P9CAT5
0342 F85FB5 0577 DEC R21 LDIA1 OR ..CHECK FOR NON-ZERO DATA IN WORDS
0343 F85FB6 0578 ANI 0FH ..AND 7 NO NUMBER 5 DATA
0344 F85FB7 0579 5I NOT357 ..WORD 4
0345 F85FB8 0580 IPCAT7 DC A.011P9CA+191, A.011P9TAB, 0 ..INCLUDE 0 DATA
0346 F85FB9 0581 0401 0H1 R41 ADI A.011P9CA1-111 PLO R4 ..TEST DATA RECORDED
0347 F85FBA 0582 LDM R41 ANI 31 5H1 1P9AT ..DO NOT OVERWRITE
0348 F85FBB 0583 OLO R41 ADI 41 PLO R4 ..SINCEWISE PGCT DATA.
0349 F85FBC 0584 5H1 1P9P1 ..WORD 5
0350 F85FBD 0585 SEP COMPU
0351 F85FBE 0586 DC A.011P9CA+111, A.011P9TAB, 0 ..WORD 6
0352 F85FBF 0587 0H1 R41 ADI A.011P9CA5-511 PLO R4
0353 F85FC0 0588 5H1 1P9P1 ..WORD 6
0354 F85FC1 0589 IPCAT5 SEP COMPU
0355 F85FC2 0590 DC A.011P9CA+31, A.011P9TAB, 0
0356 F85FC3 0591 0H1 R41 ADI A.011P9CA9-911 PLO R4
0357 F85FC4 0592 5H1 1P9P1 ..PUT DATA IN OUTPUT BUFFER
0358 F85FC5 0593 DEC R21 DEC R21 DEC R2
0359 F85FC6 0594 LDM R21 STR R21 ..POINT TO WORD 4
0360 F85FC7 0595 LDM R21 STR R21 ..BITS 0 AND 1
0361 F85FC8 0596 LDM R21 STR R21 ..CATEGORY 2 EVENT
0362 F85FC9 0597 LDM R21 STR R21 ..CATEGORY 4 EVENT
0363 F85FCA 0598 LDM R21 STR R21 ..CATEGORY 5 EVENT
0364 F85FCB 0599 LDM R21 STR R21 ..NO MORE 1P9P DATA
0365 F85FCC 0600 LDM R21 STR R21 ..WORD 4
0366 F85FCD 0601 IPCAT6 SEP COMPU
0367 F85FCE 0602 DC A.011P9CA+151, A.011P9TAB, 0
0368 F85FCF 0603
0369 F85FD0 0604
0370 F85FD1 0605
0371 F85FD2 0606
0372 F85FD3 0607
0373 F85FD4 0608
0374 F85FD5 0609
0375 F85FD6 0610
0376 F85FD7 0611
0377 F85FD8 0612
0378 F85FD9 0613
0379 F85FDA 0614
0380 F85FDB 0615
0381 F85FDC 0616
0382 F85FDD 0617
0383 F85FDE 0618
0384 F85FDF 0619
0385 F85FEE 0620
0386 F85FEF 0621
0387 F85FF0 0622
0388 F85FF1 0623
0389 F85FF2 0624
0390 F85FF3 0625
0391 F85FF4 0626
0392 F85FF5 0627
0393 F85FF6 0628
0394 F85FF7 0629
0395 F85FF8 0630
0396 F85FF9 0631
0397 F85FFA 0632
0398 F85FFB 0633
0399 F85FFC 0634
0400 F85FFD 0635
0401 F85FFE 0636
0402 F85FFF 0637
0403 F86000 0638
0404 F86001 0639
0405 F86002 0640
0406 F86003 0641
0407 F86004 0642
0408 F86005 0643
0409 F86006 0644
0410 F86007 0645
0411 F86008 0646
0412 F86009 0647
0413 F8600A 0648
0414 F8600B 0649
0415 F8600C 0650
0416 F8600D 0651
0417 F8600E 0652
0418 F8600F 0653
0419 F86010 0654
0420 F86011 0655
0421 F86012 0656
0422 F86013 0657
0423 F86014 0658
0424 F86015 0659
0425 F86016 0660
0426 F86017 0661
0427 F86018 0662
0428 F86019 0663
0429 F8601A 0664
0430 F8601B 0665
0431 F8601C 0666
0432 F8601D 0667
0433 F8601E 0668
0434 F8601F 0669
0435 F86020 0670
0436 F86021 0671
0437 F86022 0672
0438 F86023 0673
0439 F86024 0674
0440 F86025 0675
0441 F86026 0676
0442 F86027 0677
0443 F86028 0678
0444 F86029 0679
0445 F8602A 0680
0446 F8602B 0681
0447 F8602C 0682
0448 F8602D 0683
0449 F8602E 0684
0450 F8602F 0685
0451 F86030 0686
0452 F86031 0687
0453 F86032 0688
0454 F86033 0689
0455 F86034 0690
0456 F86035 0691
0457 F86036 0692
0458 F86037 0693
0459 F86038 0694
0460 F86039 0695
0461 F8603A 0696
0462 F8603B 0697
0463 F8603C 0698
0464 F8603D 0699
0465 F8603E 0700
0466 F8603F 0701
0467 F86040 0702
0468 F86041 0703
0469 F86042 0704
0470 F86043 0705
0471 F86044 0706
0472 F86045 0707
0473 F86046 0708
0474 F86047 0709
0475 F86048 0710
0476 F86049 0711
0477 F8604A 0712
0478 F8604B 0713
0479 F8604C 0714
0480 F8604D 0715
0481 F8604E 0716
0482 F8604F 0717
0483 F86050 0718
0484 F86051 0719
0485 F86052 0720
0486 F86053 0721
0487 F86054 0722
0488 F86055 0723
0489 F86056 0724
0490 F86057 0725
0491 F86058 0726
0492 F86059 0727
0493 F8605A 0728
0494 F8605B 0729
0495 F8605C 0730
0496 F8605D 0731
0497 F8605E 0732
0498 F8605F 0733
0499 F86060 0734
0500 F86061 0735
0501 F86062 0736
0502 F86063 0737
0503 F86064 0738
0504 F86065 0739
0505 F86066 0740
0506 F86067 0741
0507 F86068 0742
0508 F86069 0743
0509 F8606A 0744
0510 F8606B 0745
0511 F8606C 0746
0512 F8606D 0747
0513 F8606E 0748
0514 F8606F 0749
0515 F86070 0750
0516 F86071 0751
0517 F86072 0752
0518 F86073 0753
0519 F86074 0754
0520 F86075 0755
0521 F86076 0756
0522 F86077 0757
0523 F86078 0758
0524 F86079 0759
0525 F8607A 0760
0526 F8607B 0761
0527 F8607C 0762
0528 F8607D 0763
0529 F8607E 0764
0530 F8607F 0765
0531 F86080 0766
0532 F86081 0767
0533 F86082 0768
0534 F86083 0769
0535 F86084 0770
0536 F86085 0771
0537 F86086 0772
0538 F86087 0773
0539 F86088 0774
0540 F86089 0775
0541 F8608A 0776
0542 F8608B 0777
0543 F8608C 0778
0544 F8608D 0779
0545 F8608E 0780
0546 F8608F 0781
0547 F86090 0782
0548 F86091 0783
0549 F86092 0784
0550 F86093 0785
0551 F86094 0786
0552 F86095 0787
0553 F86096 0788
0554 F86097 0789
0555 F86098 0790
0556 F86099 0791
0557 F8609A 0792
0558 F8609B 0793
0559 F8609C 0794
0560 F8609D 0795
0561 F8609E 0796
0562 F8609F 0797
0563 F860A0 0798
0564 F860A1 0799
0565 F860A2 0800
0566 F860A3 0801
0567 F860A4 0802
0568 F860A5 0803
0569 F860A6 0804
0570 F860A7 0805
0571 F860A8 0806
0572 F860A9 0807
0573 F860AA 0808
0574 F860AB 0809
0575 F860AC 0810
0576 F860AD 0811
0577 F860AE 0812
0578 F860AF 0813
0579 F860B0 0814
0580 F860B1 0815
0581 F860B2 0816
0582 F860B3 0817
0583 F860B4 0818
0584 F860B5 0819
0585 F860B6 0820
0586 F860B7 0821
0587 F860B8 0822
0588 F860B9 0823
0589 F860BA 0824
0590 F860BB 0825
0591 F860BC 0826
0592 F860BD 0827
0593 F860BE 0828
0594 F860BF 0829
0595 F860C0 0830
0596 F860C1 0831
0597 F860C2 0832
0598 F860C3 0833
0599 F860C4 0834
0600 F860C5 0835
0601 F860C6 0836
0602 F860C7 0837
0603 F860C8 0838
0604 F860C9 0839
0605 F860CA 0840
0606 F860CB 0841
0607 F860CC 0842
0608 F860CD 0843
0609 F860CE 0844
0610 F860CF 0845
0611 F860D0 0846
0612 F860D1 0847
0613 F860D2 0848
0614 F860D3 0849
0615 F860D4 0850
0616 F860D5 0851
0617 F860D6 0852
0618 F860D7 0853
0619 F860D8 0854
0620 F860D9 0855
0621 F860DA 0856
0622 F860DB 0857
0623 F860DC 0858
0624 F860DD 0859
0625 F860DE 0860
0626 F860DF 0861
0627 F860E0 0862
0628 F860E1 0863
0629 F860E2 0864
0630 F860E3 0865
0631 F860E4 0866
0632 F860E5 0867
0633 F860E6 0868
0634 F860E7 0869
0635 F860E8 0870
0636 F860E9 0871
0637 F860EA 0872
0638 F860EB 0873
0639 F860EC 0874
0640 F860ED 0875
0641 F860EE 0876
0642 F860EF 0877
0643 F860F0 0878
0644 F860F1 0879
0645 F860F2 0880
0646 F860F3 0881
0647 F860F4 0882
0648 F860F5 0883
0649 F860F6 0884
0650 F860F7 0885
0651 F860F8 0886
0652 F860F9 0887
0653 F860FA 0888
0654 F860FB 0889
0655 F860FC 0890
0656 F860FD 0891
0657 F860FE 0892
0658 F860FF 0893
0659 F86100 0894
0660 F86101 0895
0661 F86102 0896
0662 F86103 0897
0663 F86104 0898
0664 F86105 0899
0665 F86106 0900
0666 F86107 0901
0667 F86108 0902
0668 F86109 0903
0669 F8610A 0904
0670 F8610B 0905
0671 F8610C 0906
0672 F8610D 0907
0673 F8610E 0908
0674 F8610F 0909
0675 F86110 0910
0676 F86111 0911
0677 F86112 0912
0678 F86113 0913
0679 F86114 0914
0680 F86115 0915
0681 F86116 0916
0682 F86117 0917
0683 F86118 0918
0684 F86119 0919
0685 F8611A 0920
0686 F8611B 0921
0687 F8611C 0922
0688 F8611D 0923
0689 F8611E 0924
0690 F8611F 0925
0691 F86120 0926
0692 F86121 0927
0693 F86122 0928
0694 F86123 0929
0695 F86124 0930
0696 F86125 0931
0697 F86126 0932
0698 F86127 0933
0699 F86128 0934
0700 F86129 0935

```


APPENDIX 2

Byte corrections for spurious resets.

In section 5.4.3 a description was given of the effect caused by a number of resets that occurred in the last 40s before closest approach. Corrected counts are listed below which correspond to the count rate that would have been recorded by the sensor had it integrated for the normal 1.13s period.

A summary of the each block affected by the resets is also presented.

43429	IPM	D23	D4	D5
00:10:23	5		9.5	0
	0		2	0
	1.5		0	0
	0		0	0
43430	IPM	D23	D4	D5
00:10:25	6.5	13	11	0
	0	1.5	0.5	0
	0	0	0	0
	0	0	0	0
43435	IPM	D23	D4	D5
00:10:31	4.5	19	13	0
	0	2	2	0
	3	0	0	0
	0	0	0	0
43437	IPM	D23	D4	D5
00:10:35	15		19.5	0
	1		2.5	0
	1.5		1	0
	3		0	0
43448	IPM	D23	D4	D5
00:10:47	62	73	47	0
	0	0	0	0
	6.5	0	0	0
	0	0	0	0
43449	IPM	D23	D4	D5
00:10:48	85	58.5	36.5	0
	4.5	0	8.5	1
	3.5	0	1	0
	2.5	0	0	0

Block/Time	COMMENT
43428 00:10:22	First 56 bytes transmitted before spurious reset, DGI re-transmitted after block 43429 with first 56 bytes set to zero.
43429 00:10:23	Integrated for time taken to transmit block 43429 before reset plus time to transmit preceding bytes in DGI. Change in mode on reset makes DID2/3 counts invalid.
43430 00:10:25	Integrated for between 2.26s for first byte in DGI and 1.13s for last byte in DGI.
43434 00:10:30	First 79 bytes transmitted before format related reset, DGI re-transmitted immediately with first 79 bytes set to zero.
43435 00:10:31	Integrated for 1.13s plus time to transmit block 43434 before reset.
43436 00:10:33	First 115 bytes transmitted before spurious reset, DGI re-transmitted immediately with first 115 bytes set to zero.
43437 00:10:35	Integrated for 1.13s plus time to transmit block 43436 before reset. Change in mode on reset makes DID2/3 counts invalid.
43447 00:10:46	First 15 bytes transmitted before spurious reset, DGI re-transmitted after block 43448 with first 15 bytes set to zero.
43448 00:10:47	Integrated over time taken to transmit block 43447 before reset plus time taken to transmit preceding bytes in DGI.
43449 00:10:48	Integrated for between 2.26s for first byte in DGI and 1.13s for last byte in DGI. An unknown number of resets occur in this DGI extending the integration time for block 43450.
43450 00:10:53	Integrated for approximately 4.5s. Only first few bytes in DGI are non-zero perhaps due to further resets, valid data looks saturated.

APPENDIX 3

'Category 4' events.

In Section 7.2 a method was described for calculating a mass for each event in the 'Category 4' DID 4 only 'discrete' data set. These values are listed below:-

Column 1 contains the ground receive time of the DGI containing the event.

Column 2 contains the block number of the DGI

Column 3 contains the category counter for 'Category 4'.

Column 4 contains the digital amplitude of the event.

Column 5 contains the calculated mass of the event.

23: 1: 0	39755	1	137	5.1974522E-11
23:13:50	40435	1	110	2.8972567E-11
23:17:14	40615	1	127	3.9416369E-11
23:18: 0	40655	1	103	2.6387718E-11
23:27:47	41173	1	109	2.8574759E-11
23:30: 3	41293	1	143	6.4908315E-11
23:33:51	41494	1	142	6.2317110E-11
23:33:55	41498	1	134	4.7329425E-11
23:38:29	41740	1	107	2.7821023E-11
23:41:23	41893	1	106	2.7403335E-11
23:41:49	41916	1	133	4.5815806E-11
23:42:55	41974	1	173	4.0920006E-10
23:43:41	42015	1	137	5.1974522E-11
23:43:49	42022	1	141	5.9818595E-11
23:46:23	42158	1	132	4.4754343E-11
23:46:59	42190	1	143	6.4908315E-11
23:47:56	42240	1	122	3.5535980E-11
23:48:19	42260	1	137	5.1974522E-11
23:48:51	42288	1	177	5.4287258E-10
23:49:21	42315	1	72	1.9688719E-11
23:50: 1	42350	1	159	1.5079976E-10
23:51:10	42411	1	136	5.0414284E-11
23:52: 1	42456	1	143	6.4908315E-11
23:52:10	42464	1	117	3.2378874E-11
23:52:42	42492	1	127	3.9416369E-11
23:53: 1	42509	1	103	2.6387718E-11
23:53:51	42553	1	156	1.2700457E-10
23:54:50	42605	1	117	3.2378874E-11
23:55: 6	42619	1	149	8.5256677E-11
23:55:26	42637	1	142	6.2317110E-11
23:56: 9	42675	1	151	9.3839256E-11
23:56:40	42702	1	77	2.0459263E-11
23:57: 8	42727	1	123	3.6137867E-11
23:57:16	42734	1	111	2.9447483E-11
23:57:41	42756	1	126	3.8526359E-11
23:57:58	42771	1	163	2.0004934E-10
23:58: 2	42775	1	149	8.5256677E-11
23:58: 8	42780	1	127	3.9416369E-11
23:58:14	42785	1	133	4.5815806E-11
23:58:16	42787	1	165	2.2820530E-10
23:58:27	42797	2	133	4.5815806E-11
23:59: 8	42833	1	134	4.7329425E-11
23:59:20	42843	2	105	2.7107587E-11
23:59:21	42844	1	127	3.9416369E-11
23:59:22	42845	1	105	2.7107587E-11

23:59:29	42851	1	114	3.0743536E-11
23:59:43	42864	1	91	2.3142880E-11
23:59:50	42870	1	156	1.2700457E-10
23:59:51	42871	1	149	8.5256677E-11
0: 0: 7	42885	1	152	9.9314043E-11
0: 0:42	42916	1	143	6.4908315E-11
0: 0:45	42918	1	137	5.1974522E-11
0: 1: 6	42937	1	127	3.9416369E-11
0: 1: 7	42938	2	127	3.9416369E-11
0: 1: 9	42940	2	93	2.3594579E-11
0: 1:15	42945	1	105	2.7107587E-11
0: 1:32	42960	1	134	4.7329425E-11
0: 1:33	42961	1	85	2.1867497E-11
0: 1:34	42962	1	153	1.0512276E-10
0: 1:40	42967	1	117	3.2378874E-11
0: 1:43	42970	1	119	3.3577068E-11
0: 1:47	42973	1	126	3.8526359E-11
0: 2:16	42999	1	159	1.5079976E-10
0: 2:27	43008	1	148	8.0590479E-11
0: 3: 6	43043	1	98	2.4923102E-11
0: 3:18	43053	1	132	4.4754343E-11
0: 3:38	43071	1	109	2.8574759E-11
0: 3:41	43074	1	132	4.4754343E-11
0: 3:46	43078	2	113	3.0290201E-11
0: 4:13	43102	1	124	3.6896604E-11
0: 4:37	43123	1	105	2.7107587E-11
0: 4:38	43124	2	148	8.0590479E-11
0: 5: 1	43144	1	101	2.5755117E-11
0: 5:15	43157	1	110	2.8972567E-11
0: 5:20	43161	1	158	1.4241130E-10
0: 5:28	43168	1	95	2.4099417E-11
0: 5:39	43178	1	115	3.1340326E-11
0: 5:57	43194	1	75	2.0140417E-11
0: 6: 9	43204	1	119	3.3577068E-11
0: 6:10	43205	1	85	2.1867497E-11
0: 6:15	43210	1	150	8.9447352E-11
0: 6:20	43214	1	101	2.5755117E-11
0: 6:25	43218	1	180	6.7768707E-10
0: 6:34	43226	2	149	8.5256677E-11
0: 6:53	43243	1	127	3.9416369E-11
0: 6:55	43245	1	75	2.0140417E-11
0: 7: 6	43255	1	119	3.3577068E-11
0: 7: 9	43257	1	147	7.7451427E-11
0: 7:13	43261	1	125	3.7731131E-11
0: 7:18	43265	1	127	3.9416369E-11
0: 7:25	43271	1	134	4.7329425E-11
0: 7:34	43279	1	127	3.9416369E-11
0: 7:35	43280	1	95	2.4099417E-11
0: 7:43	43287	1	116	3.1772231E-11
0: 7:50	43293	1	90	2.2903747E-11
0: 7:51	43294	1	136	5.0414284E-11
0: 7:54	43297	1	126	3.8526359E-11
0: 7:57	43300	1	127	3.9416369E-11
0: 8: 2	43304	1	138	5.3537969E-11
0: 8:11	43312	1	151	9.3839256E-11
0: 8:13	43314	1	107	2.7821023E-11
0: 8:20	43320	1	127	3.9416369E-11
0: 8:24	43323	2	140	5.7412165E-11
0: 8:33	43331	2	118	3.2934176E-11
0: 8:35	43333	1	127	3.9416369E-11
0: 8:37	43335	1	140	5.7412165E-11
0: 8:38	43336	1	121	3.4786306E-11
0: 8:39	43337	1	38	1.6008708E-11

0: 8:41	43338	2	122	3.5535980E-11
0: 8:42	43339	1	143	6.4908315E-11
0: 8:45	43342	1	102	2.6106327E-11
0: 8:47	43344	2	137	5.1974522E-11
0: 8:50	43346	1	93	2.3594579E-11
0: 8:52	43348	3	155	1.1781479E-10
0: 8:53	43349	2	135	4.8863972E-11
0: 8:55	43351	1	90	2.2903747E-11
0: 8:56	43352	1	88	2.2478618E-11
0: 8:59	43354	2	125	3.7731131E-11
0: 9: 0	43355	1	115	3.1340326E-11
0: 9: 1	43356	3	114	3.0743536E-11
0: 9: 3	43358	1	61	1.8253912E-11
0: 9:11	43365	2	116	3.1772231E-11
0: 9:12	43366	1	134	4.7329425E-11
0: 9:13	43367	3	41	1.6261128E-11
0: 9:15	43368	1	125	3.7731131E-11
0: 9:16	43369	1	154	1.1128337E-10
0: 9:18	43371	1	121	3.4786306E-11
0: 9:20	43373	1	103	2.6387718E-11
0: 9:27	43379	3	143	6.4908315E-11
0: 9:32	43383	1	85	2.1867497E-11
0: 9:34	43385	1	154	1.1128337E-10
0: 9:35	43386	2	138	5.3537969E-11
0: 9:37	43388	3	70	1.9396445E-11
0: 9:38	43389	1	122	3.5535980E-11
0: 9:41	43391	1	76	2.0299840E-11
0: 9:43	43393	1	126	3.8526359E-11
0: 9:45	43395	1	137	5.1974522E-11
0: 9:46	43396	3	116	3.1772231E-11
0: 9:47	43397	3	127	3.9416369E-11
0: 9:49	43398	3	136	5.0414284E-11
0: 9:50	43399	2	149	8.5256677E-11
0: 9:54	43403	3	147	7.7451427E-11
0: 9:58	43406	1	113	3.0290201E-11
0: 9:59	43407	1	125	3.7731131E-11
0:10: 0	43408	3	102	2.6106327E-11
0:10: 1	43409	2	148	8.0590479E-11
0:10: 2	43410	4	108	2.8174456E-11
0:10: 3	43411	2	124	3.6896604E-11
0:10: 4	43412	2	119	3.3577068E-11
0:10: 6	43413	3	113	3.0290201E-11
0:10: 7	43414	2	115	3.1340326E-11
0:10: 8	43415	4	160	1.6259831E-10
0:10: 9	43416	4	117	3.2378874E-11
0:10:10	43417	5	134	4.7329425E-11
0:10:11	43418	6	134	4.7329425E-11
0:10:12	43419	3	135	4.8863972E-11
0:10:13	43420	1	148	8.0590479E-11
0:10:15	43421	3	138	5.3537969E-11
0:10:16	43422	3	99	2.5188806E-11
0:10:17	43423	5	127	3.9416369E-11
0:10:18	43424	3	148	8.0590479E-11
0:10:19	43425	6	104	2.6740561E-11
0:10:20	43426	6	107	2.7821023E-11
0:10:21	43427	9	73	1.9821571E-11
0:10:29	43433	8	115	3.1340326E-11
0:10:30	43434	21	117	3.2378874E-11
0:10:32	43435	15	139	5.5454818E-11
0:10:33	43436	10	127	3.9416369E-11
0:10:37	43439	2	170	3.2428632E-10
0:10:39	43441	2	138	5.3537969E-11
0:10:41	43442	2	142	6.2317110E-11

0:10:43	43444	1	118	3.2934176E-11
0:10:44	43445	1	105	2.7107587E-11
0:10:45	43446	8	157	1.3448732E-10
0:10:46	43448	3	127	3.9416369E-11
0:11:20	43458	15	158	1.4241130E-10
0:11:22	43459	15	146	7.3238651E-11
0:11:23	43460	9	137	5.1974522E-11
0:11:24	43461	16	150	8.9447352E-11
0:11:27	43464	17	170	3.2428632E-10
0:11:31	43467	17	135	4.8863972E-11
0:11:34	43470	11	134	4.7329425E-11
0:11:37	43473	9	132	4.4754343E-11
0:11:41	43475	9	151	9.3839256E-11
0:11:42	43476	5	137	5.1974522E-11
0:11:43	43477	5	166	2.4579361E-10
0:11:45	43479	4	118	3.2934176E-11
0:11:46	43480	11	167	2.6464916E-10
0:11:50	43483	4	157	1.3448732E-10
0:11:54	43487	3	122	3.5535980E-11
0:11:55	43488	1	117	3.2378874E-11
0:11:57	43489	1	135	4.8863972E-11
0:11:58	43490	1	160	1.6259831E-10
0:11:59	43491	2	79	2.0778108E-11
0:12: 0	43492	4	156	1.2700457E-10
0:12: 2	43494	1	172	3.7487655E-10
0:12: 6	43497	2	102	2.6106327E-11
0:12: 9	43500	1	58	1.7908498E-11
0:12:10	43501	4	178	5.9051403E-10
0:12:14	43504	2	98	2.4923102E-11
0:12:15	43505	1	143	6.4908315E-11
0:12:16	43506	2	119	3.3577068E-11
0:12:19	43509	3	212	2.0139329E-07
0:12:25	43514	1	148	8.0590479E-11
0:12:26	43515	1	89	2.2691182E-11
0:12:27	43516	1	168	2.8485217E-10
0:12:28	43517	1	100	2.5454510E-11
0:12:34	43522	1	95	2.4099417E-11
0:12:43	43530	2	127	3.9416369E-11
0:12:46	43533	1	175	4.7170368E-10
0:12:54	43540	1	171	3.5441344E-10
0:12:58	43543	1	161	1.7528604E-10
0:12:59	43544	2	149	8.5256677E-11
0:13: 6	43550	1	149	8.5256677E-11
0:13:14	43557	1	74	1.9980994E-11
0:13:15	43558	1	173	4.0920006E-10
0:13:18	43561	1	140	5.7412165E-11
0:13:33	43574	1	163	2.0004934E-10
0:13:40	43580	1	158	1.4241130E-10
0:13:49	43588	1	110	2.8972567E-11
0:14: 5	43602	1	151	9.3839256E-11
0:14: 6	43603	1	109	2.8574759E-11
0:14: 9	43606	1	65	1.8732182E-11
0:14:20	43616	1	120	3.4168744E-11
0:14:40	43633	1	151	9.3839256E-11
0:14:47	43639	1	136	5.0414284E-11
0:14:56	43647	1	71	1.9542581E-11
0:15:33	43680	1	107	2.7821023E-11
0:15:59	43703	1	93	2.3594579E-11
0:16:20	43721	1	161	1.7528604E-10
0:16:37	43736	1	132	4.4754343E-11
0:16:52	43750	1	91	2.3142880E-11
0:17: 6	43762	1	96	2.4338550E-11
0:17:40	43792	1	139	5.5454818E-11

0:18:19	43826	1	174	4.3943008E-10
0:18:46	43850	1	126	3.8526359E-11
0:18:50	43854	1	104	2.6740561E-11
0:19:16	43877	1	125	3.7731131E-11
0:19:33	43892	1	121	3.4786306E-11
0:19:49	43906	1	97	2.4604254E-11
0:19:56	43912	1	141	5.9818595E-11
0:20: 5	43920	1	89	2.2691182E-11
0:20:19	43932	-9	87	2.2266055E-11
0:20:30	43942	2	150	8.9447352E-11
0:20:39	43950	1	126	3.8526359E-11
0:20:46	43956	1	132	4.4754343E-11
0:20:56	43965	1	147	7.7451427E-11
0:21:56	44018	1	173	4.0920006E-10
0:22:54	44069	1	101	2.5755117E-11
0:23: 1	44075	1	173	4.0920006E-10
0:23: 9	44082	1	132	4.4754343E-11
0:24:50	44171	1	121	3.4786306E-11
0:25:45	44220	1	123	3.6137867E-11
0:26: 3	44236	1	166	2.4579361E-10
0:28: 2	44341	1	141	5.9818595E-11
0:28:52	44385	1	122	3.5535980E-11
0:31:18	44514	1	89	2.2691182E-11
0:32:49	44594	1	114	3.0743536E-11
0:32:53	44598	1	93	2.3594579E-11
0:34:35	44688	1	144	6.7592439E-11
0:36: 8	44770	1	78	2.0618686E-11
0:39:56	44971	1	99	2.5188806E-11
0:45:14	45251	1	132	4.4754343E-11
1: 0:13	46045	1	85	2.1867497E-11

APPENDIX 4

Publications

- Green S.F., McDonnell J.A.M., Perry C.H., Nappo S., and Zarnecki J.C., **1987**, 'P/Halley dust coma: Grains or Rocks?', *ESA SP-278*, pp.379-384.
- Maas D., Göller J.R., Grün E., Lange G., McDonnell J.A.M., Nappo S., Perry C., and Zarnecki J.C., **1989**, 'Cometary dust particles detected by the DIDSY - IPM-P sensor on board Giotto', *Adv. Space Res.*, **9**, 3, pp.247-252.
- McDonnell J.A.M., Kissel J., Grün E., Grard R.J., Langevin Y., Olearczyk R.E., Perry C.H., and Zarnecki J.C., **1986c**, 'Giotto's dust impact detections system DIDSY and particulate impact analyser PIA: interim assessment of the dust distribution and properties within the coma', *ESA SP-250*, II, pp.25-38.
- McDonnell J.A.M., Alexander W.M., Burton W.M., Bussoletti E., Evans G.C., Evans S.T., Firt J.G., Grard R.J.L., Green S.F., Grün E., Hanner M.S., Hughes D.W., Igenbergs E., Kissel J., Kuczera H., Lindblad B.A., Langevin Y., Mandeville J.C., Nappo S., Pankiewicz G.S., Perry C.H., Schwehm G.H., Sekanina Z., Stevenson T.J., Turner R.F., Weishaupt U., Wallis M.K., and Zarnecki J.C., **1987**, 'The dust distribution within the inner coma of comet P/Halley 1982i: Encounter by Giotto's impact detectors', *Astron. Astrophys.*, **187**, pp.719-741.
- McDonnell J.A.M., Green S.F., Grün E., Kissel J., Nappo S., Pankiewicz G.S., and Perry C.H., **1989**, 'In-situ exploration of the dusty coma of comet P/Halley at Giotto's encounter: Flux rates and time profiles from 10-19kg to 10-5kg', *Adv. Space Res.*,
- McDonnell J.A.M., Green S.F., Nappo S., Pankiewicz G.S., Perry C.H. and Zarnecki J.C., 'Dust mass distributions: The perspective from Giotto's measurements at P/Halley', presented at the 'Comets in the post - Halley era' colloquium, Bamberg (FRG), (April 24-28 1989)
- McDonnell J.A.M., Pankiewicz G.S., Birchley P.N.W., Green S.F., and Perry C.H., **1990**, 'The Comet Nucleus: Ice and Dust Morphological Balances in a Production Surface of Comet P/Halley', *Proceedings of the 20th Lunar and Planetary Science Conference*, pp.373-378.
- Pankiewicz G.S., Nappo S. and Perry C.H., **1988**, 'The Giotto - Halley encounter: Dust impact analysis at Kent', *JBIS*, **41**, pp.411-419.

- Pankiewicz G.S., McDonnell J.A.M. and Perry C.H., 1989, 'In-situ exploration of the dusty coma of comet P/Halley at Giotto's encounter: Nucleus emission and production rates from temporal variability', *Adv. Space Res.*,
- Perry C.H., Green S.F. & McDonnell J.A.M., 1987, 'A possible explanation for the inconsistency between the Giotto grain mass distribution and groundbased observations', in '*Infrared observations of comets Halley and Wilson and properties of the grains*', NASA conference publication 3004, pp. 178-180.
- Perry C.H. and Nappo S., 'A Search for non-random effects in Giotto dust impact data', *Poster paper presented at Comets, Asteroids, Meteors III, Uppsala, June 12-15, 1989.*

